Characterization and Modeling of Spatiotemporal Behaviors in Corals, Elastic Metamaterials and Origami

Shuaifeng Li

A dissertation
submitted in partial fulfillment of the
requirements for the degree of

Doctor of Philosophy

University of Washington

2023

Reading Committee:

Jinkyu Yang, Chair

Marco Salviato

Krithika Manohar

Dana Dabiri

Program Authorized to Offer Degree:
Aeronautics and Astronautics

University of Washington

Abstract

Characterization and Modeling of Spatiotemporal Behaviors in Corals, Elastic Metamaterials and Origami

Shuaifeng Li

Chair of the Supervisory Committee:
Professor Jinkyu Yang
Department of Aeronautics and Astronautics

Spatiotemporal behaviors have been widely found in natural and artificial systems, indicating the movement and dynamics that occur in both space and time. These behaviors have significant impact on numerous fields, including ecology, finance, transportation and mechanical engineering. Some examples of spatiotemporal behaviors in these fields include the movement of animals, human behaviors, traffic flow, and vibrations. Understanding spatiotemporal behaviors is essential for developing effective management strategies and gaining insights into the underlying physical mechanisms that motivate these behaviors.

Coral reef ecosystems harbor a vast range of species and biological activities, but they are facing a severe crisis caused by the increasingly intensive anthropogenic activities and climate change. To better understand the impact of these challenges on coral reef survival and fitness, it is essential to comprehend the behaviors of corals in a timely manner. Coral motion, encompassing the movements of tissues, polyps, and tentacles, is a fundamental behavioral trait of the coral holobiont that plays a critical role in feeding, competition, reproduction, and ultimately survival. As a result, characterizing coral behaviors through motion analysis can aid our understanding in basic biological and physical functions. Nevertheless, characterization and modeling of coral motion are challenging and largely unexplored, given the complexity of the biological system and the inherent spatiotemporal multi-scale features of these movements. Apart from the corals, artificial systems such as elastic metamaterials

and origami structures also possess spatiotemporal behaviors such as elastic wave propagation and structural dynamics. However, the lack of corresponding data-driven analysis and nonlinear nature of origami structures result in the research voids.

To address these challenges in characterization and modeling of spatiotemporal behaviors, in terms of coral motions, we have implemented a range of approaches, including observation techniques, imaging processing techniques, and theoretical/data-driven modeling. Specifically, we have employed several techniques used in the engineering fields such as digital image correlation, motion magnification and object tracking, as well as modeling methods such as the Langevin equation and dynamic mode decomposition. These methods have been proven effective in characterizing and modeling the motion of coral tissues, polyps and tentacles. By combining these different approaches, we aim to better understand the underlying biophysics of corals and to develop new tools and methodologies for managing the impact of climate change on coral reef ecosystems. Furthermore, in terms of elastic metamaterials and origami, we use theoretical modeling and dynamic mode decomposition (and its variants) to characterize and model the corresponding systems. Our approaches provide insights into the underlying physics in wave dynamics and structural dynamics, and develop models for predicting the future responses under external stimuli.

Our work has not only resulted in unparalleled understanding of coral biophysical behaviors in terms of motions, providing a useful toolkit for the coral research community to face the challenges in the future climate change, but also paved the way in characterizing and modeling elastic wave propagation and origami dynamics using theoretical/data-driven methods. We anticipate that our methods, particularly the data-driven approach of dynamic mode decomposition, will be applicable to solve problems of dynamics in a variety of complex systems in the future research.

TABLE OF CONTENTS

Page

List of Figures v

List of Tables xvi

Chapter 1: Introduction 1
- 1.1 Background 1
- 1.2 Spatiotemporal behaviors in corals 3
- 1.3 Spatiotemporal behaviors in elastic metamaterials and origami 6
- 1.4 Data-driven modeling by dynamic mode decomposition 8
- 1.5 Organization of the dissertation 11

Chapter 2: Digital image processing to detect subtle motion in stony coral 13
- 2.1 Introduction 13
- 2.2 Experimental system 16
- 2.3 Characterization by digital image correlation 17
- 2.4 Characterization by optical flow 20
- 2.5 Motion microscope for the coral tissue surface 22
- 2.6 Conclusion and discussion 24
- 2.7 Author contribution 25

Chapter 3: Spatiotemporal dynamics of coral polyps on a fluidic platform 26
- 3.1 Introduction 26
- 3.2 Experimental system 28
- 3.3 Motion correlation of polyps 30
- 3.4 Fractional Brownian motion and its power spectral densities 33
- 3.5 Theoretical modeling via Langevin dynamics 36
- 3.6 Conclusion and discussion 39
- 3.7 Author contribution 40

Chapter 4: Data-driven discovery of spatiotemporal coherent patterns in pulsating soft coral tentacle motion with dynamic mode decomposition . . . 42
4.1 Introduction 42
4.2 Experimental system 44
4.3 DMD spectrum and $1/f$-type motion 45
4.4 Characterization of dynamic coherent patterns 52
4.5 Effect of light conditions 57
4.6 Conclusion and discussion 59
4.7 Author contribution 60

Chapter 5: Elastic chiral Landau level and snake states in origami metamaterials . 62
5.1 Introduction 62
5.2 Design of origami metamaterials 64
5.3 Emergence of elastic Landau levels 66
5.4 Elastic snake states 70
5.5 Conclusions and discussion 72
5.6 Author contribution 73

Chapter 6: Characterization of elastic topological states using dynamic mode decomposition 74
6.1 Introduction 74
6.2 Design of topological elastic metamaterials 76
6.3 Characterization by dynamic mode decomposition 79
6.4 Classification of topological and traditional metamaterials 86
6.5 Conclusion and discussion 89
6.6 Author contribution 91

Chapter 7: Geometry-informed dynamic mode decomposition in origami dynamics 92
7.1 Introduction 92
7.2 Geometry-informed DMD for Kresling origami 94
7.3 Topological boundary states in the origami chain 99
7.4 Dynamic motion in the dual origami structure 103
7.5 Conclusion and discussion 106
7.6 Author contribution 109

Chapter 8: Conclusion and future challenges 110

Bibliography 113

Appendix A: Digital image processing to detect subtle motion in stony coral 137
- A.1 Experimental methods 137
- A.2 Extraction of luminance of images 138
- A.3 Digital image correlation of the coral skeleton 139
- A.4 Optical flow of the coral skeleton 142

Appendix B: Spatiotemporal dynamics of coral polyps on a fluidic platform 144
- B.1 Experimental methods 144
- B.2 Data-driven parameterization of the Langevin equation 146
- B.3 Modeling of the stochastic term in Langevin dynamics by the maximum-likelihood method 148
- B.4 The model of in-plane waving motion of coral polyps at different temperatures 150

Appendix C: Data-driven discovery of spatiotemporal coherent patterns in pulsating soft coral tentacle motion with dynamic mode decomposition . . . 152
- C.1 Experimental methods 152

Appendix D: Elastic chiral Landau level and snake states in origami metamaterials . 155
- D.1 Simulation setup 155
- D.2 $\mathbf{k} \cdot \mathbf{p}$ perturbation method 157
- D.3 Theoretical Landau level dispersion 158

Appendix E: Characterization of elastic topological states using dynamic mode decomposition 160
- E.1 The truncation of singular values of the data matrix 160
- E.2 DMD spectra and modes of wave propagation along interface with different shapes 161
- E.3 DMD implementation on the topological state propagation excited by a transient source 162
- E.4 Dynamic mode decomposition with time-delay embedding 164
- E.5 Classification of topological and traditional metamaterials with different interfaces 165
- E.6 Synthetic wave propagation along the given interface using DMD 166

Appendix F: Geometry-informed dynamic mode decomposition in origami dynamics 170
- F.1 Data acquisition 170

F.2 Error analysis in different training ratios 172
F.3 Identification of state in different training ratios 174

LIST OF FIGURES

Figure Number Page

2.1 Experimental observation of *Montipora capricornis*. (a) Schematic of experimental setup of a DSLR camera, aimed at the corals in the aquarium. (b) Daylight pictures were taken under white light, while (c) nighttime pictures were taken under blue light. Daylight pictures were taken under white light, while (c) nighttime pictures were taken under blue light. 16

2.2 Displacements of the coral tissue surface from digital image correlation. (a) The displacements u_x along horizontal direction between the reference picture and the second picture at day and night are shown in the left and right panel, respectively. (b) The displacements u_y along horizontal direction between the reference picture and the second picture at day and night are shown in the left and right panel, respectively. (c) The percentage histograms of displacement u_x and displacement u_y are shown in the left and right panels, respectively. The red and blue curves indicate the means of each displacement during day and night. The pink and cyan regions are variations during day and night, respectively. 18

2.3 Strains of the coral tissue surface from digital image correlation. (a)-(c) Strains ϵ_{xx}, ϵ_{xy} and ϵ_{yy} between the first and the second picture from day and night are shown in the left and right panel, respectively. Green curves in (a) and (b) represents the edge of the fragment and white curves enclose the polyps. (d) The percentage histogram of the strains, ϵ_{xx}, ϵ_{xy} and ϵ_{yy} are shown in the left, middle and right panels, respectively. The red and blue curves indicate the means of each strain during day and night. The pink and cyan regions are variations during day and night. 19

2.4 Optical flow of the coral tissue surface. (a)(b) Optical flow between the second and first pictures from day and night, respectively. White circles mark the position of polyps. (c) The percentage histograms of velocities v_x and v_y along horizontal and vertical directions. The red and blue curves indicate the means of each velocity from day and night. The pink and cyan regions are variations between day and night. (d) The percentage histogram of direction of velocity. The red and blue curves indicate the means of each angle from day and night. The pink and cyan regions are variations during day and night. 21

2.5 Mode shape of coral tissue motion during day and night. (a)-(c) Mode shapes of coral tissue motion during day at frequencies 0.05 min^{-1}, 0.15 min^{-1} and 0.25 min^{-1}, respectively. (d)-(f) Mode shapes of coral tissue motion during night at frequencies 0.05 min^{-1}, 0.15 min^{-1} and 0.25 min^{-1}, respectively. . . 23

3.1 Experimental observation of coral on the fluidic platform. (a) Schematic of our octagonal fluidic platform with a coral nubbin in the chamber. Inset shows our octagonal fluidic platform for experiment made by 3D printing with VeroClear resin. Valves control the flow of fluid. (b) Coral nubbin observed under the microscope under normal light conditions and 25°C. Polyps being analyzed in this case are labeled by numbers and color codes used in subsequent figures. (c) Trajectory of polyps. (d) Azimuthal angles, θ, of different polyps as a function of duration. (e) Probability density function of the azimuthal angles, θ, of different polyps after being centered on zero. Colors in (c) and (d) correspond to the colors of labels in (b). 29

3.2 Analysis of correlation and phase synchronization. (a) Correlation coefficients between polyps on the same coral nubbin under different light conditions (wavelength). Correlations and anticorrelations are shown in orange and green, respectively. (b) Correlation coefficients between polyps on the same coral nubbin under different temperatures. Correlations and anticorrelations are shown in orange and green, respectively. (c) Phase-locking value characterizing phase synchronization between polyps on the same coral nubbin under different light conditions. (d) Phase-locking value characterizing phase synchronization between polyps on the same coral nubbin under different temperatures. Cross and triangle symbols in (a)-(d) represent the outliers and mean, respectively. 32

3.3 Power spectrum analysis of experimental data sets under different light conditions. (a) PSD of representative in-plane waving motions represented by the azimuthal angle, θ, under different light conditions. Dashed gray lines show the $1/f^{1.08}$ and $1/f^{1.42}$ trends for normal light, $1/f^{1.19}$ and $1/f^{1.28}$ trends for blue light, $1/f^{1.41}$ and $1/f^{2}$ trends for green light, and $1/f^{1.77}$ and $1/f^{2}$ trends for red light. (b) PSDs evaluated at zero frequency shown in dots for normal light, blue light, green light, and red light from left to right. Solid lines show the fitted results. Both x and y axes are on the logarithmic scale. (c) Hurst indices for cases under normal light, blue light, green light, and red light. Subdiffusion and superdiffusion areas are shaded in green and orange, respectively. 34

3.4 Power spectrum analysis of experimental data sets under different temperatures. (a) PSD of representative in-plane waving motions represented by the azimuthal angle, θ, under different temperatures. Dashed gray lines show the $1/f^{1.20}$ and $1/f^2$ trends for 15°C, $1/f^{1.08}$ and $1/f^{1.42}$ trends for 25°C, and $1/f^{1.25}$ and $1/f^2$ trends for 30°C. (b) PSDs evaluated at zero frequency shown in dots for 15°C, 25°C and 30°C from left to right. Solid lines show the fitted results. Both x and y axes are on the logarithmic scale. (c) Hurst indices for cases at 15°C, 25°C and 30°C. Subdiffusion and superdiffusion areas are shaded in green and orange, respectively. 36

3.5 Model of the in-plane waving motion of coral polyps under different light conditions. (a) Value of the memory-kernel function at the Markovian limit, $\hat{K}(\infty)$, of polyps under normal, blue, green, and red light. (b) Parameter λ for the exponential distribution to model the white-noise term under normal, blue, green, and red light. (c) Fitted PDF of the white-noise terms under different light conditions by using the average parameter λ. (d) Simulated in-plane waving motions of five polyps under normal light and 25°C based on the generalized Langevin equation. Hurst indices are shown below the simulated results. Corresponding PDFs of simulated results are exhibited on the right panel. Cross and triangle symbols in (a)(b) represent the outliers and mean, respectively. 38

4.1 The reconstruction error as a function of number of stacks. The error decreases as the number of stacks increases. 300 stacks are chosen in our study indicated by blue dashed line. 46

4.2 The reconstruction error as a function of number of stacks. The error decreases as the number of stacks increases. 300 stacks are chosen in our study indicated by blue dashed line. 48

4.3 DMD eigenvalues analysis and spectrum. (a) Eigenvalues λ are visualized as complex values on the complex plane with a unit circle. (b) The relation between the real part of $\ln \lambda$ and frequency is displayed. The vertical black dashed line indicates that the real part of $\ln \lambda$ is zero. The color in (a) and (b), which is logarithm scaled, represents the corresponding mode amplitude. (c) The mode amplitude varies as a function of frequency. The purple dots and orange dots show the modes with magnitudes within the $1/f^{\alpha}$ fit and larger than $0.8\times$ standard deviations of the $1/f^{\alpha}$ fit. The green solid line is the fitted result using the robust regression in the form of $1/f^{\alpha}$. 49

4.4 Sliding-window DMD. (a) The raw motion signals of eight tentacles in terms of the x, y and z coordinates are shown from top to bottom in different colors. (b) The DMD spectra of the corresponding segments of motion signals are shown from left to right. (c) The map formed by sliding-window DMD with the width = 120 min and translation = 5 min is shown. The arrows, from top to bottom, indicate the raw motion signals used to calculate the spectrum and indicate how the spectrum is oriented, respectively. The logarithm-scaled mode amplitude is encoded by the color. 51

4.5 Sliding-window DMD of replicate experiments under different light conditions. From top to bottom, three panels in each row represent the maps formed by sliding-window DMD of three replicate experiments under lab, blue, green and red light conditions. The black dashed lines indicate the frequencies of 0.005 Hz and 0.012 Hz. 52

4.6 The DMD modes of eight tentacles. (a) The magnitudes of DMD modes representing displacements along the x, y, and z directions are shown from left to right. The sequence of the tentacles is marked counterclockwise in the first panel. (b) The phases of DMD modes representing displacements along the x, y, and z directions are shown from left to right. (c) The reconstruction using the DMD mode shown in (a) and (b) illustrates the elliptical motions of tentacles with different angular velocities. The elliptical motions of tentacles #2, #3, and #7 with arrows indicating the moving directions are shown from left to right. (d) The correlation coefficients are calculated by the distances between each tentacle tip and central position of the tentacle crown. (e) The snapshots of pulsation motion when tentacles approach each other and when they are away from each other are shown from top to bottom, respectively. The sequence of the tentacles is marked counterclockwise. 54

4.7 The reconstruction of trajectories of coral tentacles using the DMD spatial mode with increased power. The DMD spatial mode with the largest power is chosen as the exemplar spatial mode among the DMD spatial modes with increased power. The number of data points is 200 (around 33 min). 56

4.8 The pulsation motion reconstructed using the DMD spatial mode with increased power. The snapshots of the whole process of pulsation motion from 0 s to 140 s. The slight open and closure of tentacles can be seen. 57

4.9 The effect of light conditions on the DMD modes. (a) The DMD spectra under different light wavelengths are shown from top to bottom. The light in different colors in each graph represent modes with magnitudes within $1/f^{\alpha}$ fit, while the dark colors represent those exceeding the criteria of $1/f^{\alpha}$ fit. (b) The power α under different light wavelengths. (c) The frequencies of the spatial DMD modes with pulsation under different light wavelengths. (d) The ratio of the number of spatial DMD modes with pulsation under different light wavelengths. The blue triangles represent the mean of the data in (b), (c), and (d). 58

5.1 Design of the origami metamaterials. (a) The top view of the origami metamaterials with the Kresling origamis arranged in the honeycomb lattice. The origamis are connected by the reverse torsional spring. $\mathbf{a_1}$ and $\mathbf{a_2}$ denote two basis vectors of the unit cell enclosed by the black dashed line. (b) The side view of the unit cell composed of two origamis with initial heights h_1 and h_2 and initial rotaional angle $\theta_0 = 70°$. Each origami has three degrees of freedom u_t, ϕ_t and θ_b with the bottom disk pinned to the ground. (c) The band structure calculated from the linearized truss model of origami. The Dirac cone emerges in six corners of the Brillouin zone, which is marked as red line. 65

5.2 Synthetic gauge field and Landau level. (a) The schematic of the supercell composed of 41 unit cells (82 origamis) with height gradient. The initial height of origami h_1, h_2 are linearly varying from 30 mm to 10 mm and from 10 mm to 30 mm, respectively. (b) The band structure along Γ-K-M-Γ calculated by the unit cell with different configurations. (c) The projected band structure of the supercell under the periodic boundary condition along y direction. Two ends of the supercell are connected to the wall. The dotted lines denote the calculated Landau levels, while the solid lines denote the theoretical Landau levels. (d) The eigenmodes representing u_t, ϕ_t and θ_b are from top to bottom panel. Red and blue lines correspond to the red and blue circles in (c). 68

5.3 Robust zeroth Landau level. The field distributions θ_b for the zeroth Landau level in (a) lower frequency and (b) higher frequency. The corresponding cases with obstacles along the propagation path are shown in (c) and (d). Two excitation sources with phase difference are put in the middle. The excitation frequencies are 106 Hz and 225 Hz, respectively. 70

5.4 Elastic snake states. (a) The projected band structure of the supercell at the lower frequency. (b) Top panel: real parts of the eigenmode θ_{b1} and θ_{b2} along the supercell, corresponding to the red and blue dots in (a). Bottom panel: the newly-defined modes $|\theta_{b1} + \theta_{b2}|$ and $|\theta_{b1} - \theta_{b2}|$. (c) The simulated θ_b distribution under the excitation frequency at 103.9 Hz, corresponding to the solid line in (a). (d) The simulated θ distribution with the obstacle in the middle under the excitation frequency at 103.9 Hz. The theoretical trajectory of the snake state is shown in orange solid line in (c) and (d). 71

6.1 Band structure of the valley topological metamaterials. (a) Schematic of our elastic metamaterials based on the spring-mass system. Basic vectors of unit cell are shown in $\mathbf{a}_1$ and $\mathbf{a}_2$. Length of the spring is a. First Brillouin zone with high symmetry points Γ, M and K is shown in the middle panel. The sandwiched supercell for the calculation of projected band structure is shown in the right panel. (b) Band structure when (left) $m_1 = 0.8$ kg, $m_2 = 1.2$ kg, (middle) $m_1 = 1$ kg, $m_2 = 1$ kg and (right) $m_1 = 1.2$ kg, $m_2 = 0.8$ kg are shown. The eigenmodes corresponding to the $\mathbf{K}$ valley are shown in the first panel and the third panel. Motions along horizontal and vertical directions are marked on the two sites. Berry curvatures around the valley of the first band for each case are shown in the inset. (c) Projected band structure with two topological states inside the bandgap. The black dashed line indicates the excitation frequency of the simulation setup. 78

6.2 Setup for simulation and for the numerical DMD implementation. (a) Simulation of wave propagation along the Z-shaped interface in a valley topological metamaterial built by means of a spring-mass system. Two different unit cells with two different topological phases are shown on the two sides. Magnified view of the topological boundary (black line) is shown in the inset. (b)(c) Snapshots of original and reconstructed wave propagation represented by the horizontal displacement u_x along the Z-shaped interface at $t = 2$, 192, 380, 570 and 758 ms (with the time evolving from the bottom to the top), respectively. 82

6.3 DMD spectrum and DMD modes. (a) Eigenvalues are visualized on the complex plane located around the unit circle. (b) Mode amplitude varies as a function of frequency. The shading area indicates the bandgap region. (c) Magnitude of the DMD mode with the largest amplitude inside the bandgap region. (d) Phase of the DMD mode with the largest amplitude inside the bandgap region. Inset shows the magnified view around the interface (black line) illustrating the phase difference and valley pseudospin. Black and green arrows show the pseudospin up and pseudospin down indicated by the phase evolution around hexagon corners, respectively. 83

6.4 Reconstruction error and correlation coefficient between reconstructed and original wave propagation. Relative error and correlation coefficient between the ground truth and reconstruction as a function of duration are shown in black and blue, respectively. 85

6.5 Classification of topological and traditional metamaterials. (a) Feature space formed by the second principal component of DMD modes with Z-shaped interface. (b) Projected values of each DMD mode from the topological and traditional metamaterials excited by different forces (left panel) and different excitation frequencies (right panel). Red and blue regions indicate topological and traditional DMD modes, respectively. Error bars indicate the range of the minima and maxima of projected values. 88

7.1 Illustration of giDMD and comparison between DMDc and giDMD. (a) The side view and the top view of the single Kresling origami with geometrical parameters. (b) The data matrices for the data-driven framework of giDMD. The geometrical parameters g are collected as the height h, the length of crease lines a, b, folding angle Ψ, the direction of the crease lines α, β. The state x is taken to include the displacement p and velocity v, and the control y is taken to involve the states of the input x^c and the geometrical parameters g. (c) The prediction using DMDc. (d) The prediction using giDMD. The predictions of axial displacement u and rotational displacement ϕ using DMDc are shown in the first and second row, respectively. The gray shaded areas represent the training data. The ground truth and the prediction are shown in blue and red, respectively. The insets in four graphs show the relation between frequency (f) and power amplitude (P) after the fast Fourier transform. 97

7.2 Application of giDMD on the origami chain. (a) The schematic of the origami chain composed of Kresling origami with alternating chirality. The design parameters of origami are $h_0 = 30$ mm, $\theta_0 = \pm 70°$, $R = 36$ mm where h_0, θ_0, and R are the initial height, initial rotational angle, and radius of the cross-section, respectively. (b) The band structure calculated by the unit cell enclosed by black dashed line in (a). The Zak phases of the lower band and upper band are π. (c) The modes of the supercell formed by 16 unit cells. The black dots represent the bulk band. The cyan and pink dots represent the topological boundary states within the band gap. (d) The axial and rotational modes of the topological boundary states. (e) The simulated axial displacement along the origami chain at different frequencies in the pass band (15 Hz), stop band (50 Hz) and topological boundary states (145 Hz). (f) The corresponding predicted axial displacement using 60% training data (from 0 s to 3 s). 100

7.3 Identification of topological boundary states in origami chain. (a) The rows of **K** matrix corresponding to the axial displacements of the origami chain at 15 Hz, 50 Hz and 145 Hz. The corresponding control variables are shown below. (b) The singular value spectrum of **K** matrix under different excitation frequencies from 10 to 220 Hz. The orange dash arrows on two sides indicate the range of the band gap, and one in the middle indicates the frequency of topological boundary states. (c) The zoom-in view by using 32 singular values. 102

7.4 Application of giDMD on the dual origami structure. (a) The schematic of the dual origami structure with opposite chirality. (b) The image of experimental setup for the vibration test from the reference. Copyright 2020 Springer Nature. The design parameters of origami are $h_0 = 50$ mm, $\theta_0 = \pm 70°$, $R = 36$ mm where h_0, θ_0, and R are the initial height, initial rotational angle, and radius of the cross-section, respectively. The input excitation is applied by a shaker, and the motions are captured by two action cameras and quantified by the digital image correlation program. (c)(d) The row of **K** matrix corresponding to the axial displacement u_1 at the frequency of 5 Hz and 17 Hz, respectively. The corresponding control variables are shown below. (e) The prediction of axial displacement u_1 and u_2 using giDMD at the frequency of 5 Hz. (f) The prediction of axial displacement u_1 and u_2 using giDMD at the frequency of 17 Hz. The gray shaded areas represent the training data. The ground truth is shown in blue and the prediction is shown in red. 105

7.5 Identification of intrawell periodic, interwell periodic and chaotic motion. (a) The spectrum analysis of the experimental axial displacements u_1 (the first panel) and u_2 (the second panel) under different excitation frequencies from 5 to 24 Hz. (b) The corresponding spectral analysis based on the predicted axial displacements u_1 (the first panel) and u_2 (the second panel). The white area with a cross represents the failure of the prediction. The green, orange and purple shaded areas represent the frequencies of intrawell periodic motion, interwell periodic motion and chaotic motion. (c) The singular value spectrum of **K** matrix under different excitation frequencies from 5 to 24 Hz. The Lyapunov exponents of u_1 and u_2 under different excitation frequencies are also shown in dark green and bright green, respectively. (d) The relation between the second singular values σ_2 and the Lyapunov exponents λ under different excitation frequencies. The intrawell periodic motion, interwell periodic motion and chaotic motion are represented in green, orange and purple circles. The distance correlation between logarithm-scale second singular values and Lyapunov exponents are shown in both graphs. 107

A.1 Experimental setup. The experimental setup with a DSRL camera, a timer, an aquarium equipped with a filter, a scraper and a heater. The coral is fixed on another coral skeleton. 137

A.2 Luminance extracted from pictures. Red and blue curves show the luminance at day and night, respectively. 139

A.3 Pictures taken at day and at night. The yellow curves in (a) and (b) enclose the coral skeleton in the aquarium. Scale bars are shown in (a) and (b). . . . 140

A.4 Displacements of the coral skeleton from digital image correlation. (a) The displacements u_x along horizontal direction between the first and the second picture at day and night are shown in the left and right panel, respectively. (b) The displacement u_y along vertical direction between the first and the second picture at day and night are shown in the left and right panel, respectively. (c) The percentage histograms of displacement u_x and displacement u_y are shown in the left and right panels, respectively. The red and blue curves indicate the means of each displacement at day and night. The pink and cyan regions are variation ranges at day and night. 141

A.5 Strains of the coral skeleton from digital image correlation. (a)-(c) Strains ϵ_{xx}, ϵ_{xy} and ϵ_{yy} between the first and the second picture at day and night are shown in the left and right panel, respectively. (d) The percentage histogram of the strains ϵ_{xx}, ϵ_{xy} and ϵ_{yy} are shown from left to right, respectively. The red and blue curves indicate the means of each strain at day and night. The pink and cyan regions are variation ranges at day and night. 142

A.6 Optical flow of the coral skeleton. (a)-(b) Optical flow between the second and first pictures at day and night, respectively. (c) The percentage histograms of velocities v_x and v_y along horizontal and vertical directions. The red and blue curves indicate the means of each velocity at day and night. The pink and cyan regions are variations at day and night. (d) The percentage histogram of direction of velocity. The red and blue curves indicate the means of each angle at day and night. The pink and cyan regions are variation ranges at day and night. 143

B.1 Computational fluid-dynamics simulation with different flow rates of our fluidic platform. Velocity distribution of the fluid is shown in the tubes and chamber. Three slices are shown in the chamber, one of which shows the velocity distribution near the coral nubbin. Results of using flow rates of 5, 25, and 50 μl/s are shown in (a)–(c), respectively. 145

B.2 Laplace transform of the memory kernel for modeling the in-plane motion of coral polyps. First-order, second-order, third-order, and fourth-order estimations of the Laplace transform of the memory kernel are shown in different colors. Third-order and fourth-order estimations overlap. These curves converge to a certain value with the increase of ξ. 147

B.3 Probability density function of the white-noise term. Probability density function of the white-noise term, W, is shaded in gray. Red, blue, and green dashed lines show the fitted exponential function, power-law function, and Gaussian function, respectively. 150

B.4 Model of in-plane waving motion of coral polyps under different temperatures. (a) Value of the memory-kernel function at the Markovian limit, $\hat{K}(\infty)$, of coral polyps at 15°C, 25°C, and 30°C. (b) Parameter λ for the exponential distribution to model the white-noise term at 15°C, 25°C, and 30°C. (c) Fitted PDF of the white-noise terms at different temperatures by using the average parameter λ. Cross and triangle symbols in (a)(b) represent the outliers and mean, respectively. 151

D.1 Linearized coefficients along a supercell and variations of band gap and mass term m_K. (a) The linearized coefficients α_{11} and β_{11}, α_{12} and β_{12}, α_{22} and β_{22} for origami 1 and 2 along the supercell from top panel to bottom panel. Note that $\alpha_{12} = \alpha_{21}$ and $\beta_{12} = \beta_{21}$. (b) The variation of band gap at lower and higher band gap of each unit cell along the supercell. (c) The mass term m_K at lower and higher band gap of each unit cell along the supercell. . . . 158

E.1 (a) Reconstruction error as a function of truncation and duration. Error is shown on a logarithmic scale. (b) Zoom-in reconstruction error as a function of truncation from 1 to 140 and duration. Vertical dashed lines in (a) and (b) correspond to the selected $r = 131$. 160

E.2 DMD spectrum and DMD modes of straight interface and cross interface are shown in (a), (b) and (c), (d), respectively. Insets in (a) and (c) are the configurations of elastic topological metamaterials. 161

E.3 The DMD implementation. (a),(b) Snapshots of original and reconstructed wave propagation excited by the Gaussian burst represented by the horizontal displacement u_x along a Z-shaped interface at t = 2, 192, 380, 570 and 758 ms (with the time evolving from the bottom to the top), respectively. (c) Magnitude of the DMD mode with the largest amplitude inside the bandgap region. (d) Phase of the DMD mode with the largest amplitude inside the bandgap region. Inset shows the magnified view around the interface (black line) illustrating the phase difference and valley pseudospin. Black and green arrows show the pseudospin up and pseudospin down indicated by the phase evolution around hexagon corners, respectively. 163

E.4 Relative error of reconstruction as a function of number of stacks. 165

E.5 Classification of topological and traditional waveguides with different interface. (a), (c) Feature space of topological metamaterials with straight interface and cross interface. (b), (d) Projected values of each DMD mode extracted from the system under excitation of different forces and different frequencies, corresponding to straight interface (a) and cross interface (c). Red and blue regions indicate topological and traditional DMD modes, respectively. Error bars indicate the range of the minima and maxima of projected values. 166

E.6 Synthesis of topological states propagation along the given interface. (a) Snapshots of horizontal displacement u_x from 0 to 200 ms used for training. (b) Top panel displays one of the DMD modes inside the bandgap of the training data. The bottom panel displays the corresponding extended and shifted DMD modes along the Z-shaped interface. (c) Snapshots of the horizontal displacement u_x for the synthetic wave propagation at $t = 2$, 192, 380, 570 and 758 ms. (d) Synthesis error and correlation coefficient as a function of duration are shown in black line and blue line, respectively. 167

F.1 The prediction accuracy for the dual origami structure and the origami chain using different training ratios. (a) The relative errors as a function of training ratio of axial and rotational displacement in different frequencies for dual origami structure are shown in the left and right panel, respectively. (b) The relative errors as a function of training ratio of axial and rotational displacement in different frequencies for the origami chain are shown in the left and right panel, respectively. The white regions indicate the failure of the prediction in (a) and (b). 173

F.2 The singular values of **K** matrix for dual origami structure and origami chain using different training ratios. (a) The first singular value of **K** matrix as a function of training ratio in different frequencies for dual origami structure. (b) The fifth singular value of **K** matrix as a function of training ratio in different frequencies for origami chain. 174

LIST OF TABLES

Table Number Page

B.1 White-noise model selection for different light conditions. Preferred model for each polyp in each replicated experiment is displayed based on the Akaike information criterion and the Bayesian information criterion. 149

B.2 White-noise model selection for different temperatures. Preferred model for each polyp in each replicated experiment is displayed based on the Akaike information criterion and the Bayesian information criterion. 151

D.1 Design parameters for the origami. 155

D.2 Mechanical parameters for the origami. 155

F.1 Design parameters for single origami and origami chain. 171

F.2 Mechanical parameters for single origami and origami chain. 171

ACKNOWLEDGMENTS

During my journey to pursue my doctoral degree at the University of Washington, an unexpected pandemic, COVID-19, suddenly attacked humans around the globe. My research plan was completely disrupted. Especially when I studied coral biophysics, maintaining the aquarium and doing experiments became extremely difficult due to the quarantine and public health concerns. Besides, being a beginner in the coral research. I felt frustrated and sometimes doubted the feasibility of this coral research and related initiatives, as things were entirely different from what I had imagined at the beginning. However, fortunately, I received so much support and aid from my adviser, collaborators, lab members, friends and family.

Firstly, I must express my sincere appreciation to Professor Jinkyu Yang, my Ph.D. adviser, for his dedicated supervision on my research and strong encouragement. Professor Yang always provided some novel ideas and offered me a lot of freedom in choosing research topics. He also made great efforts to proofread and revise each paper and offers new insights, which greatly improves my ability in paper writing and critical thinking. I also would like to thank my Ph.D. committee, Professor Marco Salviato, Professor Krithika Manohar, Professor Dana Dabiri, Professor Alex Gagnon for providing valuable suggestions and insights into my research.

Secondly, in the coral research, I would like to express my gratitude to all members in the project of "Synthetic Coral" for constructive and continuous collaboration. Particularly, I would like to thank Professor Nastassja Lewinski (Virgina Commonwealth University), Professor Judith Klein-Seetharaman (Colorado School of Mines, now moved to Arizona State University), Professor Hollie Putnam (University of Rhode Island), Professor Lenore Cowen (Tufts University), Professor Alex Gagnon (University of Washington) and Dr. Lokender Kumar (Currently an assistant professor at Shoolini University) for their instructions and helpful improvement to my work. I am especially grateful for Dr. Liza Roger (Currently an assistant professor at Arizona State University) and Shuyu Tian for their help during my visit to Professor Nastassja Lewinski's group in 2021.

Thirdly, in my modeling work, I want to particularly show my gratitude to Professor Panayotis Kevrekidis (University of Massachusetts) for his encouragement and fruitful discussion in every collaborating meeting. His passion and rigorous attitude towards scientific research always motivated me.

Furthermore, I want to thank current lab members, Yasuhiro Miyazawa, James O'Neil and Koshiro Yamaguchi for the fruitful discussions on the research projects and suggestions on my research. I also thank the excellent lab members who have overlapping years with me, Dr. Xiaotian Shi, Dr. Chun-wei Chen, Dr. Seunghyun Ko, Dr. Ingi Kim, Timothy Gormley, Zhisong Chen, Qingqian Li, and my mentees, Isaiah Cuadras and Kaylee Hudson, for their companionship and consideration.

Last but not least, I express my sincere thanks to my family. Without the strong support from my parents, I would not have been able to pursue my doctoral degree abroad. When I felt frustrated during the pandemic, my parents always comforted and encouraged me. I also want to thank my girlfriend for her companionship and cordial talks. Certainly, without the help from my friends, I could not have overcome these challenges.

DEDICATION

to my dear families and loved ones for their endless support

Chapter 1

INTRODUCTION

1.1 Background

Spatiotemproal behaviors, referring to the behaviors that vary over both space and time, are ubiquitous across different fields in science and engineering from natural systems to artificial systems. As a typical example in the natural systems, biological systems own rich spatiotemporal behaviors, including the movements of animals and the growth of plants [1–3]. For example, bird flocks exhibit various patterns of motion that are influenced by the interactions of individual birds and the environment, which has become a hot topic in studies of complex systems [4–8]. Interestingly, many spatiotemporal behaviors in biological systems can be influenced by factors such as competition for resources, environmental conditions, and the presence of other species [9, 10]. Likewise, in artificial systems, spatiotemporal behaviors can be observed in a variety of contexts. For example, traffic flow on a road can exhibit patterns of congestion and flow that change over time and space [11–13]. The wave dynamics and structural dynamics in mechanical systems have been attracting attentions in the scientific research [14–17]. Hence, understanding spatiotemporal behaviors is significant, since by studying the patterns of motion and dynamics in these systems, researchers can gain insights into the underlying physics and develop models that drive these behaviors. In this dissertation, we focus on the study of spatiotemporal behaviors in corals, elastic metamaterials and origami.

Coral reefs are highly valuable ecosystems that support significant biological activities and harbor an immense diversity of marine species. Corals, which belong to the phylum Cnidaria, have a rich microbiome of bacteria, fungi, bacteriophages, viruses and most importantly, photosynthetic algae [18]. They exist as colonies of individual animals called polyps and are responsible for the formation of coral reefs, which are home to a large number of species and rival only the rain forest in terms of their diversity [19]. In recent years, coral conservation and related research have been major subjects, given the unfortunate fact that coral reefs are rapidly declining due to various abiotic and biotic factors, including pollution, global warming, sea level rise, overfishing, and other human activities [20–22]. To protect corals from these challenges, it is crucial to better understand their behaviors. For instance, the size, morphology and shape of corals change over time during their lifespan which can be extremely slow. Thus, coral motions become one of the major observable spatiotemporal behaviors of corals detailed in Section 1.2. With the use of non-invasive imaging techniques, such as time-lapse imaging and photogrammetry microscopic imaging, researchers can detect changes and explore fundamental biophysical properties of corals at both reef and cellular levels. Typical experimental examples are the observations of calcareous skeleton, decalcified coral tissues and the physiological and nutritional status of their symbiotic dinoflagellates [23–27]. These techniques provide real-time information on the dynamic processes of coral components *in vivo* and have revealed biophysical processes that govern coral health and proliferation. Naturally, imaging techniques can also be used to observe the dynamics of spatiotemporal coral motions, which have yet to be fully investigated.

In terms of artificial systems, wave dynamics and structural dynamics are intriguing and attracting researchers' attentions in the mechanical systems [14–17]. Therein, elastic metamaterials and origami are two typical mechanical structures that possess topologically protected elastic wave propagation and rich structural dynamics, which have theoretical interests and promising engineering applications detailed in Section 1.3. However, associated studies are facing challenges of lacking data-driven analysis and modeling, and the strong nonlinearity of the structures [28].

There are many ways to model spatiotemporal dynamics of different systems, and generally speaking, two major approaches are theoretical modeling and data-driven modeling. In biological systems, for example, theoretical models can describe the systems statistically, considering the universal existence of interplay of deterministic laws and stochastic processes [29]. On the other hand, simplified mechanical models based on several key mechanical elements can effectively capture the static and dynamic behaviors of mechanical systems [30]. However, theoretical modeling methods often require sufficient knowledge of the theoretical frameworks for the corresponding objects, making it challenging to analyze and model complex systems. Recently, data-driven methods, such as deep neural networks [31–33] and dimensionality reduction methods [34–36], have been explored to understand the spatiotemporal behaviors in various systems, including predicting planetary motion, comprehending turbulent fluid dynamics, and forecasting global climate. Therein, while deep neural networks can be effective and powerful, their decision processes are often unknown, making them a black-box method. Dimensionality reduction techniques, on the other hand, are more straightforward and interpretable, making them suitable for modeling various systems to provide physical insights. The capability of being knowledge-free and physically interpretable is particularly useful for analyzing and modeling complex systems that lack governing equations, or have poorly understood governing equations, such as most biological systems and some mechanical systems.

Through using advanced experimental techniques, characterization and modeling approaches, the spatiotemporal behaviors of corals, elastic metamaterials, origami can be well described and understood, aiding us to discover the underlying physics and dynamics in coral ecosystems and mechanical systems.

1.2 Spatiotemporal behaviors in corals

Animal motion is one of the most fascinating and significant animal behaviors, providing essential information on feeding, habitat distribution and mobility. Coral holobionts, similar to other animals, also exhibit important behavioral features, including coral motion, which plays a vital role in feeding, competition, survival and fitness. Although scleractinian corals are generally considered to be inherently sessile organisms, where the tissues are tightly attached on the coral skeleton and the comparatively small sizes of polyps and tentacles develop small amplitude of motion, recent research has suggested that subtle tissue motion may be involved in seawater exchange within a coral [37, 38]. Compared with the imperceptible tissue motions, polyps motions and tentacles motions are more observable and can have a significant impact on coral health and survival. For example, some branched corals with small polyps will stretch their tentacles during daytime to expose photosynthetic symbionts to light. Under the strong light, however, the coral will retract its tentacles to protect photosynthetic symbionts from irradiance [39–41]. These behavioral differences illustrate how coral motions can affect ecological and physiological tradeoffs and serve as an indicator of them. In addition, some tentacles function as probes to identify and kill aggressive competitors that settle within the coral colonies [42–47]. The ciliary motion of tentacles also aids in the transfer of materials [48]. In the context of challenge in the future climate change, when abnormal environmental conditions happen, the erratic and unpredictable behaviors may occur on coral colonies, which is full of scientific interests. Therefore, characterizing coral behaviors through motion analysis can enhance our understanding of fundamental biological and physical properties of corals.

Studies of animal movement suggest that most animal motions can be described by a random walk with particular statistical patterns [49]. Although a random walk is a discrete-space and discrete-time model, Brownian motion provides a continuous model in both space and time that is more suitable for interpreting animal behaviors. The unique index named Hurst index is 0.5 for Brownian motion. Besides, some motions are discovered to follow the law of fractional Brownian motion characterized by the Hurst index being less or greater than 0.5, corresponding to subdiffusion and superdiffusion, respectively [50]. More generally, both Brownian motion and its derived fractional Brownian motion are characterized by their $1/f^{\alpha}$ power spectral densities (f being the frequency), leading to the generic terminology of $1/f$ noise. The Langevin equation, the most generic equation in stochastic process, is commonly used to simulate and model stochastic processes, including animal motions. In the meanwhile, data-driven analysis and modeling has been increasingly popular due to its knowledge-free superiority, which reduces the burden caused by the conventional theoretical modeling.

Despite the importance of inherent spatiotemporal multi-scale features of coral motions, their quantitative properties and modeling still remain challenging and unexplored. For example, coral tissue motions are imperceptible to both naked eyes and commonly-used imaging equipment, making it difficult to quantify the displacement on the coral tissue. Coral polyps and tentacles motions, despite relatively observable, lack of experimental platforms and proper modeling methods. Moreover, coral motions, similar to other animals motions, are no exception in the stochastic processes instead of deterministic processes, posing a significant challenge in parameter estimation and appropriate model selection in both theoretical modeling and data-driven modeling. Furthermore, the biophysical interpretations of coral motions are in their infancy, and more studies are needed to further understand the relation between the quantitative characteristics of coral motions and biological functions.

Here, as part of this dissertation, we present the systematical methodology and paradigm for studying the spatiotemporal behaviors of corals in terms of motions. Moreover, we demonstrate the experimental observation, numerical analysis and theoretical/data-driven modeling of coral motions in tissues, polyps and tentacles, as outlined below:

1. Motion of coral tissues

   We use digital image correlation and optical flow techniques to a series of images (~ 13 hours of high-frequency images of *Montipora capricornis*) to quantify and characterize minute coral motions under different light conditions. We also use motion magnification algorithm to magnify coral motions in different frequencies, which explicitly displays the distinctive dynamic modes of coral tissue motions. Specifically, though *Montipora capricornis* has the slow and subtle tissue motions, which is hard to capture not only with naked eyes, but also with conventional optical apparatus, our assessment of displacement, strain, optical flow, and mode shape successfully quantified coral motion under different light conditions, and they showed that *Montipora capricornis* exhibits more active motions at night compared to day, revealing the nocturnal nature.

2. Motion of coral polyps

   We observe *Pocillopora acuta in vivo* under different light and temperature conditions using a fluidic platform that allows direct microscopic observation of small live coral fragments, where the stochastic dynamics of in-plane waving motion of polyps is uncovered. The relation among polyps on nubbins is described by motion correlation analysis. Besides, fractional Brownian motions of polyps under certain light conditions and temperatures are revealed by Hurst index (generally smaller than 0.5) via power spectral analysis. Outside of optimal growth conditions (normal light and 25°C), the Hurst index becomes highly variable (spanning between diffusive, subdiffusion and superdiffusion regions) with the baseline index being around 0.2. Finally, the motions of polyps for different light conditions and temperatures are modeled by Langevin equation, numerically obtained by data-driven parameterization, which agrees excellently with experimental results.

3. Motion of coral tentacles

   We experimentally observe the tentacles motion of the pulsating soft coral *Anthelia glauca* using stereovision, where coordinates of tentacle tips in the three-dimensional space can be extracted. The stochastic dynamics of coral tentacles motion is revealed. Besides, we use a data-driven method call dynamic mode decomposition (DMD) to analyze the dynamics of the raw data, revealing the growth, decay and oscillation of each mode. The nature of $1/f$-type motion with the increased power near 0.008 Hz of tentacles is also revealed from the DMD spectrum. The physically coherent structures corresponding to the increased power are visualized to confirm that they represent the pulsation motion of tentacles. In addition, the $1/f$-type motion and pulsation motion of tentacles vary under different light conditions. Particularly, red light has a significant impact on the tentacles behaviors of *Anthelia glauca*.

1.3 Spatiotemporal behaviors in elastic metamaterials and origami

Mechanical systems are composed of building blocks, and different building blocks can achieve unique mechanical properties. In recent years, elastic metamaterials and origami structures formed by building blocks have gained increasing popularity due to their theoretical importance and the promising engineeering applications [51–54]. In static behaviors, elastic metamaterials and origami structures exhibit novel mechanical properties in static behaviors, such as negative Poisson's ratio [55], negative thermal expansion coefficient [56], and tailored stiffness [57], which never appear in the traditional materials. Apart from the static properties, they also have rich spatiotemporal behaviors in wave dynamics and structural dynamics which are compelling in potential applications in impact mitigation and vibration control [58, 59].

Therein, elastic metamaterials designed by several concepts in the condensed matter physics, especially nontrivial topological properties for mechanical responses, have been a significant breakthrough in physics over the last decade. This discovery has paved the way for designing and manufacturing metamaterials with rich physics and applications such as robust one-way waveguide, energy focusing, and harvesting [60–62]. Besides, origami structures exhibit highly nonlinear dynamics and have been used to realize intriguing wave phenomena, resulting in solitary waves and chaotic structural dynamics [28, 63, 64].

Experiments, numerical simulations based on finite element methods and simplified structural model, and theoretical modeling have been made great progress in the study of topological elastic metamaterials and origami. However, studies on the data-driven characterization and modeling remain largely unexplored, especially in the area of physically interpretable data-driven modeling. While neural networks are a popular data-driven method, they work as a black box and do not provide insights into the physics of the systems. Physically interpretable data-driven methods, on the other hand, can extract information about the physics and dynamics of the systems. Therefore, applying physically interpretable data-driven methods can potentially reveal new insights into the complex physics and dynamics in topological elastic metamaterials and origami.

Here, as part of this dissertation, we first present the theoretical modeling and numerical calculation of elastic metamaterials based on the origami. Then, we present the application of a physically interpretable data-driven method named dynamic mode decomposition in the topological elastic metamaterials and origami structures, demonstrating the revelation of physics nature and the prediction of future spatiotemporal behaviors purely using data, as outlined below:

1. Chiral Landau level in origami metamaterials

   We show the origami metamaterials with the special configuration to demonstrate the emergence of the elastic chiral Landau level and snake states theoretically and numerically. By arranging the initial height of the Kresling origami, the out-of-plane synthetic gauge field is generated, which produces the in-plane pseudomagnetic field in the origami metamaterials. The resultant quantization of energy level is regarded as the Landau level, where the robustness of zeroth Landau level and the wavy trajectory of snake states are demonstrated.

2. Wave propagation in topological elastic metamaterials

   We present the data-driven discovery of elastic topological states propagation in the topological elastic metamaterials using dynamic mode decomposition (DMD). By using DMD, we are able to learn the physics nature of the topological interface states and valley pesudospin. The DMD modes allow us to classify between topological and traditional metamaterials. Moreover, we were able to synthesize topological state propagation along a given interface using the model enabled by the DMD modes.

3. Structural dynamics in various Kresling origami structures

   We develop an improved version of DMD with control that we term geometry-informed dynamic mode decomposition (giDMD) by integrating geometry information of the origami structure to model origami dynamics. We evaluate its efficacy and interpretability on the origami chain and dual origami structure. Our results show that giDMD can accurately predict the dynamics of an origami chain across frequencies, where the topological boundary state can be identified by the characteristics of giDMD. Moreover, in the dual origami structure, the type of dynamics can be identified, where intrawell periodic motion can be accurately predicted. The influential geometrical parameters in the origami dynamics can be uncovered through the giDMD model, indicating the interpretability of this method.

1.4 Data-driven modeling by dynamic mode decomposition

Dynamical systems provide a powerful framework for describing the spatiotemporal behaviors of biological and mechanical systems. We consider the dynamical system of the form:

$$\frac{d}{dx}\mathbf{x}(t) = f(\mathbf{x}(t)) \tag{1.1}$$

The most cases we are dealing with in the biological and mechanical system in the experiments and numerical simulations are discrete-time dynamical systems:

$$\mathbf{x}_{k+1} = \mathbf{F}(\mathbf{x}_k) = \mathbf{x}_k + \int_{k\Delta t}^{(k+1)\Delta t} f(\mathbf{x}(\tau))d\tau \tag{1.2}$$

where $\mathbf{x}_k$ is sampled from the trajectory in Equation (1.1) discretely in time, so that $\mathbf{x}_k = \mathbf{x}(k\Delta t)$. $\mathbf{F}$ is the discrete-time propagator.

Koopman spectral analysis has been introduced to characterize the evolution of Hamiltonian systems, and extended to systems with continuous spectra [65]. Koopman analysis, in contrast to the more popular geometric perspective of dynamic systems, provides the evolution operator that advances the space of measurement functions of the state of the dynamical system. The Koopman operator $\mathcal{K}$ is the linear operator that advances measurement functions g of the state $\mathbf{x}$ forward in time:

$$\mathcal{K}g := g \circ \mathbf{F} \Rightarrow \mathcal{K}g(\mathbf{x}_k) = g(\mathbf{x}_{k+1}) \tag{1.3}$$

where the finite-dimensional nonlinear dynamics is transformed to the infinite-dimensional linear dynamics by the Koopman operator $\mathcal{K}$.

A linear representative of nonlinear dynamics is useful because there are numerous effective analytic tools for linear systems. However, analytical representations of the Koopman operator are uncommon. Obtaining a finite-dimensional approximation (i.e., a matrix $\mathbf{K}$) of the Koopman operator is thus a practical goal for the data-driven analysis. If such a matrix representation can be found, it is possible to define a linear system that advances the measurement functions $y = g(x)$ as follows:

$$\mathbf{y}_{k+1} = \mathbf{K}\mathbf{y}_k \tag{1.4}$$

Regression-based approaches for obtaining a finite approximation of the Koopman operator with a suitable choice of measurement functions have become widely used in the studies.

Dynamic mode decomposition (DMD) was originally proposed in the fluid dynamics community to decompose experimental or numerical data sets into leading spatiotemporal coherent structures [66]. It was soon demonstrated that the DMD provides a numerical framework to approximate the Koopman mode decomposition, where the relation between DMD and the Koopman operator was further enhanced and verified [66]. The DMD searches for a best-fit linear model to relate the following two data matrices:

$$X = \begin{bmatrix} | & | & & | \\ x_1 & x_2 & \dots & x_{m-1} \\ | & | & & | \end{bmatrix} \quad X' = \begin{bmatrix} | & | & & | \\ x_2 & x_3 & \dots & x_m \\ | & | & & | \end{bmatrix} \tag{1.5}$$

The matrix X is the state of the system in time, and compared with X, X' contains snapshots with a single step forward in time. These matrices may be related by a best-fit linear operator A:

$$X' = AX \Rightarrow A = X'X^{\dagger} \tag{1.6}$$

where $X^{\dagger}$ is the Moore-Penrose pseudoinverse. The matrix A is a best-fit linear operator minimizing the Frobenius norm error $\|X' - AX\|_F$.

For the system with large dimension, which is the common case in biological and mechanical systems, the operator A is also large, and so instead of obtaining A directly, we often look for the leading eigendecomposition of A:

1. Take the singular value decomposition (SVD) of X:

   $$X = U\Sigma V^* \tag{1.7}$$

   Here, $*$ denotes complex conjugate transpose. Often, only the first r columns of U and V, and r singular values Σ are required for a good approximation: $X = U_r \Sigma_r V_r^*$, where r denotes a rank-r truncation.

2. Project A onto U_r to obtain the $r \times r$ matrix A_r:

   $$A_r = U_r^* A U_r = U_r^* X' V_r \Sigma_r^{-1} \tag{1.8}$$

3. Compute the eigendecomposition of A_r:

   $$A_r W = W \Lambda \tag{1.9}$$

4. Obtain full-dimensional eigenvectors ϕ of A, which is the column of Φ:

   $$\Phi = X' V_r \Sigma_r^{-1} W \tag{1.10}$$

In spite of great achievement by DMD in recent years, DMD has inherent drawbacks. Because linear measurements are insufficient for many nonlinear dynamical systems, particularly chaotic systems, DMD has recently been extended to an augmented measurement function. Besides, since DMD is sensitive to the noise, several methods based on standard DMD have been developed to have better performance, such as total least-squares DMD [67], forward–backward DMD [68], variational DMD [69], and robust DMD [70].

Here, in this dissertation, we will use the dynamic mode decomposition to analyze some spatiotemporal behaviors in biological and mechanical systems including the motion of soft coral tentacles, topological state propagation in elastic topological metamaterials and the structural dynamics of origami with various configurations. Therein, we use the standard DMD and time-delay embedding DMD to characterize motions of soft coral tentacles and topological state propagation. Furthermore, we propose a new variant of DMD to address the problem about origami dynamics.

1.5 Organization of the dissertation

The dissertation is organized to describe the background of this research (Chapter 1), spatiotemporal behaviors in corals in terms of motion (Chapter 2∼Chapter 4) and spatiotemporal behaviors in elastic metamaterials (Chapter 5∼Chapter 6) and origami (Chapter 7) in sequence. The conclusion and future challenges will be presented in Chapter 8.

In Chapter 1, we show the background and motivation of this research. The significance of spatiotemporal behaviors in corals, elastic metamaterials and origami is introduced. Moreover, the data-driven modeling method, dynamic mode decomposition, applied to the complex system is presented, which will be used in biological systems and mechanical systems.

In Chapter 2, we propose and apply a systematic approach to quantify and visualize subtle coral motion across a series of light and dark cycles in the scleractinian coral *Montipora capricornis.*

In Chapter 3, we observe *Pocillopora acuta in vivo* under different light and temperature conditions using a fluidic platform, where the correlated relation among polyps and the fractional Brownian motions of polyps are revealed. The corresponding Langevin dynamics is established and numerically parameterized to model the motion of coral polyps.

In Chapter 4, we observe *Anthelia glauca* under different light conditions using the stereovision, where the $1/f$-type motion is revealed by dynamic mode decomposition. The pulsation motion of pulsating soft coral is discovered near 0.008 Hz. The impact from the light conditions on $1/f$-type motion and pulsation is also studied.

In Chapter 5, we use the theoretical modeling and numerical calculation to demonstrate the elastic chiral Landau level and snake states in the origami metamaterials, where the robustness of zeroth Landau level and wavy propagation path are observed.

In Chapter 6, we use dynamic mode decomposition to characterize the topological states in the elastic topological valley metamaterials, where the topological nature (topological interface states and valley pesudospin) is extracted from the pure data. The classification between topological and traditional metamaterials is achieved by the corresponding physically coherent structures.

In Chapter 7, we propose a data-driven framework based on dynamic mode decomposition, named geometry-informed dynamic mode decomposition. We demonstrate the excellent modeling ability of this approach on the dynamics of the single origami structure, origami chain and dual origami structure.

In Chapter 8, the conclusion of our work is presented. The limitations of current works and corresponding future research directions are proposed.

Chapter 2

DIGITAL IMAGE PROCESSING TO DETECT SUBTLE MOTION IN STONY CORAL

Coral reef ecosystems support significant biological activities and harbor huge diversity, but they are facing a severe crisis driven by anthropogenic activities and climate change. An important behavioral trait of the coral holobiont is coral motion, which may play an essential role in feeding, competition, reproduction, and thus survival and fitness. Therefore, characterizing coral behavior through motion analysis will aid our understanding of basic biological and physical coral functions. However, tissue motion in the stony scleractinian corals that contribute most to coral reef construction are subtle and may be imperceptible to both the human eye and commonly used imaging techniques. Here we propose and apply a systematic approach to quantify and visualize subtle coral motion across a series of light and dark cycles in the scleractinian coral *Montipora capricornis.* We use digital image correlation and optical flow techniques to quantify and characterize minute coral motions under different light conditions. In addition, as a visualization tool, motion magnification algorithm magnifies coral motions in different frequencies, which explicitly displays the distinctive dynamic modes of coral movement. Specifically, our assessment of displacement, strain, optical flow, and mode shape quantify coral motion under different light conditions, and they all show that *Montipora capricornis* exhibits more active motions at night compared to day. Our approach provides an unprecedented insight into micro-scale coral movement and behavior through macro-scale digital imaging, thus offering a useful empirical toolset for the coral research community.

2.1 Introduction

Reef-building corals, as keystone organisms, support diverse marine communities and provide a host of ecosystem functions for associated creatures, such as macrofauna. They are composed of coral organisms living in symbiosis with photosynthetic dinoflagellate algae and a complex of additional bacterial, archaeal and fungal communities [71]. Coral behavior, physiology and ecology are impacted by anthropogenic global climate change through the global rise in sea-surface temperatures and ocean acidification [22]. Simultaneously, coral reefs have experienced substantial decline due to disease outbreaks [72], overfishing [73], coastal development and associated runoff [74]. The increasing frequency of marine heat waves has also resulted in mass coral mortality [20, 21]. The combination of these stressors is threatening coral reefs at an unprecedented scale.

One notable aspect of corals is their dynamic motion (i.e., temporal changes of the polyp and tissue behavior), since it could play an important role in coral physiology and the coral health in a changing environment. Thus, understanding coral motion will help us to better assess coral performance in a proactive manner and understand coral physiology and the coral health in a changing environment in terms of the light condition, temperature, pH and other environmental variables [39, 75–81]. Some soft corals, such as the family of Xeniidae, exhibit a unique, rhythmic pulsation, which is believed to enhance photosynthesis [82, 83]. However, compared with the soft corals, the scleractinian corals responsible for the framework structure of most reefs mineralize a rock-like skeleton made of calcium carbonate. In many species of scleractinian corals, the motion of tissue is more subtle or imperceptible. Therefore, visualizing and quantifying the dynamic motion in order to extract information on coral behavior remains challenging for researchers studying scleractinia.

The dynamic motion of scleractinian corals interacts with a number of physiological processes and environmental responses. For example, some branched corals with small polyps will expand their tentacles to expose the photosynthetic symbionts to light during daytime [39–41]. However, under the strong light, the coral will retract the tentacles to protect photosynthetic symbionts from irradiance [39–41]. These behavioral differences indicate how coral movement can both impact and act as an indicator of ecological and physiological tradeoffs. Besides, some tentacles also serve as the probes to detect and kill competitors that settle within the wide aggressive reach of these massive corals [45]. The ciliary motion of tentacles also contributes to the mass transfer [46–48]. In areas away from coral polyps and their tentacles, the coenosarc, more subtle tissue movements have been revealed. These waves of tissue movement may speculatively be involved in enveloping or pumping seawater to different reservoirs within a coral [37, 38]. Recently, seawater exchange rates in a growing coral were found to respond to stressful conditions like extreme ocean acidification. Taken together, experiments like these hint at the rich connections that may exists between tissue movement, physiology, and how corals respond to environmental changes. New techniques that can image and quantify subtle tissue movements could uncover the role of motion in coral health and help predict the fate of coral reefs in a changing ocean.

Imaging is a powerful way to provide information about the time-varying nature of the world. Photogrammetry microscopic imaging, and time-lapse imaging have resulted in the capacity of detecting change at both reef [84, 85] and cellular levels [23–25]. New imaging techniques borrowed from other fields, such as mechanics, aerospace engineering and biological engineering, promise even more detailed and quantitative information that could be applied to address the fine-scale analysis of coral movement under a changing environment [86, 87]. For example, correlation-based image registration and tracking methods such as digital image correlation (DIC) and particle image velocimetry (PIV) measure the mechanics of materials and fluids [86, 88], and thus could be used to map movement of the coral tissue surface [48]. Optical flow is another effective method to demonstrate the movement between the camera and moving objects [87]. These approaches can potentially quantify the pixel-level motion in terms of displacement and velocity in biological fields.

To provide the evident motions, previous attempts on magnifying subtle and imperceptible movements have been made along two perspectives: Lagrangian perspective and Eulerian perspective [89–92]. For instance, the imperceptible change in face color can be magnified to estimate the heart rate [93], and the functional role of tectorial membrane in mammalian hearing can be revealed [94]. These approaches have rarely been used in marine biological systems including corals where they could quantify and visualize motion and further build a bridge between imaging techniques and biomechanics.

Here, we select one species of hard coral, *Montipora capricornis*, to study the dynamic motion of coral polyps and coenosarc under diel cycling light conditions using time lapse imaging. We first quantify the coral motion by DIC and extract barely visible mechanical quantities in terms of displacements and strains. Next we present the optical flow to show the velocity field and motion polarization. These two methods offer physiological information in corals with high consistency, which could not have been sensed by naked eyes. Typical modes of motion are visualized by the phase-based motion magnification, which clearly shows a pattern of motion related to the corals' sensitivity to the changing light conditions. We provide a systematic and quantitative approach for characterizing and analyzing subtle and/or imperceptible coral tissue movements, thereby opening a new vista in coral behavioral, physiological, and cellular analysis.

2.2 Experimental system

Figure 2.1(a) shows a schematic of the experimental setup used to observe the coral *Montipora capricornis.* The planar structure and textures on the surface of *Montipora capricornis* are beneficial to the implementation of our algorithm, which makes this species a good candidate for this proof-of-concept study. It includes a digital single lens reflex (DSLR) camera with a macro lens to take pictures of the fine structures of coral tissue surface. To study the effect of light on coral tissue motion, aquarium light and ceiling light were used to mimic light conditions during the day and the night. Experimental setup details are shown in Appendix A and related Figure A.1.

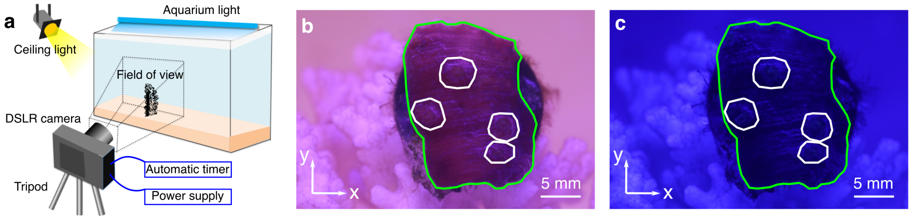

Figure 2.1: Experimental observation of *Montipora capricornis.* (a) Schematic of experimental setup of a DSLR camera, aimed at the corals in the aquarium. (b) Daylight pictures were taken under white light, while (c) nighttime pictures were taken under blue light. Daylight pictures were taken under white light, while (c) nighttime pictures were taken under blue light.

Figure 2.1(b) and Figure 2.1(c) display the pictures taken at day and at night, respectively. The green curves represent the coral tissue margins. The white curves indicate the positions of polyps. Four polyps with short tentacles are on the coral surface. The nearly planar arrangement of the coral provided the opportunity to obtain motion information from all polyps on the coral's surface. The heterogeneity of the tissue on surface creates texture that is sufficient for applying DIC and optical flow techniques. Besides, the hue is more blueish at night due to the lack of the ceiling light. Visualization of coral dynamic motion, not perceptible by the human eye, can be observed from the time-lapse video played in 10 frames per second (×1200 speed; Supplementary movie [95]).

2.3 Characterization by digital image correlation

In order to quantify coral tissue motion from a biomechanics perspective, we used a DIC technique to characterize the deformation of the surface relative to an initial reference picture (the first picture). Displacements (u_x) along horizontal direction between the reference picture and the second picture at day and night are shown in Figure 2.2(a), respectively. The strongest motions are concentrated around polyps and the edge of the fragment. At night, most of the coral tissues surface undergoes horizontal motion, while few coral tissues are moving horizontally at day. Displacements (u_y) along the vertical direction were also quantified between the reference picture and the second picture at day and night, respectively [Figure 2.2(b)]. Similar to the distribution of displacement u_x, the strongest motions are concentrated around polyps and the edge of the fragment. Vertical tissue motion is more widespread across the coral at night compared to daytime. The displacement of both u_x and u_y, in comparison to the reference picture between day and night, can be seen in videos created from two hundred pictures (Supplementary movie [95]). These visualizations highlight that the coral tissue surface is moving dynamically over time, with more movement observed during the night than during the day.

In order to explore the statistics of DIC results, we show the histogram of displacements u_x and u_y. Across around 13 hours, histograms of displacements u_x and u_y are continuously changing (Supplementary movie [95]). Figure 2.2(c) exhibits the percentage histograms of the displacement u_x and u_y during day and night in the left and right panels. The red and blue curves in each panel indicate the mean of displacement distribution during day and night. The corresponding variation ranges are shown in pink and cyan. According to the histogram [Figure 2.2(c)], most of the areas of the coral tissue surface are barely moving,

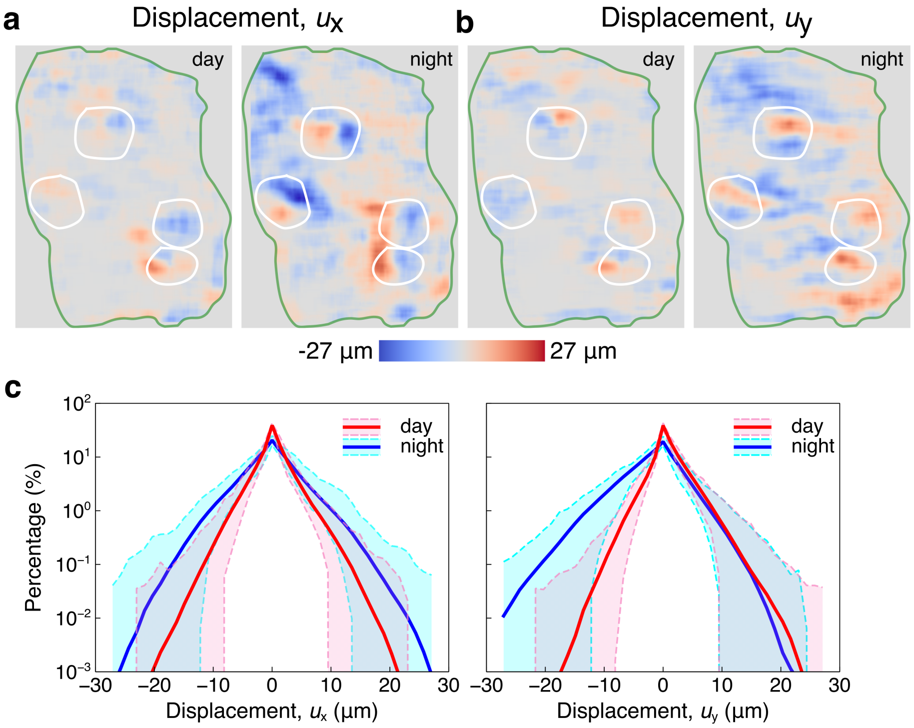

Figure 2.2: Displacements of the coral tissue surface from digital image correlation. (a) The displacements u_x along horizontal direction between the reference picture and the second picture at day and night are shown in the left and right panel, respectively. (b) The displacements u_y along horizontal direction between the reference picture and the second picture at day and night are shown in the left and right panel, respectively. (c) The percentage histograms of displacement u_x and displacement u_y are shown in the left and right panels, respectively. The red and blue curves indicate the means of each displacement during day and night. The pink and cyan regions are variations during day and night, respectively.

i.e. nearly zero displacement. For the moving part, more areas of the coral tissue surface are contributing to the motion at night since the blue curves are above the red curves, coinciding with the displacements shown in Figure 2.2(a) and Figure 2.2(b). Furthermore, the histogram of displacement u_x [Figure 2.2(c)] illustrates the nearly symmetric distribution, suggesting that there is no motion preference and the system is balanced along the horizontal direction. However, the histogram of displacement u_y shows an asymmetric distribution. During the day, the coral tissue surface tends to move upwards because there are more positive values, while at night, the tissue tends to move downwards, which indicates that motion preference based on the light condition is shown along the vertical direction.

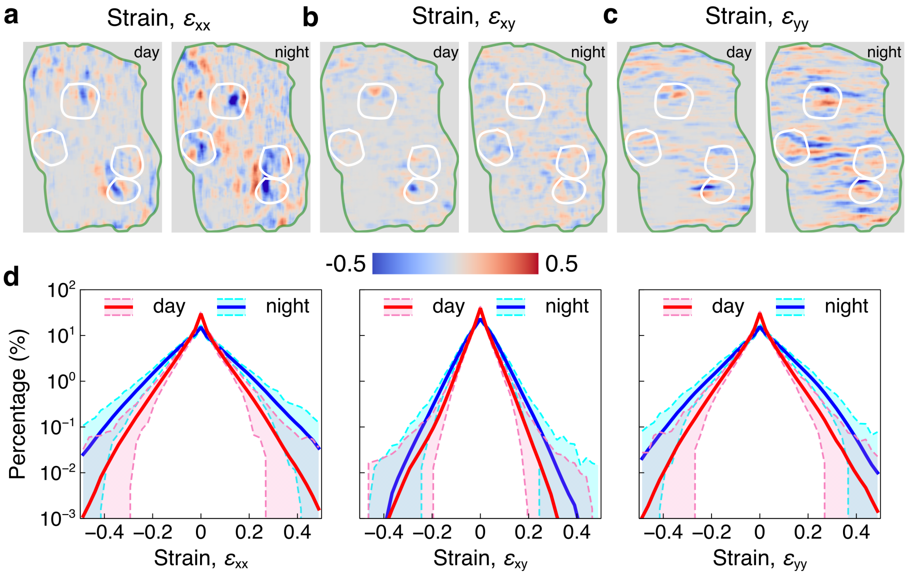

Figure 2.3: Strains of the coral tissue surface from digital image correlation. (a)-(c) Strains ϵ_{xx}, ϵ_{xy} and ϵ_{yy} between the first and the second picture from day and night are shown in the left and right panel, respectively. Green curves in (a) and (b) represents the edge of the fragment and white curves enclose the polyps. (d) The percentage histogram of the strains, ϵ_{xx}, ϵ_{xy} and ϵ_{yy} are shown in the left, middle and right panels, respectively. The red and blue curves indicate the means of each strain during day and night. The pink and cyan regions are variations during day and night.

Strain measures the deformation of the material to identify whether it is under tension or compression. The linear strain is considered here. To obtain the accurate strain, smoothing and noise reduction of displacement field are necessary. We adopt the point-wise local least-square fitting technique [96, 97]. The strain calculation window is set to 19 × 19 points, which provides a trade-off between accuracy and smoothness of strain estimation. Supplementary movie shows the normal strain ϵ_{xx} and ϵ_{yy}, shear strain ϵ_{xy} during day and night, respectively [95]. The strains between the second picture and the reference picture are shown in Figures 2.3(a)-(c). Figure 2.3(a) shows the normal strain ϵ_{xx} during day and night. The largest strain is concentrated around the polyps and obviously the distribution of ϵ_{xx} is more evident at night [Figure 2.3(a)], suggesting that more of the coral tissue surface participate in the motion at that time. Figure 2.3(b) and Figure 2.3(c), indicating shear strain ϵ_{xy} and normal strain ϵ_{yy}, show the same features as Figure 2.3(a). Compared with the ϵ_{xx}, ϵ_{yy} has clearer alignment along the wrinkles on the coral surface, indicating the anisotropy of the coral tissue surface motion. Similar to the analysis of displacement, the corresponding histograms are displayed from left to right in Figure 2.3(d). The red and blue curves in each panel indicate the mean of strain distribution during day and night throughout the strain result. The corresponding variation ranges are shown in pink and cyan. Most of the coral tissue was not either under tension or compression due to the nearly zero strains, which is corresponding to the nearly zero displacements in the above analysis. Corresponding to the displacement, strain measurements also show larger values at night.

We note that we have also conducted a noise effect study to test the statistical significance of the DIC results presented above. Although correlation functions act to normalize images during image processing, quantification of noise effects provide a further verification of the observed patterns [98]. The enclosed coral skeleton on which our coral is fixed is analyzed by DIC. Details and analysis are in the Appendix A. The results indicate that the DIC results are valid, since the noise is smaller than the extracted signal (Appendix A; Supplementary movie [95]).

2.4 Characterization by optical flow

Measuring optical flow is an effective method to explore the pixel-wise motion information such as velocity. In order to increase the signal-to-noise ratio, we assume the motion field is constant in a small window (21×21) around each pixel and the smoothing kernel (19×19) is used for reducing noise. The basic optical flow equation is solved for all pixels in the window by the least squares criterion, which is also known as the Lucas-Kanade method [99]. Similar to DIC, for each case, we take the first picture as the reference and calculate the optical flow for two hundred pictures. Supplementary movie shows the velocities of the optical flow during day and night [95]. Figure 2.4(a) and Figure 2.4(b) exhibit the optical flow between the second picture and the reference picture. The optical flow is encoded by the color square. The color indicates the direction of velocity and the saturation of color represents the magnitude of velocity. The colors with high saturation are around the polyps (marked by black crosses) and margins, and colors with low saturation are distributed around the coral tissue surface margin. At night, there are more colors with high saturation in the optical flow, suggesting that coral movement is higher in magnitude at night.

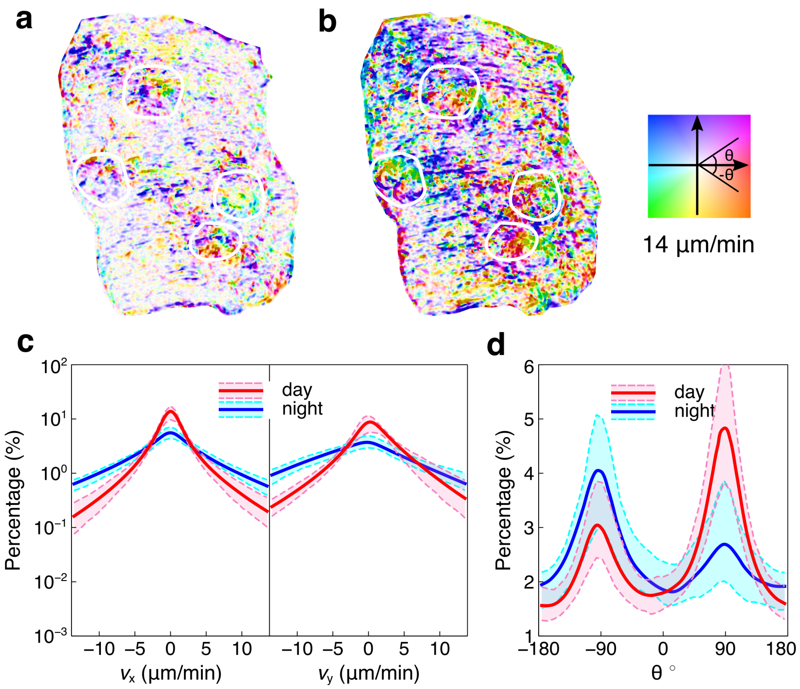

Figure 2.4: Optical flow of the coral tissue surface. (a)(b) Optical flow between the second and first pictures from day and night, respectively. White circles mark the position of polyps. (c) The percentage histograms of velocities v_x and v_y along horizontal and vertical directions. The red and blue curves indicate the means of each velocity from day and night. The pink and cyan regions are variations between day and night. (d) The percentage histogram of direction of velocity. The red and blue curves indicate the means of each angle from day and night. The pink and cyan regions are variations during day and night.

The histograms of velocity v_x and v_y along horizontal and vertical directions are studied to explore the statistics of optical flow. Figure 2.4(c) shows the histogram of v_x and v_y. The red and blue curves in each panel indicate the mean of corresponding velocity distribution from day and night. The corresponding variation ranges are shown in pink and cyan dashed lines. While the DIC extracts the displacement information, optical flow can provide pixel-wise velocity information. Similar to DIC results, along the horizontal direction, the histogram is symmetric [Figure 2.4(c)], indicating that the coral tissue surface does not have statistically significant motion preference along the horizontal direction. The histogram of v_y shows the similar trend with the displacement u_y from DIC [Figure 2.4(c)]. During the day, the coral tissue surface tends to present a positive velocity translating upwards motion, while the tissue tends to move downwards with a negative velocity at night. This observation is even more evident in Figure 2.4(d), which offers a histogram of direction of optical flow. 90° and -90° represent the upward and downward direction, respectively. According to Figure 2.4(d), the dominated motion is along the vertical direction whatever light condition the coral is under since there are evident peaks in 90° and -90°. Besides, in different light conditions, the motion directions are different. At day, there is a higher peak in 90°, which means that the tissue tends to move upwards, while at night, the higher peak in -90° suggests the downwards motion. Similarly, we conducted the noise effect study (Appendix A). The results show that the velocities on the coral skeleton is smaller, thus support the validation of the analysis mentioned above.

2.5 Motion microscope for the coral tissue surface

Exploring the biological and physical modes of coral tissue motion is crucial to understand the coral behaviors. Here we further process the optical flow result to obtain the deformation of coral tissue surface at different frequencies and magnify the biological modes of this movement to make them visible to human eyes. To this end, we perform the Fourier transform on the optical flow results and extract the absolute value of velocity in different frequencies. Zero padding is used to increase the frequency resolution. Supplementary movie shows mode shapes of coral tissue in the frequency range of 0 min^{-1} to 0.25 min^{-1} (Nyquist frequency) [95]. Typical mode shapes from day and night are shown in Figures 2.5(a)-(c) and Figures 2.5(d)-(f), respectively, after normalization. As the frequency increases, the intensity of the motion decreases. In the frequency 0.05 min^{-1} during the day, as shown in Figure 2.5(a), the motion is concentrated around the polyps and margins. In stark contrast, Figure 2.5(d) exhibits the mode shape in the frequency 0.05 min^{-1} where the motion is not only around the polyps and margins, but also on the coral tissue surface. Under both light conditions, a greater proportion of coral tissue contributes to the motion with the increasing frequency. Overall, the mode of extremely slow coral tissue motion is observed, which coincides with the phenomenon observed in DIC and optical flow.

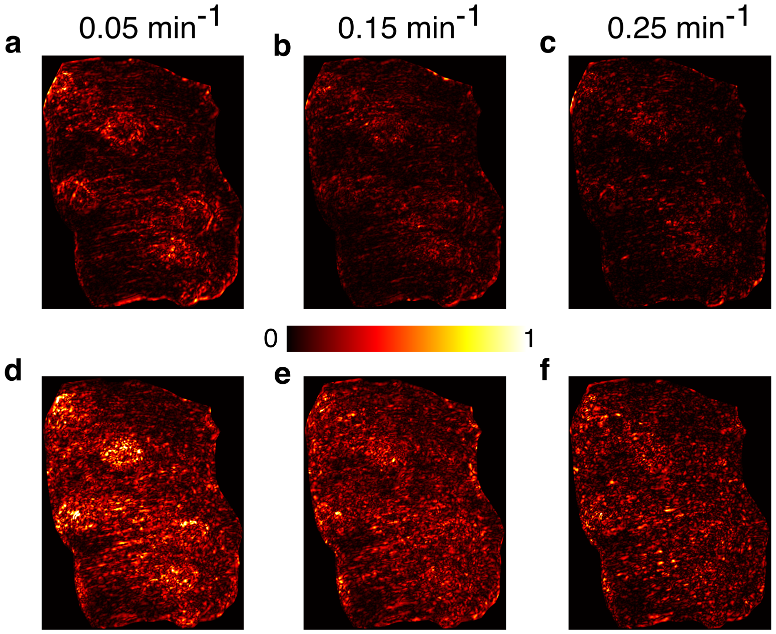

Figure 2.5: Mode shape of coral tissue motion during day and night. (a)-(c) Mode shapes of coral tissue motion during day at frequencies 0.05 min^{-1}, 0.15 min^{-1} and 0.25 min^{-1}, respectively. (d)-(f) Mode shapes of coral tissue motion during night at frequencies 0.05 min^{-1}, 0.15 min^{-1} and 0.25 min^{-1}, respectively.

In order to visualize the mode shape in different frequencies, we adopt the phase-based motion magnification [89]. The complex steerable pyramid, which is an over-complete transformation that decomposes an image according to spatial scale, orientation and position, is used to magnify the motion in a specific frequency range [100]. The image is completely decomposed into amplitudes $A_{\omega,\theta}(x,y)$ and phases $\phi_{\omega,\theta}(x,y)$ at every scale ω and orientation θ. We augment the motion 75 times by magnifying phase in the frequency range of interest. We choose three frequency ranges, 0.04 min^{-1} $\sim$ 0.06 min^{-1}, 0.14 min^{-1} $\sim$ 0.16 min^{-1} and 0.22 min^{-1} $\sim$ 0.24 min^{-1} to demonstrate the motion microscope for coral tissue mode shapes. Supplementary movie shows the magnified video played in 10 frames per second, which is made of pictures taken during the day [95]. The movie presents the polyps motion in the low frequency range and the coral tissue surface motion in the high frequency range. Besides, the motion magnitude is decreasing as the frequency increases. Supplementary movie shows the magnified video at night in the frequency range mentioned above [95]. According to the video, more coral tissues are involved in the motion, which coincides with the mode shape analysis from the optical flow.

2.6 Conclusion and discussion

We applied digital image correlation, optical flow, and motion microscopy techniques to a series of images of *Montipora capricornis*. Though this hard coral has the slow and subtle tissue motion, which is hard to capture not only with naked eyes, but also with optical apparatus, we have successfully extracted its responsiveness to light conditions based on ~ 13 hours of high-frequency images. The blending of powerful and effective tools from mechanics and computer science and coral biology opens avenues for studying coral physiology from macro-scale pictures. It is more than likely that different coral species present different levels of tissue motion in direct relation with their overall morphology (e.g. branching, corymbose, digitate, encrusting, foliose, laminar, massive, submissive, solitary, tabulate). With this consideration in mind, imaging surface tissue motion could help predict species-specific responses to sediment smothering [101, 102] and whether corals adapt the movements of the surface tissue according to particle loading in the water column in relation to flood plumes and land runoff. Reef-scale responses to flood plumes triggered by severe weather events could then be predicted according to coral surface tissue motion measurements, depending on coral cover and species representation. Investigations linked to coral tissue motion should also be considered with respect to exposure to pollutants generated by anthropogenic activities, e.g., oil and chemical dispersant [103, 104]. This systematic approach offers us possibilities to quantify and visualize the subtle coral tissue surface motion and important physical and biological mode in a time-efficient, yet accurate manner. In this proof-of-concept study, we only focus on the effect of light to motion for a single coral, but the proposed approach can be generalized to study the effect of a variety of environmental variables on coral tissue motion. Furthermore, this method could be applied to investigate the links between tissue motion and coral mucus (production, thickness, composition, spread), especially in response to excess sediment or bacterial infection [105, 106].

2.7 Author contribution

This chapter is adopted from Shuaifeng Li, Liza M. Roger, Lokender Kumar, Nastassja A. Lewinski, Judith Klein-Seetharaman, Alex Gagnon, Hollie M. Putnam and Jinkyu Yang, Digital image processing to detect subtle motion in stony coral. *Scientific Reports*, 11, 7722, 2021.

S. Li and J. Yang proposed the research; S. Li conducted the experiments; S. Li performed the numerical analysis; H. M. Putnam and J. Yang provided guidance throughout the research; S. Li, H. M. Putnam, and J. Yang prepared the manuscript; L. M. Roger, L. Kumar, N. A. Lewinski, J. Klein and A. Gagnon provided guidance during manuscript preparation and development.

Chapter 3

SPATIOTEMPORAL DYNAMICS OF CORAL POLYPS ON A FLUIDIC PLATFORM

Reef-building corals are inherently sessile organisms. However, motion is an important behavioral trait of coral polyps, which plays an essential role in feeding, competition, defense, reproduction, and thus, survival and fitness. Notwithstanding the importance of inherent temporal and spatial multiscale features of polyps, their quantitative properties and modeling still remain challenging and unexplored. Here, we observe *Pocillopora acuta in vivo* under different light and temperature conditions using a fluidic platform that allows the direct microscopic study of small live coral fragments, where the stochastic dynamics of the in-plane waving motion of polyps is uncovered. The relationship between polyps on nubbins is described by motion-correlation analysis. Additionally, the fractional Brownian motions of polyps under certain light conditions and temperatures are revealed by the Hurst index via power spectral analysis. Finally, the motion of polyps is modeled by Langevin dynamics, numerically obtained by data-driven parameterization. This combination of experimental observations, numerical analysis, and theoretical modeling opens an avenue to boost our understanding of the biological and physical behaviors of corals in relation to changing environmental conditions.

3.1 Introduction

Animal movement is one of the key features in understanding animal behaviors. The rich dynamics of movements in biological systems have been attracting the interest of many researchers in the field of biophysics for its inherent temporal and spatial multi-scale features. However, quantifying and characterizing the different types of motion in biological systems remains challenging due to randomness and intrinsically complex nature [49]. Recently, with the development of tracking technique and mathematical modeling strategies, behaviors, foraging strategies and distributions of animals are well studied. A variety of methodologies to model animal motions has been proposed, including but not limited to uncorrelated/correlated random walks [49, 107–109], Levy flight [110–114], stochastic differential equation such as the noted Ornstein-Uhlenbeck process [49, 115–119] and hidden Markov models [120, 121].

Many biophysical processes can be modeled as Brownian motion. Nevertheless, other processes reveal the existence of anomalous Brownian motion, which is also called fractional Brownian motion [122]. Such Brownian and derivative motions are widely observed not only in biological systems but also in physical systems, such as dynamics of ultracold atoms [123], quantum dots [124–126], nano-electrodes[127], heartbeat intervals [128], and in our daily lives including fluctuations of climate [129] and economic markets [130]. In biological systems, particularly in subcellular and cellular structures, the motion of proteins or submicron tracers in living cells [131–134], telomere diffusion in the cell nucleus [50] and diffusion in lipid membranes [135–138] have been characterized by fractional Brownian motions. However, the efficacy of such fractional Brownian motion to model the behavior of clonal and colonial organisms such as reef-building corals has not been reported and remains yet elusive.

Coral reefs, as keystone organisms, support rich and diverse ecosystems, and hold immense ecological and economic value. Coral organisms live in symbiosis with photosynthetic algae and complex assemblages of bacterial, archaeal and fungal communities [71]. The impacts of anthropogenic activities influence the behavior, physiology and ecology of corals through the global rise in sea-surface temperatures and ocean acidification [22]. Coral colonies are fixed to the substrate but polyps display dynamic properties, including temporal motion and their substructures which may play an important role in overall coral health, especially in relation to changing environmental conditions [139]. For example, some soft corals, such as the family of Xeniidae, exhibit a unique, rhythmic pulsation, which functions as enhancement of photosynthesis by modulating the water flow [82, 83], while in many species of scleractinian corals, the motions of polyps and tissue are more subtle or even imperceptible [139]. The erratic behaviors may occur on coral polyps and colonies due to abnormal environmental variables. Thus, understanding coral motions will help us to better assess coral health in a proactive manner and understand coral physiology in a changing environment in terms of light conditions, temperature, pH and other environmental variables [39, 75–77, 79, 80, 140]. To date, however, the motions of coral polyps remain largely unexplored, and their characterization using appropriate models is in its infancy. To evaluate the effect of environmental variables on coral motion, the fluidic platform is necessary for study of coral motion *in vivo* at the microscale [141, 142].

To this end, we design a fluidic platform which allows us to observe the coral nubbin *in vivo* in real time under the microscope so that the subtle in-plane waving motion of polyps can be captured for analysis. We conduct multiple observations of coral nubbins under different light conditions and temperatures to demonstrate how polyps adjust motions in response to these conditions. We find that both light (wavelength) and temperature impact polyp motions and modulate behaviors based on differences in correlation, phase synchronization, and the Hurst index of stochastic motion processes. Moreover, we utilize the generalized Langevin equation to model the polyps' motion under different light conditions and temperatures. This unique combination of studying coral behaviors and describing it with mathematical models can boost our understanding of coral physiology, and promote the simulation and prediction of coral behavior in response to a given environmental condition in the future.

3.2 Experimental system

Figure 3.1(a) shows the schematic of our octagonal fluidic platform with a coral nubbin in the chamber. Our fluidic platform manufactured through 3D printing is shown in the inset with the tubing connectors attached. The full design is explained in Appendix B. It is centered around a main chamber surrounded with eight valves and in/outflow channels which can be opened or closed individually. The valves can control the flow of fluid. Therein, in Figure 3.1(a), since the valves shaded in yellow are open, the flow direction of fluid is along a straight path, shown in blue. The computational fluid dynamics simulation of this fluidic platform is shown in Appendix B and Figure B.1. The velocity field shows the low impact to the coral nubbin induced by the water flow. The experimental setup and procedure are shown in Appendix B.

Figure 3.1(b) shows the coral nubbin under the microscope where the coral nubbin with

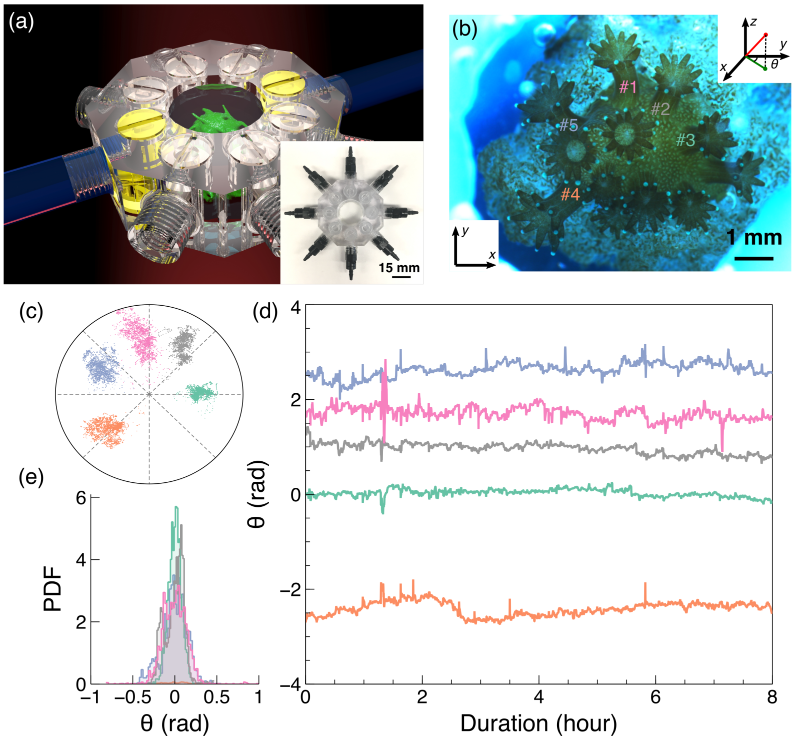

Figure 3.1: Experimental observation of coral on the fluidic platform. (a) Schematic of our octagonal fluidic platform with a coral nubbin in the chamber. Inset shows our octagonal fluidic platform for experiment made by 3D printing with VeroClear resin. Valves control the flow of fluid. (b) Coral nubbin observed under the microscope under normal light conditions and 25°C. Polyps being analyzed in this case are labeled by numbers and color codes used in subsequent figures. (c) Trajectory of polyps. (d) Azimuthal angles, θ, of different polyps as a function of duration. (e) Probability density function of the azimuthal angles, θ, of different polyps after being centered on zero. Colors in (c) and (d) correspond to the colors of labels in (b).

several polyps can be observed. This picture is taken of the experimental setup under normal light and 25°C. A time-lapse video with 300× playback, illustrating the polyps' motions, is shown in Supplementary movie [143]. The polyps are moving vibrantly, with motions including contraction, extension, and waving. Since we observe the motion right above the coral nubbin, only the orthogonal projection of three-dimensional polyps' motion is recorded. Each polyp is simplified for analysis as a line segment connecting the tentacle crown to the foot of the polyp so that the azimuthal angle can be calculated with respect to the horizontal direction. The tentacle crown and foot of the polyp are tracked using the correlation-based algorithm [144]. The azimuthal angle θ shown in the inset of Figure 3.1(b) is found to be appropriate in describing the original motion. Therefore, the azimuthal angle representing the in-plane waving motion of polyp is used for analysis and discussion below.

Figure 3.1(c) exhibits the trajectories of the tentacle crowns of the polyps in different colors corresponding to the labels in Figure 3.1(b). Each of them covers a certain area within the random pattern. Since we only study the in-plane waving motions of polyps, we extract the information of azimuthal angle and show it in Figure 3.1(d). These motion signals are all oscillating over time with several spikes at some time periods. Besides, these signals do not exhibit certain trends indicating the polyps are randomly moving around their central points. Therefore, as expected, the probability density functions (PDFs) of these motion signals after centered to zero exhibit symmetric shapes as shown in Figure 3.1(e). The PDFs indicate that most motions are around the central points.

3.3 Motion correlation of polyps

Since there are several polyps on one coral nubbin, it is interesting and natural to study the coordination of polyps' motions if the whole coral nubbin is considered as a colony of interconnected polyps. The motion correlation between polyp m and polyp n can be calculated as below:

$$r_{mn} = \frac{\sum (\theta_i^m - \bar{\theta}^m)(\theta_i^n - \bar{\theta}^n)}{\sqrt{\sum (\theta_i^m - \bar{\theta}^m)^2 \sum (\theta_i^n - \bar{\theta}^n)^2}} \tag{3.1}$$

where i and the upper bar denote the index number and the average of the temporal data. As displayed in Figure 3.2(a), the positive correlation coefficient indicates the correlated relation between two polyps while the negative one suggests the anti-correlated relation. The correlated or anti-correlated relation indicates the synchrony of two polyps in terms of moving direction. Besides, the correlation coefficient changes as a function of light conditions. Compared with the polyps' motions under normal light which is the control group, the absolute values of correlation coefficient increases with increasing wavelength. This implies that the in-plane waving motion trends of polyps on one coral nubbin (i.e., in very close proximity) become more and more pronounced (whether correlated or anti-correlated) when the light shifts from blue light to red light. When the polyps are under normal light, they generally show a stronger trend (correlation or anti-correlation) compared to single-wavelength conditions. Specifically, the case under blue light has a significant difference from the other cases in correlated motion ($p = 0.0043$).

We also study the effect of temperature on the correlation among polyps on the same coral nubbin shown in Figure 3.2(b). The experimental groups (15°C and 30°C) have slight changes in comparison with the control group (20°C), where the absolute values of correlation coefficient become smaller with increasing temperature. But for both correlation and anticorrelation, no significant difference was found according to p value. It indicates stronger trends, more and more correlated or anti-correlated, of in-plane waving motions of polyps at lower temperature.

Apart from the correlation, phase synchronization is another important feature to describe the synchrony between two motion signals. The phase denotes the angle corresponding to the momentary deflection of an oscillation. Phase synchronization, as a nonlinear measure, refers to the correlation of phase values between two in-plane waving motions of polyp m and polyp n, which can be quantified to be phase locking value (PLV) calculated as below:

$$\mathrm{PLV}_{mn} = |\frac{1}{N}\sum_{j=1}^{N} e^{i[\varphi_m(t_j)-\varphi_n(t_(j))]}| \tag{3.2}$$

where φ_m and φ_n are the phases of θ_m and θ_n, which are obtained by Hilbert transform. Figure 3.2(c) exhibits the PLV as a function of light condition. We notice that under blue light, the PLV is smaller than others, suggesting that the phases of in-plane waving motion of polyps are less synchronized than others, similar to the correlation shown in Figure 3.2(a). This obvious trend is also verified by the p-value between blue light and other light conditions ($p = 0.0001$, 0.0029 and 0.0358 for normal, green and red light). Temperature effects on phase synchronization is displayed in Figure 3.2(d). As the temperature increases, the PLV decreases similar to the correlation shown in Figure 3.2(b), indicating that in low temperature the polyps' motions have higher phase synchronization. But the temperature effect is not pronounced.

In conclusion, the motions of polyps belonging to the same coral nubbin do not happen

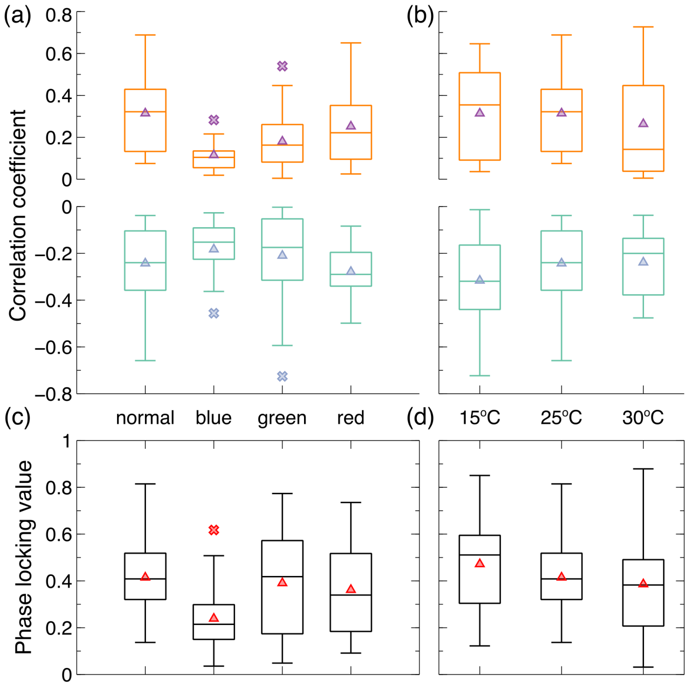

Figure 3.2: Analysis of correlation and phase synchronization. (a) Correlation coefficients between polyps on the same coral nubbin under different light conditions (wavelength). Correlations and anticorrelations are shown in orange and green, respectively. (b) Correlation coefficients between polyps on the same coral nubbin under different temperatures. Correlations and anticorrelations are shown in orange and green, respectively. (c) Phase-locking value characterizing phase synchronization between polyps on the same coral nubbin under different light conditions. (d) Phase-locking value characterizing phase synchronization between polyps on the same coral nubbin under different temperatures. Cross and triangle symbols in (a)-(d) represent the outliers and mean, respectively.

in isolation. Instead, they are coordinated in some way. This shows the connection between polyps provided by the connective tissue (coenosarc) extends to inter-polyp motion analyzed by motion correlation and phase synchronization. As a result, the in-plane waving motions of polyps on the same coral nubbin are rhythmically activated and inhibited, which can be adjusted by light conditions and temperatures.

3.4 Fractional Brownian motion and its power spectral densities

According to the observation of the polyp trajectories [Figure 3.1(c) and Figure 3.1(e)], the in-plane waving motions of polyps are the Gaussian stochastic process whose covariance function is defined as:

$$\langle \theta_{t_1} \theta_{t_2} \rangle = D(t_1^{2H} + t_2^{2H} - |t_1 - t_2|^{2H}) \tag{3.3}$$

where D is diffusion coefficient, t_1 and t_2 are two points in time, and $H \in (0, 1)$ is the Hurst index. When $H \neq 0$, the process is the fractional Brownian motion and when $H = 0.5$ the process is standard Brownian motion. This metric provides possibilities to characterize the motion of polyps from the perspective of Brownian motion. First of all, we calculate the power spectral density (PSD) of the single trajectory using the equation:

$$\text{PSD} = \frac{1}{T} | \int_0^T \theta_t e^{ift} dt|^2 \tag{3.4}$$

where T is the observation time. In total we obtain multiple (≥ 15) trajectories for the experiments under each light and temperature condition.

As shown in Figure 3.3(a), the PSDs of individual trajectories under different light conditions exhibit straight trends in the logarithm scale, suggesting the power-law relation between frequency and PSD. Besides, the slopes of PSDs are within the certain ranges that can be used to deduce the Hurst index according to the power-law relation between frequency and PSD: PSD $\sim f^{-(2H+1)}$. However, since PSD is an ensemble-averaged property, our available experimental datasets are small for such ensemble averages so that the calculated Hurst index may not be accurate. In addition, simply fitting the straight line will give us a deceptive result because in standard Brownian motion and fractional Brownian motion when $H > 0.5$, they both own the PSDs that scales as f^{-2}.

Therefore, the method calculating Hurst index by the zero frequency PSD is applied [50]. The PSD at zero frequency can be expressed as:

$$\text{PSD}(f = 0) = \frac{1}{T} | \int_0^T \theta_t dt|^2 \tag{3.5}$$

which is simply the squared area under the motion signal θ_t divided by T. It is proven that individual trajectory zero-frequency PSD is the gamma distribution with scale 2μ and shape

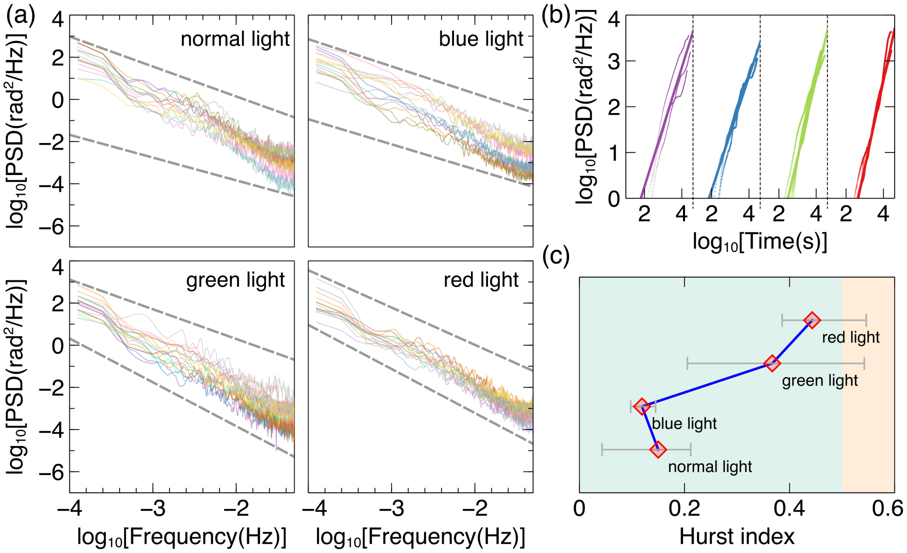

Figure 3.3: Power spectrum analysis of experimental data sets under different light conditions. (a) PSD of representative in-plane waving motions represented by the azimuthal angle, θ, under different light conditions. Dashed gray lines show the $1/f^{1.08}$ and $1/f^{1.42}$ trends for normal light, $1/f^{1.19}$ and $1/f^{1.28}$ trends for blue light, $1/f^{1.41}$ and $1/f^{2}$ trends for green light, and $1/f^{1.77}$ and $1/f^{2}$ trends for red light. (b) PSDs evaluated at zero frequency shown in dots for normal light, blue light, green light, and red light from left to right. Solid lines show the fitted results. Both x and y axes are on the logarithmic scale. (c) Hurst indices for cases under normal light, blue light, green light, and red light. Subdiffusion and superdiffusion areas are shaded in green and orange, respectively.

parameter 1/2, where μ is the ensemble-averaged zero-frequency PSD. μ has the power-law relation with observation time universally (for both subdiffusive and superdiffusive cases) expressed by:

$$\mu(f = 0) = \frac{DT^{2H+1}}{H+1} \tag{3.6}$$

Therefore, we can easily leverage this relation to calculate the reliable Hurst index. As shown in Figure 3.3(b), from left to right, the zero-frequency PSDs of θ under normal light, blue light, green light and red light are increasing as a function of observation time. We notice that in the logarithm scale they have linear trends (dots) and then are fitted by straight lines (solid lines), which agrees with the dots and coincides with the theory above.

Furthermore, the Hurst index for each case can be extracted shown in Figure 3.3(c). From this graph, we notice that in most cases the Hurst index is less than 0.5 (area shaded in green), indicating the in-plane waving motions of polyps are subdiffusive in fractional Brownian motion. To entail a subdiffusive motion, the increments are negatively correlated, such that it is most likely that after an increasing step a decreasing one will follow. It is obvious in Figure 3.3(c) that the in-plane waving motions of polyps under the blue light have the smallest Hurst index. With the increasing wavelength from blue light to red light, the Hurst index is increasing close to 0.5, which implies that a decreasing step will be less likely to follow an increasing step. Given the power-law relation between frequency and PSD, the trends PSD $\sim f^{-(2H+1)}$ based on the calculated Hurst index from zero frequency PSD are illustrated in Figure 3.3(a). The gray dashed lines in Figure 3.3(a) show the $f^{-1.08}$ and $f^{-1.42}$ trends for normal light, $f^{-1.19}$ and $f^{-1.28}$ trends for blue light, $f^{-1.41}$ and f^{-2} trends for green light, and $f^{-1.77}$and f^{-2} trends for red light. It turns out that the estimated PSD and the PSD of individual trajectory of polyp show the good agreement.

Similarly, the PSDs under different temperatures are shown in Figure 3.4(a). In the logarithm-scale graphs, PSDs have the linear trends which agree with the power-law relation between frequency and PSD. As shown in Figure 3.4(b), from left to right, the zero-frequency PSDs as a function of time for 15°C, 25°C and 30°C have the linear trends (dots) with fitted straight lines (solid lines). Therefore, we can extract the Hurst index from the slopes of the straight lines. Figure 3.4(c) shows the Hurst index for 15°C, 25°C and 30°C, where the control group (25°C) is in the subdiffusion region. We notice that under 15°C and 30°C Hurst index is extremely variable, which spans from subdiffusion region to superdiffusion region, suggesting uncertain diffusive mode in in-plane waving motion of polyps outside the optimum thermal range. Likewise, the dashed gray lines in Figure 3.4(a) show the $f^{-1.20}$ and f^{-2} trends for 15°C, $f^{-1.08}$ and $f^{-1.42}$ trends for 25°C, and $f^{-1.25}$ and f^{-2} trends for 30°C, to indicate the agreement between the estimated PSD and the PSD of individual trajectory of polyps.

It should be noted that under normal conditions (normal light and 25°C), the Hurst index is around 0.2, which can be set to be baseline. Hurst index will deviate away from this baseline in other conditions especially under the green and red light, higher and lower temperatures. In some conditions, the diffusive type is extremely variable, switching from subdiffusion to superdiffusion. We note in passing that the findings presented here are only

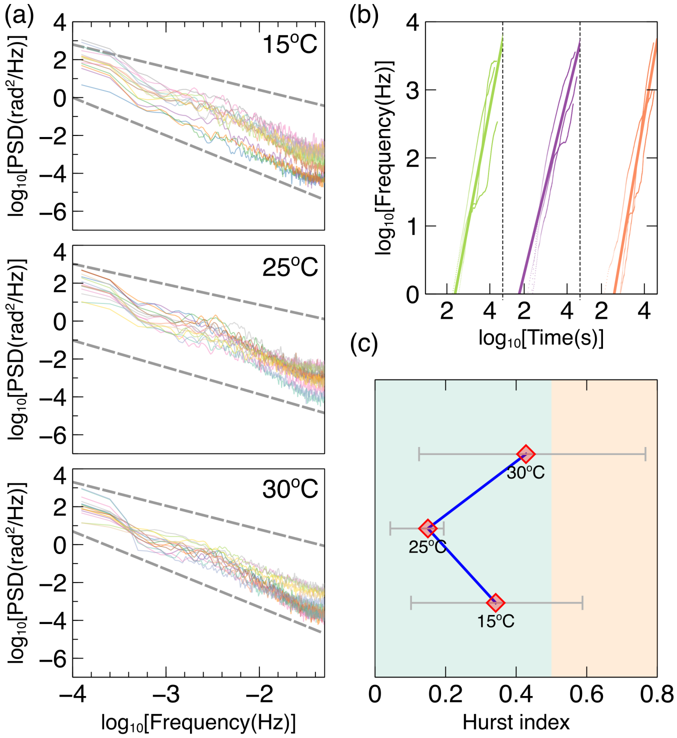

Figure 3.4: Power spectrum analysis of experimental data sets under different temperatures. (a) PSD of representative in-plane waving motions represented by the azimuthal angle, θ, under different temperatures. Dashed gray lines show the $1/f^{1.20}$ and $1/f^2$ trends for 15°C, $1/f^{1.08}$ and $1/f^{1.42}$ trends for 25°C, and $1/f^{1.25}$ and $1/f^2$ trends for 30°C. (b) PSDs evaluated at zero frequency shown in dots for 15°C, 25°C and 30°C from left to right. Solid lines show the fitted results. Both x and y axes are on the logarithmic scale. (c) Hurst indices for cases at 15°C, 25°C and 30°C. Subdiffusion and superdiffusion areas are shaded in green and orange, respectively.

relevant for *Pocillopora acuta* under the given experimental conditions, while the extension to other reef-building corals in various conditions can be explored in the future.

3.5 Theoretical modeling via Langevin dynamics

According to the discussion above, the in-plane waving motions of polyps are fractional Brownian motion that is affected by light conditions and temperatures. This stochastic Brownian process can be modelled using generalized Langevin equation without conservative force term which can be expressed by:

$$\ddot{\theta} = -\int_0^t K(t-\tau)\dot{\theta}(\tau)d\tau + R(t) \tag{3.7}$$

where K is the memory kernel function, and $R(t)$ is the random noise term with zero mean, satisfying the second fluctuation-dissipation theorem [145]: $\langle R(t)R(t')\rangle = k_B T K(t-t')$, where k_B denotes Boltzmann constant. Hence, the main focus is to model the memory kernel function and the random noise term. Here we use the data-driven method to discover the parameterization of generalized Langevin equation [146, 147]. The generalized Langevin equation becomes $G(t) = -\int_0^t K(t-\tau)H(\tau)d\tau$ after $\dot{\theta}(0)^T$ is right-multiplied to the generalized Langevin equation. Note that the correlation matrices $G(t) = \langle\ddot{\theta}\dot{\theta}(0)^T\rangle$, $H(t) = \langle\dot{\theta}\dot{\theta}(0)^T\rangle$ and $\langle R(t)\dot{\theta}(0)^T\rangle = 0$ [148]. However, this equation may lead to an unreliable solution due to the integral equation of the first kind [146]. We then obtain $\hat{G}(\xi) = -\hat{K}(\xi)\hat{H}(\xi)$ by conducting the Laplace transform, where the hat means the Laplace transform of corresponding functions. The memory kernel function in the Markovian limit $\hat{K}(\infty)$, also known as friction tensor, is estimated to compare in each experimental setup. As shown in Figure 3.5(a), the $\hat{K}(\infty)$ calculated by:

$$\hat{K}(\infty) = -\hat{G}(\infty)\hat{H}(\infty) = -(\int_0^\infty G(t)dt)(\int_0^\infty H(t)dt)^{-1} \tag{3.8}$$

is summarized for different light conditions. From Figure 3.5(a), generally, compared with the case under normal light, other cases under blue light and green light have larger memory kernel function on average. In experimental group, the memory kernel functions of most cases are smaller under the red light than those under the other light conditions. Physically, $\hat{K}(\infty)$ is a dissipation term and should be inversely proportional to motion correlation (Figure 3.2) and Hurst index (Figure 3.3). The memory kernel function can also be estimated by the rational function in different orders. The details on calculation of memory kernel function are shown in Appendix B.

Once we determine the memory kernel function, the next step is to estimate the random noise term. The non-Markovian nature of fractional Brownian motion makes the computation and simulation difficult. Therefore, we define the auxiliary variable $d(t) = -\int_0^t K(t-\tau)\dot{\theta}(\tau)d\tau + R(t)$. For simplicity, the demonstration of motion simulation is

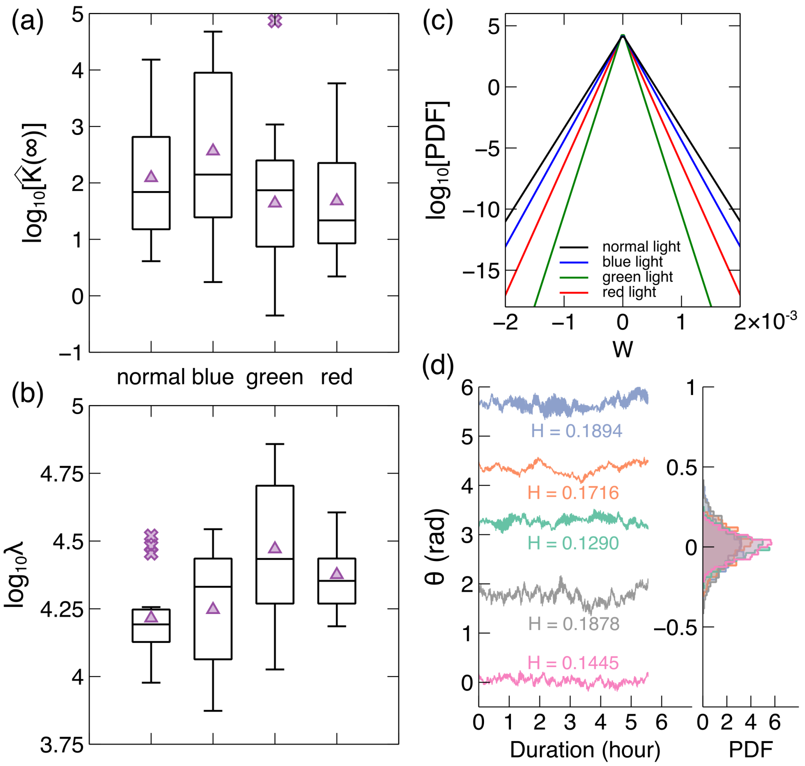

Figure 3.5: Model of the in-plane waving motion of coral polyps under different light conditions. (a) Value of the memory-kernel function at the Markovian limit, $\hat{K}(\infty)$, of polyps under normal, blue, green, and red light. (b) Parameter λ for the exponential distribution to model the white-noise term under normal, blue, green, and red light. (c) Fitted PDF of the white-noise terms under different light conditions by using the average parameter λ. (d) Simulated in-plane waving motions of five polyps under normal light and 25°C based on the generalized Langevin equation. Hurst indices are shown below the simulated results. Corresponding PDFs of simulated results are exhibited on the right panel. Cross and triangle symbols in (a)(b) represent the outliers and mean, respectively.

based on the first-order approximation, where the auxiliary variable can be simplified as $d(t) = -\int_0^t A_1 e^{B_1(t-\tau)}\dot{\theta}(\tau)d\tau + R(t)$, which can be further expressed in terms of coefficients in first-order approximation A_1, B_1 and white noise W:

$$\begin{cases} \ddot{\theta} = d \\ \dot{d} = B_1 d - A_1\dot{\theta} + W \end{cases} \tag{3.9}$$

The probability density function of W is characterized by a peak in small values and rapid decays to large values (Appendix B). Since direct fitting of distributions on the histogram and a visual comparison with the assumed distribution are shown to be unreliable [149], we use the maximum likelihood method to determine the optimal parameter for several distribution candidates: (a) $\rho_\lambda(W) = ce^{-\lambda|W|}$, (b) $\rho_\mu(W) = c|W|^{-\mu}$ and (c) $\rho_\sigma(W) = \frac{1}{\sqrt{2\pi\sigma^2}}e^{-\frac{W^2}{2\sigma^2}}$ which are the exponential distribution, power law distribution, and normal distribution, respectively. After determining the optimal parameter by the maximum likelihood method, the Akaike information criterion and Bayesian information criterion are used to determine the most appropriate function to model the white noise term [150]. It turns out that the exponential distribution is the preferred model for the white noise term (Appendix B). Figure 3.5(b) exhibits the parameter λ for the exponential distribution under different light conditions. Compared with normal light, the parameters are larger under green light, which results in clear differences in the exponential distribution using the average parameter λ under different light conditions [Figure 3.5(c)]. Likewise, the model of white noise of in-plane waving motion of polyps under different temperatures is shown in Appendix B and clearly demonstrates the distinction in different temperatures.

The next step is to simulate the in-plane waving motion of polyps under different light conditions and temperatures based on the generalized Langevin dynamics. Here, Figure 3.5(d) shows the simulated results under normal light and 25°C spanning around 5.5 hours, which are clearly stochastic. The Hurst indices are shown below the curves with typical subdiffusion nature, where the Hurst index is less than 0.5. To check the statistical similarity between our simulated results and experimental results, the PDFs of corresponding in-plane waving motions are exhibited on the right panel of Figure 3.5(d). The PDFs with characteristic bell-shaped curves can be observed, which are consistent with the PDF trends shown in Figure 3.5(d).

3.6 Conclusion and discussion

Here, we have tested the hypothesis that the motions of corals are affected by abiotic factors such as light and temperature in the context of environmental change. To test this hypothesis, we designed a fluidic platform to observe the motions of coral at the scale of single polyps experimentally. This allowed us to explore the in-plane waving motion through correlation and synchronization analysis, resulting in the correlated and phase-synchronized motion of polyps on the same coral nubbin which is affected by light and temperature. In addition, the in-plane waving motions of polyps are found to be the fractional Brownian motion with Hurst index generally smaller than 0.5 by the power spectral density analysis. Outside of optimal growth conditions (normal light and 25°C), the Hurst index becomes highly variable (spanning between diffusive, subdiffusion and superdiffusion mode) with the baseline index being around 0.2. Finally, the model of in-plane waving motion of polyps is established for different light conditions and temperatures using the Langevin dynamics, which statistically agrees well with experimental results. The memory kernel function and noise term are calculated by data-driven method, in which the light conditions and temperatures also play important roles.

Increasing temperature and decreasing wavelength can both be respectively associated with global warming and sea-level rise, since it is well known that longer wavelengths (red light) have only shallow penetration in the ocean compared to shorter wavelengths (blue light). With global sea-level rise, corals face a shift in light composition to more blue light which will probably weaken or even reverse the current in-plane waving motion trends of polyps and potentially entire colonies in the future. Our research with scaled experimental observations, numerical analysis and theoretical modeling, paves the way to studying the motion of polyps, clonal and colonial organisms and boost our understanding of the impacts of abiotic factors on the behavior of coral polyps and coral colonies as a whole. The modeling of spatiotemporal dynamics of coral polyps may have promising applications in constructing more realistic scenes in virtual reality and the prediction of coral behavior in response to environmental change.

3.7 Author contribution

This chapter is adopted from Shuaifeng Li, Liza M. Roger, Judith Klein-Seetharaman, Nastassja A. Lewinski, and Jinkyu Yang, Spatiotemporal dynamics of coral polyps on a fluidic platform, *Physical Review Applied*, 18, 024078, 2022.

S. Li and J. Yang proposed the research; S. Li and L. M. Roger conducted the experiments; S. Li performed the data analysis and modeling; N. A. Lewinski and J. Yang provided guidance throughout the research; S. Li and J. Yang prepared the manuscript; J. Klein, N. A. Lewinski, and J. Yang provided guidance during manuscript preparation and development.

Chapter 4

DATA-DRIVEN DISCOVERY OF SPATIOTEMPORAL COHERENT PATTERNS IN PULSATING SOFT CORAL TENTACLE MOTION WITH DYNAMIC MODE DECOMPOSITION

Tentacles on soft corals exhibit intriguing spatiotemporal dynamics of motions, which may benefit their survival and fitness. Despite their significance, studies of their quantitative properties still remain challenging and unexplored. Such motions are characterized by coherent patterns across both space and time, yet computational methods that address spatiotemporal dynamics are rare. Here, we introduce a data-driven method called dynamic mode decomposition (DMD) to explore the spatiotemporal behavior of tentacles of *Anthelia glauca*, where the motions of eight tentacles are captured by stereovision and object tracking techniques. The DMD reveals the stochastic motions of the tentacles, which can be well modeled as $1/f$-type motion. Additionally, the pulsation behaviors of our soft corals are also captured by analyzing the DMD spectrum and the sliding-window DMD, where these behaviors emerge as spatial DMD modes with increased power. Finally, the impact of light conditions on the $1/f$-type motion and pulsation behaviors is explored, where certain light conditions can manipulate the $1/f$-type motion and emergence of pulsation behaviors. Our work, combining experimental observation and a data-driven method to characterize spatiotemporal motions of coral tentacles, paves the way to exploring the complex behaviors of individual organisms and colonies, and the effect from changing environmental variables.

4.1 Introduction

The spatiotemporal behaviors are ubiquitous across science and engineering, including fluid dynamics, wave propagation, climate change, and animal movements. Various methods have been proposed to model and predict the spatiotemporal behaviors in numerous systems. Therein, data-driven methods, such as deep neural networks and dimensionality reduction methods, are currently being used to solve the fundamental problems including comprehending turbulent fluid dynamics and forecasting the global climate change [151–153]. One of the most powerful dimensionality reduction methods used in recent years is the dynamic mode decomposition (DMD) method because of its straightforwardness and interpretability. Given the advantages of DMD and the relation between DMD and Koopman spectral analysis, they are well suited to characterize various nonlinear physical and biological systems. DMD first obtains popularity for its ability in the fluid dynamics community to identify spatiotemporal coherent structures from high-dimensional data [154, 155]. Beyond fluid dynamics, DMD has been successfully applied to robotics [156], neurology [157, 158], and epidemiology [159]. However, DMD has not yet been used to characterize the animal behaviors in biological systems.

Soft corals (Cnidaria: Octocorallia), similar to hard corals, harbor great diversity and support significant biological activities in the ocean although they are facing a severe crisis threatening their survival due to the anthropogenic activities and climate change [22]. They both host endosymbiotic dinoflagellate algae and coral colonies. However, different from the stony corals, soft corals lack calcium carbonate skeletons. Apart from differences in biological structures, there is a variety of distinctions from the perspective of spatiotemporal dynamics of motion. For example, *Montipora capricornis* (stony coral) displays imperceptible and subtle motions of tissues [139]. The polyps of *Pocillopora acuta* (stony coral) follow the fractional Brownian motion that can be affected by the environmental conditions [160].

In comparison, although rarely quantitatively studied, tentacle motions are usually studied in soft corals. Tentacles of soft corals often serve to capture food and particles in the water where the tentacles wave around and are intermittently wiped across the mouth, and as probes to locate and kill rivals [42–48]. In addition, pulsating soft corals, one type of the soft corals, are found to have perpetual pulsation by tentacles and hence affect the surrounding fluid flow and photosynthesis of the symbionts [82, 83, 161]. The tentacles of pulsating soft corals exhibit rich dynamics of motion yet there is a lack of computational tools to characterize them. Additionally, most of the aforementioned studies about soft coral tentacle behaviors lack consideration of variable light wavelength exposure. There is also a lack of prior quantitative studies that can reveal the underlying physics. In the field of coral research in general, quantitative and physical characterization of tentacle behaviors will also help with the in-depth understanding of pulsating soft corals.

Therefore, the assistance from DMD is necessary and intriguing to explore, as it may also broaden the application of DMD and advance our understanding to pulsating soft coral behaviors in response to environmental variables. Moreover, distinct from the commonly studied pulsating *Xenia* coral, some pulsating soft corals may have subtle pulsation due to environmental conditions and inherent biological structures, which poses the challenge to identify and visualize the pulsation mode. Since DMD can provide not only dimensionality reduction in terms of a reduced set of modes, but also a model for how these modes change over time, it can help with mode identification and visualization.

Here, we investigate the tentacle motions of a pulsating soft coral, *Anthelia glauca*. The three-dimensional motions of the eight tentacles, which display a stochastic nature, are extracted by stereovision techniques [144]. We then use DMD to discover and analyze the dynamic modes with oscillations at frequencies with growth/decay rate involved in tentacle motions. The DMD spectrum and sliding-window DMD are introduced, where we discover the $1/f$-type motion of pulsating soft coral tentacles and the spatial DMD modes with increased power in a specific frequency range. Furthermore, we visualize the exemplar DMD mode with increased power, which is confirmed to represent the pulsation behavior of our pulsating soft corals. For each tentacle, the elliptical motion with certain polarization is displayed, where correlation analysis among tentacles further indicates the collective pulsation motion of our soft coral. In addition, we investigate the emergence and frequency variation of pulsation under the effects of different light conditions. Our research, combining experimental observation techniques and a data-driven method, offers physical insights into the motions of pulsating soft coral tentacles, which will boost our understanding of pulsating soft coral behaviors and physiology. Also, this work will contribute to expanding the use of DMD to individual organisms and, potentially, their combined motion within colonies such as those formed by pulsating soft corals and their reef-building cousins.

4.2 Experimental system

To study the motion of tentacles, we chose *Anthelia glauca* in the family of Xeniidae, a pulsating soft coral with eight long tentacles on the tubular polyps, to ensure the noticeable motion of tentacles, although *Anthelia glauca* does not pulse as much as pulsating *Xenia* coral does in the wild and in captivity. The coral was reared in an aquarium under adequate control of environmental conditions including light, temperature and water quality. The detailed aquarium parameters are shown in Appendix C. Before initiating the experiment, the aquarium pump was paused to minimize the effect of water flow on tentacle motions. As shown in the schematic in Figure 4.1, stereovision with two synchronized cameras was used to take images of one of the polyps of *Anthelia glauca* to obtain motion information in three-dimensional space so that the position of each tentacle and the polyp mouth can be identified. Images were taken every 10 seconds for 11 hours. The full time-lapse video created from the images by the two cameras is shown in Supplementary movie (×300 speed) [162]. To simplify the problem, in this study, we focus on one polyp and only track the tips of eight tentacles instead of depicting the motions of the entire colony. To avoid the impact from polyp motion, we consider the relative tentacle motion with regard to the polyp mouth. The detailed experimental procedures and tracking techniques are described in Appendix C.

The trajectories of eight tentacles are illustrated in Figure 4.1. All eight trajectories in three-dimensional space are stochastic and form random areas. The tentacles occasionally wander from the center of the trajectories but usually return rapidly. Some tentacles have strong motion preference along a specific direction. For example, tentacles #2, #3 and #4 exhibit a waving motion along the horizontal direction rather than vertical. Nevertheless, the featured pulsation behavior cannot be directly observed from these trajectories.

4.3 DMD spectrum and $1/f$-type motion

Since the motion of tentacles is a typical spatiotemporal behavior of pulsating soft corals, identifying these spatiotemporal patterns enables the reduction of complex measurements through projection onto coherent structures, where it may be tractable to build dynamical models and apply machine learning tools for pattern analysis. We introduce DMD as a novel and effective approach to exploring spatiotemporal patterns in pulsating soft coral tentacle motions, which combines two major advantages of current data analysis tools: power spectral analysis in time and principal components analysis in space. After collecting

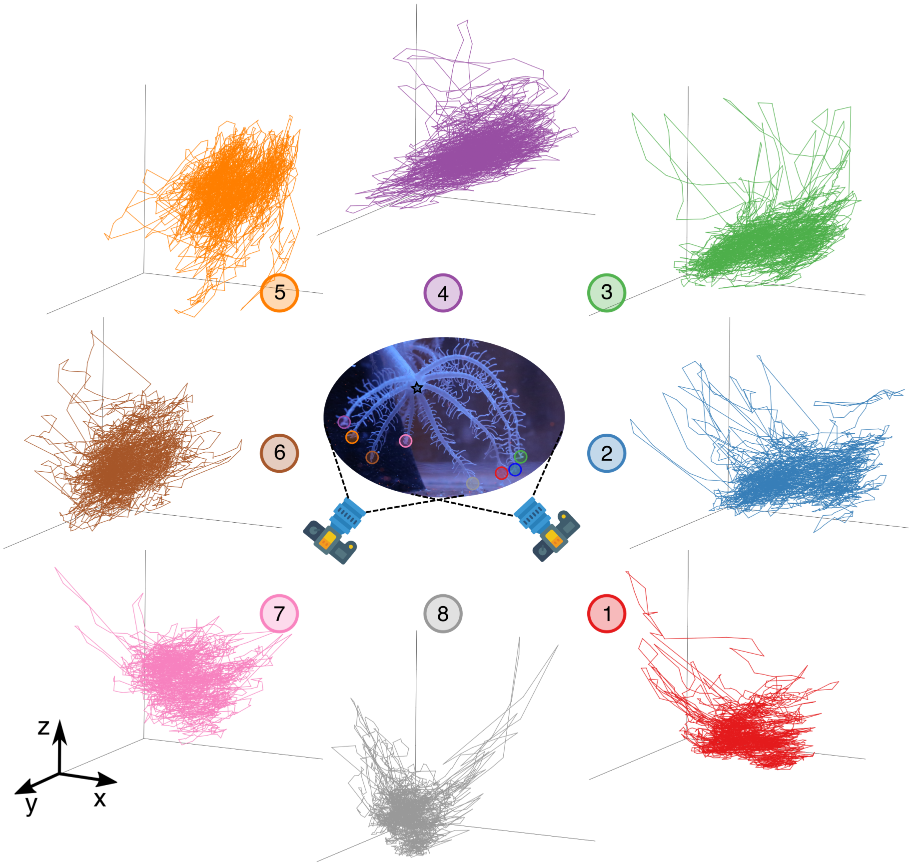

Figure 4.1: The reconstruction error as a function of number of stacks. The error decreases as the number of stacks increases. 300 stacks are chosen in our study indicated by blue dashed line.

the measurements (positions of tentacle tips), we constructed two $n \times (m-1)$ matrices, where n is the number of tentacles multiplied by the degrees of freedom ($n = 24$ in our study) and m is the number of snapshots over time (11 h with 10 s time intervals):

$$X = \begin{bmatrix} | & | & & | \\ x_1 & x_2 & \dots & x_{m-1} \\ | & | & & | \end{bmatrix} \quad X' = \begin{bmatrix} | & | & & | \\ x_2 & x_3 & \dots & x_m \\ | & | & & | \end{bmatrix} \tag{4.1}$$

These two matrices can be related by a best-fit linear operator A that minimizes the Frobenius norm error $\|X' - AX\|_F$ given by

$$X' = AX \Rightarrow A = X'X^\dagger \tag{4.2}$$

where $X^\dagger$ is the pseudoinverse of data matrix X. Usually $n \gg m$ for many systems, so, instead of obtaining A directly, we seek the eigendecomposition of A. After the decomposition of X using singular value decomposition and the rank-r truncation selection, the matrix representation A_r formed by projecting A onto the r dominant modes can be written as

$$A_r = U_r^* X' V_r \Sigma_r^{-1} \tag{4.3}$$

where U_r, Σ_r and V_r are the left unitary matrix, diagonal matrix with singular values, and right unitary matrix, respectively. The eigendecomposition of A_r results in the DMD eigenvalue λ and eigenvector W, which further derives the corresponding DMD mode ϕ being the column of $\Phi = X'V_r\Sigma_r^{-1}W$.

On the contrary, here, $n \ll m$ in data matrix X, with $n = 24$, resulting in a small number of eigenvalues that cannot fully capture the dynamics of the system [157, 163]. Therefore, the augmented data matrix X_{aug} by the time-delay embedding with h stacks is shown as follows:

$$X_{aug} = \begin{bmatrix} | & | & & | \\ x_1 & x_2 & \dots & x_{m-h} \\ | & | & & | \\ | & | & & | \\ x_2 & x_3 & \dots & x_{m-h+1} \\ | & | & & | \\ | & | & & | \\ x_h & x_{h+1} & \dots & x_{m-1} \\ | & | & & | \end{bmatrix} \tag{4.4}$$

The X'_{aug} can be induced similarly. The DMD with the time-delay embedding aims to provide extra observables to realize the Koopman operator to accurately capture and predict the dynamics, but there is no guarantee that the resultant models are closed under the

Koopman operator. Note the DMD modes are stacks of h repeats because of the shift-stacking data matrix.

Here, we choose 300 stacks to obtain the augmented data matrix to minimize the DMD reconstruction error expressed as $\frac{\|X-\hat{X}\|_F}{\|X\|_F}$, where $\hat{X}$ is the reconstructed data matrix that will be detailed in Section 4.4, and $\|\cdot\|_F$ is the Frobenious norm (Figure 4.2). Note that the DMD reconstruction error resulting from X and X', is different from the 3D reconstruction error in stereovision that refers to the difference between the estimated and true 3D coordinates. Sufficient eigenvalues are thus obtained to capture the dynamics of the system. Each DMD mode ϕ corresponds to an eigenvalue λ. The temporal dynamics, referring to growth/decay and the frequency of oscillation of each DMD mode ϕ, are reflected by the magnitude and phase of eigenvalue λ, respectively. In this case, because the raw data is strictly real, the decomposition yields complex conjugate pairs of eigenvalues and modes.

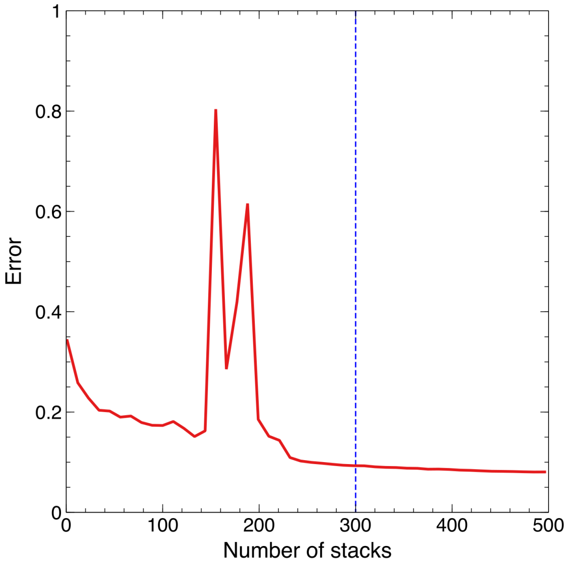

Figure 4.2: The reconstruction error as a function of number of stacks. The error decreases as the number of stacks increases. 300 stacks are chosen in our study indicated by blue dashed line.

As shown in Figure 4.3(a), the eigenvalues are visualized on a unit circle in the complex plane, where most are near the unit circle, suggesting most modes are oscillating with certain frequencies. A few eigenvalues are inside the unit circle, indicating the decay modes. The relation between the real parts of the logarithm eigenvalues and frequencies defined as $f = |\frac{\mathrm{imag}(\omega)}{2\pi}|$ where $\omega = \frac{\ln\lambda}{\Delta t}$ is described in Figure 4.3(b). Most real parts of the logarithm eigenvalues are slightly smaller than zero, coinciding with the observation that eigenvalues are on the unit circle in Figure 4.3(a), which indicates modes with low decaying rates. The mode amplitude defined as $P = \|\phi\|_2^2$ is encoded by color in both Figures 4.3(a) and 4.3(b). They both show that the modes near the zero frequency have the largest mode amplitude that declines as the frequency increases. Interestingly, another area with comparatively large amplitude near 0.008 Hz is also present, which will be discussed in the following paragraph.

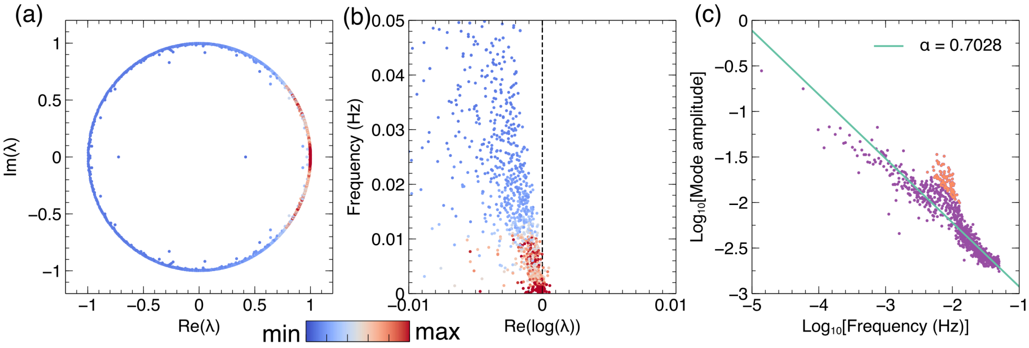

Figure 4.3: DMD eigenvalues analysis and spectrum. (a) Eigenvalues λ are visualized as complex values on the complex plane with a unit circle. (b) The relation between the real part of $\ln\lambda$ and frequency is displayed. The vertical black dashed line indicates that the real part of $\ln\lambda$ is zero. The color in (a) and (b), which is logarithm scaled, represents the corresponding mode amplitude. (c) The mode amplitude varies as a function of frequency. The purple dots and orange dots show the modes with magnitudes within the $1/f^{\alpha}$ fit and larger than 0.8× standard deviations of the $1/f^{\alpha}$ fit. The green solid line is the fitted result using the robust regression in the form of $1/f^{\alpha}$.

Figure 4.3(c) gives the DMD spectrum in the logarithm-scaled graph, which displays similarities to the power spectrum. However, the power spectrum is calculated for motion of a certain tentacle along each direction independently whereas the DMD spectrum provides specific spatial modes across all tentacles. The DMD spectrum is composed of a nearly linear area and a peak area in the logarithm-scaled graph. The linear relation in the logarithm-scaled graph suggests a power-law relation between mode amplitude (P) and frequency (f) with $P \sim 1/f^{\alpha}$. In this case, by using a robust linear regression to identify the outliers and peak area with comparatively large amplitude, and using reduced major axis regression to fit the DMD spectrum to obtain the reliable α, the $1/f$-type motion is revealed where $\alpha = 0.7028$ [164]. In general, we refer colloquially to $1/f$ noise, whenever the process is modeled by $1/f^{\alpha}$ noise, where $0 < \alpha \leq 3$. $1/f$ noise has been prevalent in biological systems such as brain science [157, 165, 166] and diffusion processes [29, 167]. In addition, the notable Brownian motion as well as their derived fractional Brownian motion are $1/f$ noise with $1 < \alpha < 3$.

Apart from the power-law relation marked in purple dots, the modes with increased power are illustrated as orange dots in Figure 4.3(c). Note that the criteria for the detection of the modes with comparatively large amplitudes is when their power amplitudes exceed $0.8\times$ standard deviations of the $1/f^{\alpha}$ fit. The frequency of this peak area is around 0.008 Hz, near which the pulsating soft coral tentacles have relatively strong oscillating motion.

Similar to the idea of a spectrogram in Fourier analysis, we introduce sliding-window DMD to analyze the DMD spectrum variation over time. Here, the width of the sliding window is chosen to be 720 (120 min), as shown by the brackets in Figure 4.4(a). The raw data of tentacle position in the three-dimensional Cartesian coordinate system (x, y, z) is also shown in Figure 4.4(a). Figure 4.4(b) displays three examples of a DMD spectrum of the windowed data. We notice that these spectra still preserve features of linear relation and peak area in the logarithm-scaled graph, implying that the $1/f^{\alpha}$ relation and modes with increased power near 0.008 Hz hold for these periods of tentacle motion. To see whether these features always exist in tentacle motions, we slide the window with a certain translation (5 min) and align these calculated DMD spectra to form a map similar to the spectrogram, where we can obtain the information in both time and frequency with adequate resolution, as shown in Figure 4.4(c). The logarithm-scaled mode amplitude is encoded by the color. The visible trend is characterized by the mode amplitude being highest near zero frequency and decreasing as the frequency increases. Moreover, we observe the presence of spatial DMD modes with increased power in tentacle motion despite variation in a certain frequency range enclosed by black dashed lines ($0.005 \sim 0.012$ Hz). The maps formed by

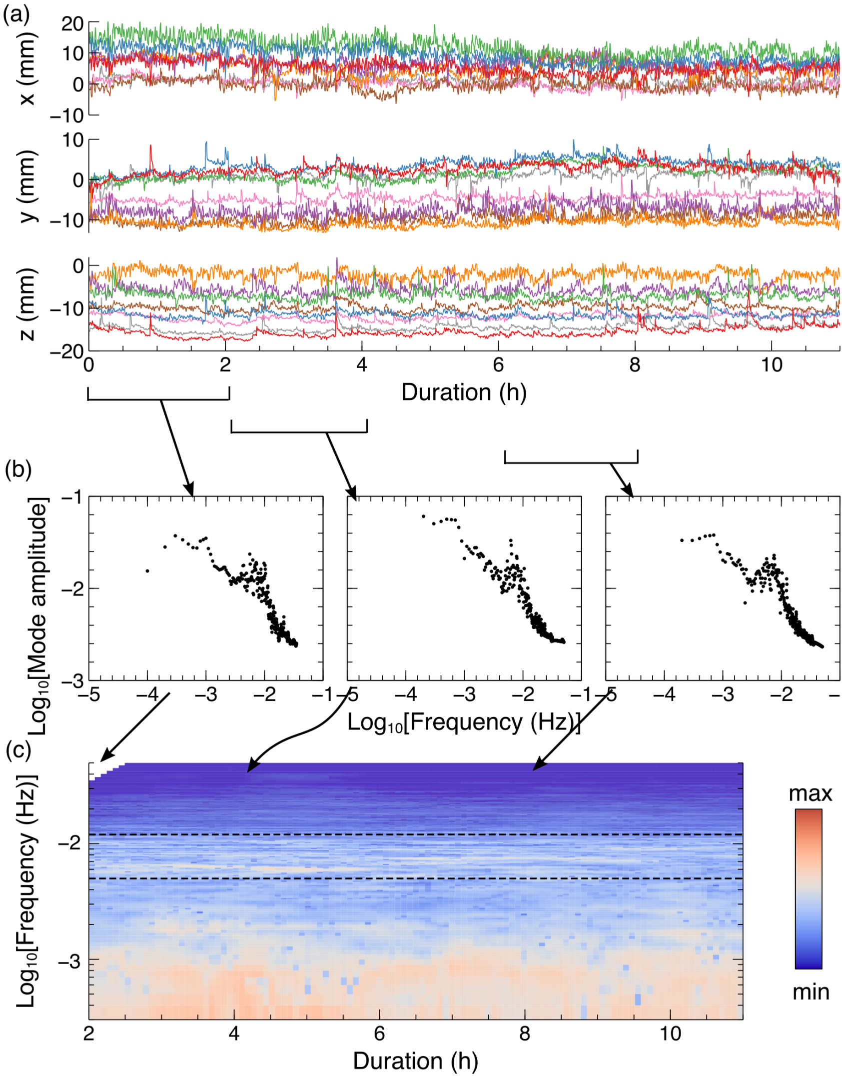

Figure 4.4: Sliding-window DMD. (a) The raw motion signals of eight tentacles in terms of the x, y and z coordinates are shown from top to bottom in different colors. (b) The DMD spectra of the corresponding segments of motion signals are shown from left to right. (c) The map formed by sliding-window DMD with the width = 120 min and translation = 5 min is shown. The arrows, from top to bottom, indicate the raw motion signals used to calculate the spectrum and indicate how the spectrum is oriented, respectively. The logarithm-scaled mode amplitude is encoded by the color.

sliding-window DMD in replicate experiments and under different light conditions show similarities and differences, as displayed in Figure 4.5.

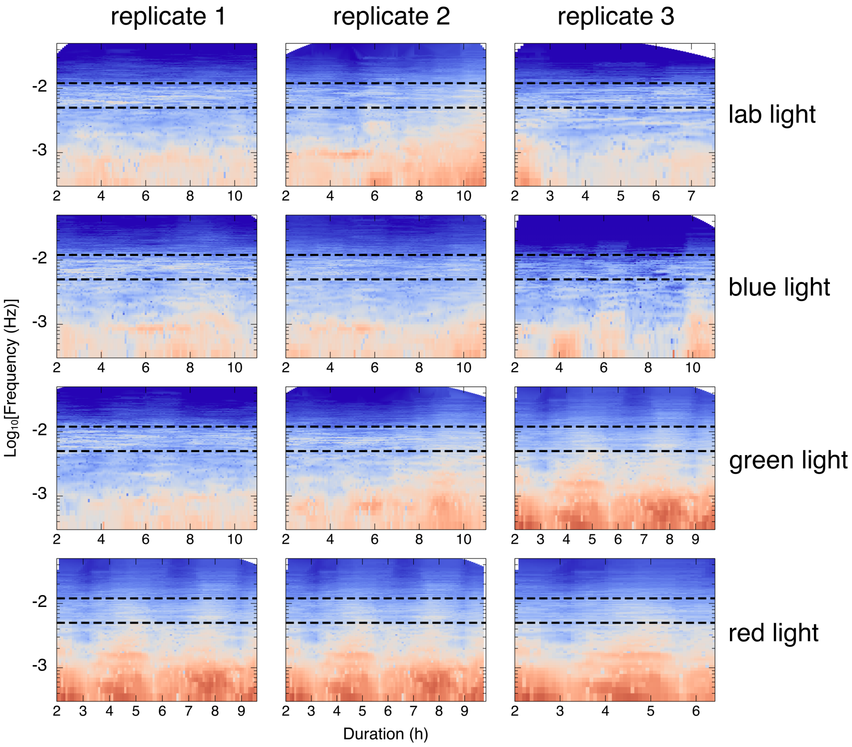

Figure 4.5: Sliding-window DMD of replicate experiments under different light conditions. From top to bottom, three panels in each row represent the maps formed by sliding-window DMD of three replicate experiments under lab, blue, green and red light conditions. The black dashed lines indicate the frequencies of 0.005 Hz and 0.012 Hz.

4.4 Characterization of dynamic coherent patterns

Since the tentacle motion always has DMD modes with increased power, it is natural to extract the spatial mode and examine the motion pattern. The mode with the largest amplitude between 0.005 and 0.012 Hz is chosen as the exemplar mode. Figures 4.6(a) and 4.6(b) exhibit the magnitude and phase of spatial DMD modes of eight tentacles marked counterclockwise by the sequence number, respectively. Specifically, the absolute values of displacements along the x, y, and z directions of the eight tentacles are shown from left to right in Figure 4.6(a). The waving motions along the x direction are distinct between tentacles but tentacles #1, #2, #3 and #4 have relatively large displacements compared with the others. This phenomenon is also reflected by the trajectories of eight tentacles in

Figure 4.1, where tentacles #1, #2, #3, and #4 have larger waving motions along the x direction than the other tentacles. The corresponding phases of displacement along the x direction are exhibited in the first panel of Figure 4.6(b), where the phases of tentacles #1, #2, #3, and #4 are significantly greater than zero while others are close to or smaller than zero, implying that tentacles #1, #2, #3, and #4 approach and leave the others along the x direction rhythmically.

Likewise, the absolute values and phases of displacements along the y and z directions in the second and third panels of Figures 4.6(a) and 4.6(b) can be interpreted. Displacements along the y and z directions are generally smaller than those along the x direction, indicating that the waving motion along the x direction is dominant. Displacements vary between tentacles and the largest displacements along the y and z directions are on tentacles #4 and #5, respectively. In contrast with tentacle displacement along the x direction, we notice that displacements along the y axis are in phase due to the consistent negative phases [the second panel in Figure 4.6(b)], suggesting consistent tentacle motions towards the center of the tentacle crown. The displacements along the z axis, which represents the vertical waving motion, have the phase difference [the third panel in Figure 4.6(b)]. The phases of tentacles #7 and #8 are close to or smaller than zero while the others are significantly greater than zero, suggesting that tentacles #1 $\sim$ #6 approach and leave the others along the z direction rhythmically.

Overall, this DMD mode is dominated by the displacement along the x direction and the displacement of tentacles #1 $\sim$ #5. Therefore, combined with the phase differences of the tentacles, we conclude that this spatial DMD mode represents the pulsation behavior of our pulsating soft coral. However, compared with the pulsation behaviors of the commonly studied Xeniid corals, *Xenia* and *Heteroxenia fuscescens*, where each tentacle moves close to the center almost synchronously with certain displacement resulting in the nearly symmetric pulsation process [82, 83], *Anthelia glauca* pulsates by moving its tentacles with different displacements and different phases leading to an asymmetric pulsation process. Specifically, the tentacles #1 $\sim$ #5 have larger displacements while others have smaller displacement. Taking advantage of the phase difference along the x and z directions, tentacles approach and leave each other rhythmically. This pulsation behavior could have implications related

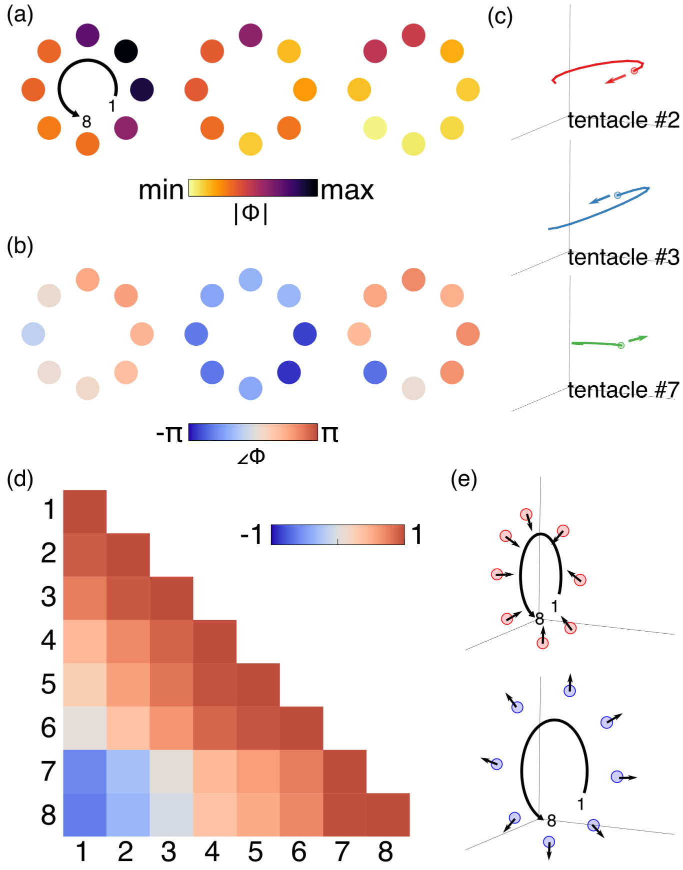

Figure 4.6: The DMD modes of eight tentacles. (a) The magnitudes of DMD modes representing displacements along the x, y, and z directions are shown from left to right. The sequence of the tentacles is marked counterclockwise in the first panel. (b) The phases of DMD modes representing displacements along the x, y, and z directions are shown from left to right. (c) The reconstruction using the DMD mode shown in (a) and (b) illustrates the elliptical motions of tentacles with different angular velocities. The elliptical motions of tentacles #2, #3, and #7 with arrows indicating the moving directions are shown from left to right. (d) The correlation coefficients are calculated by the distances between each tentacle tip and central position of the tentacle crown. (e) The snapshots of pulsation motion when tentacles approach each other and when they are away from each other are shown from top to bottom, respectively. The sequence of the tentacles is marked counterclockwise.

to feeding, survival, and fitness of the colony, as it is known that the functions of pulsating soft coral tentacles may enhance photosynthesis and prey capture [43, 82]. However, the specific biological functions of tentacle pulsation in different soft corals still need further exploration.

To further examine this specific DMD mode, next, we reconstructed the spatiotemporal motions of coral tentacles by only using the mode characterized above Φ, mathematically expressed as follows:

$$\hat{X} = \Phi \Lambda^{t-1} Z \tag{4.5}$$

where the diagonal entries of Λ contain DMD eigenvalues and $Z = \Phi \backslash x_1$ (backslash to solve the linear system with `MATLAB` notation). x_1 is the initial position of the tentacles. Figure 4.6(c) shows the 2 min trajectories of tentacles #2, #3, and #7 with the arrows indicating the direction of movement. The reconstruction of trajectories of eight tentacles with 200 time slots (around 33 min) is shown in Figure 4.7. In general, the trajectories are ellipses that have polarizations along certain directions and the directions of the angular velocity of each tentacle are different. Since the eight tentacles are on the same tubular polyp, it is necessary to explore the pulsation relations among them.

We chose the distance between each tentacle tip and the central position of the tentacle crown from the reconstructed data to study the pulsation relation. When the tentacles approach each other, the distances will become smaller and vice versa. To show the pulsation relation, we calculate the correlation coefficient between the distance from tentacle m to the center and the distance from tentacle n to the center as follows:

$$r_{mn} = \frac{\sum (d_t^m - \bar{d^m})(d_t^n - \bar{d^n})}{\sqrt{\sum (d_t^m - \bar{d^m})^2 \sum (d_t^n - \bar{d^n})^2}} \tag{4.6}$$

where t and the upper bar denote the time and the average of the temporal data. The positive correlation coefficient suggests that tentacles move towards or away from the center in synchrony, while the negative one indicates the opposite scenario, dyssynchronous movement. As shown in Figure 4.6(d), most correlation coefficients are positive, indicating the collective pulsation motion. Tentacles #1 and #2 have negative correlation coefficients with tentacles #7 and #8. However, according to the Figure 4.7, the displacements of tentacles #7 and #8 are quite small and thus have a small effect on the collective pulsation. The correlation analysis further confirms that this spatial DMD mode represents the pulsation behaviors by each tentacle collectively moving to or leaving from the center.

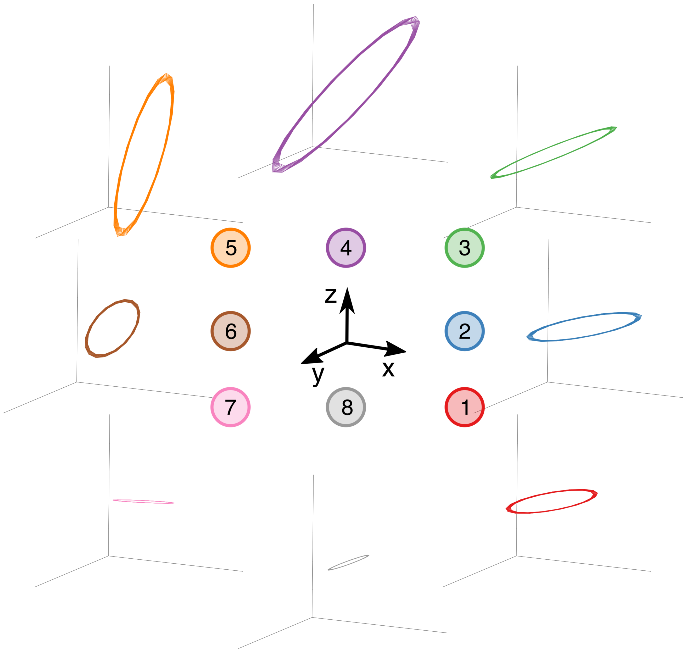

Figure 4.7: The reconstruction of trajectories of coral tentacles using the DMD spatial mode with increased power. The DMD spatial mode with the largest power is chosen as the exemplar spatial mode among the DMD spatial modes with increased power. The number of data points is 200 (around 33 min).

Figure 4.6(e) shows two snapshots when eight tentacles approach each other (the first panel) and when eight tentacles are away from each other (the second panel). By comparing two snapshots, tentacles #1 $\sim$ #4 have significant motion that coincides with our analysis above. In addition, these motions are dominant along the x direction, where the obvious closing and opening of the tentacle crown can be observed. As shown in the schematic in Supplementary movie (×300 speed) [162], the periodic closing and opening of the tentacles results from the reciprocating elliptical motion of each tentacle. The sizes of elliptical trajectories become smaller gradually because of this decaying mode (the absolute value of the eigenvalue of this mode is smaller than 1). In reality, the pulsation behavior is accompanied with our soft coral, resulting in the stable oscillating mode where the absolute value of the eigenvalue should be 1. This may result from the error of this numerical reconstruction.

A series of snapshots over time illustrating the closing and opening process of the tentacle crown are shown in Figure 4.8. The tentacle motion described here could be leveraged to further study fluid dynamics in soft coral colonies in relation to enhance photosynthesis of the symbiotic algae and prevent refiltration of surrounding water by neighboring polyps [82, 83, 161]. Note that the extracted pulsation motion of our soft coral is not as obvious and powerful as that of the widely studied pulsating *Xenia* coral, which coincides with the characteristics of *Anthelia glauca*. In addition, from this study, DMD demonstrates the capability of extracting the weak pulsation modes from $1/f$ noise.

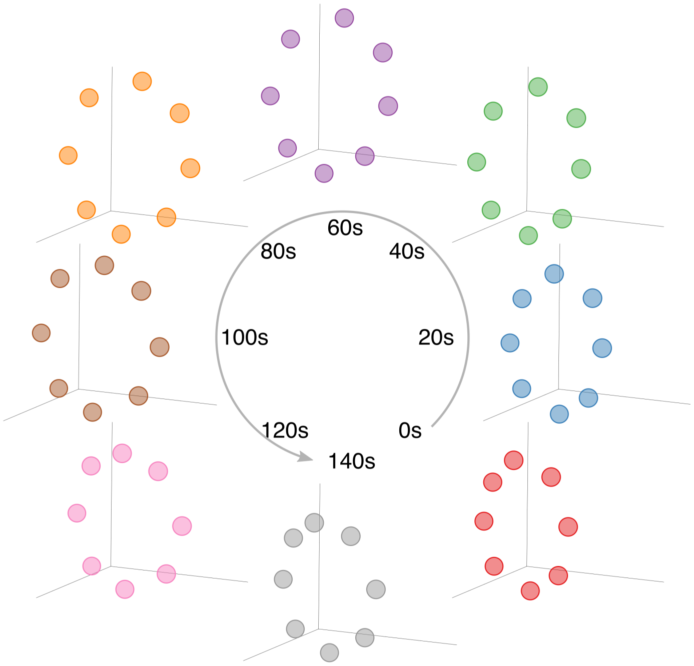

Figure 4.8: The pulsation motion reconstructed using the DMD spatial mode with increased power. The snapshots of the whole process of pulsation motion from 0 s to 140 s. The slight open and closure of tentacles can be seen.

4.5 Effect of light conditions

So far, we have focused the analysis on the pulsating soft coral under the light conditions in our laboratory. However, environmental variables, such as the wavelength of light, are known to have impacts on coral behaviors [39, 80, 139, 160]. Therefore, it is interesting to investigate whether different wavelengths of light can affect pulsation behaviors. Figure 4.9(a) shows the DMD spectra obtained under the laboratory, blue, green, and red light conditions from top to bottom, respectively. The linear trend in the logarithm-scaled graph and the area with increased power still exist when the light condition changes to light in other colors. Note that regression and mode detection are the same here as above; however, some differences can be observed such as the slope, frequency range, and the number of modes with pulsation. To investigate the effect of variation in the color of light, each light treatment experiment was replicated three times while keeping other conditions the same.

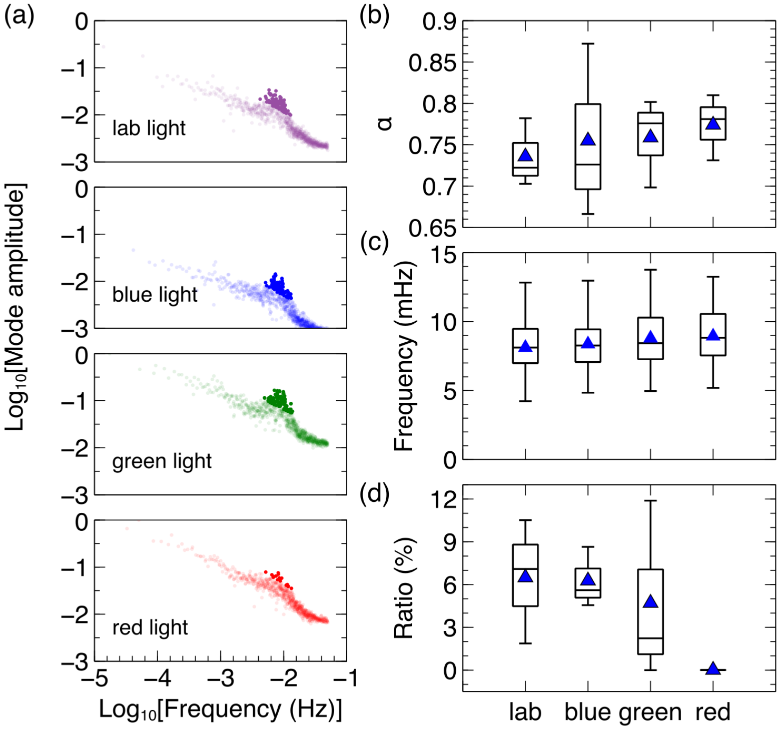

Figure 4.9: The effect of light conditions on the DMD modes. (a) The DMD spectra under different light wavelengths are shown from top to bottom. The light in different colors in each graph represent modes with magnitudes within $1/f^{\alpha}$ fit, while the dark colors represent those exceeding the criteria of $1/f^{\alpha}$ fit. (b) The power α under different light wavelengths. (c) The frequencies of the spatial DMD modes with pulsation under different light wavelengths. (d) The ratio of the number of spatial DMD modes with pulsation under different light wavelengths. The blue triangles represent the mean of the data in (b), (c), and (d).

Figure 4.9(b) shows the power α as a function of light wavelength. α slightly increases with increasing wavelength on average, suggesting that the low-frequency modes have more power when the light condition shifts to red light. But no significant difference is found according to the p value. The frequency ranges of DMD pulsation modes under different light conditions are shown in Figure 4.9(c), where no significant differences are visible according to the p value. Hence, the wavelength of light does not appear to have a major impact on the frequency range of the pulsation behaviors. In addition, the number of modes with pulsation detected using our criteria is normalized by the total number of modes, which is visualized in Figure 4.9(d) as the ratio. As the wavelength increases from blue to red, the ratio declines on average. Specifically, when the light condition shifts to red, the number of DMD pulsation modes drops significantly to almost zero, indicating the submergence of these DMD pulsation modes into the $1/f$ noise. Under the red light, the number of DMD pulsation modes is significantly different from that in the other light conditions tested ($p < 0.05$). Moreover, this trend can be observed from the map formed by the sliding-window DMD shown in Figure 4.5, where the corresponding modes nearly disappear as the light shifts to red. This indicates dormant pulsation behavior under red light conditions. Here is one possible interpretation of this result. *Anthelia glauca* is found to live deeper than many other soft corals, so the red light is difficult to reach and photosynthesis is limited [168]. The pulsation motion is able to capture food particles in the water or obtain dissolved matter from the surrounding water as a source of energy [42–44]. When there exists sufficient red light, there is probably little need for pulsation motion to catch prey, which will submerge into the $1/f$-type motion, resulting in the increasing low-frequency modes (increasing α).

4.6 Conclusion and discussion

In our study, stereovision is used to capture the motion of the eight tentacles forming the crown of one polyp of the pulsating soft coral, *Anthelia glauca.* The stochastic motion is revealed taking advantage of the use of synchronized dual cameras. Dynamic mode decomposition, a data-driven method, is used to analyze the growth/decay and oscillation involved in this process. Therein, the $1/f$-type motion is identified in the tentacle motion, which is common in biological systems. Furthermore, the DMD spatial modes with increased power constantly appearing in tentacle motion are captured in the DMD spectrum. We also visualize these spatial modes in terms of magnitude and phase, along with the correlation analysis among elliptical motions of tentacles, to confirm that these spatial modes represent the pulsation behaviors of soft corals of the Xeniidae family. Moreover, we find clear evidence that the wavelength of light has impacts on the $1/f$-type motion and the emergence of pulsation behaviors. Specifically, the red light plays an important role in manipulating the pulsation behaviors, which shares the similar phenomenon with the polyps of *Pocillopora acuta* (stony coral) under the impact of red light [160].

Anthelia glauca pulses far less than *Xenia* corals do, in addition to the emergence of the pulsation behaviors in the $1/f$-type motion in our study, which results in the difficulty in observing pulsation directly from the field and aquarium. However, our data-driven method successfully extracts the pulsation mode, demonstrating the ability of DMD. Note that our experiment is conducted without the seawater flow, which opens up the following application of DMD on the more practical scenario with the seawater flow in the field or aquarium. Additionally, every individual tentacle has a special mode and behaves differently, which inspires the further exploration of biological neuron structures in pulsating soft corals. In the same phylum of cnidarians owning the diffuse nervous system that coordinates behaviors, sea anemones can be a good example to guide a similar study in tentacles motion [169].

Our proposed data-driven method, DMD, can be a powerful tool for the analysis, understanding, and extraction of the attractive behaviors of pulsating soft corals. Our study also broadens the applications of DMD, which is applied to the field of coral behaviors. In the future study, the DMD method could be expanded beyond the motion analysis by correlating spatiotemporal behaviors of animals with the corresponding spatiotemporal observable.

4.7 Author contribution

This chapter is adopted from Shuaifeng Li, Liza M. Roger, Judith Klein-Seetharaman, Lenore J. Cowen, Nastassja A. Lewinski, and Jinkyu Yang, Data-driven discovery of spatiotemporal coherent patterns in pulsating soft coral tentacle motion with dynamic mode decomposition, *Physical Review Research*, 5, 013175, 2023.

S. Li and J. Yang proposed the research; S. Li conducted the experiments; S. Li performed the data analysis and modeling; J. Yang provided guidance throughout the research; S. Li and J. Yang prepared the manuscript; L. M. Roger, J. Klein, L. J. Cowen, N. A. Lewinski and J. Yang provided guidance during manuscript preparation and development.

Chapter 5

ELASTIC CHIRAL LANDAU LEVEL AND SNAKE STATES IN ORIGAMI METAMATERIALS

The behavior of electrons under strong magnetic fields has long been of great interest to researchers. Recently, it has been demonstrated that a pseudomagnetic field induced by a synthetic gauge field can mimic the effects of a genuine magnetic field, even in phononic systems that are typically insensitive to magnetic fields. In this study, we present a method for generating a synthetic gauge field in origami metamaterials with continuously varying geometrical parameters. By modulating the mass term in the Dirac equation linearly, we create a synthetic gauge field in the vertical direction, which allows for the quantization of Landau levels through the generated pseudomagnetic field. Furthermore, we demonstrate the existence and robustness of the chiral zeroth Landau level. The unique elastic snake state is realized using the coupling between the zeroth and the first Landau levels. Our results, supported by theory and simulations, establish a feasible framework for generating pseudomagnetic fields in origami metamaterials, which may enable the manipulation of elastic waves in conceptually innovative ways with potential applications in waveguides and cloaking.

5.1 Introduction

The physical realization of the synthetic gauge field $\mathbf{A}$ has been an engaging field of condensed matter physics research as it provides an additional degree of freedom for modulating waves [170–176]. The resulting pseudomagnetic fields $\mathbf{B} = \nabla \times \mathbf{A}$ captivate researchers' attention due to their ability to induce a nontrivial band topology. Specifically, in phononic systems, the inertness of the elastic waves to the genuine magnetic field makes the realization of pseudomagnetic fields especially demanding for inducing intriguing phenomena such as Landau quantization and artificial Lorentz forces.

In previous studies, the deformation of the artificial elastic periodic structures has been used to shift the Dirac cone in the k_x-k_y momentum space, creating the synthetic gauge field in the x-y plane and a corresponding pseudomagnetic field perpendicular to the x-y plane [177–179]. In addition, the variation of geometrical parameters of the structure with gradient can modulate the position of the Dirac cone in the k_x-k_y momentum space, which offers a simple and practical way to realize the pseudomagnetic fields [180–182]. The resulting pseudomagnetic field facilitates the observation of various magnetic-field-related phenomena in phononic systems such as Landau plateaus and quantum-Hall-like edge states [177, 179–182]. Nevertheless, there is a lack of the exploration of out-of-plane synthetic gauge field (in-plane pseudomagnetic field), which may result in the distinctive form of Landau quantization. Furthermore, an intriguing transport phenomenon, namely a snake state, has been realized in the on-chip structures with the opposite pseudomagnetic field, but achieving opposite pseudomagnetic field needs the sophisticated design and fabrication [182]. A better strategy is still in its infancy and worth exploration.

Origami, an ancient art of paper folding, has recently attracted the attention of the physics and engineering communities due to its remarkable potential for various applications. Origami metamaterials, which are composed of origami elements with intricate folding techniques, offer unique kinematic motions, functionalities, and mechanical properties that are not found in traditional materials [30, 183, 184]. These properties make origami metamaterials ideal for use in diverse applications, such as aerospace ones [185], architected materials [186, 187], and biomedical devices [188–190]. In addition to static and quasi-static mechanical properties, origami metamaterials also possess rich dynamics that can be utilized to develop prospective devices for impact mitigation and vibration control, revealing the potentials in revolutionizing these fields [28, 64, 191, 192]. Furthermore, the folding patterns and geometric properties of origami metamaterials have shown significant potential in condensed matter physics, particularly in the study of topological states [192–194]. The unique mechanical properties of origami metamaterials, coupled with their ability to be easily adjusted through initial configurations and crease pattern engineering, make them the ideal platforms to produce synthetic gauge fields, and thereby generate pseudomagnetic fields, where the gradient of system properties is the key ingredient (geometry gradient, modulus gradient, etc.). This opens up intriguing possibilities for exploration in origami metamaterials, which have yet to be investigated.

In our work, we introduce an origami metamaterial composed of Kresling origamis arranged in a honeycomb lattice bearing a gradient in geometrical parameters, as explained below. By appropriately designing the height of the origami, we generate a synthetic gauge field along the vertical direction through a linear variation of the Dirac effective mass, leading to the formation of a pseudomagnetic field. With the application of this pseudomagnetic field, we observe the quantization of Landau levels, where the robustness of the zeroth Landau level is confirmed by the weak backscattering of chiral elastic wave propagation against obstacles. Furthermore, we use the coupling between the zeroth and first Landau levels to demonstrate the elastic snake state, where the wavy propagation trajectory of elastic waves enables the bypassing of obstacles. Our work, supported by the excellent agreement of numerical calculations and theoretical analysis, provides a promising path towards achieving chiral Landau levels in origami metamaterials, with potential applications in origami-based architectures for the sophisticated manipulation of elastic waves.

5.2 *Design of origami metamaterials*

As shown by the top view in Figure 5.1(a), we design our origami metamaterials by coupling Kresling origamis in the honeycomb lattice using reversed torsional springs k_c. The introduction of k_c can induce opposite torque in the connected units [195, 196]. The bottom plates are pinned to the ground. The primary unit cell is chosen to be a rhombus enclosed by the black dashed line with basic vector $\mathbf{a_1} = (\sqrt{3}a, 0)$ and $\mathbf{a_2} = (\frac{\sqrt{3}}{2}a, \frac{3}{2}a)$, where $a = 100$ mm is the side length of the honeycomb. Figure 5.1(b) displays the side view of the unit cell. The design parameters and mechanical parameters are shown in Appendix D. Therein, the initial heights are denoted as h_1 and h_2, while the initial rotation angles are kept the same as $\theta_0 = 70^\circ$. Here, the initial rotation angle θ_0 indicates the initial angle difference between bottom plate and top plate after fabrication. Each origami has three degrees of freedom: axial displacement of the top plate u_t, rotational displacements of the top plate ϕ_t and bottom plate θ_b. Note that here rotational displacement of the bottom plate θ_b should not be confused with the initial rotation angle in the origami configuration θ_0.

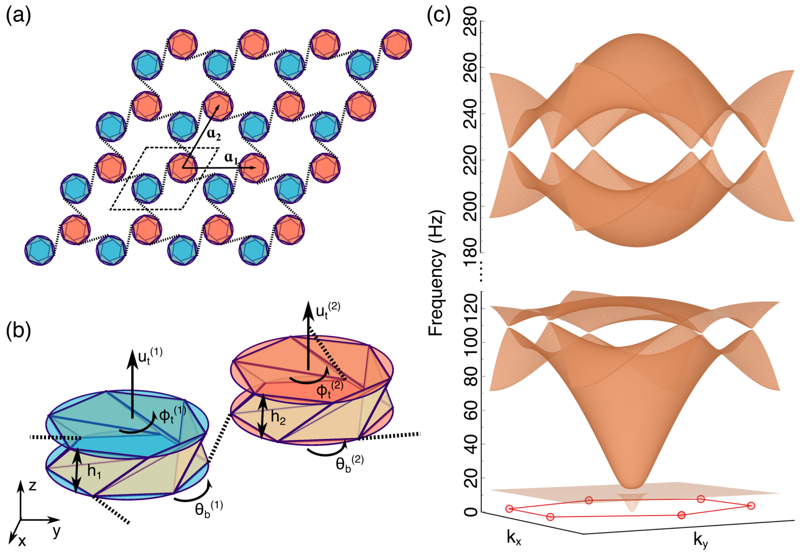

Figure 5.1: Design of the origami metamaterials. (a) The top view of the origami metamaterials with the Kresling origamis arranged in the honeycomb lattice. The origamis are connected by the reverse torsional spring. $\mathbf{a_1}$ and $\mathbf{a_2}$ denote two basis vectors of the unit cell enclosed by the black dashed line. (b) The side view of the unit cell composed of two origamis with initial heights h_1 and h_2 and initial rotaional angle $\theta_0 = 70°$. Each origami has three degrees of freedom u_t, ϕ_t and θ_b with the bottom disk pinned to the ground. (c) The band structure calculated from the linearized truss model of origami. The Dirac cone emerges in six corners of the Brillouin zone, which is marked as red line.

When the heights of two origamis are the same ($h_1 = h_2 = 20$ mm), the spatial inversion symmetry is preserved. As shown in Figure 5.1(c), the associated band structure featuring six bands is calculated using the linearlized truss model of Kresling origami (see Appendix D) [192, 194, 197]. Using the discrete model of the origami structure, we pursue the effective wave motion in the finite wavenumber and finite frequency, and analyze origami behaviors near spectral singularities (Dirac cone). The lowest two bands are almost flat except $\mathbf{k} = 0$, within the frequency range of 12 Hz to 14 Hz and are illustrated in high transparency because they are not considered in our discussion below. The third and the fourth bands, the fifth and sixth bands degenerate to form the Dirac cones at lower frequency and higher frequency. Here, the problem of determining the dispersion relation in each frequency range can be cast in the form of a 2×2 eigenvalue problem associated with the following Hamiltonian:

$$H = v(k_x\sigma_x \pm k_y\sigma_y) \tag{5.1}$$

where v is the Dirac velocity at (k_x, k_y), and σ_x and σ_y are Pauli matrices. This Hamiltonian maps to the massless Dirac equation associated with locally linear dispersion. When the heights of two origamis are not the same, the spatial inversion symmetry is broken since the coupling behaviors of Kresling origami between axial and rotational displacements are changing as a function of height (Appendix D). This broken spatial inversion symmetry essentially introduces a σ_z component into the Hamiltonian which can be expressed as:

$$H = v(k_x\sigma_x \pm k_y\sigma_y) + m_K\sigma_z \tag{5.2}$$

The effective mass term m_K will break the Dirac degeneracy and open the band gap locally. The theoretically predicted width of the band gap is $2|m_K|$. Therefore, we can expect that the Dirac cone at lower and higher frequency will open up when the heights for two origamis are not the same, which will be elaborated below to show its important role for the formation of the synthetic gauge field. A similar band gap opening mechanism is through the bistability of Stewart platform in the honeycomb lattice to realize topological phase transition [195].

5.3 Emergence of elastic Landau levels

We study the evolution of the band structure when the height difference of two origamis $\Delta h = h_1 - h_2$ varies from 20 mm to -20 mm, while keeping $h_1 + h_2 = 40$ mm. This variation and such configuration in the form of the supercell with 41 unit cells is shown in Figure 5.2(a). The band structures along $\Gamma - K - M - \Gamma$ for the corresponding configurations are displayed from left to right in Figure 5.2(b). The band gaps between the third and the fourth bands, the fifth and sixth bands experience the open-close-reopen process. The formation of a band gap at the vicinity of $\mathbf{K}$ point is due to the mass term in the Dirac equation as explained in Equation (5.2). Besides, the larger band gap results from the larger mass term, which can be theoretically calculated by the $\mathbf{k} \cdot \mathbf{p}$ perturbation method (see Appendix D) [198–202]. The band gap and resulting mass term at the lower and higher frequency of the corresponding configuration in Figure 5.2(a) are discussed in the Appendix D, and are featured by the linear variations of the width of band gap and mass term m_K along the x direction.

With this configuration, one can obtain an effective Hamiltonian:

$$H = v(\hat{k}_x\sigma_x \pm \hat{k}_y\sigma_y) + m_K(x)\sigma_z \tag{5.3}$$

where $\hat{k}_x$ and $\hat{k}_y$ are the wave vector operators. Therein, $\hat{k}_x = -i\partial_x$ with the translational symmetry being broken along the x direction, while $\hat{k}_y = k_y$ with the translational symmetry being preserved with periodic boundary condition along the y direction. Besides, the mass term m_K in the Dirac Hamiltonian is linear with respect to x ($m_K = qx$) and the signs of q are opposite at lower and higher frequency (Appendix D). According to the form of the Hamiltonian, a vector potential along the z direction $A_z = m_K(x)$ is introduced, suggesting an effective canonical momentum $\hat{k}_z = k_z + A_z$ ($k_z = 0$) in the system. Hence, we can expect the in-plane pseudomagnetic field $B_y = \nabla \times A_z$. Note that previous studies focus on the synthetic gauge field in the x-y plane, resulting in the out-of-plane pseudomagnetic field. For our origami metamaterial, the uniform pseudomagnetic field of magnitude $B_y = 12.5$ T and $B_y = 19.5$ T can be constructed for lower frequency and higher frequency, respectively, where the directions of pseudomagnetic field are opposite. With such a pseudomagnetic field affecting our system, the energy levels will be quantized as below (see theoretical derivations in the Appendix D):

$$\omega_n = \begin{cases} \mathrm{sgn}(q)vk_y, & n = 0 \\ \pm\sqrt{v^2k_y^2 + 2n|q|v}, & n \geq 1 \end{cases} \tag{5.4}$$

where ± correspond to the $\mathbf{K}$ and $\mathbf{K'}$ valley, respectively. Here, we derive the dispersion relation with the chiral Landau levels in a two-dimensional system, whereas previous discussions on such chiral Landau levels are based on three-dimensional Weyl systems [203–205].

According to this equation, the energy levels beyond $k_y = 0$ are dispersive in the k_y direction. When $n = 0$, corresponding to zeroth order Landau level, it has a linear dispersion and the group velocities are opposite at lower and higher frequency. As for the higher order Landau levels, they are quantized with certain increments. In addition, we use the supercell

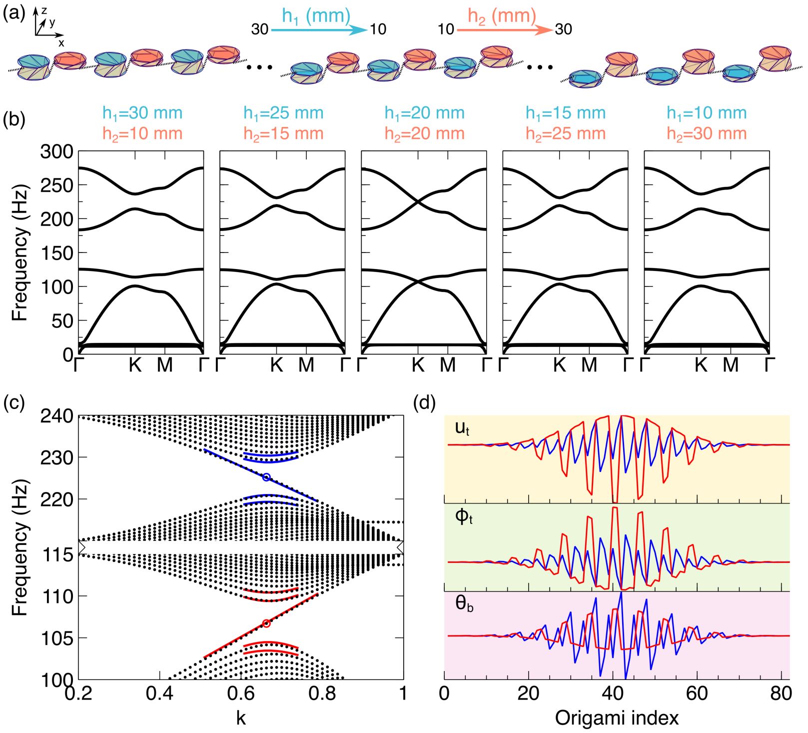

Figure 5.2: Synthetic gauge field and Landau level. (a) The schematic of the supercell composed of 41 unit cells (82 origamis) with height gradient. The initial height of origami h_1, h_2 are linearly varying from 30 mm to 10 mm and from 10 mm to 30 mm, respectively. (b) The band structure along Γ-K-M-Γ calculated by the unit cell with different configurations. (c) The projected band structure of the supercell under the periodic boundary condition along y direction. Two ends of the supercell are connected to the wall. The dotted lines denote the calculated Landau levels, while the solid lines denote the theoretical Landau levels. (d) The eigenmodes representing u_t, ϕ_t and θ_b are from top to bottom panel. Red and blue lines correspond to the red and blue circles in (c).

shown in Figure 5.2(a) to calculate the projected band structure. In Figure 5.2(c), we show the excellent agreement of the zeroth Landau level and higher order Landau levels between numerical calculation and theoretical derivation in the vicinity of the **K** valley. There appear some slight differences when **k** is away from the **K** valley because the theoretical dispersion relation is approximated based on the approximate continuum Hamiltonian in the **K** valley. Besides, when n becomes larger (higher order Landau levels), the difference between numerical calculation and theoretical result becomes notable.

The eigenmodes of the zeroth Landau level are illustrated in Figure 5.2(d), corresponding to red and blue dots at lower and higher frequency. The three degrees of freedom of our origami metamaterial u_t, ϕ_t and θ_b are concentrated near the middle of the supercell (21^{st} unit cell). However, we also notice that compared with the distribution of confined states arising from topological states or defect states, the confined states in the zeroth Landau level are less concentrated.

We construct our origami metamaterial by extending the supercell along the direction of the wave vector so that an origami metamaterial with 60×41 unit cells can be formed. We set the chiral excitation source on the axial displacement u_t in the middle of the origami metamaterial to excite the modes subjected to the $\mathbf{K}$ valley corresponding to the zeroth Landau level. The corresponding frequency response of our origami metamaterials is shown in Figure 5.3. Figure 5.3(a) shows the field distribution of θ_b under the excitation of the lower frequency (106 Hz), where elastic waves propagate along the $+y$ direction. In stark contrast, elastic waves propagate along the opposite direction under the excitation of the higher frequency (225 Hz). This is due to the opposite group velocity of the zeroth Landau level in the two different frequency regions.

Although the Landau levels are considered as bulk states, which are distinct from the topological edge states, the zeroth Landau level is topologically protected [205, 206]. This is on account of the negligible intervalley scattering ($\mathbf{K}$ and $\mathbf{K}'$ valleys are widely separated in $\mathbf{k}$ space), resulting in the weak backscattering of elastic waves. To confirm the robustness of the zeroth Landau level, obstacles (origamis with double mass m and rotational inertia j) are put along the wave propagation path while the same excitation is conducted. As shown in Figures 5.3(c)-(d), the elastic waves propagate along the middle path similar to what is shown in Figures 5.3(a)-(b), instead of jamming and backscattering. This clearly exhibits the robustness of the transport of the chiral zeroth Landau level. We also notice in Figures 5.3(a)-(d) the elastic wave propagation along the top or bottom edge of the origami metamaterial, which may result from the boundary modes due to the free boundary conditions on the two edges subjected to the pseudomagnetic field.

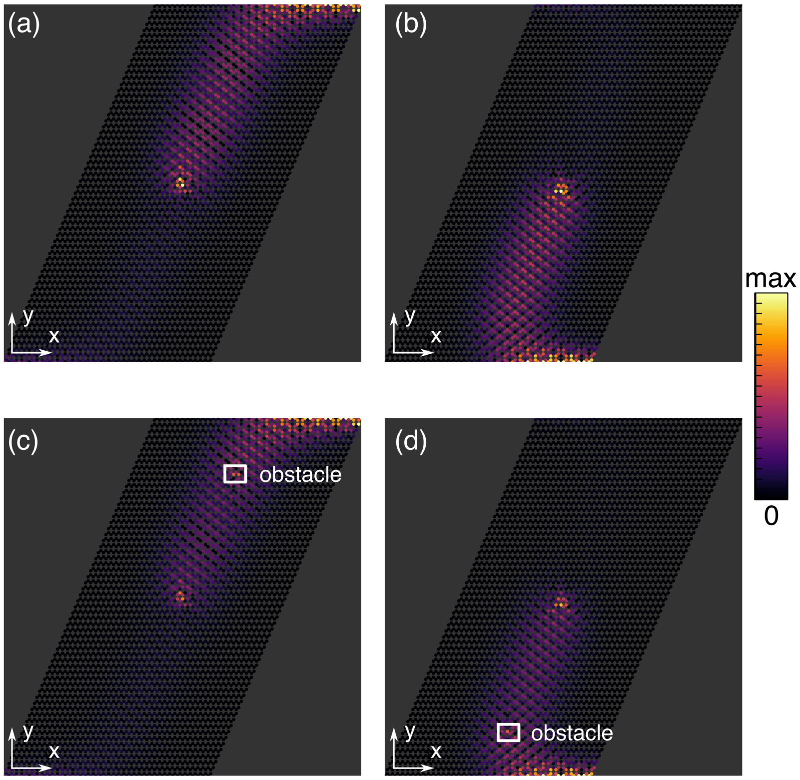

Figure 5.3: Robust zeroth Landau level. The field distributions θ_b for the zeroth Landau level in (a) lower frequency and (b) higher frequency. The corresponding cases with obstacles along the propagation path are shown in (c) and (d). Two excitation sources with phase difference are put in the middle. The excitation frequencies are 106 Hz and 225 Hz, respectively.

5.4 Elastic snake states

The snake state is a novel transport phenomenon that has been observed in two-dimensional electron gases in p-n junctions of graphene [207–209], when subjected to an external magnetic field. This transport is characterized by a snake-like propagation path, which is driven by the Lorentz force due to the cyclotron motion of electrons in opposite magnetic fields at the interface of two domains with opposite magnetic field [210]. It has been predicted that the pseudomagnetic field can also induce the snake states. In what follows the relation between the zeroth and first Landau levels in the projected band structure shown in Figure 5.2(c) is exploited to realize elastic snake states in the origami metamaterial. The difference of topological phase on two domains provides two opposite topological charges, which makes snake states possible in our system with uniform pseudomagnetic field.

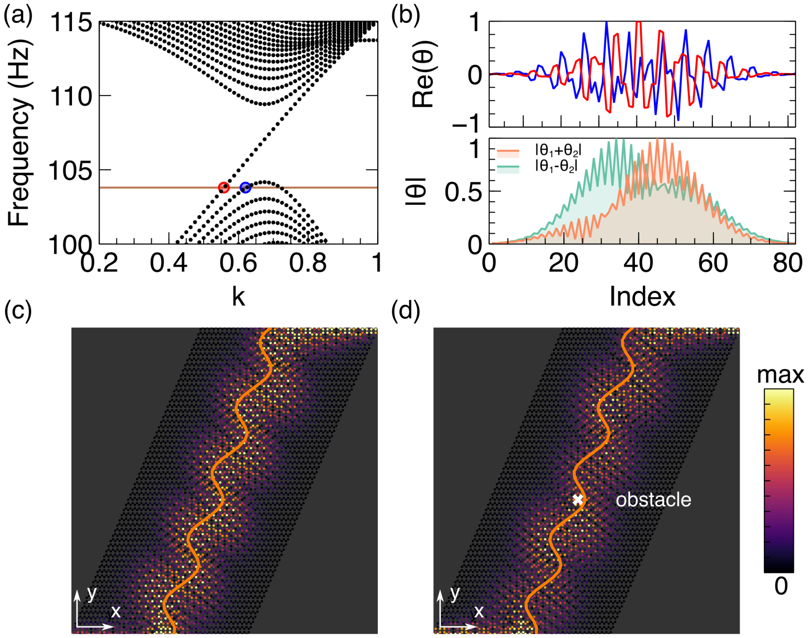

Figure 5.4: Elastic snake states. (a) The projected band structure of the supercell at the lower frequency. (b) Top panel: real parts of the eigenmode θ_{b1} and θ_{b2} along the supercell, corresponding to the red and blue dots in (a). Bottom panel: the newly-defined modes $|\theta_{b1} + \theta_{b2}|$ and $|\theta_{b1} - \theta_{b2}|$. (c) The simulated θ_b distribution under the excitation frequency at 103.9 Hz, corresponding to the solid line in (a). (d) The simulated θ distribution with the obstacle in the middle under the excitation frequency at 103.9 Hz. The theoretical trajectory of the snake state is shown in orange solid line in (c) and (d).

Figure 5.4(a) shows the projected band structure at the lower frequency. Due to the square root relation in the dispersion when $n \neq 0$ (higher order Landau level), there is a hump near the zeroth Landau level. We examine the states represented by θ_b of the zeroth and the first Landau levels with the positive group velocity, which are marked by red (θ_{b1} at k_1) and blue dots (θ_{b2} at k_2) in Figure 5.4(a). These two states have definite parity with respect to mirror symmetry along the x direction. The real parts of the field distributions in the top panel of Figure 5.4(b) reveal that the states θ_{b1} and θ_{b2} have odd and even parities, respectively, suggesting they are orthogonal. In this way, we can define two other orthogonal states: $\langle +| = (\theta_{b1} + \theta_{b2})/\sqrt{2}$ and $\langle -| = (\theta_{b1} - \theta_{b2})/\sqrt{2}$. The state $\langle +|$ tends to be centered to the right of the middle (of the domain), whereas the state $\langle -|$ tends to be centered to the left side of the middle [bottom panel of Figure 5.4(b)]. We can then derive $\theta_{b1} = (\langle +| + \langle -|)/\sqrt{2}$ and $\theta_{b2} = (\langle +| - \langle -|)/\sqrt{2}$. Using this basis, a general interface state ψ propagating along the middle of the origami metamaterial can be expressed in the form $\psi = c_1\theta_{b1}e^{ik_1 y} + c_2\theta_{b2}e^{ik_2 y}$, where c_1 and c_2 are determined by the specific excitation. Assuming that the excitation is placed on the right side of the middle, i.e., $\psi(y = 0) = \langle +|$, we have $c_1 = c_2 = 1/\sqrt{2}$. Therefore, $|\langle +|\psi\rangle|^2 = \cos^2(\delta k_y y)$ and $|\langle -|\psi\rangle|^2 = \sin^2(\delta k_y y)$, where $\delta k_y = (k_2 - k_1)/2$. This implies that on the right side of the middle, the excited state will be oscillating in the form of $\cos^2(\delta k_y y)$. In contrast, on the left side of the middle, the excited state will be oscillating in the form of $\sin^2(\delta k_y y)$. Consequently, the excited state will propagate similar to a snake along the middle. The theoretical trajectory of the snake state is shown in orange solid lines in Figures 5.4(c) and (d), which has a good agreement with the simulation results.

In Figure 5.4(c), we illustrate the elastic wave propagation depicting the snake state represented by θ_b. The excitation source on the axial displacement u_t with 103.9 Hz [solid line in Figure 5.4(a)] is put at the middle bottom of the origami metamaterial. The elastic wave starts with a clockwise rotation at the left side and then enters the right side with a counterclockwise rotation. This motion repeats, and the clear observation of the elastic snake state is illustrated. Since the snake state originates from the bulk and thus does not have robustness, there will be the strong backscattering when the elastic waves encounter the obstacles. Nevertheless, if the obstacles are placed at the appropriate positions along the middle of the origami metamaterial, the wavy snake state can bypass the obstacles, making it appear as if the objects are cloaked [Figure 5.4(d)].

5.5 Conclusions and discussion

In conclusion, our study presents a prototypical realization of an out-of-plane synthetic gauge field in origami metamaterials, leading to the emergence of a pseudomagnetic field that enables the quantization of Landau levels. The results of the numerical simulations and theoretical analysis are in good agreement, in the appropriate wavenumber range, confirming the validity of the long wavelength approximation used. By leveraging the unique dispersion relation of Landau levels, we have explored the topologically protected chiral elastic wave propagation and the emergence of elastic snake states. Therein, this metamaterial can serve as an effective alternative to topological elastic metamaterials due to its robust zeroth Landau level. The reconfigurability and simple manufacturing of origami structures make them attractive for a variety of possible applications such as waveguiding and obstacle bypassing due to the robust nature and associated wave propagation. Although the origami metamaterial in our study is in the centimeter scale, the scalability of this structure allows it to be applied to manipulate elastic waves at different frequencies. Besides, our scheme is not limited to Kresling origami, and other types of origami can be explored in the future. Importantly, the features considered herein have been limited to quasi-continuum linear features, in the vicinity of Dirac cones. The configuration, however, proposed herein bears a wide range of interesting phenomena including ones beyond the quasi-continuum approximation, as well as, importantly, nonlinear features within the band gaps. Studies along these veins are currently in progress and will be reported in future publications.

5.6 Author contribution

This chapter is adopted from Shuaifeng Li, Panayotis G. Kevrekidis and Jinkyu Yang, Elastic chiral Landau level and snake states in origami metamaterials (in submission).

S. Li and J. Yang proposed the research; S. Li performed the simulation and modeling; P. G. Kevrekidis and J. Yang provided guidance throughout the research; S. Li and J. Yang prepared the manuscript; P. G. Kevrekidis and J. Yang provided guidance during manuscript preparation and development.

Chapter 6

CHARACTERIZATION OF ELASTIC TOPOLOGICAL STATES USING DYNAMIC MODE DECOMPOSITION

Elastic topological states have been receiving increased attention in numerous scientific and engineering fields due to their defect-immune nature, resulting in applications of vibration control and information processing. Here, we present the data-driven discovery of elastic topological states using dynamic mode decomposition (DMD). The DMD spectrum and DMD modes are retrieved from the propagation of the relevant states along the topological boundary, where their nature is learned by DMD. Applications such as classification and synthesis of wave propagation can be achieved by the underlying characteristics from DMD. We demonstrate the classification between topological and traditional metamaterials using DMD modes. Moreover, the model enabled by the DMD modes realizes the synthesis of topological state propagation along the given interface. Our approach to characterizing topological states using DMD can pave the way towards data-driven discovery of topological phenomena in material physics and more broadly lattice systems.

6.1 Introduction

Wave propagation is a typical spatiotemporal phenomenon, which is ubiquitous across science and engineering, especially in fluid dynamics [211, 212], geoscience [213, 214], plasmas [215], optics [216], atomic and condensed matter physics [217], as well as the more recent field of metamaterials [218–220]. Topological metamaterials have attracted considerable attention not only because of their theoretical significance but also for practical purposes related to materials applications. Wave propagation in elastic topological metamaterials has prominent applications, such as information transmission and vibration control, due to the topological protection [221–226].

The computations involving the propagation of associated waveforms rely mostly on numerical discretization, e.g., finite element and discrete element methods, rather than analytic closed-form solutions which are rarely available in exact form. This naturally generates high-dimensional representations of the solution to accurately reflect the underlying dynamics in both time and space [221, 223, 224, 227]. However, this may occasionally be in contrast with the low-dimensional nature of the underlying dynamics and poses a computational challenge, especially in higher-dimensional settings. In a concurrent study, topological wave propagation has been decomposed into a limited subset of closely spaced modes inside the bandgap, possessing nontrivial phase differences. The prediction of group velocity and the application of such a method on a damped system have also been demonstrated [228]. Although the underlying idea of a reduced-order description is similar to that of the present work, still, the data-driven (and possibly model agnostic) analysis and modeling of elastic topological states remain far less explored, in stark contrast with the extensive studies on experimental observation, numerical computation and theoretical modeling. The data-driven approach can also provide an equation-free and model agnostic way to reveal the spatiotemporal dynamics and underlying physics purely from data. It is the purpose of the present work to offer a step forward towards filling that void.

Reduced-order models offer representations of the spatiotemporal wave propagation based on the inherently low-rank structure of the simulation data. Within the palette of relevant techniques, dynamic mode decomposition is a powerful dimensionality reduction method to create reduced-order models which identifies spatiotemporal coherent structures from high-dimensional data [155]. DMD offers a modal decomposition, where each mode contains spatially correlated structures with the same linear behavior in time, such as oscillations at a certain frequency with growth or decay. Compared with one of the most commonly used dimensionality reduction methods, proper orthogonal decomposition, DMD demonstrates not only dimensionality reduction, but also a reduced model that accounts for how these modes evolve over time. Lately, DMD has been successfully applied to fluid dynamics [154, 155], control [229], robotics [156] and biological science [157, 158, 230]. Hence, developing such an approach for wave propagation in topological metamaterials is highly desirable.

Here, we develop a data-driven framework using DMD for identifying interpretable low-dimensional representations for wave propagation in elastic topological metamaterials created by a select spring-mass system example. The low-dimensional spatiotemporal coherent structures of topological state propagation in our system are extracted, which correspond to the topological edge states inside the bandgap region. These spatiotemporal coherent structures allow for the qualitative reconstruction of the topological state propagation. Moreover, we first demonstrate how to classify the topological and traditional metamaterials using DMD modes via unsupervised clustering. Furthermore, a portion of the data, referred to as the training data, is used to synthesize the future evolution of the topological states of interest along a pre-defined interface with arbitrary shape. Our study provides a computationally tractable data-driven characterization of the relevant states and their propagation, paving the way towards the classification and synthesis of wave propagation in elastic metamaterials.

Our presentation hereafter will be structured as follows. In Section 6.2 we offer details about the physical system under consideration including the band structure and topological properties. In Section 6.3 we provide a concise introduction in the mathematical and computational details of the DMD algorithm (including technical modifications to the standard algorithm such as the use of a stacking data matrix leveraged herein) and illustrate how it can be used to represent the wave dynamics. In Section 6.4, we use DMD modes to classify the topological and traditional metamaterials. Finally, in Section 6.5, we summarize our findings and provide some directions for future study. The Appendix E offers details about further technical aspects of the DMD implementation, such as the DMD spectra, the application of time-delay embedding and synthesis of topological state propagation.

6.2 Design of topological elastic metamaterials

To demonstrate DMD on the wave propagation in the topological elastic metamaterials system of interest, we first construct the topological valley metamaterials using a spring-mass system, which is realized by alternating the masses at different sites of the unit cell of the honeycomb lattice [199, 224, 227, 231]. As displayed in Figure 6.1(a), the unit cell is composed of two masses m_1 and m_2 connected by a spring. The length and the spring constant are a and k_{spring}. Therefore, the basic vectors for this unit cell are $\mathbf{a}_1 = [a_x, -a_y]$, $\mathbf{a}_2 = [a_x, a_y]$, where $a_x = 3a/2$ and $a_y = \sqrt{3}a/2$. The unit cell has four degrees of freedom specified by the displacement of m_1 and m_2 ($U = [u_x^{m_1}, u_y^{m_1}, u_x^{m_2}, u_y^{m_2}]^T$). After applying the periodic boundary condition to the unit cell (Bloch's theorem), equations of motion of two masses in one unit cell can be written as:

$$\begin{aligned} -\omega^2 m_1 \mathbf{u}^{(1)} =& k_{spring}[(\mathbf{u}^{(2)} - \mathbf{u}^{(1)}) \cdot \mathbf{e}_x]\mathbf{e}_x \\ &+ k_{spring}[(\mathbf{u}^{(2)} e^{i\mathbf{k}\cdot\mathbf{a}_1} - \mathbf{u}^{(1)}) \cdot \mathbf{e}_k]\mathbf{e}_k \\ &+ k_{spring}[(\mathbf{u}^{(2)} e^{i\mathbf{k}\cdot\mathbf{a}_2} - \mathbf{u}^{(1)}) \cdot \mathbf{e}'_k]\mathbf{e}'_k \end{aligned} \tag{6.1}$$

$$\begin{aligned} -\omega^2 m_2 \mathbf{u}^{(2)} =& k_{spring}[(\mathbf{u}^{(1)} - \mathbf{u}^{(2)}) \cdot \mathbf{e}_x]\mathbf{e}_x \\ &+ k_{spring}[(\mathbf{u}^{(1)} e^{-i\mathbf{k}\cdot\mathbf{a}_1} - \mathbf{u}^{(2)}) \cdot \mathbf{e}_k]\mathbf{e}_k \\ &+ k_{spring}[(\mathbf{u}^{(1)} e^{-i\mathbf{k}\cdot\mathbf{a}_2} - \mathbf{u}^{(2)}) \cdot \mathbf{e}'_k]\mathbf{e}'_k \end{aligned} \tag{6.2}$$

where $\mathbf{e}_x = [1, 0]^T$, $\mathbf{e}_k = [-\frac{1}{2}, \frac{\sqrt{3}}{2}]^T$ and $\mathbf{e}'_k = [-\frac{1}{2}, -\frac{\sqrt{3}}{2}]^T$ are three unit vectors along the springs on one mass. The band structure $\omega(\mathbf{k})$ of our system can be obtained by solving the eigenvalue equation as a function of Bloch wave vector $\mathbf{k}$ in the first Brillouin zone.

$$[D(\mathbf{k}) + \omega^2 M]U = 0 \tag{6.3}$$

Here, ω denotes the angular frequency of the propagating wave. M is the mass matrix and $D(\mathbf{k})$ is the stiffness matrix as a function of Bloch wave vector $\mathbf{k}$. The corresponding eigenmodes $U = [u_x^{m_1}, u_y^{m_1}, u_x^{m_2}, u_y^{m_2}]^T$ can also be obtained.

As for our specific system, we choose the equal masses on two sites ($m_1 = m_2 = 1$ kg) and $k_{spring} = 10^5$ N/m to find the Dirac point at the corner of the Brillouin zone (**K** point), as shown in the middle panel of Figure 6.1(a). After breaking spatial inversion symmetry by unequal masses on two sites, two bands can be opened to form a bandgap. The left and right panels exhibit the band structure when $m_1 = 0.8$ kg, $m_2 = 1.2$ kg and $m_1 = 1.2$ kg, $m_2 = 0.8$ kg, respectively. At the **K** valley, eigenmodes corresponding to two bands when $m_1 = 0.8$ kg and $m_2 = 1.2$ kg are $U_1 = \frac{1}{\sqrt{2}}[0, 0, 1, -i]^T$ and $U_2 = \frac{1}{\sqrt{2}}[1, i, 0, 0]^T$, while the eigenmodes are $U_1 = \frac{1}{\sqrt{2}}[1, i, 0, 0]^T$ and $U_2 = \frac{1}{\sqrt{2}}[0, 0, 1, -i]^T$ after alternating the masses on two sites (see the insets with black arrows that represent the eigenmodes). The obvious band inversion can be seen from the eigenmodes of the unit cell.

To further confirm the band inversion in this process, the topological properties of our topological valley system are also explored to show the topological phase transition. Af-

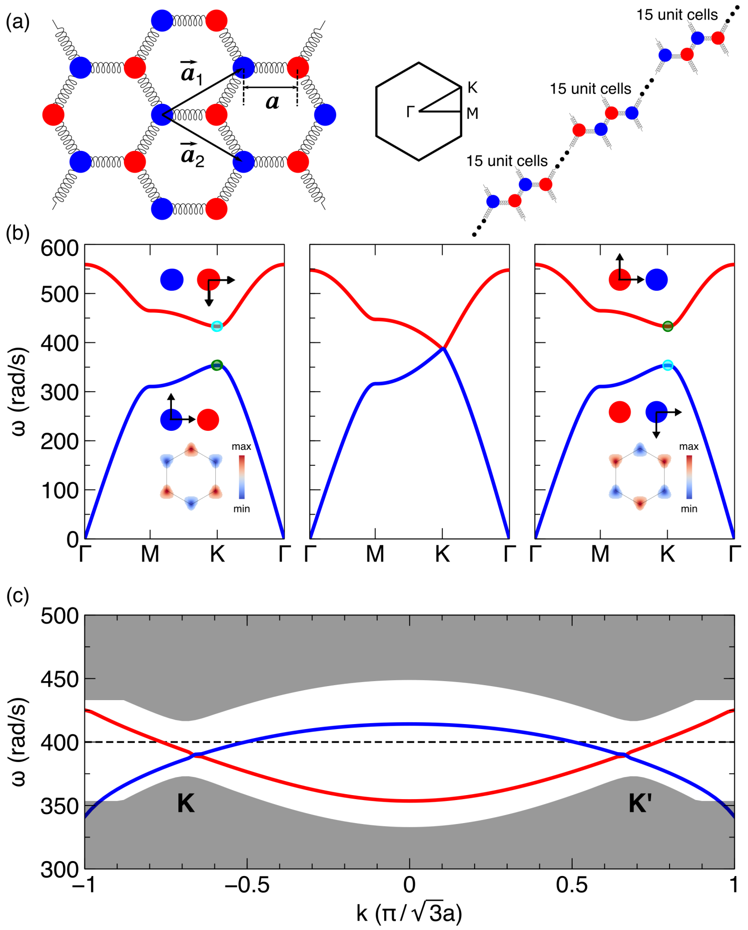

Figure 6.1: Band structure of the valley topological metamaterials. (a) Schematic of our elastic metamaterials based on the spring-mass system. Basic vectors of unit cell are shown in $\mathbf{a}_1$ and $\mathbf{a}_2$. Length of the spring is a. First Brillouin zone with high symmetry points Γ, M and K is shown in the middle panel. The sandwiched supercell for the calculation of projected band structure is shown in the right panel. (b) Band structure when (left) $m_1 = 0.8$ kg, $m_2 = 1.2$ kg, (middle) $m_1 = 1$ kg, $m_2 = 1$ kg and (right) $m_1 = 1.2$ kg, $m_2 = 0.8$ kg are shown. The eigenmodes corresponding to the **K** valley are shown in the first panel and the third panel. Motions along horizontal and vertical directions are marked on the two sites. Berry curvatures around the valley of the first band for each case are shown in the inset. (c) Projected band structure with two topological states inside the bandgap. The black dashed line indicates the excitation frequency of the simulation setup.

ter obtaining the band structure $\omega(\mathbf{k})$ and the corresponding eigenmode $U(\mathbf{k})$, we calculate the Berry curvature $\Omega(\mathbf{k}) = i\nabla_{\mathbf{k}} \times \langle U(\mathbf{k})|\nabla_{\mathbf{k}}|U(\mathbf{k})\rangle$ using a numerical discretization method (in momentum space) [221, 222]. For our two-dimensional system, the Brillouin zone is discretized to numerous small patches centered at $A(k_x, k_y)$ with vertices $A_1(k_x - \delta k_x/2, k_y - \delta k_y/2)$, $A_2(k_x - \delta k_x/2, k_y + \delta k_y/2)$, $A_3(k_x + \delta k_x/2, k_y + \delta k_y/2)$ and $A_4(k_x + \delta k_x/2, k_y - \delta k_y/2)$, where the Berry curvature for each small patch can be expressed as:

$$\Omega(A) = \frac{\mathrm{Im}[\langle U(A_1)|U(A_2)\rangle + \langle U(A_2)|U(A_3)\rangle + \langle U(A_3)|U(A_4)\rangle + \langle U(A_4)|U(A_1)\rangle]}{\delta k_x \times \delta k_y} \tag{6.4}$$

As shown in the inset of Figure 6.1(b), the nonzero Berry curvatures are distributed near the corners of the Brillouin zone (**K** points) and different valleys possess opposite Berry curvatures. Due to our system with time reversal symmetry, the integration of the Berry curvature around the whole Brillouin zone is expected to be zero. However, the local integration around the valleys of the Berry curvature converges to nonzero quantized value, which is referred to as valley Chern number $C_v = \frac{1}{2\pi}\int_v \Omega(\mathbf{k})d^2\mathbf{k}$, representing the valley topology. The obvious inversion of Berry curvature distribution and the sign of the valley Chern number after alternating the masses on two sites clearly shows the topological phase transition [compare the insets of the right and left panels in Figure 6.1(b)].

The projected band structure is then calculated using a sandwiched supercell shown in the right panel of Figure 6.1(a). The sandwiched supercell combines the metamaterials of three arrangements: (i) $m_1 = 0.8$ kg, $m_2 = 1.2$ kg, (ii) $m_1 = 1.2$ kg, $m_2 = 0.8$ kg, and (iii) $m_1 = 0.8$ kg, $m_2 = 1.2$ kg, which has two opposite Berry curvature distributions in the Brillouin zone. When two systems are interfaced with opposite Berry curvature, the bulk-boundary correspondence principle ensures that two topological states with different pseudospins corresponding to two types of interfaces emerge inside the bandgap, as shown in Figure 6.1(c). The bulk featured by **K** and **K**' valleys can also be observed from the projected band structure. In the following study, the excitation frequency of our simulation is 400 rad/s as indicated by the black dashed line in Figure 6.1(c).

6.3 Characterization by dynamic mode decomposition

As shown in Figure 6.2(a), our system bears a Z-shaped interface which is formed by combining metamaterials with two opposite topological phases. In Figure 6.2(a), one such interface is formed by $m_1 = 0.8$ kg (blue) and $m_2 = 1.2$ kg (red) shown in the bottom, while the other is formed by $m_1 = 1.2$ kg (red) and $m_2 = 0.8$ kg (blue) shown in the top, i.e., with the masses flipped. The spring constant is fixed to be 10^5 N/m. As analyzed in the previous section, with such a configuration, the topological states will emerge along the interface formed by two metamaterials.

The system is excited by an oscillating force with the angular frequency of 400 rad/s at the input port of the Z-shaped interface shown in Figure 6.2(a). The masses at the boundaries of the system are connected to springs fixed to the wall, i.e., $\mathbf{F}_{boundary} = -k_{spring}\mathbf{u}$, where $\mathbf{u}$ contains horizontal displacement u_x and vertical displacement u_y. Because of the topological protection of wave propagation, the elastic wave can travel through the sharp bend robustly, the horizontal displacement u_x of which is visualized as the time-series snapshots in Figure 6.2(b).

Next we attempt to reconstruct this wave propagation phenomenon using the DMD approach. Let us present the result of the DMD approach first. Figure 6.2(c) shows the reconstruction of the horizontal displacement u_x. We find the trend of the DMD-based approach is similar to the one by the original evolution dynamics. Particularly, the DMD technique successfully captures the robust propagation of topological waves around the sharp corners, which is the signature characteristic of the topological waveguide. The difference of the color intensity between the original and the reconstructed results is due to inherent deficiency of the DMD to capture transient dynamics which will be elaborated later.

As introduced in the Section 6.1, DMD serves as the dimensionality reduction method to generate low-dimensional model. The basic idea of DMD is to find a matrix representation A to relate two matrices X and X'. In our case, two data matrices are constructed for standard DMD by stacking the horizontal displacement u_x and vertical displacement u_y as follows, resulting in two $2n \times (m-1)$ matrices, where n is the number of masses and m is the number of used snapshots over time ($n = 2700$ and $m = 379$ for the Z-shaped interface based on the numerical simulations of 758 ms duration with 2 ms time interval:

$$X = \begin{bmatrix} | & | & & | \\ x_1 & x_2 & \dots & x_{m-1} \\ | & | & & | \end{bmatrix} \quad X = \begin{bmatrix} | & | & & | \\ x_2 & x_3 & \dots & x_m \\ | & | & & | \end{bmatrix} \tag{6.5}$$

where $\begin{bmatrix} | \\ x_m \\ | \end{bmatrix} = \begin{bmatrix} | \\ u_{xm} \\ | \\ | \\ u_{ym} \\ | \end{bmatrix}$ for simplicity of description. X and X' may be related by a best-fit linear operator A that minimizes the Frobenius norm error $\|X' - AX\|_F$ given by

$$X' = AX \Rightarrow A = X'X^\dagger \tag{6.6}$$

where $X^\dagger$ is the Moore-Penrose pseudo-inverse [232]. Because $2n \gg m$ for our systems, instead of obtaining A directly, we seek the eigen decomposition of A. After X is decomposed using singular value decomposition (SVD) and the proper rank-r truncation is chosen so that $X_r = U_r \Sigma_r V_r^T$, where $U_r \in \mathbb{R}^{2n\times r}$, $\Sigma_r \in \mathbb{R}^{r\times r}$ and $V_r \in \mathbb{R}^{(m-1)\times r}$ are the left unitary matrix, diagonal matrix with singular values, and right unitary matrix, respectively, the matrix representation A_r can be written as

$$A_r = U_r^* X' V_r \Sigma_r^{-1} \tag{6.7}$$

where the $*$ denotes the conjugate transpose. The eigen-decomposition of A_r results in the matrix of eigenvectors W and eigenvalues λ, which are the DMD eigenvalues. This further derives the corresponding DMD mode ϕ, which is the column of $\Phi = X' V_r \Sigma_r^{-1} W$.

As discussed in Appendix E, the rank-r truncation is chosen to be $r = 131$ to minimize the reconstruction error and also to eliminate the noise in the simulation data. Each DMD mode ϕ corresponds to an eigenvalue λ. The temporal dynamics, referring to growth/decay and the frequency of oscillation of each DMD mode ϕ, is reflected through the magnitude and phase of eigenvalue λ, respectively. In our case, because the raw data are strictly real valued, the decomposition yields complex conjugate pairs of eigenvalues and modes.

In Figure 6.3(a), the eigenvalues λ are visualized on the unit circle in the complex plane, suggesting the corresponding modes are oscillating with certain frequencies. The frequencies are defined as $\omega = |\text{imag}\frac{\log\lambda}{\Delta t}|$ and the mode amplitudes are defined as $P = \|\phi\|_2^2$, which is the squared l^2-norm of the DMD modes. Figure 6.3(b) gives the DMD spectrum which

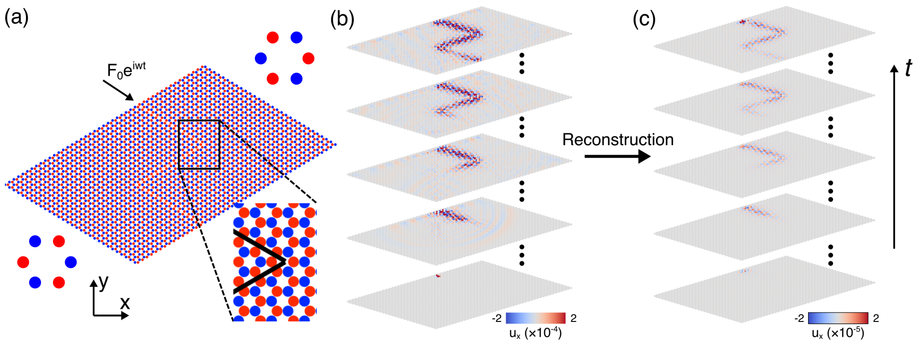

Figure 6.2: Setup for simulation and for the numerical DMD implementation. (a) Simulation of wave propagation along the Z-shaped interface in a valley topological metamaterial built by means of a spring-mass system. Two different unit cells with two different topological phases are shown on the two sides. Magnified view of the topological boundary (black line) is shown in the inset. (b)(c) Snapshots of original and reconstructed wave propagation represented by the horizontal displacement u_x along the Z-shaped interface at $t = 2$, 192, 380, 570 and 758 ms (with the time evolving from the bottom to the top), respectively.

provides specific spatial modes in our system for different frequencies. It is obvious that there is a region with large mode amplitudes corresponding to the bandgap region (shaded area). The mode with the largest amplitude inside the bandgap region is chosen as the prototypical mode used to visualize the motion of our system. The horizontal displacement u_x is chosen for the description below. Note that there are two small peaks outside the bandgap region due to the resonance of the masses at the boundary, corresponding to the resonant frequencies $\omega = \sqrt{\frac{7-\sqrt{33}}{4}}\omega_0$ and $\omega = \sqrt{\frac{1}{2}}\omega_0$ approximated by a simple model that one mass is connected to two walls and two masses on nearest honeycomb corners by springs.

Figure 6.3(c) exhibits the magnitude of this most dominant DMD mode of our system, also showcasing the interface-involving dynamics. The decaying magnitude from the input along the Z-shaped interface is due to the constant force excitation at the input. The characteristics of interface states present concentrated displacement along the Z-shaped interface and rapid decay away from the interface. Moreover, the DMD modes showcase the fact that the elastic wave can travel along an interface featuring bends. Apart from the magnitude, the phases of the DMD mode also reflect the important characteristics of

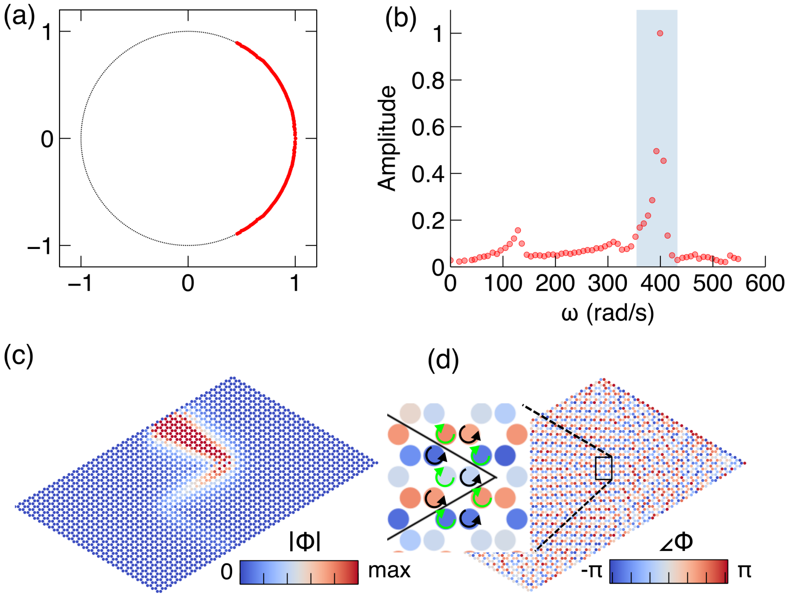

Figure 6.3: DMD spectrum and DMD modes. (a) Eigenvalues are visualized on the complex plane located around the unit circle. (b) Mode amplitude varies as a function of frequency. The shading area indicates the bandgap region. (c) Magnitude of the DMD mode with the largest amplitude inside the bandgap region. (d) Phase of the DMD mode with the largest amplitude inside the bandgap region. Inset shows the magnified view around the interface (black line) illustrating the phase difference and valley pseudospin. Black and green arrows show the pseudospin up and pseudospin down indicated by the phase evolution around hexagon corners, respectively.

our topological valley metamaterials, as shown in Figure 6.3(d). The distribution of phase along the interface has a certain alignment, where the magnified view around the interface clearly shows the phase difference around the corners of the honeycomb, indicating specific valley polarization along a certain topological interface. The counterclockwise and clockwise phase evolutions are shown on three corners and the other three corners of the honeycomb, suggesting the valley pseudospin of the excited valley in our system. The valley pseudospin here refers to the phase difference of DMD modes around the corners of honeycomb. Note that the other DMD modes inside the bandgap have a similar pattern and it is these modes that will be primarily used to reconstruct the dynamical evolution below.

The DMD spectra of wave propagation in topological metamaterials with a straight interface and a cross-shaped interface will be further illustrated in Appendix E. Similarities between the DMD spectra and modes can be found in topological state propagation along different interfaces including the high amplitude inside the bandgap and the topological interface states reflected by the DMD modes. This demonstrates the ability of the DMD to robustly show the frequency spectrum of the system purely from the data and to discover the nature of topological state propagation.

Using the extracted DMD modes and corresponding time dynamics, we can reconstruct the wave propagation in topological metamaterials using the following expression:

$$\hat{X} = \Phi\Lambda^{t-1}Z \tag{6.8}$$

where the diagonal entries of Λ contains DMD eigenvalues and $Z = \Phi \backslash x_1$. x_1 is the initial condition of our system and backslash is to solve the linear system following the `MATLAB` notation. Here, we only use the DMD modes inside the bandgap region (10 pairs of DMD modes) and the corresponding eigenvalues to reconstruct the whole process of wave propagation, as displayed in Figure 6.2(c) with several time-series snapshots representing the wave propagation in our system. Similar patterns can be found compared with the original snapshots of wave propagation.

In Figure 6.4, we quantify the reconstruction error as a function of duration (black line) calculated by $E(t) = \frac{\|X(t)-\hat{X}(t)\|_2}{\|X(t)\|_2}$, where $\|\cdot\|_2$ represents l^2-norm that is the square root of the sum of the absolute squares of the vector entries. Most relative errors are around 0.97 and oscillating over time. This nontrivial relative error may result from the reduction of inessential modes with extremely small singular values by the SVD, the significant reduction of DMD modes when considering solely modes within the bandgap, the l^2-norm error requiring the high accuracy of displacement for every mass and, most importantly, the inherent deficiency of the DMD method to capture transient phenomena [157, 233, 234]. This is caused by the fact that temporal dynamics cannot be well approximated by $e^{\omega t}$ where the imaginary number $\omega = \frac{\ln \Lambda}{\Delta t}$. The SVD-based method also performs poorly on handling translational symmetry of the wave propagation due to the coupling between time and space. Although the relative error is rather nontrivial, the wave propagation along the Z-shaped interface can be clearly observed from Figure 6.1 and Supplementary movie [235], which can be considered as the qualitative representation of the original wave propagation. To measure the qualitative reconstruction using DMD, we propose an additional quantity, namely the correlation coefficient, to show the similarity between reconstructed and original wave propagation at each time point:

$$r(t) = \frac{\sum_{i=1}^{2n}(x_{i,t} - \bar{x}_{*,t})(\hat{x}_{i,t} - \bar{\hat{x}}_{*,t})}{\sqrt{\sum_{i=1}^{2n}(x_{i,t} - \bar{x}_{*,t})^2 \sum_{i=1}^{2n}(\hat{x}_{i,t} - \bar{\hat{x}}_{*,t})^2}} \tag{6.9}$$

where the hat indicates the reconstructed data and the bar indicates the mean. The correlation coefficient as a function of time shown in blue line in Figure 6.4 is over 0.8, suggesting the high similarity between reconstructed and original wave propagation. Therefore, the DMD reconstruction using the modes inside the bandgap region qualitatively captures the evolution dynamics despite the substantially reduced dimensionality of the system.

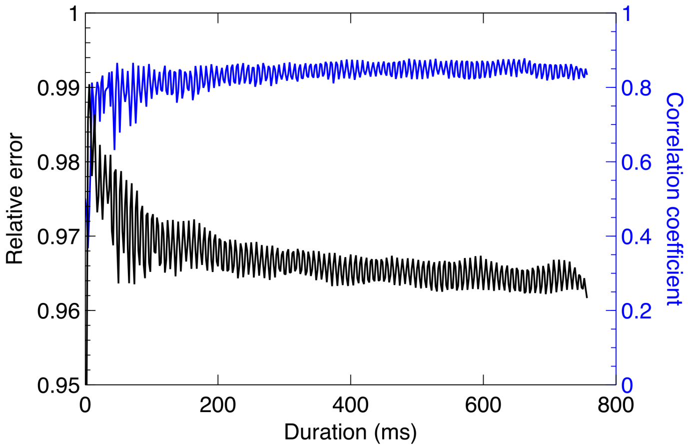

Figure 6.4: Reconstruction error and correlation coefficient between reconstructed and original wave propagation. Relative error and correlation coefficient between the ground truth and reconstruction as a function of duration are shown in black and blue, respectively.

DMD can accurately capture the frequency range and characteristics of topological states of elastic topological metamaterials. The nature of the valley pseudospin in our valley system can also be revealed, suggesting that DMD, functioning as a data-driven method, is able to learn the topological nature. In stark contrast with the original transient displacement data, the DMD spatial mode can explicitly show the topological nature. In addition, the propagation of topological states can be reconstructed qualitatively only by the DMD modes inside the bandgap and the corresponding time dynamics. The additional study in Appendix E is carried out on the topological metamaterial excited by a transient force, which further demonstrates the ability of DMD to qualitatively reconstruct the dynamics under different forms of excitations. Note that we use standard DMD based on SVD in the main text, but another variant, DMD with time-delay embedding, has demonstrated the ability of increasing the accuracy of reconstruction in several applications [157, 158, 163, 236, 237]. In Appendix E and the associated figure, we also show the partial decrease of reconstruction error using the augmented data matrix formed by shift-stacking the original data matrix.

6.4 Classification of topological and traditional metamaterials

Compared with the topological metamaterials, traditional metamaterials function by defect states that cannot support robust transport of elastic waves [238–241]. By using the transient displacement data, it is difficult to classify the topological and traditional metamaterials using simple classification methods because of the high-dimensional nature. Here, we demonstrate how to use the extracted DMD modes from topological and traditional metamaterials to classify them. The topological metamaterial is in the aforementioned configuration and the traditional metamaterial is constructed based on the defect states by the metamaterial with $m_1 = 0.8$ kg and $m_2 = 1.2$ kg, where the masses are replaced by $m_2 = 1.2$ kg along the Z-shaped interface to create defects. Because of the defect state, the traditional metamaterial serves as a waveguide similar to the topological metamaterial but without the topological protection.

The original DMD modes are high-dimensional and thus difficult to classify using a classification algorithm directly. Therefore, the feasible way is to find a feature space to project the DMD modes on, resulting in a low-dimensional representation. Specifically, we construct a library of DMD modes inside the bandgap from topological metamaterials and traditional metamaterials L:

$$L = \begin{bmatrix} | & | & & | \\ \phi_1 & \phi_2 & \dots & \phi_N \\ | & | & & | \end{bmatrix} \tag{6.10}$$

For the purpose of classification, we consider the absolute value of every element of normalized DMD modes and denote the resulting matrix as $|L|$. To simplify this problem, clusters are determined in one-dimensional principal component space, using the projections of each column of $|L|$ onto the proper principal components of $|L|$:

$$|L| = U_L \Sigma_L V_L^T \tag{6.11}$$

With this expression yielding the SVD of the matrix $|L|$ and using

$$P = U_i^T |L| = \Sigma_i V_i^T \tag{6.12}$$

where U_i^T, Σ_i and V_i^T are the transpose of the i-th column of U_L, i-th singular value and the transpose of the i-th column of V_L, respectively.

The principal components can explain a significant proportion of the variance in the features in topological and traditional metamaterials. Therefore, finding a proper principal component U_i^T is key to distinguish two types of metamaterials. Also, the proper principal component is physically interpretable to contain the features differentiating two types of metamaterials. After examining all principal components, we have found that the second principal component is a suitable feature towards the classification task at hand (classification results are the same as the labeled dataset). The second principal component of $|L|$ is shown in Figure 6.5(a) [see the second principal components of $|L|$ for straight and cross interfaces shown in Figures E.5(a) and E.5(b) in Appendix E]. The reason why the second principal component is optimally suited to serve as the feature space is that this pattern of the principal component shows the difference between topological and traditional metamaterials at the beginning of the input port (positive vs. negative values, respectively). We find that it corresponds to the distinction of backscattering in topological and traditional metamaterials. In the traditional metamaterial, due to the interference of elastic waves traveling in opposite directions, elastic waves experience strong backscattering when encountering bends, obstacles or even traveling along the straight interface. Therefore, when $|L|$ is projected onto this principal component, the two types of metamaterials can be classified whereas they cannot be classified when $|L|$ is projected onto other principal components. The relevant diagnostic allows us to distinguish topological and traditional metamaterials purely from the wave propagation phenomena represented by the displacement, corresponding to topologically protected wave propagation and non-topological wave propagation, and hence, accordingly classify them. Note that from the perspective of the underlying topological physics, the topological invariants of the bulk and the bulk-edge correspondence are principles used to classify topological and traditional systems.

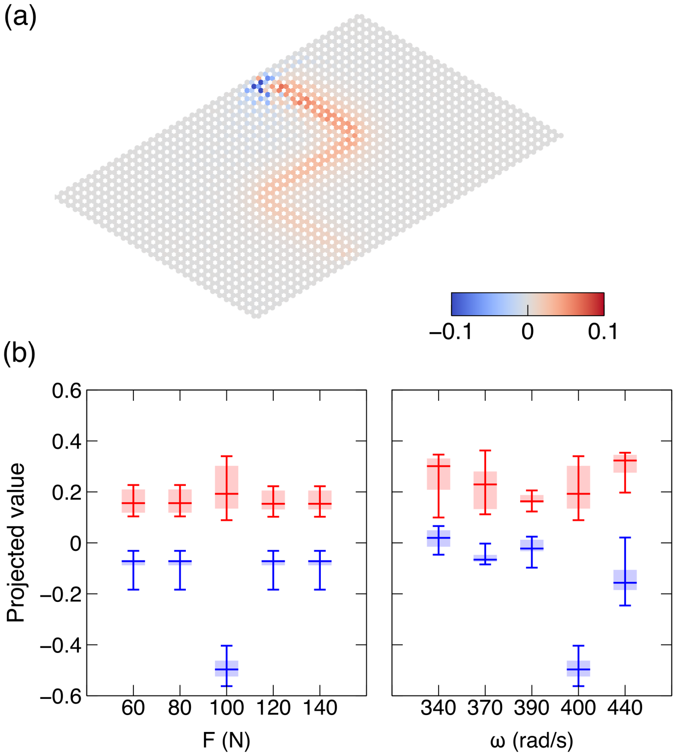

Figure 6.5: Classification of topological and traditional metamaterials. (a) Feature space formed by the second principal component of DMD modes with Z-shaped interface. (b) Projected values of each DMD mode from the topological and traditional metamaterials excited by different forces (left panel) and different excitation frequencies (right panel). Red and blue regions indicate topological and traditional DMD modes, respectively. Error bars indicate the range of the minima and maxima of projected values.

Then, in order to test whether this feature space can be generalized to classify topological and traditional systems, we apply the feature space (of the second principal component) obtained above to the topological and traditional metamaterials under the excitation of different forces F_0 and different angular frequencies ω_0. As shown in Figure 6.5(b), it is obvious that the projected values for topological and traditional metamaterials under the excitation of different forces can be separated well and can be simply classified using the k-means unsupervised clustering [242]. Likewise, under the excitation of different frequencies, the projected values for topological and traditional metamaterials are separated well, leading to good classification results. Using the same method, the wave propagation along different interfaces (straight and cross interfaces) in topological and traditional metamaterials under the excitation of different forces and frequencies can also be classified, as detailed in Appendix E. The classification results for straight and cross interfaces are demonstrated in the relevant figure therein. The case for the straight interface indicates that elastic waves in the traditional metamaterial experience backscattering without the bend because of the interference of guided waves propagating to opposite directions. The classification results and ground truth have excellent agreement. The DMD modes with improved accuracy calculated by DMD with time-delay-embedding (Appendix E and Figure E.4) can also be used in the classification, resulting in better separation of topological and traditional metamaterials in the feature space. It should be expected that with the decrease of the Berry curvature in the topological metamaterials induced by the decrease in degree of broken inversion symmetry, the classification of two types of metamaterials would become progressively more difficult. This is because the intervalley scattering becomes larger in the topological metamaterials, resulting in the similar wave propagation in topological and traditional metamaterials [222, 226].

6.5 Conclusion and discussion

In this paper, we provide a guide towards the potential impacts of the application of the DMD method on the wave propagation in topological elastic metamaterials. The analysis of DMD eigenvalues and spectrum shows the oscillation and frequency of the DMD modes. The notable topological interface states and valley pseudospin of the valley system can be reflected by the DMD modes. Furthermore, the reconstruction of topological state propagation is achieved by the low-dimensional model constructed only by the DMD modes inside the bandgap and the corresponding time dynamics. Apart from the fundamental characterization by DMD, we demonstrate the potential that the method bears as concerns the tasks of classification and synthesis of wave propagation along the given interface using DMD modes and associated reduced dynamical descriptions (Appendix E). We find a feature space with particular characteristics to project the DMD modes on for the classification of topological and traditional metamaterials. The synthesis of wave propagation along the given interface can be achieved by the extension and shift of DMD modes, where the l^2-norm error and correlation coefficient are at an acceptable level to visualize the future wave propagation. The DMD provides a data-driven method to explore the wave propagation in topological metamaterials and to reveal the potential topological nature, filling an important research void at the interface of the corresponding fields. It also opens up an avenue to classify and synthesize the wave propagation through a purely data-driven approach.

Naturally, this is only a first step along this direction and raises several questions that still merit further addressing. One key aspect of interest concerns how to reduce the error and overcome the inherent deficiency of DMD. While the results presented herein represent adequate reconstructions (and even synthetic wave propagation along the given interface) of the time evolution dynamics, it would be highly desirable for such examples to match far more adequately, in a quantitative sense, the real system dynamics. From the point of view of applications, it would be relevant to explore the method in other classes of systems including in ones stemming from higher dimensions and to explore how adequately the method can fare in such more data-intensive settings. Additionally, the characterization of the topological metamaterials with different Berry curvatures by DMD can be conducted through the same process. Similar results, such as DMD spectrum, modes and low-dimensional model, are expected but classification between two types of metamaterials can be less efficient as discussed in Section 6.4. Such topics are presently under consideration and associated potential progress will be reported in future publications.

6.6 Author contribution

This chapter is adopted from Shuaifeng Li, Panayotis G. Kevrekidis and Jinkyu Yang, Characterization of elastic topological states using dynamic mode decomposition, *Physical Review B*, 107, 184308, 2023.

S. Li and J. Yang proposed the research; S. Li performed the simulation and modeling; P. G. Kevrekidis and J. Yang provided guidance throughout the research; S. Li and J. Yang prepared the manuscript; P. G. Kevrekidis and J. Yang provided guidance during manuscript preparation and development.

Chapter 7

GEOMETRY-INFORMED DYNAMIC MODE DECOMPOSITION IN ORIGAMI DYNAMICS

Origami structures often serve as the building block of mechanical systems due to their rich static and dynamic behaviors. Experimental observation and theoretical modeling of origami dynamics have been reported extensively, whereas the data-driven modeling of origami dynamics is still challenging due to the intrinsic nonlinearity of the system. In this study, we show how the dynamic mode decomposition (DMD) method can be enhanced by integrating geometry information of the origami structure to model origami dynamics in an efficient and accurate manner. In particular, an improved version of DMD with control, that we term geometry-informed dynamic mode decomposition (giDMD), is developed and evaluated on the origami chain and dual Kresling origami structure to reveal the efficacy and interpretability. We show that giDMD can accurately predict the dynamics of an origami chain across frequencies, where the topological boundary state can be identified by the characteristics of giDMD. Moreover, the periodic intrawell motion can be accurately predicted in the dual origami structure. The type of dynamics in the dual origami structure can also be identified. The model learned by the giDMD also reveals the influential geometrical parameters in the origami dynamics, indicating the interpretability of this method. The accurate prediction of chaotic dynamics remains a challenge for the method. Nevertheless, we expect that the proposed giDMD approach will be helpful towards the prediction and identification of dynamics in complex origami structures, while paving the way to the application to a wider variety of lightweight and deployable structures.

7.1 Introduction

Origami, as an ancient handcrafted paper folding art, captivates not only artists and mathematicians with its exquisite design principles, but also engineers with its enormous (and increasingly leveraged in recent years) potential in engineering applications. By introducing the principles of creasing and folding to the flat materials, origami structures can be formed, which lead to stiffness enhancement [30], negative Poisson's ratio [183, 243] and multistability in the architecture [197, 244, 245]. These developments also inspire further applications in the robotics [185, 188], medical equipment [189, 246], and mechanical metamaterials with unprecedented mechanical properties [187, 247]. Aside from the aforementioned static and quasi-static mechanical properties, origami also possesses rich dynamics that can be used to construct prospective engineering devices for impact mitigation and vibration control, which has been studied using experiments, numerical simulations, and modelings [28, 64, 191, 192, 248].

In recent years, the modeling and analysis of dynamical systems via data-driven approaches have grown in popularity because they require little expert knowledge of the governing equations [249–251]. Specifically, origami nonlinear dynamics have been realized with excellent accuracy by machine learning methods based on neural networks [28]. However, machine learning based on the neural networks is typically computationally intensive and time-consuming at the training stage. Furthermore, the model works as a gigantic black box where the decision processes are difficult to understand and cannot explicitly reveal the underlying physics behind the origami dynamics, despite the fact that a recent study based on the recurrent neural network can mimic the Lyapunov exponent of chaotic origami motions from the hidden layer [28].

Dynamic mode decomposition (DMD), as one of the most effective machine learning techniques, has recently been used in many fields for its simplicity and interpretability [233]. Given the advantages of DMD and relation between DMD and Koopman mode decomposition, DMD is suitable for characterizing various nonlinear physical and biological systems [66]. Originally, DMD was developed to identify spatiotemporal coherent structures from high-dimensional data in the fluid dynamics community [155]. In addition to fluid dynamics, DMD has been successfully applied to the analysis of biological signals and structural dynamics [230, 252, 253], as well as more recently to topological metamaterials [254]. In these studies, DMD features fast computation and excellent interpretability by a series of physically coherent structures. However, as for the systems with control, DMD is not capable of uncovering the role that the control plays in the system. In light of this, DMD with control (DMDc), a variant of DMD, is proposed to relate the state and the control of a system, highlighting the importance of the control and improving the accuracy of the DMD model [229, 255]. On the other hand, DMDc often ends up with low accuracy or failure to model several nonlinear systems [256]. Therefore, it would be worthwhile to investigate an improved version of DMD for origami dynamics given the needs of data-driven modeling in this field and inherent deficiencies in the current DMD formulations.

In our work, we introduce a data-driven framework called geometry-informed dynamic mode decomposition (giDMD), which is capable of capturing spatiotemporal dynamics of the Kresling origami structures under excitation. By integrating the geometry information of origami into the DMDc, it becomes possible to not only demonstrate the high accuracy of our approach compared with the DMDc, but also reveal the role of the geometrical parameters in the dynamics, showcasing the interpretability. This approach can also be applied to more complicated Kresling origami structures: origami chain and dual origami structure. In the origami chain, the dynamics across frequencies can be predicted precisely and the frequency of the topological boundary state is identified from the features of giDMD. In the dual origami structure under the excitation in different frequencies, the intrawell periodic motion is predicted accurately. The interwell periodic motion and chaotic dynamics can be identified from the characteristics of giDMD, yet the latter also poses some limitations (regarding the accuracy of its temporal representation) which are of relevance to consider in future studies. Our approach, which is considerably easier to operate and more interpretable than the machine learning based on the neural networks, offers a general technique to handle the origami dynamics in the presence of geometrical parameters.

7.2 Geometry-informed DMD for Kresling origami

Figure 7.1(a) illustrates the side and top views of the single Kresling origami structure. This single origami structure has two coupled degrees of freedom: translation along the vertical direction u and rotation around vertical direction ϕ, resulting in the rotation of the top surface following the compression of the origami. This coupled behavior is described by a truss model which is composed of the lumped masses and discs connected by the springs. Appendix F shows the governing equations of motion for the origami coupled features. The creasing and folding of the origami structure also introduce numerous geometrical variables which are marked in Figure 7.1. h, a, b, α, β and Ψ represent the height, the length of crease lines, the angles between the crease lines and the vertical direction, and folding angle (the angle between the horizontal plane and facet). During the compression and tension of the origami structure, according to the geometric constraints, these geometrical variables will change as a function of axial and rotational displacement as shown below:

$$h = h_0 - \delta u \tag{7.1}$$

$$a = \sqrt{(h_0 - \delta u)^2 + 4R^2 \sin^2(\frac{\delta\phi}{2} + \frac{\theta_0}{2} - \frac{\pi}{2N})} \tag{7.2}$$

$$b = \sqrt{(h_0 - \delta u)^2 + 4R^2 \sin^2(\frac{\delta\phi}{2} + \frac{\theta_0}{2} + \frac{\pi}{2N})} \tag{7.3}$$

$$\Psi = \arctan \frac{h_0 - \delta u}{R[\cos(\frac{\pi}{N}) - \cos(\delta\phi + \theta_0)]} \tag{7.4}$$

where the δu and $\delta\phi$ represent the differences of axial and rotational displacements between top and bottom surfaces, respectively. h_0, θ_0, R and N are initial height, initial rotation angle representing the chirality, radius and number of vertices of the polygonal cross-section. Accordingly, the angles between the crease lines and the vertical direction can be easily calculated. Under the excitation, axial and rotational displacement will vary over time, hence leading to the variation of geometrical parameters. In Figure 7.1(b), the vector of geometrical parameters for n-th origami element at time t is shown as g_t^n containing h_t^n, a_t^n, b_t^n, Ψ_t^n, α_t^n and β_t^n. Note that the geometrical variables are not limited to the aforementioned six parameters, but can be extended to further geometrical variables potentially present within the origami structures.

DMDc is a data-driven approach to model the systems under control, which includes the scenario that the origami structure is excited by an input (the control). DMDc uses a state transition matrix $\mathbf{A}$ and the control matrix $\mathbf{B}$ to relate the system displacement d_t and the control d_t^c according to:

$$d_{t+1} = \mathbf{A}d_t + \mathbf{B}d_t^c \tag{7.5}$$

Depending on whether $\mathbf{B}$ is known or not, DMDc has different procedures to obtain the model [229]. Herein, we propose a variant that we term geometry-informed DMD based on

DMDc. In particular, we refer to geometry-informed DMD (giDMD) as the DMDc learning framework that integrates underlying knowledge of the origami geometrical variables g_t^n. More concretely, in our present origami setting, we create an augmented state of the n-th origami x_t^n composed of the displacement d_t^n and velocity v_t^n in both axial and rotational directions, resulting in $x_t \in \mathbb{R}^{4n}$. An augmented control y_t^n is also created by concatenating the augmented state of the control and the vector of geometrical parameters, resulting in $y_t \in \mathbb{R}^l$, where l is the number of control variables. The vector of geometrical parameters also includes the trigonometric functions (sine and cosine functions) of quantities related to angles, but for simplicity of depicting our approach in a general way, we do not illustrate them in Figure 7.1(b). A similar idea using the augmented state and control variables can also be found in the modeling of swarm dynamics [255]. Therefore, the system can be modeled in the form:

$$x_{t+1} = x_t + \mathbf{K}y_t \tag{7.6}$$

where $\mathbf{K} \in \mathbb{R}^{4n\times l}$. In giDMD, motivated from the earlier work [255], the state transition matrix $\mathbf{A}$ is assumed to be identity ($\mathbf{A} = \mathbf{I}$) because we assume that the difference between x_{t+1} and x_t ascribes to the contribution of the control. The Equation (7.6) can be rewritten as:

$$x_{t+1} - x_t = \mathbf{K}y_t \tag{7.7}$$

Furthermore, Equation (7.7) can be written in the matrix form:

$$\mathbf{X'} - \mathbf{X} = \mathbf{KY} \tag{7.8}$$

$$\mathbf{S} = \mathbf{KY} \tag{7.9}$$

where $\mathbf{X'} \in \mathbb{R}^{4n\times(T-1)}$ is one snapshot forward compared with $\mathbf{X} \in \mathbb{R}^{4n\times(T-1)}$, $\mathbf{S} = \mathbf{X'} - \mathbf{X}$ and $\mathbf{Y} \in \mathbb{R}^{l\times(T-1)}$ contains m control variables and $(T-1)$ snapshots. T is the total number of snapshots.

Therefore, the matrix $\mathbf{K}$ is the key for giDMD modeling, which can be solved by the optimization problem:

$$\arg\min_{\mathbf{K}} \left[\frac{1}{2}\|\mathbf{S} - \mathbf{KY}\|^2 + \eta R(\mathbf{K})\right] \tag{7.10}$$

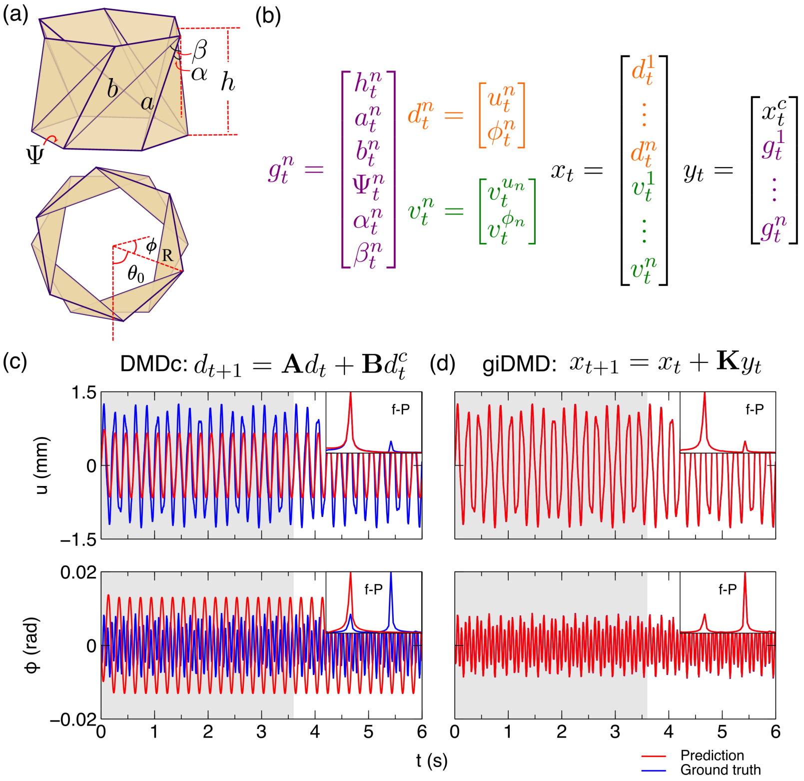

Figure 7.1: Illustration of giDMD and comparison between DMDc and giDMD. (a) The side view and the top view of the single Kresling origami with geometrical parameters. (b) The data matrices for the data-driven framework of giDMD. The geometrical parameters g are collected as the height h, the length of crease lines a, b, folding angle Ψ, the direction of the crease lines α, β. The state x is taken to include the displacement p and velocity v, and the control y is taken to involve the states of the input x^c and the geometrical parameters g. (c) The prediction using DMDc. (d) The prediction using giDMD. The predictions of axial displacement u and rotational displacement ϕ using DMDc are shown in the first and second row, respectively. The gray shaded areas represent the training data. The ground truth and the prediction are shown in blue and red, respectively. The insets in four graphs show the relation between frequency (f) and power amplitude (P) after the fast Fourier transform.

where $R(\cdot)$ is a regularizer that promotes sparsity and η is a hyperparameter to determine the strength of the regularization. A sparse matrix $\mathbf{K}$ can be useful to promote the interpretation of the role geometries play in the origami dynamics and to discover the dominant geometric components. We use the non-convex regularizer, l_0 norm, in our optimization problem, where sequential thresholded least squares method is performed, which is also widely used in the dynamics discovery [257]. l_0 regularization works by encouraging the coefficients of the model below a certain threshold value to be completely ignored and has convergence guarantees [258]. To be specific, first of all, the standard least squares fitting is performed. Then, a parameter η is given to specify the minimum magnitude for coefficients in $\mathbf{K}$ and all coefficients with magnitude below the threshold are zeroed out. This process of fitting and thresholding is performed until convergence. In this way, a sparse matrix $\mathbf{K}$ that balances the tradeoff between accuracy and minimizing the number of the control elements can be obtained. In our examples demonstrated below, the rapid convergence is realized within several iterating steps (at most 1 step for single origami, 2 steps for dual origami structures and 10 steps for origami chain).

Next, we demonstrate the superiority of our method over the standard DMDc. We simulate the dynamics of a single origami element under the harmonic excitation at the frequency of 5 Hz using the truss model, as detailed in Appendix F. Due to the coupled behavior of the origami features, the output is the axial displacement u and rotational displacement ϕ. When the origami dynamics is modeled by DMDc using 60% training data, both predicted displacements $\hat{u}$ and $\hat{\phi}$ exhibit large discrepancies compared with the simulated displacements u and ϕ in Figure 7.1(c). The relative errors calculated by $\frac{\|u-\hat{u}\|_F}{\|u\|_F}$ and $\frac{\|\phi-\hat{\phi}\|_F}{\|\phi\|_F}$ are around 50% and 247% for u and ϕ. In comparison, the significant improvement is achieved by giDMD model, as shown by the agreement between prediction (red lines) and ground truth (blue lines) in Figure 7.1(d). The relative errors for u and ϕ are around 0.26% and 1.37%. This improvement can also be seen in the spectra [insets in Figure 7.1(c) and Figure 7.1(d)] given by the fast Fourier transform. Under the excitation of 5 Hz, there is another peak other than the excitation frequency in the spectrum because of the nonlinearity. In stark contrast with the DMDc, giDMD can predict two peaks in the spectrum, implying that giDMD can fully capture the origami dynamics. The drastic improvement in accuracy in both time and frequency domain demonstrates the effectiveness of giDMD towards modeling origami dynamics.

7.3 Topological boundary states in the origami chain

The effectiveness of our method has emerged in the single origami structure above. Next, we further demonstrate this method on more complex origami structures. The first example we demonstrate our method on is the elastic topological metamaterials built by the origami structure. The elastic topological metamaterials are inspired by the electronic topological insulators, where the vibration is isolated in the bulk yet propagating along the boundary or surface. The topologically protected defect-immune wave propagation in the elastic topological metamaterials has been attracting significant attention [221–223, 225, 259, 260]. Recently, the origami structures have been used as building blocks to construct topological metamaterials [192]. We adopt the existing design to construct the origami chain shown in Figure 7.2(a). The unit cell enclosed by black dashed line contains two origamis with opposite chirality represented by initial rotational angle θ_0.

The band structure can be calculated by the linearized truss model (Appendix F) based on the small amplitude approximation after the application of periodic boundary condition (Bloch's theorem). As shown in Figure 7.2(b), four bands appear in the first Brillouin zone. Two lower bands nearly overlap, and two upper bands are crossing to form a degeneracy point at the edge of the first Brillouin zone. To characterize the topology of this system, we calculate the topological invariant Zak phase for the 1D system. Because the bands are degenerate at the edge of the first Brillouin zone, the topological invariant Zak phase φ for q-th and $(q+1)$-th bands is calculated through the Wilson-loop eigenvalues as indicated below:

$$\varphi_{q,q+1} = -\sum_{k=0}^{k-1} \operatorname{Im} \ln \begin{vmatrix} \langle U_k^q | U_k^q \rangle & \langle U_k^q | U_{k+1}^{q+1} \rangle \\ \langle U_k^{q+1} | U_{k+1}^q \rangle & \langle U_k^{q+1} | U_{k+1}^{q+1} \rangle \end{vmatrix} \tag{7.11}$$

where U_k^q denotes the mode at the Bloch wave vector k for the q-th band [261]. This produces $\varphi_{1,2} = \varphi_{3,4} = \pi$ which are marked in Figure 7.2(b). The nonzero topological invariant of the lower bands also ensures the topologically nontrivial band gap between the lower bands and the upper bands.

According to the bulk-edge correspondence, the topological boundary state will emerge within the band gap in the truncated origami chain. In Figure 7.2(c), the eigenmodes of the truncated origami chain with 16 unit cells is calculated. As expected, two degenerate modes appear within the band gap. After checking the axial and rotational modes of these two degenerate modes shown in Figure 7.2(d), we confirm that these two degenerate modes are topological boundary states due to the concentrated displacement at the boundary.

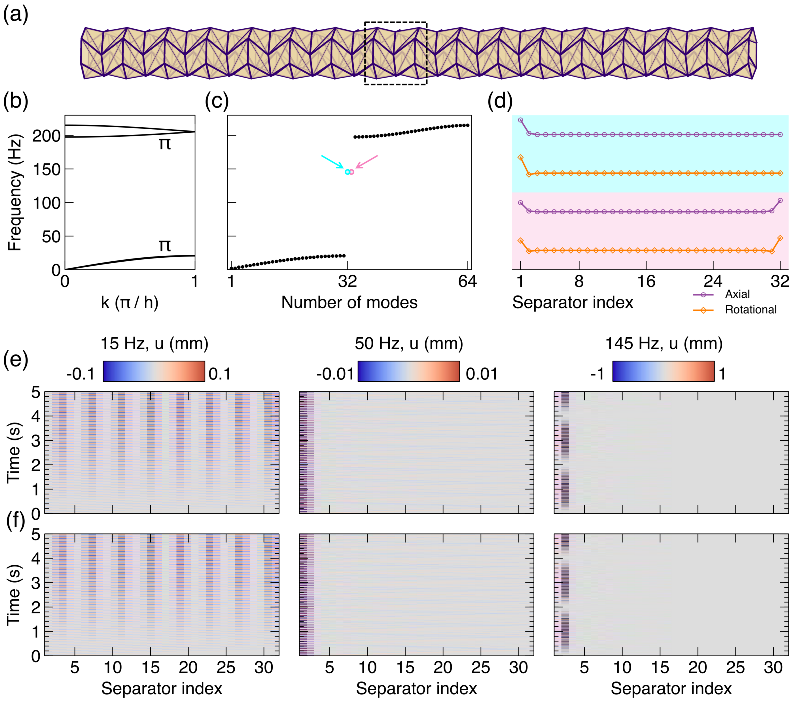

Figure 7.2: Application of giDMD on the origami chain. (a) The schematic of the origami chain composed of Kresling origami with alternating chirality. The design parameters of origami are $h_0 = 30$ mm, $\theta_0 = \pm 70^\circ$, $R = 36$ mm where h_0, θ_0, and R are the initial height, initial rotational angle, and radius of the cross-section, respectively. (b) The band structure calculated by the unit cell enclosed by black dashed line in (a). The Zak phases of the lower band and upper band are π. (c) The modes of the supercell formed by 16 unit cells. The black dots represent the bulk band. The cyan and pink dots represent the topological boundary states within the band gap. (d) The axial and rotational modes of the topological boundary states. (e) The simulated axial displacement along the origami chain at different frequencies in the pass band (15 Hz), stop band (50 Hz) and topological boundary states (145 Hz). (f) The corresponding predicted axial displacement using 60% training data (from 0 s to 3 s).

Then, the wave propagation along the origami chain is calculated by the truss model (Appendix F) using the small-amplitude approximation (i.e., in the linear regime). The axial displacements of each separator over time are illustrated in Figure 7.2(e) under different excitation frequencies, represented by the frequencies in pass band (15 Hz), stop band (50 Hz) and at the topological boundary state (145 Hz). At the frequency of 15 Hz, the vibration can affect the whole origami chain, while the vibration is localized at the boundary at the frequency of 50 Hz, as expected for such a band gap frequency. At the frequency of 145 Hz, where the topological boundary state emerges, the vibration is also localized at the boundary but with larger amplitude, representing the excitation of the corresponding eigenmode.

The giDMD model for the origami chain is put forward using 60% training data (from 0 s to 3 s). The prediction and ground truth agree excellently, as evidenced by the same patterns in Figure 7.2(e) and Figure 7.2(f), and relative error smaller than 0.1% in general. The highly accurate modeling of origami chain across frequencies confirms the ability of giDMD to model complex structures in the nearly linear regime of the corresponding dynamics.

We take the first 31 rows of the $\mathbf{K}$ matrix responsible for the calculation of the axial displacement of each separator in the origami chain. As shown in Figure 7.3(a), the $\mathbf{K}$ matrix is fairly sparse with sparsity around 0.6 (the number of zero values in the matrix divided by the total number of elements in the matrix) for all three cases, where nonzero values are concentrated near the position indicating the information of height h, angles between crease lines and vertical direction α, β, and corresponding sine functions $\sin\alpha$, $\sin\beta$. It suggests that these geometrical variables are mainly important and responsible for the axial displacement of origami chain. Especially, at the frequency of the topological boundary state (145 Hz), the values for $\sin\alpha$, $\sin\beta$ are smaller than those of the other two frequencies, suggesting less importance of these two geometrical variables in forming topological boundary states. This may result from the strong localization of vibrations near the boundary, causing most geometrical variables to remain almost unchanged. Furthermore, the nonzero values shift linearly with the increase of the row of $\mathbf{K}$, indicating that the displacement of each separator is related to geometrical variables of nearest origami elements. Note that the geometry information such as h marked in Figure. 7.3(a) generally indicates the geometrical variables of every origami component.

Similar to the DMD where the eigenvalue of the linear operator can characterize the

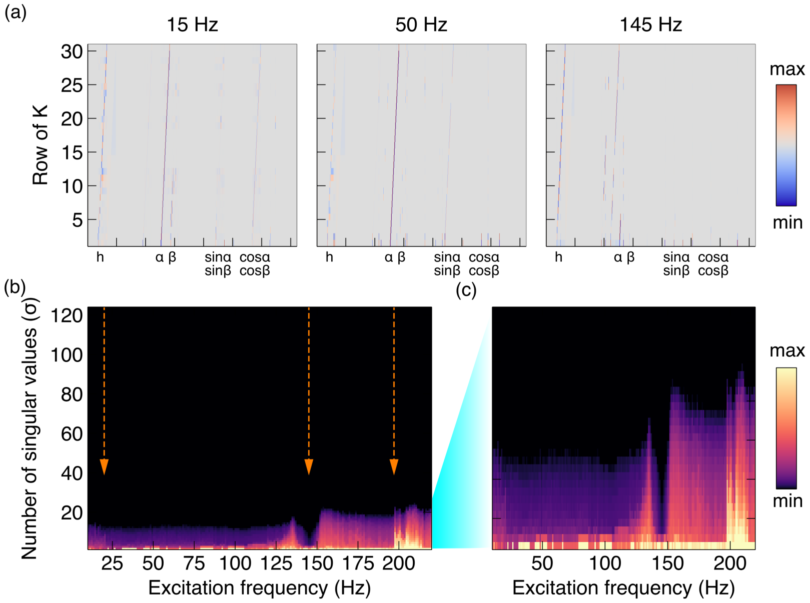

Figure 7.3: Identification of topological boundary states in origami chain. (a) The rows of **K** matrix corresponding to the axial displacements of the origami chain at 15 Hz, 50 Hz and 145 Hz. The corresponding control variables are shown below. (b) The singular value spectrum of **K** matrix under different excitation frequencies from 10 to 220 Hz. The orange dash arrows on two sides indicate the range of the band gap, and one in the middle indicates the frequency of topological boundary states. (c) The zoom-in view by using 32 singular values.

system dynamics, we use the singular values of the **K** matrix to identify the 'state' of the system. The singular value spectra of the **K** matrix from 10 Hz to 220 Hz are shown in Figure 7.3(b) to illustrate the difference. In the region of the pass band ($f \leq 20$ Hz, $f \geq 198$ Hz), the first several singular values are significantly larger than those in the region of stop band (20 Hz $\leq f \leq$ 198 Hz). At the frequency of topological boundary states, the singular values are particularly smaller than any of other frequencies as detailed in zoom-in view in Figure 7.3(c). The smaller singular values at the frequency of topological boundary state may be induced by the absence of contribution from $\sin\alpha$, $\sin\beta$ compared with other frequencies. We also notice that there are smaller singular values around 145 Hz but the smallest one is at 145 Hz. The singular values are large outside 145 Hz and the ones within the band gap region (20 Hz $\leq f \leq$ 198 Hz) are used to describe the localized states near the boundary due to the band gap.

7.4 Dynamic motion in the dual origami structure

The next example is the dual origami structure exhibiting rich dynamic motions under excitation. This structure is composed of two bistable origami elements with opposite chirality as shown in Figure 7.4(a), in which u_0 and ϕ_0 are the input axial and rotational excitations at the first separator, and u_1, ϕ_1 and u_2, ϕ_2 are the axial and rotational displacements at the second and third separators, respectively. In the previously reported experimental study [28], under the excitation in different frequencies, the structure will feature periodic motion ($5-9$ Hz, $14-16$ Hz, 18 Hz, $23-24$ Hz) and chaotic motion ($10-13$ Hz, 17 Hz, $19-22$ Hz). Note that due to combination of two bistable origamis, the periodic motion can be further identified as intrawell periodic motion ($5-9$ Hz, 18 Hz, $23-24$ Hz), and interwell periodic motion ($14-16$ Hz). The intra- and inter- well behaviors are further elaborated in the reference [28]. The experimental setup is shown in Figure 7.4(b) and detailed in Appendix F. Although this structure is simpler than the previous example, it is under the large-amplitude excitation region and hence displays the corresponding hallmarks of nonlinear dynamics, including the above mentioned chaotic motion.

To demonstrate our method, we choose two typical cases where periodic motion and chaotic motion are represented by 5 Hz and 17 Hz, respectively. After obtaining the $\mathbf{K}$ matrix from the sparse regression, where the sparsity of $\mathbf{K}$ matrix is around 0.7, we check the first row of the $\mathbf{K}$ matrix responsible for the calculation of axial displacement u_1. The case for 5 Hz is shown in Figure 7.4(c). The first row of the $\mathbf{K}$ matrix is sparse so that nonzero values only appear in several positions standing for the information of h, a, Ψ, α, β, sine and cosine functions of α and β, suggesting that these geometrical variables are responsible for the axial motion of the second separator. In comparison, at the frequency of 17 Hz, nonzero values emerge in similar positions but with much smaller values in Figure 7.4(d). Besides, the sine and cosine functions of α and β are contributing less to the axial motion of the second separator due to the smaller values than other geometrical variables. Compared with the origami chain where the length of crease lines and the folding angle do not significantly contribute to the axial displacement, in the present case, the length of crease lines and folding angle are major contributions to the axial displacement for the dual origami structure. The possible reason can be the smaller amplitude excitation (i.e., linear regime) of the origami chain, leading to the representation of a, b and Ψ by the function of h. After sparse regression, the contributions of a, b and Ψ can be approximated by h, whereas large-amplitude excitation (nonlinear regime) in dual origami structure results in the failure to represent a, b and Ψ using h. Similar to the analysis of $\mathbf{K}$ matrix in Section 7.3, the geometry information marked in Figure. 7.4(c) generally indicates the geometrical variables of two origami components.

We then predict the axial displacements u_1 and u_2 at the frequency of 5 Hz and 17 Hz. As shown in Figure 7.4(e), the prediction and ground truth agree excellently with 60% training data, as evidenced by the overlap of red curves and blue curves. In stark contrast, the predictions at the frequency of 17 Hz do not match with the ground truth in a precise manner [Figure 7.4(f)]. Although the sudden change in the chaotic motion cannot be predicted, the predicted results still show clear differences from the periodic motion [Figure 7.4(e)], i.e., they carry the blueprint of the observed chaotic dynamics. Therein, u_1 is more chaotic than u_2 and thus the prediction is better in u_2. Note that the prediction results of intrawell periodic motion at other frequencies are similar to the Figure 7.4(e), while the ones of chaotic motion at other frequencies are similar to the Figure 7.4(f).

The spectral analysis is conducted to show the frequency response under the excitation in different frequencies. In Figure 7.5(a), the spectra for u_1 and u_2 in different frequencies are obtained by the fast Fourier transform of the experimental data after normalization. It is obvious that along the diagonal direction of each panel, there are responses at the same frequency as the excitation frequency. Apart from that, the periodic motion and the chaotic motion can be clearly identified from the increase of lower frequency components. The ‘state’ of the structure is also marked in Figure 7.5(a) and Figure 7.5(b), where green, orange and purple shaded areas indicate the intrawell periodic motion, interwell periodic motion and chaotic motion. Figure 7.5(b) illustrates the spectra for u_1 and u_2 based on the prediction results. It can be seen that the spectra in the region of intrawell periodic motion ($5 - 9$ Hz, 18 Hz, $23 - 24$ Hz) agree with the ground truth excellently. However, giDMD fails to predict the interwell periodic motion ($14 - 16$ Hz), where the predictions

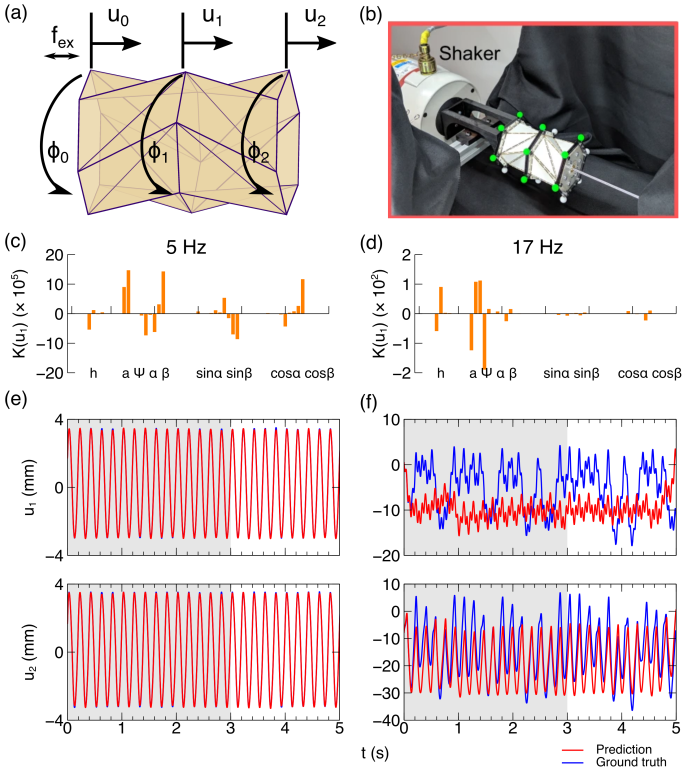

Figure 7.4: Application of giDMD on the dual origami structure. (a) The schematic of the dual origami structure with opposite chirality. (b) The image of experimental setup for the vibration test from the reference. Copyright 2020 Springer Nature. The design parameters of origami are $h_0 = 50$ mm, $\theta_0 = \pm 70°$, $R = 36$ mm where h_0, θ_0, and R are the initial height, initial rotational angle, and radius of the cross-section, respectively. The input excitation is applied by a shaker, and the motions are captured by two action cameras and quantified by the digital image correlation program. (c)(d) The row of $\mathbf{K}$ matrix corresponding to the axial displacement u_1 at the frequency of 5 Hz and 17 Hz, respectively. The corresponding control variables are shown below. (e) The prediction of axial displacement u_1 and u_2 using giDMD at the frequency of 5 Hz. (f) The prediction of axial displacement u_1 and u_2 using giDMD at the frequency of 17 Hz. The gray shaded areas represent the training data. The ground truth is shown in blue and the prediction is shown in red.

blow up to infinity at some time point, resulting in the failure of spectral analysis. The interwell periodic motion describes the scenario where u_1 and u_2 feature a large difference, as well as ϕ_1 and ϕ_2, i.e., in the regime of significant axial and rotational differences across origami separators. In such case, the blow-up phenomena in the prediction are due to the unstable dynamical system produced by the giDMD model. Understanding how to extend the giDMD approach to capture such a scenario remains an interesting open question for further investigation. In the region of chaotic motion ($10-13$ Hz, 17 Hz, $19-22$ Hz), the spectra from the predicted results show qualitative agreement with the ground truth featured by the increased magnitude in the low frequency range, despite the failure to capture the intermittent variation in chaotic motion as shown in Figure 7.4(f). These findings imply that giDMD can predict the chaotic motion to some extent.

Similar to the section 7.3, we study the $\mathbf{K}$ matrix to identify the 'state' of the dual origami structure. Figure 7.5(c) shows the singular values σ of the $\mathbf{K}$ matrix at different frequencies, where different singular value spectra appear in different frequencies. We notice that in the frequency range corresponding to the chaotic motion, the singular values are particularly smaller than others. To characterize the origami dynamics, the Lyapunov exponents for u_1 and u_2 are shown by bright green and dark green in Figure 7.5(c), calculated by the Rosenstein's method [262]. As is well-known, the larger Lyapunov exponent suggests more chaotic dynamics. From our results, we can deduce that smaller singular values correspond to larger Lyapunov exponent. In Figure 7.5(d), we choose the second singular value of each $\mathbf{K}$ matrix σ_2 to compare with Lyapunov exponents for u_1 (top panel) and u_2 (bottom panel). It is noticed that there are clear boundaries among chaotic motion (smallest values), interwell periodic motion and intrawell periodic motion (largest values). Besides, there is the fairly strong relation characterized by the distance correlation (quotient of the distance covariance and the product of the distance standard deviations) between logarithm-scaled second singular values and Lyapunov exponents, resulting in $dCor = 0.7628$ and $dCor = 0.5649$ for u_1 and u_2. The correlation between the singular values and Lyapunov exponent of the dynamics system has not only emerged in our data-driven study, but also in several theoretical studies to calculate Lyapunov exponent [263, 264]. Therefore, from the singular values of $\mathbf{K}$, one can identify intrawell, or interwell periodic motion or the chaotic motion of the dual origami structure.

7.5 Conclusion and discussion

The $\mathbf{K}$ matrix serves as the control matrix in the giDMD, which will convert the control $\mathbf{Y}$ to $\mathbf{S}$, expressed by $\mathbf{S} = \mathbf{X} - \mathbf{X}'$. Since the state $\mathbf{X}$ corresponds to the displacement

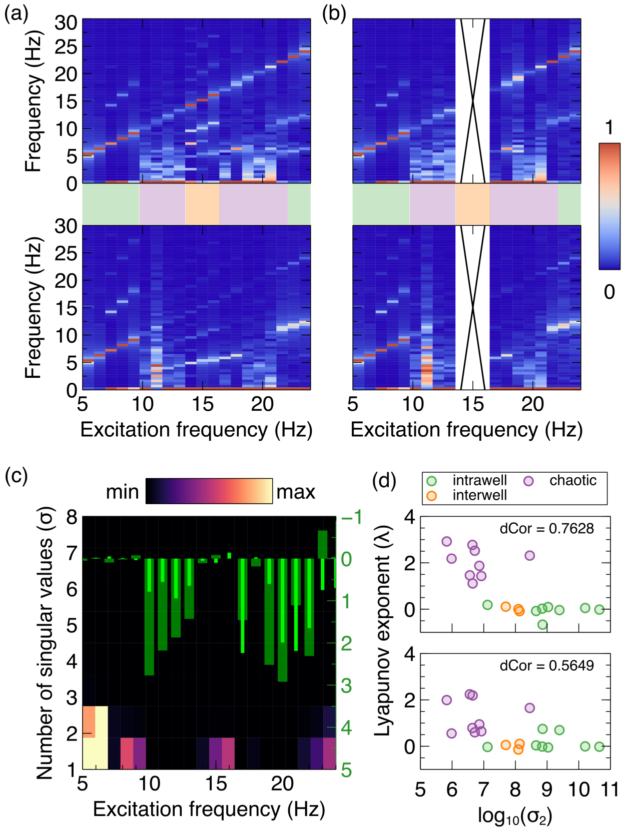

Figure 7.5: Identification of intrawell periodic, interwell periodic and chaotic motion. (a) The spectrum analysis of the experimental axial displacements u_1 (the first panel) and u_2 (the second panel) under different excitation frequencies from 5 to 24 Hz. (b) The corresponding spectral analysis based on the predicted axial displacements u_1 (the first panel) and u_2 (the second panel). The white area with a cross represents the failure of the prediction. The green, orange and purple shaded areas represent the frequencies of intrawell periodic motion, interwell periodic motion and chaotic motion. (c) The singular value spectrum of **K** matrix under different excitation frequencies from 5 to 24 Hz. The Lyapunov exponents of u_1 and u_2 under different excitation frequencies are also shown in dark green and bright green, respectively. (d) The relation between the second singular values σ_2 and the Lyapunov exponents λ under different excitation frequencies. The intrawell periodic motion, interwell periodic motion and chaotic motion are represented in green, orange and purple circles. The distance correlation between logarithm-scale second singular values and Lyapunov exponents are shown in both graphs.

and velocity of each separator at each time step, **S** contains the information of velocity and acceleration. Essentially, **K** is found to describe the velocity and acceleration using geometrical parameters in origami structures. The sparsity of $\mathbf{K}$ matrix shows that the velocity and acceleration of the origami structure are only related to a few geometrical parameters. This can also be implied by the governing equation of motion of origami as shown in the Appendix F and derived equations. These governing equations of motion of origami contain the combination of geometrical parameters explicitly or implicitly. $\mathbf{K}$ matrix essentially selects the geometrical parameters in the $\mathbf{Y}$ matrix, resulting in the approximated forms of governing equations of origami motion. This is the reason why giDMD works well in origami dynamics and is only related to the several geometrical variables, resulting in the sparse $\mathbf{K}$ matrix. In a sense, one can argue that the material in Appendix F represents the traditional modeling approach (based on constitutive laws) towards the origami system of interest, while the giDMD represents a modern, data-driven variant thereof. Indeed, our method, from the idea of dynamics discovery using sparse regression, is quite similar to the sparse identification of nonlinear dynamics (SINDy) [257]. The sparse $\mathbf{K}$ in giDMD and the sparse $\mathbf{\Xi}$ in SINDy both serve to select the active terms in the library (control variables in giDMD and candidate functions in SINDy). However, there are some differences. In SINDy, there exists an extensive library of candidate functions that is provided as a possible basis to represent the dynamics, while $\mathbf{Y}$ in giDMD only contains the origami geometrical variables. Moreover, the exact velocity and acceleration of the system are used in the SINDy, while $\mathbf{S}$ in giDMD, motivated by the DMDc approach, is composed of the difference of displacement and the difference of velocity, which is different from the implementation of SINDy. Furthermore, our method can also be interpreted by the mode superposition, since the individual entries k_{ij} of $\mathbf{K}$ matrix can be expressed as $k_{ij} = \mathbf{u}_j^T \mathbf{\Sigma}^{-1} \mathbf{V}^T \mathbf{s}_i$ after the singular value decomposition, $\mathbf{Y} = \mathbf{U}\mathbf{\Sigma}\mathbf{V}^T$, where $\mathbf{u}_j^T$ is the j-th row of $\mathbf{U}$ and $\mathbf{s}_i^T$ is the i-th row of $\mathbf{S}$. This results in different $\mathbf{K}$ matrix in the same origami structure under different frequencies. For the consistency of the narrative, we fix the training ratio to be 60% in the main text, but we also show the giDMD modeling in other training ratios in Appendix F and Appendix F including error analysis and identification of states of origami structures. Our approach demonstrates the efficacy in different training ratios and the ability to identify origami dynamics.

In this work, we propose the method of giDMD to learn the origami dynamics that gives rise to origami coupled motions from pure observation data (experiment data and simulation data). We show the better performance of giDMD characterized by the prediction accuracy compared with DMDc. In the two example origami structures we apply our method on, giDMD can not only predict the origami behaviors under different frequencies, but also highlight an ability to identify the 'state' of origami structures. Furthermore, giDMD offers the insights into the importance of geometries in the governing motion law of origami. giDMD has better performance in the linear (or nearly linear) region of origami dynamics, while there are still some challenges in describing chaotic dynamics within the nonlinear regime. In the latter, giDMD starts to fail in connection to the goal of accurate prediction, but it can still help with the identification of the origami state. The giDMD provides a substantial capability to model origami dynamics in an efficient (fast computation) and interpretable way. Although we primarily demonstrate our method on two specific structures, the studied origami structures can be more complex across scales and not limited to the Kresling origami in the future work. Indeed, the further extension of giDMD to other such geometrically nonlinear systems is a topic currently under active investigation and relevant results will be reported in due course.

7.6 Author contribution

This chapter is adopted from Shuaifeng Li, Yasuhiro Miyazawa, Koshiro Yamaguchi, Panayotis G. Kevrekidis and Jinkyu Yang, Geometry-informed dynamic mode decomposition in origami dynamics, arXiv:2303.04323, 2023 (under review).

S. Li and J. Yang proposed the research; S. Li performed the simulation and modeling; P. G. Kevrekidis and J. Yang provided guidance throughout the research; S. Li and J. Yang prepared the manuscript; Y. Miyazawa, K. Yamaguchi, P. G. Kevrekidis and J. Yang provided guidance during manuscript preparation and development.

Chapter 8

CONCLUSION AND FUTURE CHALLENGES

Through a series of studies, we successfully characterize and model the spatiotemporal behaviors in corals, elastic metamaterials and origami by experimental observation, data analysis and theoretical/data-driven modeling, which have yielded significant insights into the underlying physics and dynamics of these systems. In the natural system represented by corals, we find the universal law in the spatiotemporal behaviors of corals: the interplay between deterministic law and stochastic processes. Generally speaking, motions of coral tissues, polyps and tentacles are all stochastic processes arising from inherent biotic factors, which cannot be predicted and modeled accurately. However, they also show certain statistical patterns in their characteristics, which is governed by the deterministic law, such as statistical distribution of displacement and larger motion amplitude at nighttime on the coral tissues, $1/f^{2H+1}$ fractional Brownian motion of coral polyps, and $1/f$-type motion and pulsation motion of coral tentacles. It is noted that this general phenomenon is not only found in coral ecosystems, but also in many other biological systems. This finding may provide a novel perspective on how to model spatiotemporal behaviors in a biological system.

In the artificial systems represented by elastic metamaterials and origami, In the numerical and theoretical way, we present the realization of Landau level in the origami metamaterials. In the data-driven way, we study how to use DMD to not only model the wave dynamics and structural dynamics, but also extract the information about underlying physics and dynamics from the characteristics of DMD and giDMD. The topological nature and frequency response of elastic metamaterials can be revealed from pure data. Low-dimensional model qualitatively describing the topological state propagation is put forward based on DMD. The nonlinear dynamics of origami is modeled by a new approach, giDMD, which accurately predicts the origami dynamics in various origami structures and identifies the type of dynamics. Our approach to addressing spatiotemporal behaviors in elastic metamaterials and origami paves the way to characterizing and modeling more mechanical systems.

However, there still exist some limitations in our works and challenges to be addressed in the future, as detailed in the following:

1. Although we successfully characterize and model the spatiotemporal behaviors in corals in terms of motions of tissues, polyps and tentacles, the functions of these motions and the reason why the motions follow certain rules still remain mysteries to us. So far, we can only speculate the motion of coral tissue may be related to the nutrition transfer inside the coral and is more active at night. We can also deduce that the motion of coral polyps is related to the prey searching because the fractional Brownian motion is a excellent search strategy statistically. Likewise, the $1/f$-type motion and pulsation motion of pulsating soft coral tentacles are beneficial to the food searching and photosynthesis, respectively. Nonetheless, our speculations do not have enough previous or current biological experiments to verify. The future efforts can be devoted to the relation between biological functions and spatiotemporal behaviors of corals with the collaboration with marine biologists.

2. Despite the fact that the model from DMD can describe the topological state propagation in topological elastic metamaterials, the inherent deficiency of DMD hinders the quantitative description of the wave propagation. While the similarity between model and ground truth is acceptable, the relative error is large. The transient phenomenon including wave propagation is always a drawback in DMD, though we show the noticeable improvement by DMD with time-delay embedding. The future effort can be devoted to finding DMD variants or another data-driven method to build a model for wave propagation in a quantitative manner.

3. Our new approach, giDMD, developed based on the DMD, can excellently model the origami dynamics. When the dynamics is within the linear regime and nearly linear regime, this approach works well. However, when the excitation amplitude becomes larger to push the dynamics to the highly nonlinear regime, giDMD fails to predict the

> dynamics in an accurate manner. Moreover, giDMD cannot ensure the model with stable dynamics, implying that the system will probably blow up at some time point. This has already confirmed in the interwell periodic motion in dual origami structures. Therefore, how to accurately model the nonlinear (especially highly nonlinear) origami dynamics and how to ensure the generation of the stable dynamics from data-driven methods are challenges to be addressed, which can be promising research directions in the future.

Our systematic methodology including experimental techniques, data analysis and modeling techniques, can also be used to characterize and model spatiotemporal behaviors in other systems beyond those studied in current work, such as human behaviors and transportation engineering. We anticipate that our work can inspire more discoveries into the underlying physics and dynamics of spatiotemporal behaviors.

BIBLIOGRAPHY

1. Richter, C. P. Animal behavior and internal drives. *The Quarterly Review of Biology* **2,** 307–343 (1927).
2. Rusak, B. & Zucker, I. Biological rhythms and animal behavior. *Annual review of psychology* **26,** 137–171 (1975).
3. Prusinkiewicz, P. Modeling plant growth and development. *Current opinion in plant biology* **7,** 79–83 (2004).
4. Cavagna, A. & Giardina, I. Bird flocks as condensed matter. *Annu. Rev. Condens. Matter Phys.* **5,** 183–207 (2014).
5. Parrish, J. K. & Edelstein-Keshet, L. Complexity, pattern, and evolutionary trade-offs in animal aggregation. *Science* **284,** 99–101 (1999).
6. Emlen, J. T. Flocking behavior in birds. *The Auk* **69,** 160–170 (1952).
7. Reynolds, C. W. *Flocks, herds and schools: A distributed behavioral model* in *Proceedings of the 14th annual conference on Computer graphics and interactive techniques* (1987), 25–34.
8. Bajec, I. L. & Heppner, F. H. Organized flight in birds. *Animal Behaviour* **78,** 777–789 (2009).
9. Holway, D. A. & Suarez, A. V. Animal behavior: an essential component of invasion biology. *Trends in ecology & evolution* **14,** 328–330 (1999).
10. Went, F. The effect of temperature on plant growth. *Annual Review of Plant Physiology* **4,** 347–362 (1953).
11. Chen, Z. *et al.* Spatial–temporal short-term traffic flow prediction model based on dynamical-learning graph convolution mechanism. *Information Sciences* **611,** 522–539 (2022).

12. Avila, A. M. & Mezić, I. Data-driven analysis and forecasting of highway traffic dynamics. *Nature communications* **11,** 2090 (2020).

13. Vlahogianni, E. I., Karlaftis, M. G. & Golias, J. C. Short-term traffic forecasting: Where we are and where we're going. *Transportation Research Part C: Emerging Technologies* **43,** 3–19 (2014).

14. Graff, K. F. *Wave motion in elastic solids* (Courier Corporation, 2012).

15. Kraut, E. A. Advances in the theory of anisotropic elastic wave propagation. *Reviews of Geophysics* **1,** 401–448 (1963).

16. Kerschen, G., Worden, K., Vakakis, A. F. & Golinval, J.-C. Past, present and future of nonlinear system identification in structural dynamics. *Mechanical systems and signal processing* **20,** 505–592 (2006).

17. Lin, R. & Wang, W. Structural dynamics of microsystems—current state of research and future directions. *Mechanical systems and signal processing* **20,** 1015–1043 (2006).

18. Ainsworth, T. D., Thurber, R. V. & Gates, R. D. The future of coral reefs: a microbial perspective. *Trends in ecology & evolution* **25,** 233–240 (2010).

19. Saxena, A. Coral reefs and their conservation—a review. *Biological and Chemical Research,* 187–206 (2015).

20. Hughes, T. P. *et al.* Global warming and recurrent mass bleaching of corals. *Nature* **543,** 373–377 (2017).

21. Hughes, T. P. *et al.* Global warming transforms coral reef assemblages. *Nature* **556,** 492–496 (2018).

22. Bellwood, D. R., Hughes, T. P., Folke, C. & Nyström, M. Confronting the coral reef crisis. *Nature* **429,** 827–833 (2004).

23. Downs, C. A. *et al.* Cellular pathology and histopathology of hypo-salinity exposure on the coral Stylophora pistillata. *Science of the Total Environment* **407,** 4838–4851 (2009).

24. Pernice, M. *et al.* A single-cell view of ammonium assimilation in coral–dinoflagellate symbiosis. *The ISME journal* **6,** 1314–1324 (2012).

25. Tchernov, D. *et al.* Membrane lipids of symbiotic algae are diagnostic of sensitivity to thermal bleaching in corals. *Proceedings of the National Academy of Sciences* **101,** 13531–13535 (2004).

26. Blank, R. Cell architecture of the dinoflagellate Symbiodinium sp. inhabiting the Hawaiian stony coral Montipora verrucosa. *Marine Biology* **94,** 143–155 (1987).

27. Uwizeye, C. *et al.* In-cell quantitative structural imaging of phytoplankton using 3D electron microscopy. *BioRxiv,* 2020–05 (2020).

28. Yasuda, H. *et al.* Data-driven prediction and analysis of chaotic origami dynamics. *Communications Physics* **3,** 1–8 (2020).

29. Tsimring, L. S. Noise in biology. *Reports on Progress in Physics* **77,** 026601 (2014).

30. Filipov, E. T., Tachi, T. & Paulino, G. H. Origami tubes assembled into stiff, yet reconfigurable structures and metamaterials. *Proceedings of the National Academy of Sciences* **112,** 12321–12326 (2015).

31. Koehler, J. & Kuenzer, C. Forecasting spatio-temporal dynamics on the land surface using earth observation data—A review. *Remote Sensing* **12,** 3513 (2020).

32. Wikle, C. K. & Zammit-Mangion, A. Statistical Deep Learning for Spatial and Spatiotemporal Data. *Annual Review of Statistics and Its Application* **10,** 247–270 (2023).

33. Wang, S., Cao, J. & Yu, P. Deep learning for spatio-temporal data mining: A survey. *IEEE transactions on knowledge and data engineering* (2020).

34. Alassaf, A. & Fan, L. *Dynamic mode decomposition in various power system applications* in *2019 North American Power Symposium (NAPS)* (2019), 1–6.

35. Le Clainche, S., Vega, J. M. & Soria, J. Higher order dynamic mode decomposition of noisy experimental data: The flow structure of a zero-net-mass-flux jet. *Experimental Thermal and Fluid Science* **88,** 336–353 (2017).

36. Le Clainche, S. & Vega, J. M. Analyzing nonlinear dynamics via data-driven dynamic mode decomposition-like methods. *Complexity* **2018,** 1–21 (2018).
37. Raz-Bahat, M., Erez, J. & Rinkevich, B. In vivo light-microscopic documentation for primary calcification processes in the hermatypic coral Stylophora pistillata. *Cell and tissue research* **325,** 361–368 (2006).
38. Venn, A. A., Bernardet, C., Chabenat, A., Tambutté, E. & Tambutté, S. Paracellular transport to the coral calcifying medium: effects of environmental parameters. *Journal of Experimental Biology* **223,** jeb227074 (2020).
39. Laissue, P. P., Roberson, L., Gu, Y., Qian, C. & Smith, D. J. Long-term imaging of the photosensitive, reef-building coral Acropora muricata using light-sheet illumination. *Scientific reports* **10,** 1–12 (2020).
40. Levy, O., Dubinsky, Z. & Achituv, Y. Photobehavior of stony corals: responses to light spectra and intensity. *Journal of Experimental Biology* **206,** 4041–4049 (2003).
41. Levy, O., Dubinsky, Z., Achituv, Y. & Erez, J. Diurnal polyp expansion behavior in stony corals may enhance carbon availability for symbionts photosynthesis. *Journal of experimental marine biology and ecology* **333,** 1–11 (2006).
42. Schlichter, D. Epidermal nutrition of the alcyonarian Heteroxenia fuscescens (Ehrb.): absorption of dissolved organic material and lost endogenous photosynthates. *Oecologia* **53,** 40–49 (1982).
43. Lewis, J. B. Feeding behaviour and feeding ecology of the Octocorallia (Coelenterata: Anthozoa). *Journal of Zoology* **196,** 371–384 (1982).
44. Fabricius, K. & Klumpp, D. Widespread mixotrophy in reef-inhabiting soft corals: the influence of depth, and colony expansion and contraction on photosynthesis. *Marine Ecology Progress Series* **125,** 195–204 (1995).
45. Lapid, E. D., Wielgus, J. & Chadwick-Furman, N. E. Sweeper tentacles of the brain coral Platygyra daedalea: induced development and effects on competitors. *Marine Ecology Progress Series* **282,** 161–171 (2004).

46. Malul, D., Holzman, R. & Shavit, U. Coral tentacle elasticity promotes an out-of-phase motion that improves mass transfer. *Proceedings of the Royal Society B* **287,** 20200180 (2020).

47. Shapiro, O. H. *et al.* Vortical ciliary flows actively enhance mass transport in reef corals. *Proceedings of the National Academy of Sciences* **111,** 13391–13396 (2014).

48. Pacherres, C. O., Ahmerkamp, S., Schmidt-Grieb, G. M., Holtappels, M. & Richter, C. Ciliary vortex flows and oxygen dynamics in the coral boundary layer. *Scientific reports* **10,** 7541 (2020).

49. Codling, E. A., Plank, M. J. & Benhamou, S. Random walk models in biology. *Journal of the Royal society interface* **5,** 813–834 (2008).

50. Krapf, D. *et al.* Spectral content of a single non-Brownian trajectory. *Physical Review X* **9,** 011019 (2019).

51. Zhou, X., Liu, X. & Hu, G. Elastic metamaterials with local resonances: an overview. *Theoretical and Applied Mechanics Letters* **2,** 041001 (2012).

52. Valipour, A., Kargozarfard, M. H., Rakhshi, M., Yaghootian, A. & Sedighi, H. M. Metamaterials and their applications: an overview. *Proceedings of the Institution of Mechanical Engineers, Part L: Journal of Materials: Design and Applications* **236,** 2171–2210 (2022).

53. Bertoldi, K., Vitelli, V., Christensen, J. & Van Hecke, M. Flexible mechanical metamaterials. *Nature Reviews Materials* **2,** 1–11 (2017).

54. Turner, N., Goodwine, B. & Sen, M. A review of origami applications in mechanical engineering. *Proceedings of the Institution of Mechanical Engineers, Part C: Journal of Mechanical Engineering Science* **230,** 2345–2362 (2016).

55. Ren, X., Das, R., Tran, P., Ngo, T. D. & Xie, Y. M. Auxetic metamaterials and structures: a review. *Smart materials and structures* **27,** 023001 (2018).

56. Liang, E. *et al.* Negative thermal expansion: Mechanisms and materials. *Frontiers of Physics* **16,** 53302 (2021).

57. Yu, X., Zhou, J., Liang, H., Jiang, Z. & Wu, L. Mechanical metamaterials associated with stiffness, rigidity and compressibility: A brief review. *Progress in Materials Science* **94,** 114–173 (2018).

58. Ji, J., Luo, Q. & Ye, K. Vibration control based metamaterials and origami structures: A state-of-the-art review. *Mechanical Systems and Signal Processing* **161,** 107945 (2021).

59. Dalela, S., Balaji, P. & Jena, D. A review on application of mechanical metamaterials for vibration control. *Mechanics of advanced materials and structures* **29,** 3237–3262 (2022).

60. Huang, H., Chen, J. & Huo, S. Recent advances in topological elastic metamaterials. *Journal of Physics: Condensed Matter* **33,** 503002 (2021).

61. Pal, R. K., Vila, J. & Ruzzene, M. Topologically protected edge states in mechanical metamaterials. *Advances in Applied Mechanics* **52,** 147–181 (2019).

62. Xin, L., Siyuan, Y., Harry, L., Minghui, L. & Yanfeng, C. Topological mechanical metamaterials: A brief review. *Current Opinion in Solid State and Materials Science* **24,** 100853 (2020).

63. Yasuda, H., Chong, C., Charalampidis, E. G., Kevrekidis, P. G. & Yang, J. Formation of rarefaction waves in origami-based metamaterials. *Physical Review E* **93,** 043004 (2016).

64. Yasuda, H. *et al.* Origami-based impact mitigation via rarefaction solitary wave creation. *Science advances* **5,** eaau2835 (2019).

65. Koopman, B. O. & Neumann, J. v. Dynamical systems of continuous spectra. *Proceedings of the National Academy of Sciences* **18,** 255–263 (1932).

66. Kutz, J. N., Brunton, S. L., Brunton, B. W. & Proctor, J. L. *Dynamic mode decomposition: data-driven modeling of complex systems* (SIAM, 2016).

67. Hemati, M. S., Rowley, C. W., Deem, E. A. & Cattafesta, L. N. De-biasing the dynamic mode decomposition for applied Koopman spectral analysis of noisy datasets. *Theoretical and Computational Fluid Dynamics* **31,** 349–368 (2017).

68. Dawson, S. T., Hemati, M. S., Williams, M. O. & Rowley, C. W. Characterizing and correcting for the effect of sensor noise in the dynamic mode decomposition. *Experiments in Fluids* **57,** 1–19 (2016).

69. Azencot, O., Yin, W. & Bertozzi, A. Consistent dynamic mode decomposition. *SIAM Journal on Applied Dynamical Systems* **18,** 1565–1585 (2019).

70. Askham, T. & Kutz, J. N. Variable projection methods for an optimized dynamic mode decomposition. *SIAM Journal on Applied Dynamical Systems* **17,** 380–416 (2018).

71. Hernandez-Agreda, A., Gates, R. D. & Ainsworth, T. D. Defining the core microbiome in corals' microbial soup. *Trends in microbiology* **25,** 125–140 (2017).

72. Alvarez-Filip, L., Estrada-Saldívar, N., Pérez-Cervantes, E., Molina-Hernández, A. & González-Barrios, F. J. A rapid spread of the stony coral tissue loss disease outbreak in the Mexican Caribbean. *PeerJ* **7,** e8069 (2019).

73. Zaneveld, J. R. *et al.* Overfishing and nutrient pollution interact with temperature to disrupt coral reefs down to microbial scales. *Nature communications* **7,** 11833 (2016).

74. Nguyen, A. *et al.* Impact of recent coastal development and human activities on Nha Trang Bay, Vietnam: evidence from a Porites lutea geochemical record. *Coral Reefs* **32,** 181–193 (2013).

75. Rosenberg, Y., Doniger, T. & Levy, O. Sustainability of coral reefs are affected by ecological light pollution in the Gulf of Aqaba/Eilat. *Communications Biology* **2,** 289 (2019).

76. Mollica, N. R. *et al.* Ocean acidification affects coral growth by reducing skeletal density. *Proceedings of the National Academy of Sciences* **115,** 1754–1759 (2018).

77. Kamenos, N. A. & Hennige, S. J. Reconstructing four centuries of temperature-induced coral bleaching on the Great Barrier Reef. *Frontiers in Marine Science,* 283 (2018).

78. Bessell-Browne, P., Negri, A. P., Fisher, R., Clode, P. L. & Jones, R. Impacts of light limitation on corals and crustose coralline algae. *Scientific Reports* **7,** 11553 (2017).

79. Wijgerde, T. *et al.* Red light represses the photophysiology of the scleractinian coral Stylophora pistillata. *PLoS one* **9,** e92781 (2014).

80. Wijgerde, T., Silva, C. I., Scherders, V., van Bleijswijk, J. & Osinga, R. Coral calcification under daily oxygen saturation and pH dynamics reveals the important role of oxygen. *Biology open* **3,** 489–493 (2014).

81. Abdo, D. A., Bellchambers, L. M. & Evans, S. N. Turning up the heat: increasing temperature and coral bleaching at the high latitude coral reefs of the Houtman Abrolhos Islands (2012).

82. Kremien, M., Shavit, U., Mass, T. & Genin, A. Benefit of pulsation in soft corals. *Proceedings of the National Academy of Sciences* **110,** 8978–8983 (2013).

83. Samson, J. E. *et al.* A novel mechanism of mixing by pulsing corals. *Journal of Experimental Biology* **222,** jeb192518 (2019).

84. Price, D. M. *et al.* Using 3D photogrammetry from ROV video to quantify cold-water coral reef structural complexity and investigate its influence on biodiversity and community assemblage. *Coral Reefs* **38,** 1007–1021 (2019).

85. Rossi, P., Castagnetti, C., Capra, A., Brooks, A. J. & Mancini, F. Detecting change in coral reef 3D structure using underwater photogrammetry: critical issues and performance metrics. *Applied Geomatics* **12,** 3–17 (2020).

86. Pan, B. Digital image correlation for surface deformation measurement: historical developments, recent advances and future goals. *Measurement Science and Technology* **29,** 082001 (2018).

87. Tamada, A. & Igarashi, M. Revealing chiral cell motility by 3D Riesz transform-differential interference contrast microscopy and computational kinematic analysis. *Nature Communications* **8,** 2194 (2017).

88. Westerweel, J., Elsinga, G. E. & Adrian, R. J. Particle image velocimetry for complex and turbulent flows. *Annual Review of Fluid Mechanics* **45,** 409–436 (2013).

89. Wadhwa, N., Rubinstein, M., Durand, F. & Freeman, W. T. Phase-based video motion processing. *ACM Transactions on Graphics (TOG)* **32,** 1–10 (2013).

90. Wu, H.-Y. *et al.* Eulerian video magnification for revealing subtle changes in the world. *ACM transactions on graphics (TOG)* **31,** 1–8 (2012).
91. Wang, J., Drucker, S. M., Agrawala, M. & Cohen, M. F. The cartoon animation filter. *ACM transactions on graphics (TOG)* **25,** 1169–1173 (2006).
92. Liu, C., Torralba, A., Freeman, W. T., Durand, F. & Adelson, E. H. Motion magnification. *ACM transactions on graphics (TOG)* **24,** 519–526 (2005).
93. Poh, M.-Z., McDuff, D. J. & Picard, R. W. Non-contact, automated cardiac pulse measurements using video imaging and blind source separation. *Optics express* **18,** 10762–10774 (2010).
94. Wadhwa, N. *et al.* Motion microscopy for visualizing and quantifying small motions. *Proceedings of the National Academy of Sciences* **114,** 11639–11644 (2017).
95. See Supplementary Information at https://www.nature.com/articles/s41598-021-85800-7.
96. Wattrisse, B., Chrysochoos, A., Muracciole, J.-M. & Némoz-Gaillard, M. Analysis of strain localization during tensile tests by digital image correlation. *Experimental Mechanics* **41,** 29–39 (2001).
97. Pan, B., Asundi, A., Xie, H. & Gao, J. Digital image correlation using iterative least squares and pointwise least squares for displacement field and strain field measurements. *Optics and Lasers in Engineering* **47,** 865–874 (2009).
98. Pan, B., Xie, H. & Wang, Z. Equivalence of digital image correlation criteria for pattern matching. *Applied optics* **49,** 5501–5509 (2010).
99. Lucas, B. D. & Kanade, T. *An iterative image registration technique with an application to stereo vision* in *IJCAI'81: 7th international joint conference on Artificial intelligence* **2** (1981), 674–679.
100. Simoncelli, E. P. & Freeman, W. T. *The steerable pyramid: A flexible architecture for multi-scale derivative computation* in *Proceedings., International Conference on Image Processing* **3** (1995), 444–447.

101. Jones, R., Fisher, R. & Bessell-Browne, P. Sediment deposition and coral smothering. *PLoS One* **14,** e0216248 (2019).

102. Erftemeijer, P. L., Riegl, B., Hoeksema, B. W. & Todd, P. A. Environmental impacts of dredging and other sediment disturbances on corals: a review. *Marine pollution bulletin* **64,** 1737–1765 (2012).

103. Studivan, M. S., Hatch, W. I. & Mitchelmore, C. L. Responses of the soft coral Xenia elongata following acute exposure to a chemical dispersant. *Springerplus* **4,** 1–10 (2015).

104. Baussant, T., Nilsen, M., Ravagnan, E., Westerlund, S. & Ramanand, S. Effects of suspended drill cuttings on the coral Lophelia pertusa using pulsed and continuous exposure scenarios. *Journal of Toxicology and Environmental Health, Part A* **81,** 361–382 (2018).

105. Guppy, R., Brown, B. & Bythell, J. C. Preserving the viscous coral surface mucus layer using low-acid glycol methacrylate (GMA) resin. *Coral Reefs* **38,** 521–526 (2019).

106. Brown, B. & Bythell, J. Perspectives on mucus secretion in reef corals. *Marine Ecology Progress Series* **296,** 291–309 (2005).

107. McClintock, B. T. *et al.* A general discrete-time modeling framework for animal movement using multistate random walks. *Ecological Monographs* **82,** 335–349 (2012).

108. Nicosia, A., Duchesne, T., Rivest, L.-P. & Fortin, D. A general hidden state random walk model for animal movement. *Computational Statistics & Data Analysis* **105,** 76–95 (2017).

109. Bailey, J. D., Wallis, J. & Codling, E. A. Navigational efficiency in a biased and correlated random walk model of individual animal movement. *Ecology* **99,** 217–223 (2018).

110. Fritz, H., Said, S. & Weimerskirch, H. Scale–dependent hierarchical adjustments of movement patterns in a long–range foraging seabird. *Proceedings of the Royal Society of London. Series B: Biological Sciences* **270,** 1143–1148 (2003).

111. Pyke, G. H. Understanding movements of organisms: it's time to abandon the Lévy foraging hypothesis. *Methods in Ecology and Evolution* **6,** 1–16 (2015).

112. Benhamou, S. & Collet, J. Ultimate failure of the Lévy Foraging Hypothesis: Two-scale searching strategies outperform scale-free ones even when prey are scarce and cryptic. *Journal of theoretical biology* **387,** 221–227 (2015).

113. Benhamou, S. How many animals really do the Lévy walk? *Ecology* **88,** 1962–1969 (2007).

114. Viswanathan, G. M. *et al.* Optimizing the success of random searches. *Nature* **401,** 911–914 (1999).

115. Blackwell, P. G., Niu, M., Lambert, M. S. & LaPoint, S. D. Exact B ayesian inference for animal movement in continuous time. *Methods in Ecology and Evolution* **7,** 184–195 (2016).

116. Ovaskainen, O. Habitat-specific movement parameters estimated using mark–recapture data and a diffusion model. *Ecology* **85,** 242–257 (2004).

117. Benhamou, S. Detecting an orientation component in animal paths when the preferred direction is individual-dependent. *Ecology* **87,** 518–528 (2006).

118. Benhamou, S. Spatial memory and searching efficiency. *Animal Behaviour* **47,** 1423–1433 (1994).

119. Lenz, F., Ings, T. C., Chittka, L., Chechkin, A. V. & Klages, R. Spatiotemporal dynamics of bumblebees foraging under predation risk. *Physical review letters* **108,** 098103 (2012).

120. Adam, T. *et al.* Joint modelling of multi-scale animal movement data using hierarchical hidden Markov models. *Methods in Ecology and evolution* **10,** 1536–1550 (2019).

121. Whoriskey, K. *et al.* A hidden Markov movement model for rapidly identifying behavioral states from animal tracks. *Ecology and evolution* **7,** 2112–2121 (2017).

122. Metzler, R., Jeon, J.-H., Cherstvy, A. G. & Barkai, E. Anomalous diffusion models and their properties: non-stationarity, non-ergodicity, and ageing at the centenary of single particle tracking. *Physical Chemistry Chemical Physics* **16,** 24128–24164 (2014).

123. Afek, G., Coslovsky, J., Courvoisier, A., Livneh, O. & Davidson, N. Observing power-law dynamics of position-velocity correlation in anomalous diffusion. *Physical Review Letters* **119,** 060602 (2017).

124. Sadegh, S., Barkai, E. & Krapf, D. $1/f$ noise for intermittent quantum dots exhibits non-stationarity and critical exponents. *New Journal of Physics* **16,** 113054 (2014).

125. Frantsuzov, P. A., Volkán-Kacsó, S. & Jankó, B. Universality of the fluorescence intermittency in nanoscale systems: experiment and theory. *Nano letters* **13,** 402–408 (2013).

126. Pelton, M., Grier, D. G. & Guyot-Sionnest, P. Characterizing quantum-dot blinking using noise power spectra. *Applied physics letters* **85,** 819–821 (2004).

127. Krapf, D. Nonergodicity in nanoscale electrodes. *Physical Chemistry Chemical Physics* **15,** 459–465 (2013).

128. Peng, C.-K. *et al.* Long-range anticorrelations and non-Gaussian behavior of the heartbeat. *Physical review letters* **70,** 1343 (1993).

129. Rempel, A., Waddington, E., Wettlaufer, J. & Worster, M. Possible displacement of the climate signal in ancient ice by premelting and anomalous diffusion. *Nature* **411,** 568–571 (2001).

130. Tóth, B. *et al.* Anomalous price impact and the critical nature of liquidity in financial markets. *Physical Review X* **1,** 021006 (2011).

131. Di Rienzo, C., Piazza, V., Gratton, E., Beltram, F. & Cardarelli, F. Probing short-range protein Brownian motion in the cytoplasm of living cells. *Nature communications* **5,** 5891 (2014).

132. Norregaard, K., Metzler, R., Ritter, C. M., Berg-Sørensen, K. & Oddershede, L. B. Manipulation and motion of organelles and single molecules in living cells. *Chemical reviews* **117,** 4342–4375 (2017).

133. Tabei, S. A. *et al.* Intracellular transport of insulin granules is a subordinated random walk. *Proceedings of the National Academy of Sciences* **110,** 4911–4916 (2013).

134. Jeon, J.-H. *et al.* In vivo anomalous diffusion and weak ergodicity breaking of lipid granules. *Physical review letters* **106,** 048103 (2011).

135. Sadegh, S., Higgins, J. L., Mannion, P. C., Tamkun, M. M. & Krapf, D. Plasma membrane is compartmentalized by a self-similar cortical actin meshwork. *Physical Review X* **7,** 011031 (2017).

136. Metzler, R., Jeon, J.-H. & Cherstvy, A. Non-Brownian diffusion in lipid membranes: Experiments and simulations. *Biochimica et Biophysica Acta (BBA)-Biomembranes* **1858,** 2451–2467 (2016).

137. Jeon, J.-H., Javanainen, M., Martinez-Seara, H., Metzler, R. & Vattulainen, I. Protein crowding in lipid bilayers gives rise to non-Gaussian anomalous lateral diffusion of phospholipids and proteins. *Physical Review X* **6,** 021006 (2016).

138. Krapf, D. Mechanisms underlying anomalous diffusion in the plasma membrane. *Current topics in membranes* **75,** 167–207 (2015).

139. Li, S. *et al.* Digital image processing to detect subtle motion in stony coral. *Scientific reports* **11,** 1–9 (2021).

140. Nishita, M. *et al.* Ror2 signaling regulates Golgi structure and transport through IFT20 for tumor invasiveness. *Scientific Reports* **7,** 1–15 (2017).

141. Shapiro, O. H., Kramarsky-Winter, E., Gavish, A. R., Stocker, R. & Vardi, A. A coral-on-a-chip microfluidic platform enabling live-imaging microscopy of reef-building corals. *Nature communications* **7,** 10860 (2016).

142. Roger, L. M. *et al.* Applying model approaches in non-model systems: A review and case study on coral cell culture. *PLoS One* **16,** e0248953 (2021).

143. See Supplementary Information at https://doi.org/10.1103/PhysRevApplied.18.024078.

144. Hedrick, T. L. Software techniques for two-and three-dimensional kinematic measurements of biological and biomimetic systems. *Bioinspiration & biomimetics* **3,** 034001 (2008).

145. Kubo, R. The fluctuation-dissipation theorem. *Reports on progress in physics* **29,** 255 (1966).

146. Lei, H., Baker, N. A. & Li, X. Data-driven parameterization of the generalized Langevin equation. *Proceedings of the National Academy of Sciences* **113,** 14183–14188 (2016).

147. Grogan, F., Lei, H., Li, X. & Baker, N. A. Data-driven molecular modeling with the generalized Langevin equation. *Journal of computational physics* **418,** 109633 (2020).

148. Chen, M., Li, X. & Liu, C. Computation of the memory functions in the generalized Langevin models for collective dynamics of macromolecules. *The Journal of Chemical Physics* **141,** 064112 (2014).

149. Edwards, A. M. Using likelihood to test for Lévy flight search patterns and for general power-law distributions in nature. *Journal of Animal Ecology* **77,** 1212–1222 (2008).

150. Edwards, A. M. *et al.* Revisiting Lévy flight search patterns of wandering albatrosses, bumblebees and deer. *Nature* **449,** 1044–1048 (2007).

151. Kutz, J. N. Deep learning in fluid dynamics. *Journal of Fluid Mechanics* **814,** 1–4 (2017).

152. Kochkov, D. *et al.* Machine learning–accelerated computational fluid dynamics. *Proceedings of the National Academy of Sciences* **118,** e2101784118 (2021).

153. Rolnick, D. *et al.* Tackling climate change with machine learning. *ACM Computing Surveys (CSUR)* **55,** 1–96 (2022).

154. Rowley, C. W., Mezić, I., Bagheri, S., Schlatter, P. & Henningson, D. S. Spectral analysis of nonlinear flows. *Journal of fluid mechanics* **641,** 115–127 (2009).

155. Schmid, P. J. Dynamic mode decomposition of numerical and experimental data. *Journal of fluid mechanics* **656,** 5–28 (2010).

156. Berger, E., Sastuba, M., Vogt, D., Jung, B. & Ben Amor, H. Estimation of perturbations in robotic behavior using dynamic mode decomposition. *Advanced Robotics* **29,** 331–343 (2015).

157. Brunton, B. W., Johnson, L. A., Ojemann, J. G. & Kutz, J. N. Extracting spatial–temporal coherent patterns in large-scale neural recordings using dynamic mode decomposition. *Journal of neuroscience methods* **258,** 1–15 (2016).

158. Shiraishi, Y. *et al.* Neural decoding of electrocorticographic signals using dynamic mode decomposition. *Journal of neural engineering* **17,** 036009 (2020).

159. Proctor, J. L. & Eckhoff, P. A. Discovering dynamic patterns from infectious disease data using dynamic mode decomposition. *International health* **7,** 139–145 (2015).

160. Li, S., Roger, L. M., Klein-Seetharaman, J., Lewinski, N. A. & Yang, J. Spatiotemporal Dynamics of Coral Polyps on a Fluidic Platform. *Physical Review Applied* **18,** 024078 (2022).

161. Wild, C. & Naumann, M. S. Effect of active water movement on energy and nutrient acquisition in coral reef-associated benthic organisms. *Proceedings of the National Academy of Sciences* **110,** 8767–8768 (2013).

162. See Supplementary Information at https://doi.org/10.1103/PhysRevResearch.5.013175.

163. Kamb, M., Kaiser, E., Brunton, S. L. & Kutz, J. N. Time-delay observables for Koopman: Theory and applications. *SIAM Journal on Applied Dynamical Systems* **19,** 886–917 (2020).

164. Vieira, V. M. *et al.* On the choice of linear regression algorithms for biological and ecological applications. *Annual Research & Review in Biology,* 1–9 (2016).

165. Bedard, C., Kroeger, H. & Destexhe, A. Does the $1/f$ frequency scaling of brain signals reflect self-organized critical states? *Physical review letters* **97,** 118102 (2006).

166. Miller, K. J., Sorensen, L. B., Ojemann, J. G. & Den Nijs, M. Power-law scaling in the brain surface electric potential. *PLoS computational biology* **5,** e1000609 (2009).

167. Szendro, P., Vincze, G. & Szasz, A. Pink-noise behaviour of biosystems. *European Biophysics Journal* **30,** 227–231 (2001).

168. Benayahu, Y. & Loya, Y. Competition for space among coral-reef sessile organisms at Eilat, Red Sea. *Bulletin of Marine Science* **31,** 514–522 (1981).

169. Westfall, J. A., Elliott, C. F. & Carlin, R. W. Ultrastructural evidence for two-cell and three-cell neural pathways in the tentacle epidermis of the sea anemone Aiptasia pallida. *Journal of morphology* **251,** 83–92 (2002).

170. Cooper, N., Dalibard, J. & Spielman, I. Topological bands for ultracold atoms. *Reviews of modern physics* **91,** 015005 (2019).

171. Fang, K. & Fan, S. Controlling the flow of light using the inhomogeneous effective gauge field that emerges from dynamic modulation. *Physical review letters* **111,** 203901 (2013).

172. Lin, Q. & Fan, S. Light guiding by effective gauge field for photons. *Physical Review X* **4,** 031031 (2014).

173. Yang, Y. *et al.* Demonstration of negative refraction induced by synthetic gauge fields. *Science Advances* **7,** eabj2062 (2021).

174. Lu, L., Joannopoulos, J. D. & Soljačić, M. Topological photonics. *Nature photonics* **8,** 821–829 (2014).

175. Khanikaev, A. B. & Shvets, G. Two-dimensional topological photonics. *Nature photonics* **11,** 763–773 (2017).

176. Yang, Z. *et al.* Topological acoustics. *Physical review letters* **114,** 114301 (2015).

177. Abbaszadeh, H., Souslov, A., Paulose, J., Schomerus, H. & Vitelli, V. Sonic Landau levels and synthetic gauge fields in mechanical metamaterials. *Physical review letters* **119,** 195502 (2017).

178. Peri, V., Serra-Garcia, M., Ilan, R. & Huber, S. D. Axial-field-induced chiral channels in an acoustic Weyl system. *Nature Physics* **15,** 357–361 (2019).

179. Yang, Z., Gao, F., Yang, Y. & Zhang, B. Strain-induced gauge field and Landau levels in acoustic structures. *Physical Review Letters* **118,** 194301 (2017).

180. Brendel, C., Peano, V., Painter, O. J. & Marquardt, F. Pseudomagnetic fields for sound at the nanoscale. *Proceedings of the National Academy of Sciences* **114,** E3390–E3395 (2017).

181. Wen, X. *et al.* Acoustic Landau quantization and quantum-Hall-like edge states. *Nature Physics* **15,** 352–356 (2019).

182. Yan, M. *et al.* Pseudomagnetic fields enabled manipulation of on-chip elastic waves. *Physical Review Letters* **127,** 136401 (2021).

183. Lv, C., Krishnaraju, D., Konjevod, G., Yu, H. & Jiang, H. Origami based mechanical metamaterials. *Scientific reports* **4,** 1–6 (2014).

184. Wickeler, A. L. & Naguib, H. E. Novel origami-inspired metamaterials: Design, mechanical testing and finite element modelling. *Materials & Design* **186,** 108242 (2020).

185. Zirbel, S. A. *et al.* Accommodating thickness in origami-based deployable arrays. *Journal of Mechanical Design* **135** (2013).

186. Del Grosso, A. E. & Basso, P. Adaptive building skin structures. *Smart Materials and Structures* **19,** 124011 (2010).

187. Lyu, S., Qin, B., Deng, H. & Ding, X. Origami-based cellular mechanical metamaterials with tunable Poisson's ratio: Construction and analysis. *International Journal of Mechanical Sciences* **212,** 106791 (2021).

188. Miyashita, S., Guitron, S., Ludersdorfer, M., Sung, C. R. & Rus, D. *An untethered miniature origami robot that self-folds, walks, swims, and degrades* in *2015 IEEE International Conference on Robotics and Automation (ICRA)* (2015), 1490–1496.

189. Edmondson, B. J. *et al. Oriceps: Origami-inspired forceps* in *Smart Materials, Adaptive Structures and Intelligent Systems* **56031** (2013), V001T01A027.

190. Kuribayashi, K. *et al.* Self-deployable origami stent grafts as a biomedical application of Ni-rich TiNi shape memory alloy foil. *Materials Science and Engineering: A* **419,** 131–137 (2006).

191. Zhou, C., Wang, B., Ma, J. & You, Z. Dynamic axial crushing of origami crash boxes. *International journal of mechanical sciences* **118,** 1–12 (2016).

192. Miyazawa, Y. *et al.* Topological state transfer in Kresling origami. *Communications Materials* **3,** 1–10 (2022).

193. Chen, B. G.-g. *et al.* Topological mechanics of origami and kirigami. *Physical review letters* **116,** 135501 (2016).

194. Li, S., Miyazawa, Y., Yamaguchi, K., Kevrekidis, P. G. & Yang, J. *Geometry-informed dynamic mode decomposition in origami dynamics* 2023. `https://arxiv.org/abs/2303.04323`.

195. Wu, Y., Chaunsali, R., Yasuda, H., Yu, K. & Yang, J. Dial-in topological metamaterials based on bistable stewart platform. *Scientific reports* **8,** 112 (2018).

196. Pal, R. K., Schaeffer, M. & Ruzzene, M. Helical edge states and topological phase transitions in phononic systems using bi-layered lattices. *Journal of Applied Physics* **119,** 084305 (2016).

197. Yasuda, H., Tachi, T., Lee, M. & Yang, J. Origami-based tunable truss structures for non-volatile mechanical memory operation. *Nature communications* **8,** 1–7 (2017).

198. Slonczewski, J. & Weiss, P. Band structure of graphite. *Physical review* **109,** 272 (1958).

199. Chen, Y., Liu, X. & Hu, G. Topological phase transition in mechanical honeycomb lattice. *Journal of the Mechanics and Physics of Solids* **122,** 54–68 (2019).

200. Mousavi, S. H., Khanikaev, A. B. & Wang, Z. Topologically protected elastic waves in phononic metamaterials. *Nature communications* **6,** 8682 (2015).

201. Mei, J., Wu, Y., Chan, C. T. & Zhang, Z.-Q. First-principles study of Dirac and Dirac-like cones in phononic and photonic crystals. *Physical Review B* **86,** 035141 (2012).

202. Lu, J. *et al.* Dirac cones in two-dimensional artificial crystals for classical waves. *Physical Review B* **89,** 134302 (2014).

203. Pikulin, D., Chen, A. & Franz, M. Chiral anomaly from strain-induced gauge fields in Dirac and Weyl semimetals. *Physical Review X* **6,** 041021 (2016).

204. Grushin, A. G., Venderbos, J. W., Vishwanath, A. & Ilan, R. Inhomogeneous weyl and dirac semimetals: Transport in axial magnetic fields and fermi arc surface states from pseudo-landau levels. *Physical Review X* **6,** 041046 (2016).

205. Jia, H. *et al.* Observation of chiral zero mode in inhomogeneous three-dimensional Weyl metamaterials. *Science* **363,** 148–151 (2019).

206. Jia, H. *et al. Experimental realization of chiral Landau levels in two-dimensional Dirac cone systems with inhomogeneous effective mass* 2022. arXiv: `2209.10745 [cond-mat.mtrl-sci]`.

207. Taychatanapat, T. *et al.* Conductance oscillations induced by ballistic snake states in a graphene heterojunction. *Nature communications* **6,** 6093 (2015).

208. Oroszlány, L., Rakyta, P., Kormányos, A., Lambert, C. & Cserti, J. Theory of snake states in graphene. *Physical Review B* **77,** 081403 (2008).

209. Ghosh, T., De Martino, A., Häusler, W., Dell'Anna, L. & Egger, R. Conductance quantization and snake states in graphene magnetic waveguides. *Physical Review B* **77,** 081404 (2008).

210. Müller, J. Effect of a nonuniform magnetic field on a two-dimensional electron gas in the ballistic regime. *Physical review letters* **68,** 385 (1992).

211. Infeld, E. & Rowlands, G. *Nonlinear waves, solitons and chaos* (Cambridge university press, 2000).

212. Ablowitz, M. J. *Nonlinear dispersive waves: asymptotic analysis and solitons* (Cambridge University Press, 2011).

213. Chapman, C. *Fundamentals of seismic wave propagation* (Cambridge university press, 2004).

214. Poursartip, B., Fathi, A. & Tassoulas, J. L. Large-scale simulation of seismic wave motion: A review. *Soil Dynamics and Earthquake Engineering* **129,** 105909 (2020).

215. Kono, M. & Skoric, M. *Nonlinear physics of plasmas* (Springer Science & Business Media, 2010).

216. Kivshar, Y. S. & Agrawal, G. P. *Optical solitons: from fibers to photonic crystals* (Academic press, 2003).

217. Pitaevskii, L. & Stringari, S. *Bose-Einstein condensation and superfluidity* (Oxford University Press, 2016).

218. Kim, E. & Yang, J. Wave propagation in granular metamaterials. *Functional Composites and Structures* **1,** 012002 (2019).

219. Liu, J., Guo, H. & Wang, T. A review of acoustic metamaterials and phononic crystals. *Crystals* **10,** 305 (2020).

220. Butt, M., Khonina, S. N. & Kazanskiy, N. Recent advances in photonic crystal optical devices: A review. *Optics & Laser Technology* **142,** 107265 (2021).

221. Li, S. & Yang, J. Topological transition in spiral elastic valley metamaterials. *Physical Review Applied* **15,** 014058 (2021).

222. Li, S., Kim, I., Iwamoto, S., Zang, J. & Yang, J. Valley anisotropy in elastic metamaterials. *Physical Review B* **100,** 195102 (2019).

223. Li, S., Zhao, D., Niu, H., Zhu, X. & Zang, J. Observation of elastic topological states in soft materials. *Nature communications* **9,** 1370 (2018).

224. Chen, H., Nassar, H. & Huang, G. A study of topological effects in 1D and 2D mechanical lattices. *Journal of the Mechanics and Physics of Solids* **117,** 22–36 (2018).

225. Liu, T.-W. & Semperlotti, F. Tunable acoustic valley–hall edge states in reconfigurable phononic elastic waveguides. *Physical Review Applied* **9,** 014001 (2018).

226. Zhu, H., Liu, T.-W. & Semperlotti, F. Design and experimental observation of valley-Hall edge states in diatomic-graphene-like elastic waveguides. *Physical Review B* **97,** 174301 (2018).

227. Zhou, Y., Bandaru, P. R. & Sievenpiper, D. F. Quantum-spin-Hall topological insulator in a spring-mass system. *New Journal of Physics* **20,** 123011 (2018).

228. Tempelman, J. R., Vakakis, A. F. & Matlack, K. H. A Modal Decomposition Approach to Topological Wave Propagation. *arXiv preprint arXiv:2210.11665* (2022).

229. Proctor, J. L., Brunton, S. L. & Kutz, J. N. Dynamic mode decomposition with control. *SIAM Journal on Applied Dynamical Systems* **15,** 142–161 (2016).

230. Li, S. *et al.* Data-driven discovery of spatiotemporal coherent patterns in pulsating soft coral tentacle motion with dynamic mode decomposition. *Physical Review Research* **5,** 013175 (2023).

231. Kariyado, T. & Hatsugai, Y. Manipulation of dirac cones in mechanical graphene. *Scientific reports* **5,** 18107 (2015).

232. Penrose, R. *A generalized inverse for matrices* in *Mathematical proceedings of the Cambridge philosophical society* **51** (1955), 406–413.

233. Tu, J. H., Rowley, C. W., Luchtenburg, D. M., Brunton, S. L. & Kutz, J. N. On dynamic mode decomposition: Theory and applications. *Journal of Computational Dynamics* **1,** 391 (2014).

234. Mendible, A., Brunton, S. L., Aravkin, A. Y., Lowrie, W. & Kutz, J. N. Dimensionality reduction and reduced-order modeling for traveling wave physics. *Theoretical and Computational Fluid Dynamics* **34,** 385–400 (2020).

235. See Supplementary Information at https://doi.org/10.1103/PhysRevB.107.184308.

236. Schmid, P. J. Dynamic mode decomposition and its variants. *Annual Review of Fluid Mechanics* **54,** 225–254 (2022).

237. Yuan, Y., Zhou, K., Zhou, W., Wen, X. & Liu, Y. Flow prediction using dynamic mode decomposition with time-delay embedding based on local measurement. *Physics of Fluids* **33,** 095109 (2021).

238. Khelif, A., Choujaa, A., Benchabane, S., Djafari-Rouhani, B. & Laude, V. Guiding and bending of acoustic waves in highly confined phononic crystal waveguides. *Applied physics letters* **84,** 4400–4402 (2004).

239. He, C. *et al.* Acoustic topological insulator and robust one-way sound transport. *Nature physics* **12,** 1124–1129 (2016).

240. Niu, H., Li, S. & Zang, J. Reliable and tunable elastic interface states in soft metamaterials. *physica status solidi (RRL)–Rapid Research Letters* **14,** 2000338 (2020).

241. Niu, H., Li, S. & Zang, J. Interface-dependent tunable elastic interface states in soft metamaterials. *Journal of Applied Physics* **129,** 065305 (2021).

242. Lloyd, S. Least squares quantization in PCM. *IEEE transactions on information theory* **28,** 129–137 (1982).

243. Yasuda, H. & Yang, J. Reentrant origami-based metamaterials with negative Poisson's ratio and bistability. *Physical review letters* **114,** 185502 (2015).

244. Jianguo, C., Xiaowei, D., Ya, Z., Jian, F. & Yongming, T. Bistable behavior of the cylindrical origami structure with Kresling pattern. *Journal of Mechanical Design* **137,** 061406 (2015).

245. Hanna, B. H., Lund, J. M., Lang, R. J., Magleby, S. P. & Howell, L. L. Waterbomb base: a symmetric single-vertex bistable origami mechanism. *Smart Materials and Structures* **23,** 094009 (2014).

246. Nelson, T. G., Lang, R. J., Magleby, S. P. & Howell, L. L. Curved-folding-inspired deployable compliant rolling-contact element (D-CORE). *Mechanism and Machine Theory* **96,** 225–238 (2016).

247. Deng, X., Zhao, J., Cai, J. & Liu, X. Tunable origami metamaterial with arbitrary single-curvature configuration. *Mechanism and Machine Theory* **171,** 104745 (2022).

248. Huang, C. *et al.* Origami dynamics based soft piezoelectric energy harvester for machine learning assisted self-powered gait biometric identification. *Energy Conversion and Management* **263,** 115720 (2022).

249. Champion, K., Lusch, B., Kutz, J. N. & Brunton, S. L. Data-driven discovery of coordinates and governing equations. *Proceedings of the National Academy of Sciences* **116,** 22445–22451 (2019).

250. Iten, R., Metger, T., Wilming, H., Del Rio, L. & Renner, R. Discovering physical concepts with neural networks. *Physical review letters* **124,** 010508 (2020).

251. Raissi, M., Perdikaris, P. & Karniadakis, G. E. Physics-informed neural networks: A deep learning framework for solving forward and inverse problems involving nonlinear partial differential equations. *Journal of Computational physics* **378,** 686–707 (2019).

252. Ingabire, H. N. *et al.* Analysis of ECG Signals by Dynamic Mode Decomposition. *IEEE Journal of Biomedical and Health Informatics* **26,** 2124–2135 (2021).

253. Saito, A. & Kuno, T. Data-driven experimental modal analysis by dynamic mode decomposition. *Journal of Sound and Vibration* **481,** 115434 (2020).

254. Li, S., Kevrekidis, P. G. & Yang, J. Characterization of elastic topological states using dynamic mode decomposition. *Physical Review B* **107,** 184308 (18 2023).

255. Hansen, E., Brunton, S. L. & Song, Z. Swarm Modelling with Dynamic Mode Decomposition. *IEEE Access* (2022).

256. Kaiser, E., Kutz, J. N. & Brunton, S. L. Sparse identification of nonlinear dynamics for model predictive control in the low-data limit. *Proceedings of the Royal Society A* **474,** 20180335 (2018).

257. Brunton, S. L., Proctor, J. L. & Kutz, J. N. Discovering governing equations from data by sparse identification of nonlinear dynamical systems. *Proceedings of the national academy of sciences* **113,** 3932–3937 (2016).

258. Zhang, L. & Schaeffer, H. On the convergence of the SINDy algorithm. *Multiscale Modeling & Simulation* **17,** 948–972 (2019).

259. Ma, G., Xiao, M. & Chan, C. T. Topological phases in acoustic and mechanical systems. *Nature Reviews Physics* **1,** 281–294 (2019).

260. Vila, J., Pal, R. K. & Ruzzene, M. Observation of topological valley modes in an elastic hexagonal lattice. *Physical Review B* **96,** 134307 (2017).

261. Wang, H.-X., Guo, G.-Y. & Jiang, J.-H. Band topology in classical waves: Wilson-loop approach to topological numbers and fragile topology. *New Journal of Physics* **21,** 093029 (2019).

262. Rosenstein, M. T., Collins, J. J. & De Luca, C. J. A practical method for calculating largest Lyapunov exponents from small data sets. *Physica D: Nonlinear Phenomena* **65,** 117–134 (1993).

263. Geist, K., Parlitz, U. & Lauterborn, W. Comparison of different methods for computing Lyapunov exponents. *Progress of theoretical physics* **83,** 875–893 (1990).

264. Barreira, L. & Valls, C. Lyapunov regularity via singular values. *Transactions of the American Mathematical Society* **369,** 8409–8436 (2017).

265. Wu, X. *et al.* Direct observation of valley-polarized topological edge states in designer surface plasmon crystals. *Nature communications* **8,** 1304 (2017).

266. Wang, J.-Q. *et al.* Extended topological valley-locked surface acoustic waves. *Nature communications* **13,** 1324 (2022).

267. Jiao, J., Chen, T. & Yu, D. Observation of topological valley waveguide transport of elastic waves in snowflake plates. *Composite Structures* **286,** 115297 (2022).

Appendix A

DIGITAL IMAGE PROCESSING TO DETECT SUBTLE MOTION IN STONY CORAL

A.1 Experimental methods

A.1.1 Experimental setup

Figure A.1(a) shows the experimental setup used to observe the coral *Montipora capricornis*. The coral is fixed on the skeleton to ensure that it is not affected by the water flow. It includes a DSLR camera with a macro lens to take pictures of the fine structures of coral tissue surface. It also includes necessities for the aquarium such as filter and scraper. To study the effect of light on coral tissue motion, aquarium light and ceiling light were used to mimic light conditions during the day and the night.

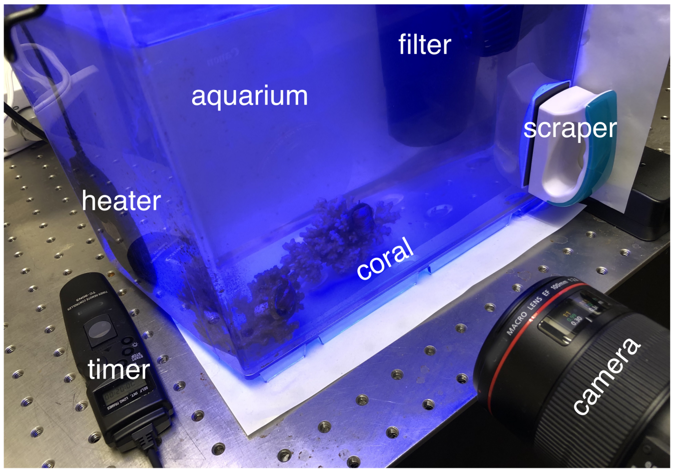

Figure A.1: Experimental setup. The experimental setup with a DSRL camera, a timer, an aquarium equipped with a filter, a scraper and a heater. The coral is fixed on another coral skeleton.

A.1.2 Aquarium maintenance

The *Montipora capricornis* (around 15 mm × 20 mm) was bought from a local store (Seattle Corals Aquariums) and was raised in a 11.36 l aquarium with specific density = 1.024 g/cm^3 and $pH = 8.4$. Artificial seawater was made from Instant Ocean Reef Crystals Reef Salt with the salinity = 34.1 g/cm^3. A one third water change was carried out every 3 days to maintain steady aquarium conditions. Regular tests on pH, NH_4^+, NO_2^- and NO_3^- were conducted to ensure suitable water quality for coral growth. The continuous water flow within the tank was provided by the Hydor Koralia Nano Aquarium Circulation Pump with 908.5 l per hour flow rate. The temperature of the water was controlled by the 50 W FREESEA submersible heater and was maintained at 25.5°C. Light was provided on a 14.5 : 9.5 light: dark cycle using a 6 W NICREW ClassicLED aquarium light and the ceiling light in the laboratory. The aquarium light emits blue light with 380 lumens, and it was turned on all day, while the ceiling light emits white light and it was controlled manually to be turned on at day and turned off at night.

A.1.3 Pictures acquisition

We used a Canon EOS 5D Mark IV and EF 100 mm f/2.8L Macro IS USM and timer to take pictures for the *Montipora capricornis* every 2 min automatically. The parameters for the camera were: F11, ISO4000, 1/10 s. The camera was put on a tripod to make it stable and ready for the long-period shooting. The macro lens was perpendicular to the wall of the aquarium to avoid the blurred effect caused by the refraction of light. The distance between the macro lens and the wall of the aquarium was 12.5 cm. Two hundred pictures are taken automatically for each light condition with a rate of 30 frames per hour with the help of the timer.

A.2 Extraction of luminance of images

In our algorithm, we use the luminance of the image to represent the light intensity. Our original images in RGB color space are converted to NTSC color space with three components: Y, I and Q, using the following equation:

$$\begin{bmatrix} Y \\ I \\ Q \end{bmatrix} = \begin{bmatrix} 0.299 & 0.587 & 0.114 \\ 0.596 & -0.274 & -0.322 \\ 0.211 & -0.523 & 0.312 \end{bmatrix} \begin{bmatrix} R \\ G \\ B \end{bmatrix} \tag{A.1}$$

where Y component represents luminance or brightness of the image in the range from 0 to 1. The other components carry the hue and saturation information. We define the mean of the Y component throughout the image as the luminance of this image. Figure A.2 shows the luminance of images taken at day and at night. The luminance at day is around 0.48 while the luminance at night is around 0.16, which coincides with the intuition that the luminance at day is larger.

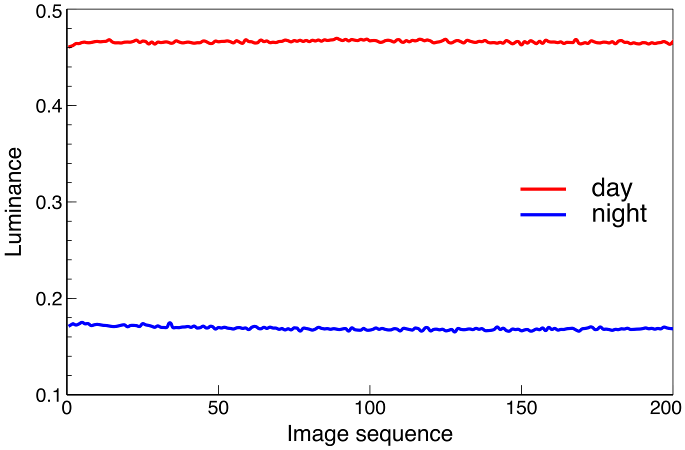

Figure A.2: Luminance extracted from pictures. Red and blue curves show the luminance at day and night, respectively.

A.3 *Digital image correlation of the coral skeleton*

The coral skeleton is in the aquarium which is indicated by the yellow curves in Figures A.3(a) and (b). The *Montipora capricornis* is fixed on a coral skeleton. The coral skeleton is not supposed to develop notable motions under the water flow or other factors, which provides a good opportunity to test the validation of DIC and optical flow. The

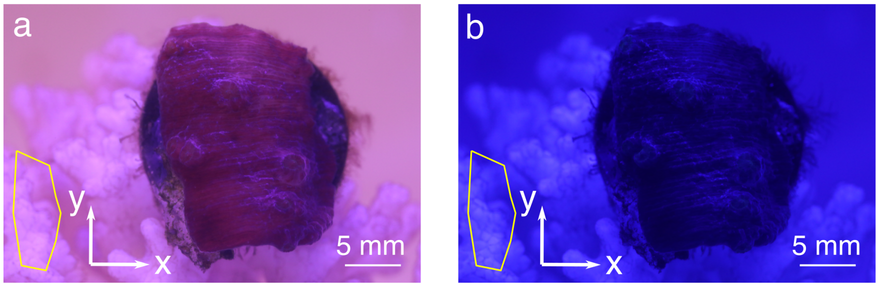

Figure A.3: Pictures taken at day and at night. The yellow curves in (a) and (b) enclose the coral skeleton in the aquarium. Scale bars are shown in (a) and (b).

first picture is considered as the reference picture. Figure A.4(a) shows the displacements u_x between the second picture and the reference picture at day and at night from left to right. In comparison with the displacement of coral shown in Figure 2.2(a), the results of coral skeleton at day and at night do not show obvious distinction but are smaller than the results of coral. We also investigate the displacements u_y at day and at night shown in Figure A.4(b). No obvious difference is observed from the results. Similarly, u_y is smaller than the results of coral. The histograms of displacements u_x and u_y are presented in Figure A.4(c). The red and blue curves in each panel indicate the mean of displacement distribution at day and at night throughout the displacement result. The corresponding variation ranges are shown in red and cyan dashed lines. The results show that most of the parts are not moving since the displacements are zeros. The means of both displacements u_x and u_y are either the same or slightly different at day and at night. Besides, the noise is smaller than the results of coral. It suggests that the results are not significantly affected by the light condition, which verify the validation of the digital image correlation algorithm.

The same phenomenon can be found in the strain information. The strains between the second picture and the reference picture are shown in Figures A.5(a)-(c). Figures A.5(a)-(c) shows the normal strain ϵ_{xx} and ϵ_{yy} at day and at night, and 5b shows the shear strain ϵ_{xy}. Similar to the displacements analyzed above, the strains also exhibit no obvious distinctions. The histograms of ϵ_{xx}, ϵ_{xy} and ϵ_{yy} shown in Figure A.5(d) make it clearer. The means of strains at day are in close proximity to the values at night. In general, the comparison of

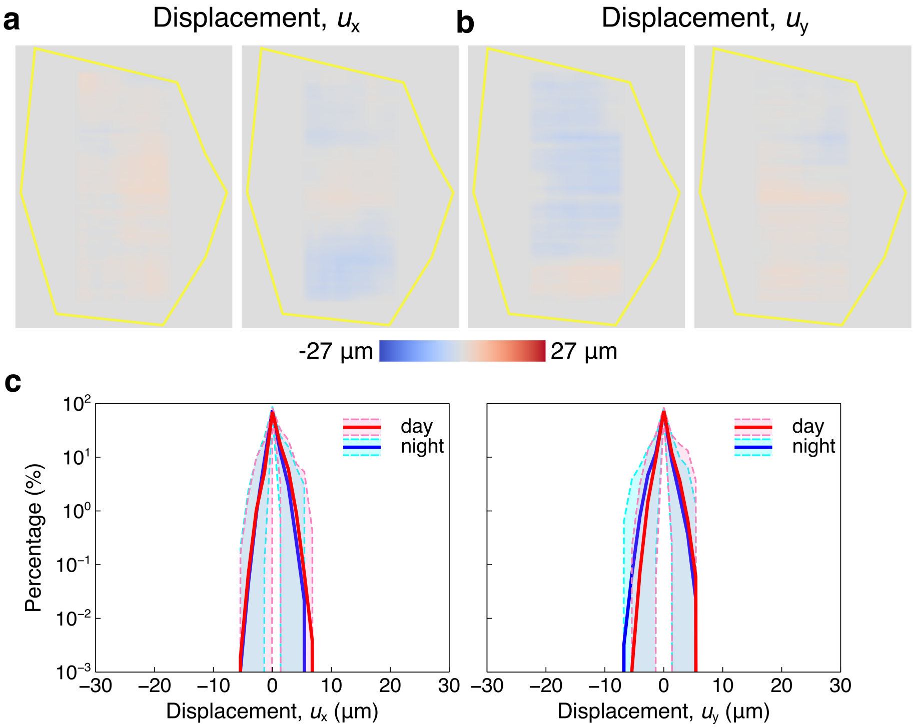

Figure A.4: Displacements of the coral skeleton from digital image correlation. (a) The displacements u_x along horizontal direction between the first and the second picture at day and night are shown in the left and right panel, respectively. (b) The displacement u_y along vertical direction between the first and the second picture at day and night are shown in the left and right panel, respectively. (c) The percentage histograms of displacement u_x and displacement u_y are shown in the left and right panels, respectively. The red and blue curves indicate the means of each displacement at day and night. The pink and cyan regions are variation ranges at day and night.

DIC results between coral and coral skeleton supports the validation of DIC algorithm.

Besides, we also analyze the possibility that the difference between day and night is caused by accident. Supplementary video shows the histograms representing the distributions of displacements when the consecutive picture is considered as the reference picture [95]. From the movie, the displacement at night is larger than that at day. Moreover, positive and negative displacements are shown in the movie, suggesting that the coral is fixed on the coral skeleton during the experiment and only motions of polyps and coral skin are recorded. Another reference picture is also considered. We also take the 20^{th}, 40^{th} and

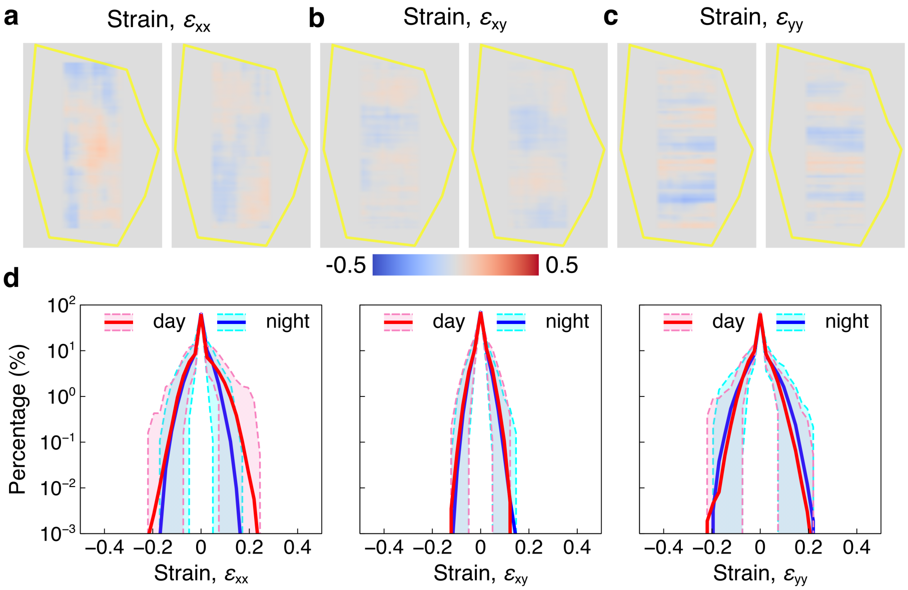

Figure A.5: Strains of the coral skeleton from digital image correlation. (a)-(c) Strains ϵ_{xx}, ϵ_{xy} and ϵ_{yy} between the first and the second picture at day and night are shown in the left and right panel, respectively. (d) The percentage histogram of the strains ϵ_{xx}, ϵ_{xy} and ϵ_{yy} are shown from left to right, respectively. The red and blue curves indicate the means of each strain at day and night. The pink and cyan regions are variation ranges at day and night.

100^{th} picture as the reference picture, respectively, and calculate the histograms of displacements, shown in Supplementary video [95]. They all show that the displacement at night is larger than that at day. Moreover, positive and negative displacements are shown in the movies. The above analysis indicates that our result is obtained statistically rather than by accident.

A.4 Optical flow of the coral skeleton

In order to verify the validation of optical flow, we also carry out the study of optical flow on coral skeleton enclosed by yellow curves in Figure A.3. Figures A.6(a) and (b) exhibit the optical flow of the coral skeleton encoded by the color square with the same scale between the second picture and the first picture at day and at night, respectively. Similar to the DIC result, the top right corner is in the low saturation, meaning that it is lack of the coral skeleton. Besides, there is no significant difference between Figure A.6(a) and (b) from the perspective of color distribution. The histograms shown in Figure A.6(c) illustrate the distribution of velocities v_x and v_y. More parts are involved in the motion at day, which is on the opposite side of the case of coral. According to the symmetry of the histograms, the coral skeleton tends to have a positive velocity v_x and a negative velocity v_y whatever light condition the coral skeleton is under. Besides, the values are smaller than the velocities on coral. The histogram of direction is shown in Figure A.6(d). Probably because of water flow, the motion direction is along the horizontal direction, which is 0° and 180°. Apart from that, there is no significant peak in the histogram. Overall, the comparison of optical flow results between coral and coral skeleton supports the validation of optical flow algorithm.

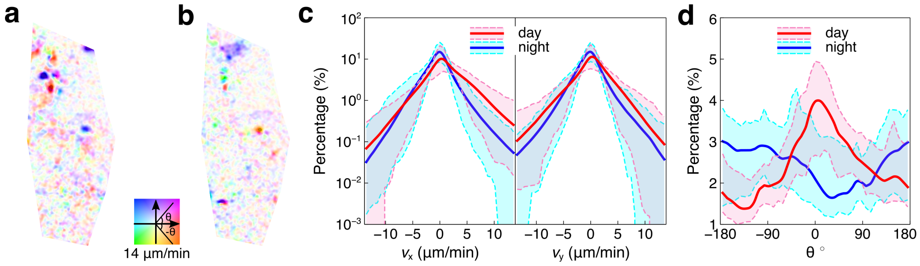

Figure A.6: Optical flow of the coral skeleton. (a)-(b) Optical flow between the second and first pictures at day and night, respectively. (c) The percentage histograms of velocities v_x and v_y along horizontal and vertical directions. The red and blue curves indicate the means of each velocity at day and night. The pink and cyan regions are variations at day and night. (d) The percentage histogram of direction of velocity. The red and blue curves indicate the means of each angle at day and night. The pink and cyan regions are variation ranges at day and night.

Appendix B

SPATIOTEMPORAL DYNAMICS OF CORAL POLYPS ON A FLUIDIC PLATFORM

B.1 Experimental methods

B.1.1 Design and fabrication of the octagonal fluidic platform

The octagonal fluidic platform is designed using the computer-assisted drawing software solidworks. The design is 3D printed using a Polyjet 3D printer (Objet Eden 260VS) with VeroClear resin (clear and transparent resin, to allow for light penetration). This fluidic platform is specifically designed for the in vivo study of small coral fragments (i.e., nubbins, $\leq$ 5 mm) as opposed to typical large fragments used (5 $\sim$ 10 cm). During printing, the main chamber is open on both faces (top and bottom), which enables its attachment (glue) onto glass slides of various thicknesses for top and/or bottom imaging.

B.1.2 Experimental setup and procedure

Coral nubbins ($\leq$ 5 mm) are cut from larger fragments of *Pocillopora acuta*, glued onto glass coverslips, and placed back into tanks to recover for two months. For the experiments, the nubbins are placed in the octagonal fluidic platform (one at a time) under a dissecting microscope (magnification is varied according to the size of the nubbin) mounted with a Nikon camera and viewing tablet. Photos are taken every 10 s from day 1 until the end of the experiment and assembled as a time series for analysis. The octagonal fluidic platform is connected to a peristaltic pump that transports the seawater from the holding vessel to the chamber (holding vessel under constant stirring at 300 rpm and heating). A low flow rate ($\sim$ 5 μl/s) is maintained to avoid impacting on polyp motion while still regularly renewing the artificial seawater inside the chamber. The computational fluid-dynamics simulation with different flow rates are exhibited in Figure B.1, where lower impact is observed at a flow rate of $\sim$ 5 μl/s.

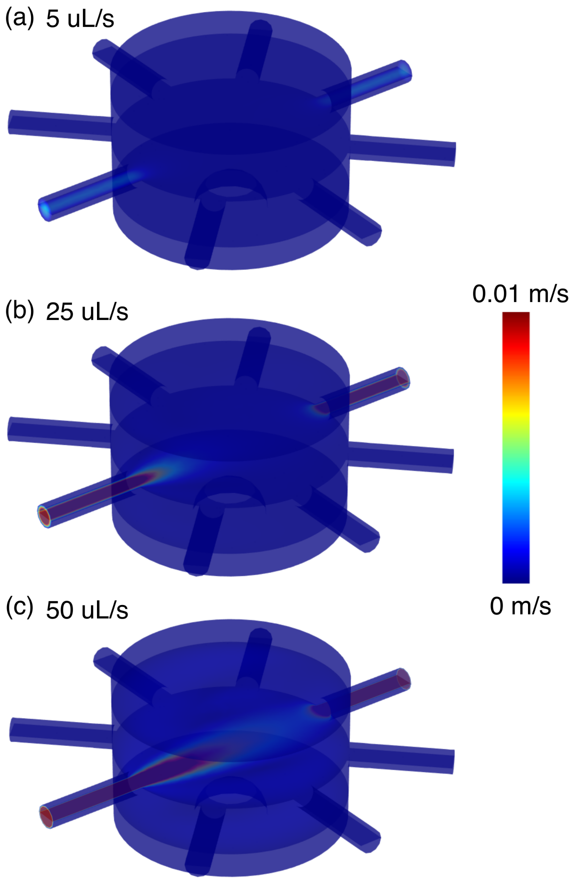

Figure B.1: Computational fluid-dynamics simulation with different flow rates of our fluidic platform. Velocity distribution of the fluid is shown in the tubes and chamber. Three slices are shown in the chamber, one of which shows the velocity distribution near the coral nubbin. Results of using flow rates of 5, 25, and 50 μl/s are shown in (a)–(c), respectively.

The AI Prime 16HD reef light system is used as the light source with constant power but adjustable wavelengths on a 10/14 h daylight cycle. To make sure the corals acclimate to the fluidic environment, we move the nubbins from the aquarium to the chamber on day 1 under normal light and temperature. On day 2, light and temperature are adjusted to the experimental conditions and maintained for 24 h. On day 3, the conditions are returned to normal, and the nubbin is placed back into the aquarium at the end of the day. The experimental settings include normal, blue, green, and red light at temperatures of 25°C, and 15, 25, and 30°C under normal light. Blue, green, and red light are monochromatic but normal light is mixed with 7% UV, 7% violet, 7% royal blue, 7% blue, 7% green, 19% deep red, 7% moonlight, and 33% cool white, according to the light settings on the AI Prime 16HD reef light system. Note that each experimental setting is replicated three times.

B.2 Data-driven parameterization of the Langevin equation

One of the main focuses of the generalized Langevin equation is to estimate the memory-kernel function. We use the data-driven method to estimate the memory-kernel function. As mentioned in the main text, after we obtain $G(t) = -\int_0^t K(t-\tau)H(\tau)d\tau$, we conduct the Laplace transform to obtain $\hat{G}(\xi) = -\hat{K}(\xi)\hat{H}(\xi)$. Note that we work with the variable ξ instead of the usual choice of s ($s = 1/\xi$), so that we obtain $\mathcal{L}(G(t)) = \hat{G}(\xi) = \int_0^\infty G(t)e^{-t/\xi}dt$, $\mathcal{L}(H(t)) = \hat{H}(\xi) = \int_0^\infty H(t)e^{-t/\xi}dt$, and $\mathcal{L}(K(t)) = \hat{K}(\xi) = \int_0^\infty K(t)e^{-t/\xi}dt$. By integrating by parts repeatedly, we can obtain the relationship between the variable before and after the Laplace transform:

$$\hat{G}^{(i)}(0) = i!G^{(i-1)}(0), \hat{H}^{(i)}(0) = i!H^{(i-1)}(0), \hat{K}^{(i)}(0) = i!K^{(i-1)}(0) \tag{B.1}$$

Additionally, when taking $\xi \to \infty$, we can obtain the Markovian limit of these parameters: $\lim_{\xi\to\infty} \hat{G}(\xi) = \int_0^\infty G(t)dt$, $\lim_{\xi\to\infty} \hat{H}(\xi) = \int_0^\infty H(t)dt$ and $\lim_{\xi\to\infty} \hat{K}(\xi) = \int_0^\infty K(t)dt$. Therefore, the memory-kernel function at the Markovian limit, $\hat{K}(\infty)$, can be calculated by

$$\hat{K}(\infty) = -\hat{G}(\infty)\hat{H}(\infty) = -(\int_0^\infty G(t)dt)(\int_0^\infty H(t)dt)^{-1} \tag{B.2}$$

To calculate $\hat{K}(\xi)$ for any ξ, we use a rational function approximation for $\hat{K}(\xi)$ in the form of

$$\hat{K}(\xi) = (I - \sum_{m=1}^{M} B_m\xi^m)^{-1}(\sum_{m=1}^{M} A_m\xi^m) \tag{B.3}$$

where the terms of expression are matrices $A_m \in \mathbb{R}^{N\times N}$ and $B_m \in \mathbb{R}^{N\times N}$. The highest-order coefficients can be found by taking the limit: $\lim_{\xi\to\infty} \hat{K}(\xi) = -B_M^{-1}A_M$.

$\hat{K}(\xi)$ can also be expanded by the Taylor expansion at $\xi = 0$:

$$\hat{K}(\xi) = \sum_{n=1}^{\infty} \frac{\hat{K}^{(n)}(0)}{n!}\xi^n \tag{B.4}$$

The rational function approximation for $\hat{K}(\xi)$ can be matched with the form of the Taylor expansion, which results in

$$\frac{\hat{K}^{(n)}(0)}{n!} = A_n + \sum_{l+m=n} B_l \frac{\hat{K}^{(m)}(0)}{m!} \tag{B.5}$$

Combined with the conversion between variables before and after the Laplace transform, we can deduce the coefficients in the rational function approximation. For example, as for the first-order approximation, $A_1 = -G^{(1)}(0)[H^{(1)}(0)]^{-1}$ and $B_1 = -A^{(1)}[\hat{K}(\infty)]^{-1}$. Likewise, we can obtain the coefficients of the higher-order rational function approximation. Then the inverse Laplace transform can be used to obtain the memory-kernel function in the time domain.

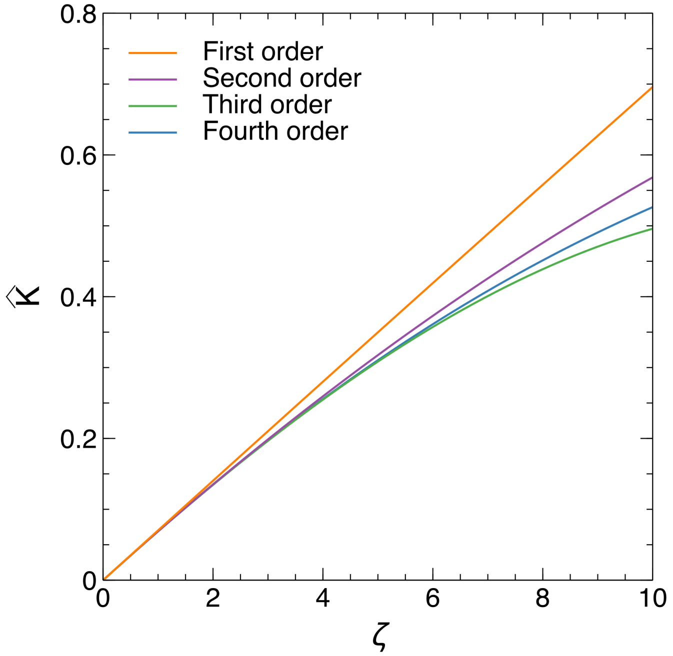

Figure B.2: Laplace transform of the memory kernel for modeling the in-plane motion of coral polyps. First-order, second-order, third-order, and fourth-order estimations of the Laplace transform of the memory kernel are shown in different colors. Third-order and fourth-order estimations overlap. These curves converge to a certain value with the increase of ξ.

We take polyp #3 labeled in Figure 3.1(c) as an example. As shown in Figure B.2, the first-order, second-order, third-order, and fourth-order rational function approximations of the memory-kernel function are presented in different colors. We notice that rational function approximations of the memory-kernel function are becoming closer and closer with increasing approximation order, suggesting that the rational function is sufficient to describe the real memory-kernel function.

B.3 Modeling of the stochastic term in Langevin dynamics by the maximum-likelihood method

Since the form of the generalized Langevin equation poses a challenge for further investigation, and $R(t)$ represents the colored-noise term in the generalized Langevin equation, we need to represent the generalized Langevin equation with extended dynamics driven by the white-noise term. For simplicity and demonstration, the first-order approximation of the memory-kernel function is used. Therefore, after the inverse Laplace transform and substitution, we can define the auxiliary variable, $d(t) = -\int_0^t A_1 e^{B_1(t-\tau)}\dot{\theta}(\tau)d\tau + R(t)$. Under the Leibniz rule, $d(t)$ can be differentiated as $\dot{d}(t) = -A_1\dot{\theta}(t) - B_1\int_0^t A_1 e^{B_1(t-\tau)}\dot{\theta}(\tau)d\tau + \dot{R}(t)$. Since $R(t)$ satisfies the second fluctuation-dissipation theorem, $R(t)$ can be expressed as the initial condition, $d(0)$, and the white noise, $W(t)$: $R(t) = \int_0^t e^{B_1(t-\tau)}W(\tau)d\tau + e^{B_1 t}d(0)$. Next, after substitution, $\dot{d}(t)$ can be rewritten as $\dot{d} = B_1 d - A_1\dot{\theta} + W$. Therefore, the in-plane waving motion of the coral polyp under the first-order approximation is governed by Equation (3.9). In this way, the in-plane waving motion can be easily simulated by solving this equation set.

As an example, the probability density function of the white-noise term of coral polyp #3 labeled in Figure 3.1(b) is shown in Figure B.3. It is difficult to determine the distribution function because this probability density function is similar to some assumed distribution by visual comparison. Therefore, the maximum-likelihood method is adopted to determine the optimal parameter, for several distribution candidates, (a) $\rho_\lambda(W) = ce^{-\lambda|W|}$, (b) $\rho_\mu(W) = c|W|^{-\mu}$ and (c) $\rho_\sigma(W) = \frac{1}{\sqrt{2\pi\sigma^2}}e^{-\frac{W^2}{2\sigma^2}}$ which are the exponential distribution, power law distribution, and normal distribution, respectively. Given a set of white-noise terms, $W = w_1, w_2, \ldots, w_n$, and a probability density function, $\rho_\lambda(W)$, where λ is a vector of k parameters, the log likelihood of the probability density function can be expressed by

$$\ln L(\lambda|R) = \ln \Pi_{j=1}^{n} \rho_\lambda(r_j) = \sum_{j=1}^{n} \ln \rho_\lambda(r_j) \tag{B.6}$$

For each candidate, we find λ to maximize the log likelihood and obtain the optimal parameters. Herein, the Nelder-Mead simplex search algorithm is used to find the extrema. Three candidates with optimal parameters are exhibited in Figure B.3. We notice that an obviously normal distribution does not fit our probability density function, but the other three distributions are difficult to distinguish. To find the preference between the different model distributions, the likelihoods, L, of which are maximized, the Akaike information criterion and the Bayesian information criterion, defined as $C_{Ai} = -2 \ln L + 2k$ and $C_{Bi} = -2 \ln L + \ln nk$, respectively, are used. The most appropriate model can minimize the information criterion. The results show that the Akaike and Bayesian information criteria make no difference for selection of the model (i.e., the Bayesian information criterion agrees with the Akaike information criterion on 100% of all data sets). Table B.1 shows the white-noise model for each polyp under different light conditions. These results show that most of the polyps prefer the exponential distribution to model the white-noise term in the generalized Langevin equation under different light conditions.

Table B.1: White-noise model selection for different light conditions. Preferred model for each polyp in each replicated experiment is displayed based on the Akaike information criterion and the Bayesian information criterion.

	Normal light	Blue light	Green light	Red light
Replicate 1	5/5 exponential	4/4 exponential	6/6 exponential	4/4 exponential
Replicate 2	5/5 exponential	5/6 exponential 1/6 power law	5/5 exponential	4/4 exponential
Replicate 3	5/5 exponential	5/5 exponential	6/6 exponential	7/7 exponential

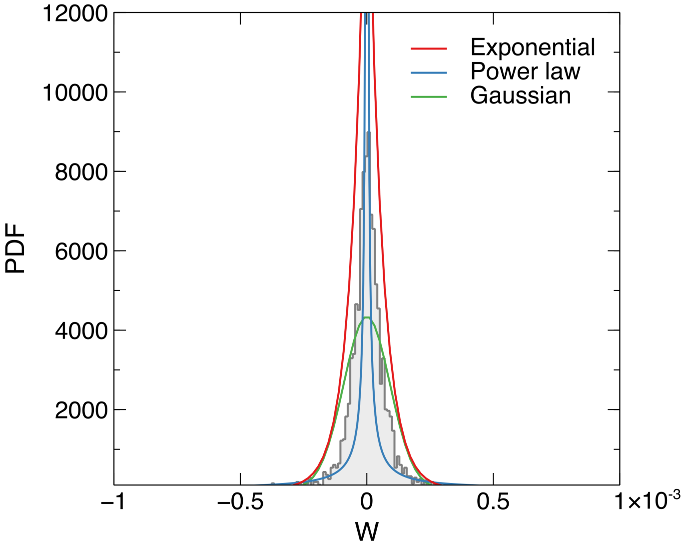

Figure B.3: Probability density function of the white-noise term. Probability density function of the white-noise term, W, is shaded in gray. Red, blue, and green dashed lines show the fitted exponential function, power-law function, and Gaussian function, respectively.

B.4 The model of in-plane waving motion of coral polyps at different temperatures

We also study the model of in-plane waving motion of coral polyps under different temperatures. Likewise, we obtain the memory-kernel function by the data-driven parameterization and the noise term by the maximum-likelihood method. From Figure B.4(a), generally, compared with the case at normal temperature, other cases at 15°C and 30°C have smaller memory-kernel functions, on average. Figure B.4(b) exhibits the parameter λ for the exponential distribution under different light conditions. Compared with normal light, λ is larger at 15°C and 30°C, which results in clear differences in the exponential distribution using the average parameter λ at 25°C [Figure B.4(c)]. Table B.2 shows the white-noise model for each polyp under different temperature conditions. These results show that most of the polyps prefer the exponential distribution to model the white-noise term in the generalized Langevin equation under different temperature conditions.

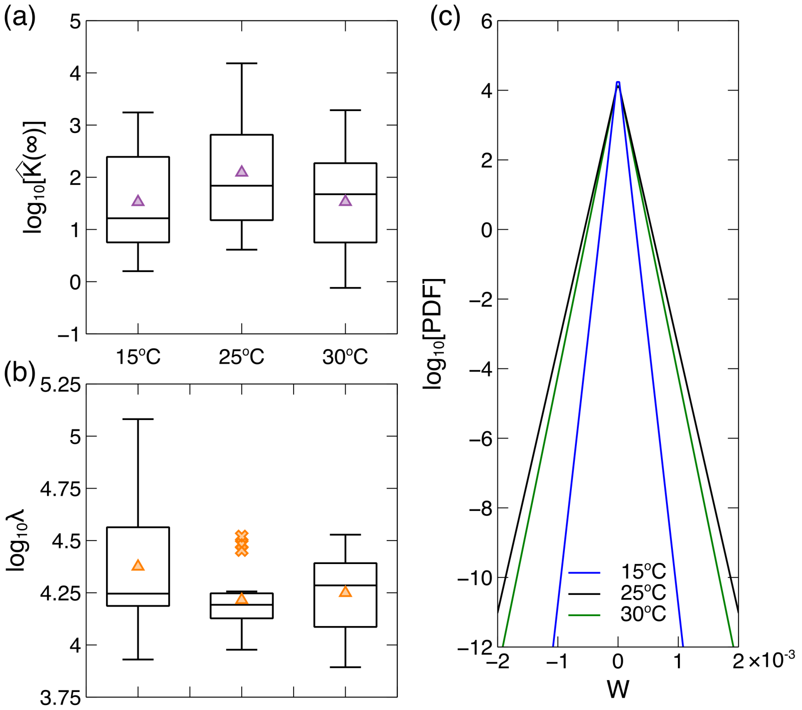

Figure B.4: Model of in-plane waving motion of coral polyps under different temperatures. (a) Value of the memory-kernel function at the Markovian limit, $\hat{K}(\infty)$, of coral polyps at 15°C, 25°C, and 30°C. (b) Parameter λ for the exponential distribution to model the white-noise term at 15°C, 25°C, and 30°C. (c) Fitted PDF of the white-noise terms at different temperatures by using the average parameter λ. Cross and triangle symbols in (a)(b) represent the outliers and mean, respectively.

Table B.2: White-noise model selection for different temperatures. Preferred model for each polyp in each replicated experiment is displayed based on the Akaike information criterion and the Bayesian information criterion.

	15°C	25°C	30°C
Replicate 1	6/6 exponential	5/5 exponential	5/5 exponential
Replicate 2	5/5 exponential	5/5 exponential	4/5 exponential 1/5 power law
Replicate 3	4/4 exponential	5/5 exponential	5/5 exponential

Appendix C

DATA-DRIVEN DISCOVERY OF SPATIOTEMPORAL COHERENT PATTERNS IN PULSATING SOFT CORAL TENTACLE MOTION WITH DYNAMIC MODE DECOMPOSITION

C.1 Experimental methods

C.1.1 Experimental setup and procedure

A specimen of *Anthelia glauca* was purchased from a local store (Seattle Corals Aquariums) and was reared in a 5.68 l aquarium with specific gravity artificial seawater = 1.025 g/cm^3 and $pH = 8.4$. Regular tests on pH, NH_4^+, NO_2^- and NO_3^- were done to make sure the water quality was suitable for coral. The continuous water flow within the tank was provided by a Hydor Koralia Nano Aquarium Circulation Pump with a 908.5 l/h flow rate. Note that 2 h before initiating the experiment, the aquarium pump was paused to minimize the effect of water flow on spontaneous tentacle motion. The temperature of the water was controlled by the 50 W FREESEA submersible heater and was maintained in 25°C. Light was provided on a 12/12 h daylight cycle using an AI Prime 16HD Reef light system. The light used to rear our coral was mixed with 20% UV, 10% violet, 10% royal blue, 10% blue, 10% moonlight, and 10% cool white in the setting options on the AI Prime 16HD Reef light system. In the experimental study of the effect of light conditions, all aquarium settings were kept the same, except the light. The settings for blue ($450 \sim 495$ nm), green ($495 \sim 570$ nm), and red ($620 \sim 750$ nm) light conditions in the experiments were monochromatic with the same power as the laboratory light.

C.1.2 Stereovision system

Two synchronized cameras with lenses (Canon EOS 5D Mark IV and EF 100mm f/2.8L Macro IS USM) were used, along with a timer to take images every 10 s. The camera settings were: F10, ISO8000, 1/200 s. The two cameras were fixed on an optical table for stability and long-period shooting for 11 h. The macro lenses of two cameras were perpendicular to the aquarium to avoid blurred effect caused by refraction. Calibration and acquisition of coefficient of direct linear transformation were implemented by using a checkerboard pattern.

C.1.3 Tracking of coral tentacle motion

Each tentacle was simplified for analysis as a line segment connecting the polyp mouth to each tip of the tentacle so that the relative position of could be easily calculated. The polyp mouth and the tip of the tentacle were tracked using the correlation-based algorithm. Note that, occasionally, the tentacles contracted into the polyp which may be related to the feeding behaviors. Hence, the corresponding data was missing due to the unavailable positions of tentacle tips.

C.1.4 Direct linear transformation

After the tentacle coordinates in each frame obtained by each camera was identified, the coordinates in three-dimensional space were calculated using the direct linear transformation (DLT). Calibration and acquisition of the coefficient of DLT were implemented by using a checkerboard pattern. With the DLT method, each calibrated camera has a set of 11 coefficients that map from world coordinates to image pixel position for a single camera from a particular view, which is mathematically expressed as follows:

$$u = \frac{L_1 X_w + L_2 Y_w + L_3 Z_w + L_4}{L_9 X_w + L_{10} Y_w + L_{11} Z_w + 1} \tag{C.1}$$

$$v = \frac{L_5 X_w + L_6 Y_w + L_7 Z_w + L_8}{L_9 X_w + L_{10} Y_w + L_{11} Z_w + 1} \tag{C.2}$$

where (u, v), (X_w, Y_w, Z_w) and $L_1 - L_{11}$ are the pixel coordinates, three dimensional (3D) coordinates, and the DLT coefficients, respectively. As long as the DLT coefficients from two camera views are obtained, the pixel coordinates of a single point in both camera views can be combined to find the corresponding 3D coordinate, which can be determined by finding the intersection of the two lines from each camera view in 3D space.

The images of the checkerboard pattern from different positions and angles are taken from both camera views. The perspective matrix $\mathbf{P}$ that can map the world coordinates to image pixel position, which is $\mathbf{K}[\mathbf{R}|\mathbf{T}]$ can be calculated, where $\mathbf{K}$ is the intrinsic matrix containing focal lengths and the camera's principle points. $\mathbf{R}$ and $\mathbf{T}$ are the rotation and translation between the world coordinate system and camera, respectively. The relation is mathematically expressed as follows:

$$s\begin{bmatrix} u \\ v \\ 1 \end{bmatrix} = \mathbf{K}[\mathbf{R}|\mathbf{T}]\begin{bmatrix} X_w \\ Y_w \\ Z_w \\ 1 \end{bmatrix} \tag{C.3}$$

Finally, the DLT coefficients can be calculated after the direct relation between $\mathbf{P}$ and the DLT coefficients from $L_1 - L_{11}$ are found.

Appendix D

ELASTIC CHIRAL LANDAU LEVEL AND SNAKE STATES IN ORIGAMI METAMATERIALS

D.1 Simulation setup

The design parameters and mechanical parameters used in the numerical simulation are shown in TABLE D.1 and TABLE D.2, respectively.

Table D.1: Design parameters for the origami.

m (kg)	j $(\mathrm{kg} \cdot \mathrm{m}^2)$	N	R (m)	θ_0 (°)
58.8×10^{-3}	6.77×10^{-5}	6	36×10^{-3}	70

Table D.2: Mechanical parameters for the origami.

k_a $(\mathrm{N} \cdot \mathrm{m}^{-1})$	k_b $(\mathrm{N} \cdot \mathrm{m}^{-1})$	k_Ψ $(\mathrm{N} \cdot \mathrm{m} \cdot \mathrm{rad}^{-1})$	k_c $(\mathrm{N} \cdot \mathrm{rad}^{-1})$
6055	3743	7.277×10^{-3}	25

The heights h_1 and h_2 for origami 1 and origami 2 from left to right are linearly varying from 30 mm to 10 mm and from 10 mm to 30 mm, respectively. The mechanical parameters k_a, k_b represent the axial spring constant along the crease a, b, and k_Ψ represents the torsional spring constant along the bottom crease. k_c represents the torsional spring constant connecting the bottom plates of origami.

The band structure of the origami metamaterials is calculated based on the linearized truss model of the Kresling origami [64, 192]. The unit cell contains two Kresling origamis on two sites (1) and (2). After applying the periodic boundary condition (Bloch's theorem), the linearized equation of motion can be expressed as:

$$m\ddot{u}_t^{(1)} - \alpha_{11}(-u_t^{(1)}) - \alpha_{12}(\theta_b^{(1)} - \phi_t^{(1)}) = 0 \tag{D.1a}$$

$$j\ddot{\phi}_t^{(1)} - \alpha_{21}(-u_t^{(1)}) - \alpha_{22}(\theta_b^{(1)} - \phi_t^{(1)}) = 0 \tag{D.1b}$$

$$\begin{aligned} &j\ddot{\theta}_b^{(1)} - \alpha_{21}u_t^{(1)} - \alpha_{22}(\phi_t^{(1)} - \theta_b^{(1)}) - k_c(-\theta_b^{(2)} - \theta_b^{(1)}) \\ &- k_c(-\theta_b^{(2)}e^{i\mathbf{k}\cdot\mathbf{a_1}} - \theta_b^{(1)}) - k_c(-\theta_b^{(2)}e^{i\mathbf{k}\cdot\mathbf{a_2}} - \theta_b^{(1)}) = 0 \end{aligned} \tag{D.1c}$$

$$m\ddot{u}_t^{(2)} - \beta_{11}(-u_t^{(2)}) - \beta_{12}(\theta_b^{(2)} - \phi_t^{(2)}) = 0 \tag{D.1d}$$

$$j\ddot{\phi}_t^{(2)} - \beta_{21}(-u_t^{(2)}) - \beta_{22}(\theta_b^{(2)} - \phi_t^{(2)}) = 0 \tag{D.1e}$$

$$\begin{aligned} &j\ddot{\theta}_b^{(2)} - \beta_{21}u_t^{(2)} - \beta_{22}(\phi_t^{(2)} - \theta_b^{(2)}) - k_c(-\theta_b^{(1)} - \theta_b^{(2)}) \\ &- k_c(-\theta_b^{(1)}e^{-i\mathbf{k}\cdot\mathbf{a_1}} - \theta_b^{(2)}) - k_c(-\theta_b^{(1)}e^{-i\mathbf{k}\cdot\mathbf{a_2}} - \theta_b^{(2)}) = 0 \end{aligned} \tag{D.1f}$$

where the linear coefficients α and β correspond to origami 1 and origami 2. These coefficients can be derived from the second derivative of the potential energy of the single origami U_P which can be expressed as:

$$U_P = \frac{N}{2}[k_a(a-a_0)^2 + k_b(b-b_0)^2 + 2k_\Psi(\Psi-\Psi_0)^2] \tag{D.2}$$

where

$$a = \sqrt{(h_0-\delta u)^2 + 4R^2\sin^2(\frac{\delta\phi}{2} + \frac{\theta_0}{2} - \frac{\pi}{2N})} \tag{D.3}$$

$$b = \sqrt{(h_0-\delta u)^2 + 4R^2\sin^2(\frac{\delta\phi}{2} + \frac{\theta_0}{2} + \frac{\pi}{2N})} \tag{D.4}$$

$$\Psi = \arctan\frac{h_0 - \delta u}{R[\cos(\frac{\pi}{N}) - \cos(\delta\phi + \theta_0)]} \tag{D.5}$$

The subscript 0 denotes the initial value with $\delta u = \delta\phi = 0$. The linear coefficients are thus calculated as $\alpha_{11} = \partial^2_{\delta u}U_P$, $\alpha_{12} = \alpha_{21} = \partial_{\delta u\delta\phi}U_P$ and $\alpha_{22} = \partial^2_{\delta\phi}U_P$. β_{11}, β_{12}, β_{21} and β_{22} can also be calculated accordingly.

Figure D.1(a) shows the variation of α and β along the x direction of our origami metamaterial. The band structure $\omega(\mathbf{k})$ can be obtained by solving the eigenvalue equation summarized from Equation (D.1a) to Equation (D.1f) as a function of Bloch wave vector $\mathbf{k}$ in the first Brillouin zone:

$$[\omega^2 M + D(\mathbf{k})]U(\mathbf{k}) = 0 \tag{D.6}$$

Here, ω denotes the angular frequency. M denotes the mass matrix containing the mass m and rotational inertia j. $D(\mathbf{k})$ is the dynamical matrix and $U(\mathbf{k})$ is the corresponding eigenmode $[u_t^{(1)}, \phi_t^{(1)}, \theta_b^{(1)}, u_t^{(2)}, \phi_t^{(2)}, \theta_b^{(2)}]^T$, as a function of $\mathbf{k}$.

The frequency response of the origami metamaterial is calculated by:

$$(\omega^2 M + D)U = F \tag{D.7}$$

where F is the excitation source exerted on the system. M and D are the mass matrix and stiffness matrix of the system. The calculated U is translated to the field distributions (u_t, ϕ_t and θ_b) of the origami metamaterial.

D.2 $\mathbf{k}\cdot\mathbf{p}$ *perturbation method*

To understand the formation of the synthetic gauge field, we use the $\mathbf{k}\cdot\mathbf{p}$ perturbation method to explain analytically [198–202]. When the heights of two origamis in the unit cell are the same, the third and the fourth bands, the fifth and the sixth bands, degenerate to the Dirac cone at $\mathbf{K}$ point, as shown in Figure. 5.1(c). However, when the heights of two origamis are not equivalent, the linear coefficients for origamis are different [Figure D.1(a)], resulting in the disappearance of degeneracy and formation of the band gap. This system can be regarded as the new system perturbed from the original one [Equation (D.6)]. The corresponding eigenvalue problem can be written as:

$$[\omega'^2 M + D'(\mathbf{k})]U'(\mathbf{k}) = 0 \tag{D.8}$$

When the perturbation is small, we can consider the eigenmode of the perturbed system can be approximated as linear combinations of eigenmodes of the original degenerate system, according to the $\mathbf{k}\cdot\mathbf{p}$ perturbation method. Following this method, the eigenmodes $U'(\mathbf{k})$ can be approximated:

$$U'(\mathbf{k}) \approx c_1 U_1(\mathbf{K}) + c_2 U_2(\mathbf{K}) \tag{D.9}$$

The Equation (D.9) is substituted into the Equation (D.8):

$$U_1^\dagger(\mathbf{K})[\omega'^2 M + D'(\mathbf{k})][c_1 U_1(\mathbf{K}) + c_2 U_2(\mathbf{K})] = 0 \tag{D.10a}$$

$$U_2^\dagger(\mathbf{K})[\omega'^2 M + D'(\mathbf{k})][c_1 U_1(\mathbf{K}) + c_2 U_2(\mathbf{K})] = 0 \tag{D.10b}$$

The problem can be further simplified as the eigenvalue problem:

$$\Delta H\psi = \Delta\omega\psi \tag{D.11}$$

where ΔH is the perturbation Hamiltonian and $\psi = (c_1, c_2)^T$. When $\mathbf{k} = \mathbf{K}$, $\Delta H = m_K\sigma_z$, where m_K is the Dirac mass term and σ_z is the Pauli matrix. In this way, we can calculate the mass term theoretically as shown in Figure D.1(c). When the gradient of mass term is achieved along x direction, the out-of-plane synthetic gauge field $A_z = m_K(x)$ can be realized, essentially indicating the in-plane pseudomagnetic field along the y direction B_y ($B_y = \nabla \times A_z$).

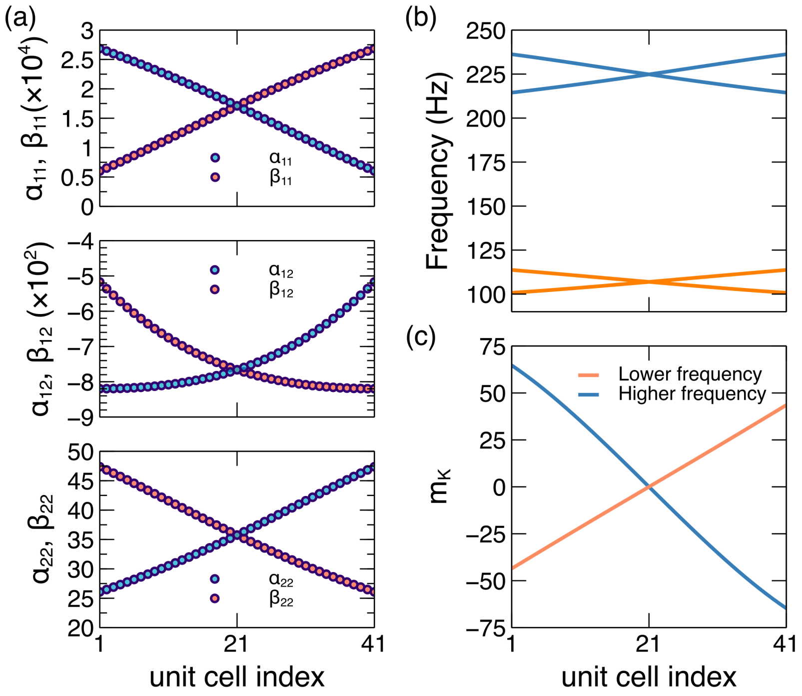

Figure D.1: Linearized coefficients along a supercell and variations of band gap and mass term m_K. (a) The linearized coefficients α_{11} and β_{11}, α_{12} and β_{12}, α_{22} and β_{22} for origami 1 and 2 along the supercell from top panel to bottom panel. Note that $\alpha_{12} = \alpha_{21}$ and $\beta_{12} = \beta_{21}$. (b) The variation of band gap at lower and higher band gap of each unit cell along the supercell. (c) The mass term m_K at lower and higher band gap of each unit cell along the supercell.

D.3 Theoretical Landau level dispersion

Here, we derive the theoretical Landau level dispersion from the linearly varying mass term along x direction shown in Figure D.1(c). The Hamiltonian of the system can be expressed as below:

$$H = v(\hat{k}_x\sigma_x \pm \hat{k}_y\sigma_y) + m_K(x)\sigma_z \tag{D.12}$$

We can observe the linear relation of $m_K(x) = qx$ in Figure D.1(c). Also, provided the commutation relations $[\hat{k}_x, \hat{k}_y] = 0$, $[\hat{k}_y, x] = 0$ and $[\hat{k}_x, x] = -i$, the Hamiltonian is then squared and written in the matrix form:

$$\begin{bmatrix} (qx)^2 + (v\hat{k}_x)^2 + (v\hat{k}_y)^2 & iqv \\ -iqv & (qx)^2 + (v\hat{k}_x)^2 + (v\hat{k}_y)^2 \end{bmatrix} \varphi = \omega^2\varphi \tag{D.13}$$

Next, we define the creation and annihilation operators:

$$\hat{a}^\dagger = N(v\hat{k}_x - i|q|x),\ \hat{a} = N(v\hat{k}_x + i|q|x) \tag{D.14}$$

The commutation relation $[\hat{a}^\dagger, \hat{a}] = 1$ requires that

$$\begin{aligned} 2N^2[v\hat{k}_x, i|q|x] &= 2N^2v|q| = 1 \\ N^2 &= \frac{1}{2v|q|} \end{aligned} \tag{D.15}$$

The particle number operator is then defined as:

$$\begin{aligned} \hat{n} = \hat{a}^\dagger\hat{a} &= N^2(v^2\hat{k}_x^2 + q^2x^2 + |q|v) \\ \frac{1}{N^2}\hat{n} &= v^2\hat{k}_x^2 + q^2x^2 + |q|v \end{aligned} \tag{D.16}$$

The Equation (D.16) is then substituted into Equation (D.13):

$$[(2|q|v\hat{n} - |q|v + v^2\hat{k}_y^2)\mathbf{I} - qv\sigma_y]\varphi = \omega^2\varphi \tag{D.17}$$

By squaring two sides of Equation (D.17) after switching $-qv\sigma_y$ and ω^2 we obtain:

$$(v^2\hat{k}_y^2 + 2|q|v\hat{n})\varphi = \omega^2\varphi \tag{D.18}$$

Finally, given that the system is connected to the wall by springs along x direction, the theoretical Landau levels dispersion can be expressed as:

$$\omega_n = \begin{cases} \operatorname{sgn}(q)vk_y, & n = 0 \\ \pm\sqrt{v^2k_y^2 + 2n|q|v}, & n \geq 1 \end{cases} \tag{D.19}$$

Therefore, as mentioned in the main text, the zeroth Landau level has the linear dispersion relation with the group velocity related to the sign of the effective Dirac mass, and other Landau levels are quantized.

Appendix E

CHARACTERIZATION OF ELASTIC TOPOLOGICAL STATES USING DYNAMIC MODE DECOMPOSITION

E.1 The truncation of singular values of the data matrix

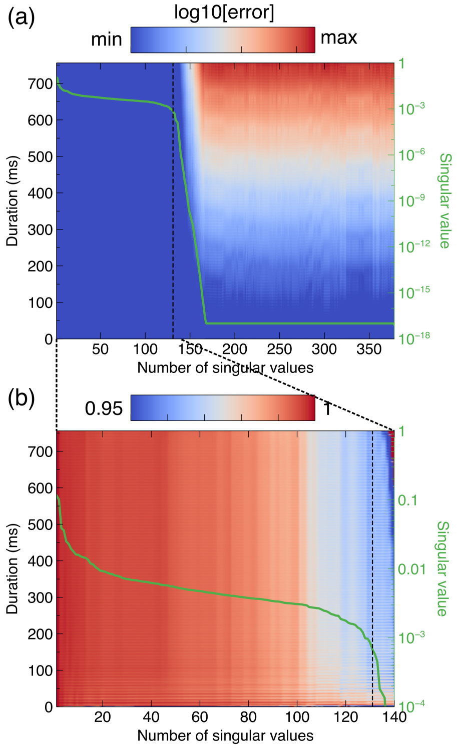

Figure E.1: (a) Reconstruction error as a function of truncation and duration. Error is shown on a logarithmic scale. (b) Zoom-in reconstruction error as a function of truncation from 1 to 140 and duration. Vertical dashed lines in (a) and (b) correspond to the selected $r = 131$.

Choosing the proper truncation of the singular value decomposition of X is important to obtain the best-fit linear operator A. To identify the truncation r of the singular values, we wish to ensure the minimization of the reconstruction error. The reconstruction $\hat{X}$ is conducted by DMD modes inside the bandgap region and corresponding time dynamics and is compared with the original wave propagation. In Figure E.1(a), the map of the reconstruction error calculated by $E(t) = \frac{\|X(t)-\hat{X}(t)\|_2}{\|X(t)\|_2}$ is given as a function of the number of singular values (truncation r) and duration. The singular value spectrum shows that singular values decay slowly, indicating that many modes are needed. Accordingly, with the increase of the number of singular values in a certain range ($1 \sim 140$), the reconstruction error does not change significantly in the logarithm scale. However, when the number of singular values further increases, the reconstruction error will significantly increase.

Therefore, the proper truncation is in the range of 1 to 140, which we magnify in Figure E.1(b). As the number of singular values increases, the reconstruction error will decrease to a minimum. We choose the $r = 131$ as the number of singular values corresponding to the inflection point in the singular value spectrum.

E.2 DMD spectra and modes of wave propagation along interface with different shapes

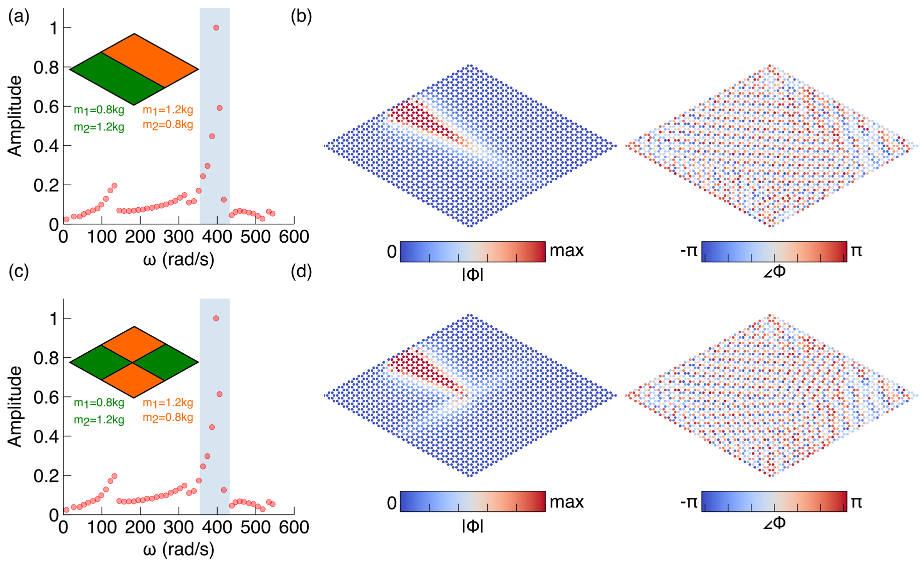

Figure E.2: DMD spectrum and DMD modes of straight interface and cross interface are shown in (a), (b) and (c), (d), respectively. Insets in (a) and (c) are the configurations of elastic topological metamaterials.

Figure E.2(a) gives the DMD spectrum indicating the relation between the frequency and the mode amplitude for the topological states propagation along the straight interface (configuration shown in the inset). Similar to Figure E.2(b), it is clear that the region with high mode amplitude corresponds to the bandgap region (shaded area). The mode inside the bandgap region with the largest amplitude is chosen as the prototypical mode of interest (and of relevance to the dynamics). Figure E.2(b) exhibits the magnitude and phase of this dynamic spatial mode of our system. The interface state can be observed from the magnitude of the DMD modes. The displacement is concentrated along the straight interface and decays rapidly away from the interface. The elastic waves can travel along the interface with bends. The phases of the DMD modes also reflect the characteristics of topological states. The distribution of phase along the interface has a certain pattern, representing the valley pseudospin of our system as described in the main text. Likewise, in Figure E.2(c) and E.2(d), we calculate the DMD spectrum and DMD modes inside the bandgap region with the largest amplitude for the topological states propagation along the cross interface (configuration shown in the inset). The DMD mode in Figure E.2(d) shows that the elastic wave travels along the path at the beginning and when it arrives at the intersection, it propagates to two sides instead of the straight path. Because of the valley-locking effect, the wave will propagate along certain interface with same valley projection [221, 265–267]. The generated elastic wave is projected by the **K** valley according to the group velocity in projected band structure [Figure 6.1(c)]. Therefore, the elastic wave will only propagate along the **K**-valley-projected topological interfaces. Note that apart from DMD modes shown in Figure E.2(b) and E.2(d) which have the largest amplitudes in the DMD spectra, other DMD modes inside the bandgap region are also interface states.

E.3 DMD implementation on the topological state propagation excited by a transient source

In the main text, our system with the Z-shaped interface is excited by a constant harmonic force. Now we explore the system excited by a transient source. In our example, we use the Gaussian tone burst $F = F_0 e^{-(\frac{\omega t}{30})^2}$ to excite our system and follow the procedure introduced in the main text to analyze the system's response using DMD. Figure E.3(a) shows

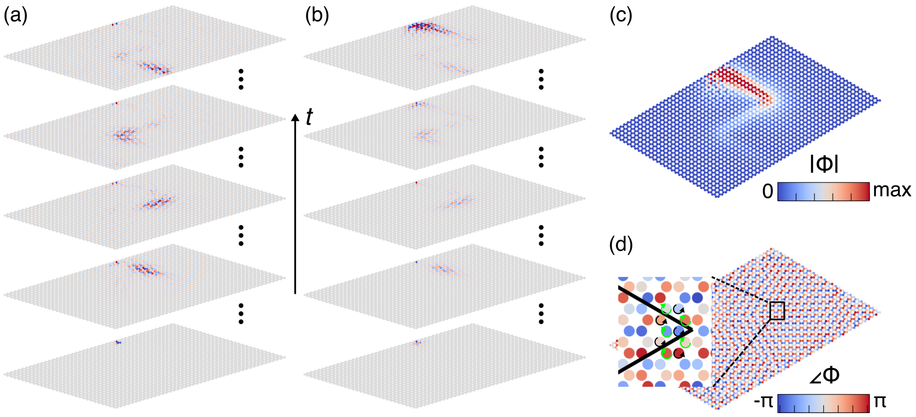

Figure E.3: The DMD implementation. (a),(b) Snapshots of original and reconstructed wave propagation excited by the Gaussian burst represented by the horizontal displacement u_x along a Z-shaped interface at $t = 2$, 192, 380, 570 and 758 ms (with the time evolving from the bottom to the top), respectively. (c) Magnitude of the DMD mode with the largest amplitude inside the bandgap region. (d) Phase of the DMD mode with the largest amplitude inside the bandgap region. Inset shows the magnified view around the interface (black line) illustrating the phase difference and valley pseudospin. Black and green arrows show the pseudospin up and pseudospin down indicated by the phase evolution around hexagon corners, respectively.

several snapshots of wave propagation along the Z-shaped interface; we can observe that an elastic wave can propagate through the shape bend smoothly due to the topological protection. Figure E.3(b) exhibits the reconstructed wave propagation by DMD reconstruction, which is visually similar to the original evolution dynamics though it starts to blow up at the input port at the end of the reported time horizon, suggesting the qualitative nature of the reconstruction. Similar to the situation in the main text, Figure E.3(c) exhibits the magnitude of DMD modes showing that an elastic wave can travel along an interface featuring bends. As shown in Figure E.3(d), the phase of the DMD mode indicates the phase difference around the corners of the honeycomb and the valley pseudospin of the excited valley in our system. This demonstrates the ability of DMD to learn the topological nature of the wave propagation in topological metamaterials.

E.4 Dynamic mode decomposition with time-delay embedding

Recently, the approach of time-delay embedding has been shown to be a general method to generate proper observable measurements to render the reconstruction more accurate as discussed in the main text. By embedding future temporally consecutive snapshots into the current snapshot, time-delay embedding augments the limited spatial observables and provides extra observables. The DMD with time-delaying embedding can be achieved by the augmented data matrix X_{aug} by shift-stacking the original data matrix as shown below:

$$X_{aug} = \begin{bmatrix} | & | & & | \\ x_1 & x_2 & \dots & x_{m-h} \\ | & | & & | \\ | & | & & | \\ x_2 & x_3 & \dots & x_{m-h+1} \\ | & | & & | \\ | & | & & | \\ x_h & x_{h+1} & \dots & x_{m-1} \\ | & | & & | \end{bmatrix} \tag{E.1}$$

where h is the number of stacks. X'_{aug} can be induced likewise. Using the augmented data matrix to conduct DMD, the reconstruction error can be reduced. As shown in Figure E.4, the relative error calculated by $E = \frac{\|X-\hat{X}\|_2}{\|X\|_2}$ decreases with the increase of the number of stacks and becomes saturated at around 0.65 even with a larger number of stacks. The error may come from the inherent deficiency of DMD on the wave propagation problem as discussed in Section 6.3. However, when the number of stacks increases, the augmented data matrix becomes large, leading to a heavy computation cost. Therefore, there is a tradeoff balance between accuracy and efficiency in the case of real-world applications and practitioners should seek to strike a relevant balance to that effect.

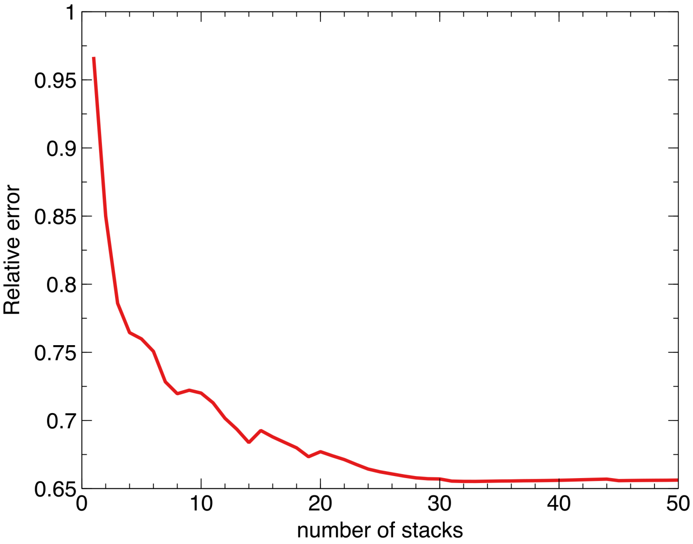

Figure E.4: Relative error of reconstruction as a function of number of stacks.

E.5 *Classification of topological and traditional metamaterials with different interfaces*

For classification of topological and traditional metamaterials with different interfaces, we follow the method we introduce in the main text. The topological metamaterial is composed of the metamaterial with $m_1 = 0.8$ kg and $m_2 = 1.2$ kg and the metamaterial with $m_1 = 1.2$ kg and $m_2 = 0.8$ kg. The traditional metamaterial is constructed based on the defect states by the metamaterial with $m_1 = 0.8$ kg and $m_2 = 1.2$ kg, where the masses are replaced by $m_2 = 1.2$ kg along the straight and cross interface to create defects. Following the method in the main text, we extract the principal components of the library composed of DMD modes of topological and traditional metamaterials with different interfaces (straight and cross interfaces). As for different shapes of the interfaces, the feature space from the principal components for the DMD modes to project on can be determined as visualized in Figures E.5(a) and E.5(c), corresponding to the straight interface and cross interface. Similarly, the feature spaces are also the second principal components in the SVD, in which the main difference between topological wave propagation and non-topological wave propagation is reflected, and hence can classify two types of metamaterials. We test the feature

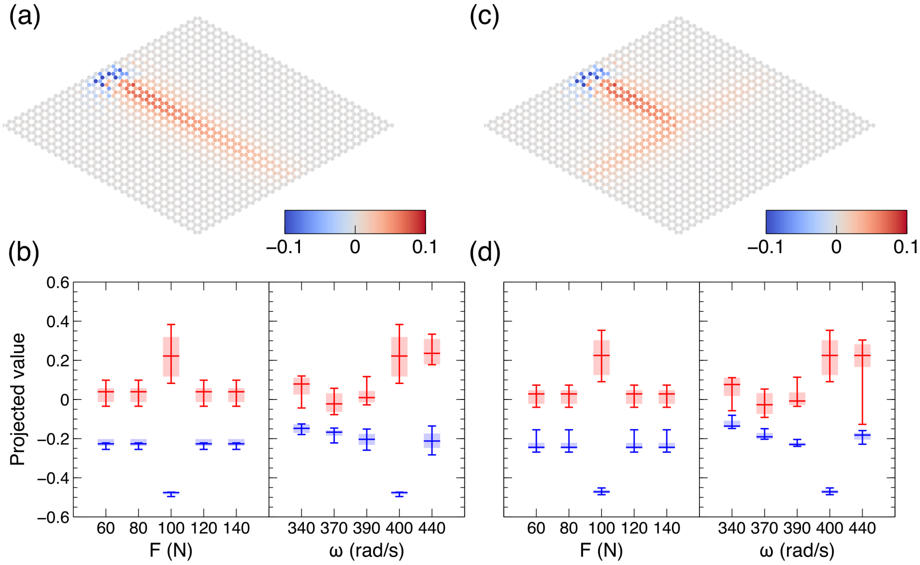

Figure E.5: Classification of topological and traditional waveguides with different interface. (a), (c) Feature space of topological metamaterials with straight interface and cross interface. (b), (d) Projected values of each DMD mode extracted from the system under excitation of different forces and different frequencies, corresponding to straight interface (a) and cross interface (c). Red and blue regions indicate topological and traditional DMD modes, respectively. Error bars indicate the range of the minima and maxima of projected values.

space on the case excited under different forces and different frequencies. After the DMD modes inside the bandgap for both topological and traditional metamaterials are projected onto the feature space, the DMD modes lead to a scalar value, which is separated well between the two families, and can be classified using the k-means unsupervised clustering, as shown in Figures E.5(b) and E.5(d). For both wave propagation along straight interface and cross interface, the classification results and ground truth have excellent agreement.

E.6 Synthetic wave propagation along the given interface using DMD

We demonstrate another application of the usefulness of DMD modes in topological metamaterials. Synthetic wave propagation along the given interface is important when there is lack of data due to the sensor problems or measurement difficulties. DMD is capable of extracting the time dynamics and corresponding dynamic modes, which can help with the synthetic topological state propagation along the given interface. Here, we use DMD modes calculated from a part of data (training data) to build a low-dimensional model, and with the knowledge of the position of interface further to synthesize the future propagation of elastic wave. Here, as shown in Figure E.6(a), we use the wave propagation in topological metamaterials from 0 to 200 ms as the training data. Then, DMD is used to extract the DMD modes inside the bandgap and the corresponding time dynamics (two pairs of DMD modes inside the bandgap are used). Since wave propagation is a process with time and space variation together, the DMD modes are limited in space due to the nature of spatial modes, resulting in stoppage of the wave and, accordingly, failure of the synthesis. A feasible way that we have found relevant towards bypassing this issue is to extend the DMD modes along the (a priori) given interface and to approximate the future wave propagation using the extended DMD modes and the time dynamics from the training data.

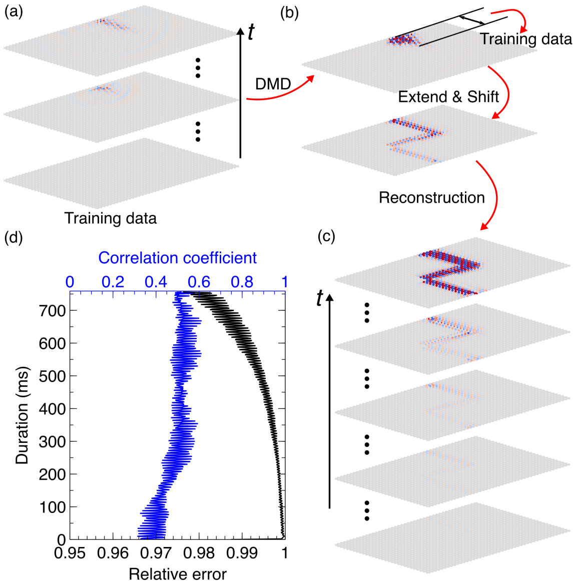

Figure E.6: Synthesis of topological states propagation along the given interface. (a) Snapshots of horizontal displacement u_x from 0 to 200 ms used for training. (b) Top panel displays one of the DMD modes inside the bandgap of the training data. The bottom panel displays the corresponding extended and shifted DMD modes along the Z-shaped interface. (c) Snapshots of the horizontal displacement u_x for the synthetic wave propagation at $t = 2$, 192, 380, 570 and 758 ms. (d) Synthesis error and correlation coefficient as a function of duration are shown in black line and blue line, respectively.

First, the least squares method is used in order to identify the time-varying wave velocity $\mathbf{c}(t)$ by a set of pairs of the positions of wave front and corresponding time. Therefore, the position of wave front can be determined at arbitrary time. Next, after the extracted DMD modes inside the bandgap are reshaped to a matrix form, they are truncated based on the displacement $\mathbf{d} = \int_0^t \mathbf{c}(t')dt'$, corresponding to the number of matrix columns, as shown in the training data in Figure E.6(b). The DMD is used again to predict the DMD modes in the future when the elastic wave propagates to the arbitrary position. The synthesis time is determined by the length of the given interface. Note that extension by DMD only considers the speed of wave propagation, assuming that it is effectively constant during each segment of the interface, instead of other associated properties such as the dispersive radiation, which is found to be minimal in the present setting. Then, the extended DMD modes ϕ_e are shifted according to the shape of the interface, resulting in the shifted DMD mode ϕ_s. As an example, one of the DMD modes inside the bandgap is shown in Figure E.6(b), where the DMD mode is constrained in space which will cause the stoppage of wave propagation after 200 ms. After being extended by DMD and shifted by the shape of interface, the DMD mode constrained in a certain space can cover the given interface (Z-shaped interface), as shown in Figure E.6(b). Finally, after we extend and shift all DMD modes inside the bandgap from the training data, the time dynamics of the training data are used to synthesize the wave propagation along the Z-shaped interface, detailed as below:

$$\hat{X} = \Phi_s \Lambda^{t-1} Z_s \tag{E.2}$$

where Φ_s is formed by ϕ_s. The diagonal entries of Λ contain DMD eigenvalues from training data and $Z_s = \Phi_s \backslash x_1$. x_1 is the initial condition of our system. As shown in Figure E.6(c), several snapshots of synthetic wave propagation clearly exhibit the elastic wave traveling along the Z-shaped interface. This process is qualitatively similar to the snapshots shown in Figure 6.2(b). According to Figure E.6(d), the relative error compared with the reconstructed results in Figure 6.2(b) is in the range of $0.95 \sim 1$. Likewise, we use the correlation coefficient to characterize the qualitative performance of reconstruction, which is around 0.5. This is smaller than that for the reconstruction due to the limited number of modes and time dynamics. Yet, this synthesis of wave propagation along the given interface still provides a reasonable visualization of future wave propagation. It should be mentioned that aforementioned approach of DMD with time-delay embedding can also be used in the synthesis since this approach can generate the dynamics and corresponding modes.

Appendix F

GEOMETRY-INFORMED DYNAMIC MODE DECOMPOSITION IN ORIGAMI DYNAMICS

F.1 Data acquisition

F.1.1 Experimental data

In the example of the dual origami structure, the raw experimental data was used for the giDMD model. The experimental data and experimental procedures were detailed in the reference [28]. The dynamic test was conducted on a dual triangulated cylindrical origami structure. The design parameters of origami were $h_0 = 50$ mm, $\theta_0 = \pm 70°$, $R = 36$ mm which are the initial height, initial rotational angle, and radius of the cross-section, respectively. The left origami is in negative chirality ($\theta_0 = -70°$) and the right origami is in positive chirality ($\theta_0 = +70°$). The left end of dual origami structure was connected to the shaker (LDS V406 M4-CE, Brüel & Kjær) which applied the single-frequency harmonic excitation to the system. The motion of spherical markers attached to the separators was captured by two action cameras in 240 frames per second and quantified by digital image correlation. The triangulation method was used to find the three-dimensional coordinates of the spherical markers, resulting in the axial displacement u and rotational displacement ϕ of each separator.

F.1.2 Simulation data

In the example of single origami and origami chain, the simulation data was used for the giDMD model. The design parameters and mechanical parameters used in the numerical simulation are shown in Table F.1 and Table F.2, respectively.

The mechanical parameters k_a, k_b represent the axial spring constant along the crease a, b, and k_Ψ represents the torsional spring constant along the bottom crease.

The simulations of the single origami and origami chain under excitation in different

Table F.1: Design parameters for single origami and origami chain.

m (kg)	j ($\mathrm{kg \cdot m^2}$)	N	h_0 (m)	R (m)	θ_0 (°)
58.8×10^{-3}	6.77×10^{-5}	6	30×10^{-3}	36×10^{-3}	±70

Table F.2: Mechanical parameters for single origami and origami chain.

k_a ($\mathrm{N \cdot m^{-1}}$)	k_b ($\mathrm{N \cdot m^{-1}}$)	k_Ψ ($\mathrm{N \cdot m \cdot rad^{-1}}$)
6055	3743	7.277×10^{-3}

frequencies are conducted based on the truss model regarding Kresling unit cell as inter-polygonal spring connecting separators with mass m and rotational inertia j [64, 192, 197]. The equation of motion of the separator can be expressed as:

$$m_n \ddot{u}_n + F_n(\delta u_n, \delta\phi_n) - F_{n-1}(\delta u_{n-1}, \delta\phi_{n-1}) = 0 \tag{F.1a}$$

$$j_n \ddot{\phi}_n + T_n(\delta u_n, \delta\phi_n) - T_{n-1}(\delta u_{n-1}, \delta\phi_{n-1}) = 0 \tag{F.1b}$$

where $\delta u_n = u_n - u_{n+1}$ and $\delta\phi_n = \phi_n - \phi_{n+1}$. The subscript n denotes the n-th separator. The force and torque in Equation (F.1a) and Equation (F.1b) can be further expanded by the summation of the contribution from each spring as below:

$$\begin{aligned} F_n(\delta u_n, \delta\phi_n) =& k_{an} N(\delta u_n - h_0)(1 - \frac{a_0}{a_n}) \\ &+ k_{bn} N(\delta u_n - h_0)(1 - \frac{b_0}{b_n}) \\ &+ 2k_{\Psi n} N R h_0 (\Psi_0 - \Psi_n) \frac{\cos\frac{\pi}{N} - \cos(\delta\phi_n + \theta_0)}{R^2[\cos\frac{\pi}{N} - \cos(\delta\phi_n + \theta_0)]^2 + (h_0 - \delta u_n)^2} \end{aligned} \tag{F.2a}$$

$$\begin{aligned} T_n(\delta u_n, \delta\phi_n) =& k_{an} N R^2 \sin(\delta\phi_n + \theta_0 - \frac{\pi}{N})(1 - \frac{a_0}{a_n}) \\ &+ k_{bn} N R^2 \sin(\delta\phi_n + \theta_0 + \frac{\pi}{N})(1 - \frac{b_0}{b_n}) \\ &+ 2k_{\Psi n} N R h_0 (\Psi_0 - \Psi_n) \frac{\sin(\delta\phi_n + \theta_0)(h_0 - \delta u_n)}{R^2[\cos\frac{\pi}{N} - \cos(\delta\phi_n + \theta_0)]^2 + (h_0 - \delta u_n)^2} \end{aligned} \tag{F.2b}$$

where the parameters with subscript 0 denote the initial origami configuration.

The calculation of the band structure is based on the linearized truss model of the unit cell in order to represent the small amplitude excitation. The unit cell contains two origami elements whose front separators denote the sites (1) and (2). The linearized equations of motion can be expressed as:

$$m_n\ddot{u}_n^{(1)} - \alpha_{11}(u_n^{(2)} - u_n^{(1)}) - \beta_{11}(u_{n-1}^{(2)} - u_n^{(1)}) - \alpha_{12}(\phi_n^{(2)} - \phi_n^{(1)}) - \beta_{12}(\phi_{n-1}^{(2)} - \phi_n^{(1)}) = 0 \quad \text{(F.3a)}$$

$$m_n\ddot{u}_n^{(2)} - \alpha_{11}(u_n^{(1)} - u_n^{(2)}) - \beta_{11}(u_{n+1}^{(1)} - u_n^{(2)}) - \alpha_{12}(\phi_n^{(1)} - \phi_n^{(2)}) - \beta_{12}(\phi_{n+1}^{(1)} - \phi_n^{(2)}) = 0 \quad \text{(F.3b)}$$

$$j_n\ddot{\phi}_n^{(1)} - \alpha_{21}(u_n^{(2)} - u_n^{(1)}) - \beta_{21}(u_{n-1}^{(2)} - u_n^{(1)}) - \alpha_{22}(\phi_n^{(2)} - \phi_n^{(1)}) - \beta_{22}(\phi_{n-1}^{(2)} - \phi_n^{(1)}) = 0 \quad \text{(F.3c)}$$

$$j_n\ddot{\phi}_n^{(2)} - \alpha_{21}(u_n^{(1)} - u_n^{(2)}) - \beta_{21}(u_{n+1}^{(1)} - u_n^{(2)}) - \alpha_{22}(\phi_n^{(1)} - \phi_n^{(2)}) - \beta_{22}(\phi_{n+1}^{(1)} - \phi_n^{(2)}) = 0 \quad \text{(F.3d)}$$

where the coefficients can be derived from the second derivative of the potential energy of each unit cell as detailed in the reference [192]. With the design parameters and mechanical parameters in Table F.1 and Table F.2, the coefficients can be determined to be $\alpha_{11} = \beta_{11} = 26850\ \mathrm{N \cdot m^{-1}}$, $\alpha_{12} = -\beta_{12} = -819.8\ \mathrm{N \cdot rad^{-1}}$ and $\alpha_{22} = \beta_{22} = 26.07\ \mathrm{N \cdot m \cdot rad^{-1}}$. The periodic boundary condition (Bloch's theorem) is then applied to the linearized equation of motion, such that $u_{n-1}^{(2)} = u_n^{(2)} e^{-2ikh_0}$, $\phi_{n-1}^{(2)} = \phi_n^{(2)} e^{-2ikh_0}$, $u_{n+1}^{(1)} = u_n^{(1)} e^{2ikh_0}$ and $\phi_{n+1}^{(1)} = \phi_n^{(1)} e^{2ikh_0}$. The band structure $\omega(\mathbf{k})$ can be obtained by solving the eigenvalue equation as a function of the Bloch wave vector $\mathbf{k}$ in the first Brillouin zone:

$$[\hat{D}(\mathbf{k}) + \omega^2]U = 0 \quad \text{(F.4)}$$

Here, ω denotes the angular frequency. $\hat{D}(\mathbf{k})$ is the dynamical matrix as a function of $\mathbf{k}$ and U is the corresponding eigenmode $U = [\sqrt{m}u^{(1)}, \sqrt{m}u^{(2)}, \sqrt{j}\phi^{(1)}, \sqrt{j}\phi^{(2)}]^T$.

F.2 Error analysis in different training ratios

Although the training ratio for the giDMD model of our aforementioned examples is set to be 60%, we also investigate the sufficiency of the training ratio to build an effective and reliable model to describe the origami dynamics. The relative error in different training ratios are calculated for two examples [Figure F.1(a) for the dual origami structure and Figure F.1(b) for the origami chain]. Figure F.1(a) shows the relative error of axial and rotational displacement in the left and right panels, respectively. It can be seen that 20% training ratio is enough to build the effective giDMD model for most cases of intrawell periodic motion in the dual origami structure. However, giDMD fails to model the interwell periodic motion no matter what the training ratio is. The effective modeling for the chaotic motion can be achieved as early as when the training ratio is 20%. The corresponding model cannot precisely describe the intermittent change of chaotic motion as illustrated in Figure 7.4(f) in the main text, resulting in the large relative error. However, it can show the spectral features of the chaotic motion (large low-frequency components) as shown in Figure 7.5(b). Note that large training ratio does not always guarantee the effective giDMD model as shown by the white areas in the region of large training ratios. Figure F.1(b)

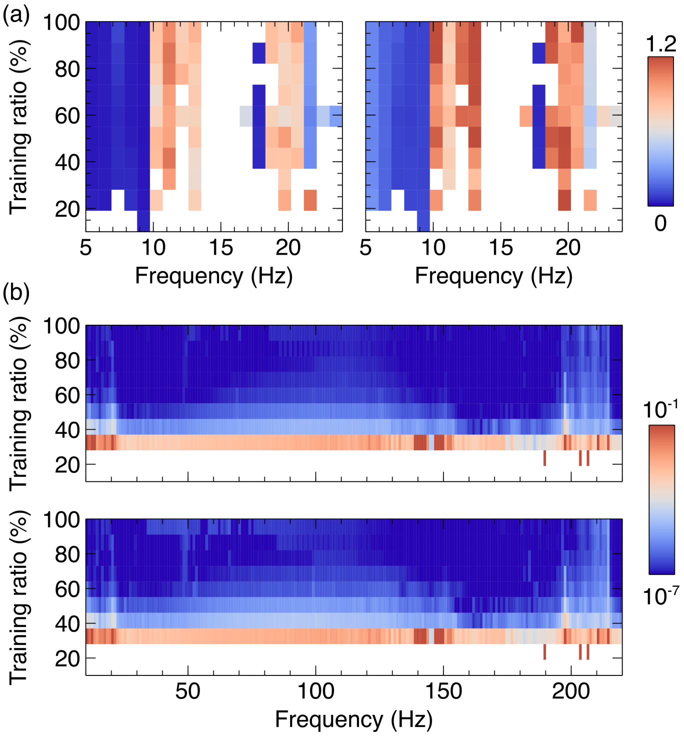

Figure F.1: The prediction accuracy for the dual origami structure and the origami chain using different training ratios. (a) The relative errors as a function of training ratio of axial and rotational displacement in different frequencies for dual origami structure are shown in the left and right panel, respectively. (b) The relative errors as a function of training ratio of axial and rotational displacement in different frequencies for the origami chain are shown in the left and right panel, respectively. The white regions indicate the failure of the prediction in (a) and (b).

shows the relative error of axial and rotational displacement in the top and bottom panels, respectively. It can be seen that the effective model can be constructed as early as when the training ratio is 30%. Besides, the model across frequencies can be built with high accuracy. The error analysis in different training ratio shows the efficacy of our approach with only a few training data, which demonstrates the possibility of early prediction in origami dynamics.

F.3 Identification of state in different training ratios

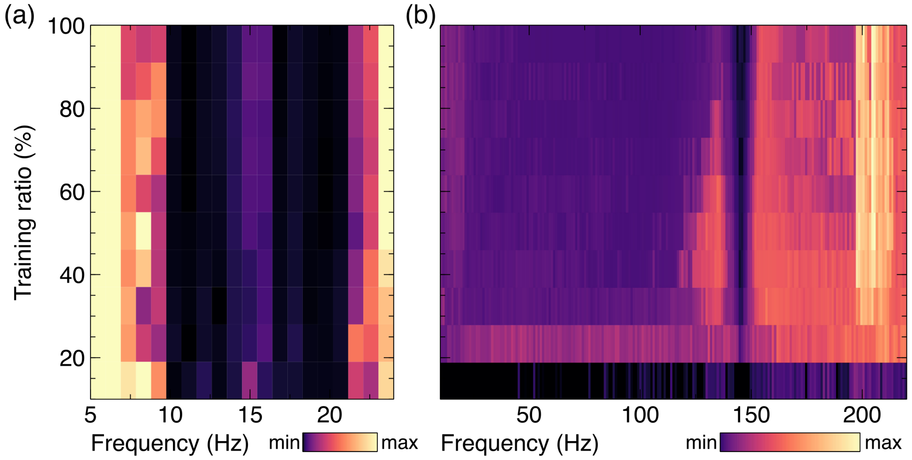

Figure F.2: The singular values of **K** matrix for dual origami structure and origami chain using different training ratios. (a) The first singular value of **K** matrix as a function of training ratio in different frequencies for dual origami structure. (b) The fifth singular value of **K** matrix as a function of training ratio in different frequencies for origami chain.

As stated in the main text, the 'state' of the origami structure may be induced by the singular value of **K** matrix. We further calculate the singular values of **K** matrix in different training ratios to identify the 'state' in origami structures. The second singular value of **K** matrix in different training ratios is calculated for the dual origami structure [Figure F.2(a)], and the fifth singular value is calculated for the origami chain [Figure F.2(b)]. Figure F.2(a) reveals that the intrawell periodic motion, interwell periodic motion and chaotic motion can be initially identified by distinct values when the training ratio is only 10%, although it should be noticed that at this training ratio the giDMD models for different frequencies are not adequate to describe the origami dynamics. In the origami chain, the fifth singular value is used to conduct identification to have a stronger contrast although other singular values also work. The topological boundary state can be identified when the training ratio is 20% even though the model is not effectively built. This study on different training ratios indicates that our approach of giDMD can identify the ‘state’ of origami structures at the early stage, which helps with the early diagnosis and identification of the origami structure.

VITA

Shuaifeng Li was born in Gansu, China. In June 2017, he graduated from Huazhong University of Science and Technology, Wuhan, China, with the Bachelor degree (B.S.) in Materials Science and Engineering. He then began working as a research assistant in Laboratory for Soft Intelligent Materials and Devices, led by Professor Jianfeng Zang, in Optical and Electronic Information at the Huazhong University of Science and Technology. Afterwards, in September 2018, he joined Laboratory for Engineered Materials and Structures, led by Professor Jinkyu Yang, at the University of Washington. In June 2023, he earned the Doctoral degree (Ph.D.) in Aeronautics and Astronautics from University of Washington, Seattle, Washington, USA.